Étude de nouveaux conducteurs protoniques pour des cellules à oxyde solide à haute température

Anastasia Iakovleva

université PARIS-SACLAY

CentraleSupélec

NNT : 2015SACLC016

THESE DE DOCTORAT
DE
L'UNIVERSITE PARIS-SACLAY
PREPAREE A
"ECOLE CENTRALESUPELEC"

ECOLE DOCTORALE N° 573
Interfaces : approches interdisciplinaires / fondements, applications et innovation

Spécialité de doctorat Chimie

Par

Mme Anastasia Iakovleva

Study of novel proton conductors for high temperature Solid Oxide Cells

Thèse présentée et soutenue à « Châtenay-Malabry », le « 30 Octobre 2015 » :

Composition du Jury :

Mme. Irina ANIMITSA	Professeur à l'Université Fédérale de l'Oural	Président
Mme. Rose-Noëlle VANNIER	Professeur à L'ENSCL	Rapporteur
M. Christos ARGIRUSIS	Professeur à l'Université Technique Nationale d'Athènes	Rapporteur
M. Anthony CHESNAUD	Responsable Scientifique à Ecole des Mines ParisTech	Examinateur
M. Guilhem DEZANNEAU	Directeur du laboratoire SPMS	Directeur de thèse

Acknowledgements

This work has been done in the Laboratoire “Structures, Propriétés et Modélisation des Solides” (SPMS) of the Ecole CentraleSupelec and Centre National de la Recherche Scientifique (C.N.R.S., U.M.R.8580).

My first huge thanks to Guilhem Dezanneau, my supervisor, for giving me the opportunity of doing my PhD in this laboratory and in his group, for guiding me during this thesis, for his help, patience and kind attention.

I would like to sincerely thank Mme. Rose-Noelle Vannier, Professor of the University of Lille, and M. Christos Argirusis, Associate Professor at National Technical University of Athens for having accepted to be the reviewers of my thesis, and M. Anthony Chesnaud for accepting as the examiner of my thesis, for his help and collaboration.

I am deeply grateful to Irina Evgenievna Animitsa, my russian Professor. Thank you for guiding me during my university years, for introducing me to solid-state electrochemistry, for your help, advices and support during my PhD thesis.

I want to say a great thanks to Igor Kornev, Professor at SPMS laboratory, for all our conversations in Russian, attention, your help and advices.

I would like to my sincere gratitude to Christine Vinée-Jacquin for all your kindness, attention and invaluable help with my professional and personal issues. I would be absolutely lost in these thousands of french papers without your help. Thank you!

I’m also thankful to Ingrid Canero-Infante for your energy, always positive mood and great time we spent together.

I would like to thank to all laboratory team: Christine Bogicevic and Fabienne Karolak for their help in experiments; Nicolas Guiblin for the help with X-Ray diffraction experiments; Gilles Boemare for the help with repair of different equipment in the lab, especially isostatic press and nice talks during that; Brahim Dkhil for your sparkling humor, energy and advices. And I would also thank to Jean-Michel Kiat, Jean-Michel Gillet, Pierre-Eymeric Janolin, Pierre Becker, Sandrine Geiger, Hichem Dammak, Pascale Salvini, Pascale Gemeiner, Michel Jouan, Thierry Martin, Agnès Bénard, Claire Roussel, Hubert Jubeau, Xavier Bril. Without their help, I could not have finished my thesis on time.

I would also like thank all PhD students and post-docs from the laboratory: Camille Exare, Romain Fayo, Yang Liu, Desirée Ciria, Cintia Hartmann, Fabien Brieuc, Mohamed Ben Hassine, Xiaofai Bai, Gentien Thorner, Bo Bo TIAN, Wen Jing Li, Xiao Xuan SHI, Bertrand Clair, Yang Hu and Michael Anoufa. They gave me many suggestions and help, and we spent a lot of unforgettable

time together.

A very special thanks to Charles Paillard and Sergei Prokhorenko for your positive mood, support, a lot of serious and funny talks, for your patience and courage during our driving lessons.

I would also like to thank Charlotte Cochard for our conversations in French and English and great concerts we attended together.

I would like to sincerely thank to my friend Nadia for your help, support and fantastic time we spent together in Russia and Europe.

I am deeply grateful to all my family and friends, who stay in Russia but never forget about me. First of all, to my mom, for your love and care, for your wise advices and patience; to my grandparents, uncle, aunt, my sister Julia and brother Danil. Thank you for believing in me, understanding and supporting me in the choices I've made even if they kept us far away from each other for a while.

université PARIS-SACLAY

ÉCOLE DOCTORALE
INTERFACES
Approches Interdisciplinaires : Fondements, Applications et Innovation

Titre : Étude de nouveaux conducteurs protoniques pour des cellules à oxyde solide à haute température

Mots clés : Céramique, pile à combustible, conductivité, conducteurs protoniques, des unités tétraédriques, la synthèse de chimie humide

Résumé : L'objectif principal de ce travail était l'étude systématique de plusieurs groupes de matériaux conducteurs protoniques: $Gd_{3-x}Me_xGaO_{6-\delta}$ (Me = Ca^{2+}, Sr^{2+}), $Ba_2Nb_{1-x}Y_{1+x}O_{6-\delta}$, and $BaZr_{0.85}Y_{0.15}O_{3-\delta}$ (BZY15). Nous avons développé une voie de synthèse pour chaque groupe de matériaux tels que le procédé de combustion sol-gel, la synthèse lyophilisation et le procédé de complexation de citrate-EDTA modifié. Des nanopoudres pures et des céramiques denses ont été obtenus après ces synthèses suives d'un processus de frittage classique. La structure et la composition des produits obtenues ont été caractérisées par diffraction des rayons X (XRD) et microscopie électronique à balayage (MEB). La variation de la conductivité en fonction de la température a été étudiée par spectroscopie d'impédance, ainsi que la dépendance en fonction de pO_2 et pH_2O. Pour la famille de $Gd_{3-x}Me_xGaO_{6-\delta}$ (Me = Ca^{2+}, Sr^{2+}), nous avons étudié l'influence de la nature et la quantité de dopant sur les propriétés structurales et électriques. Les résultats indiquent une solution solide possible jusqu'à 10% de taux du substituant. Selon les observations au MEB, la taille des grains est augmente le taux de substitution. En ce qui concerne les propriétés électriques, nous avons constaté une augmentation de la conduction avec le taux de substitution. Tous les composés présentent une bonne stabilité en milieu humide, sous hydrogène et CO_2. Dans le cas des matériaux $Ba_2Y_{1+x}Nb_{1-x}O_{6-\delta}$, les propriétés physico-chimiques des matériaux synthétisés ont été caractérisées par la diffraction des rayons X et par MEB. La taille moyenne des grains a considérablement augmenté avec l'augmentation du taux de Y^{3+}. Les propriétés de conduction ont été légèrement améliorées avec la substitution partielle de niobium par l'yttrium. La stabilité de $Ba_2Y_{1+x}Nb_{1-x}O_{6-\delta}$ composés a été étudiée sous différentes atmosphères et conditions. Les propriétés de conduction ionique restent modestes ce qui a été explique par des simulations de dynamique moléculaire. Enfin, nous avons étudié l'influence d'emploi d'un additif ZnO et NiO lors de la synthèse de BZY15, les adjuvants de frittage pouvant être utilisés pour abaisser la température de frittage. L'oxyde de zinc comme un adjuvant de frittage permet de diminuer de 300 °C la température de frittage et d'augmenter légèrement la conduction ionique.

Title : Study of novel proton conductors for high temperature Solid Oxide Cells

Keywords : Ceramics, SOFC, conductivity, proton conductors, tetrahedral units, wet chemistry synthesis

Abstract : The main objective of the present work was the systematic study of several groups of materials: $Gd_{3-x}Me_xGaO_{6-\delta}$ (Me = Ca^{2+}, Sr^{2+}), $Ba_2Y_{1+x}Nb_{1-x}O_{6-\delta}$, and $BaZr_{0.85}Y_{0.15}O_{3-\delta}$ (BZY15) as proton conductors. We developed a synthesis route for each group of materials such as microwave- Concerning electrical properties, we found an increase of conduction with increasing dopant content. All compounds present a good stability in humid, hydrogen and CO_2 containing atmosphere. In case of $Ba_2Y_{1+x}Nb_{1-x}O_{6-\delta}$ materials, the physico-chemical properties of synthesized materials have been

assisted citric acid combustion method, freeze-drying synthesis and modified citrate-EDTA complexing method. Pure nanopowders and dense ceramics were obtained after these syntheses plus a classical sintering process. The structure and composition of the obtained products were characterized by X-Ray diffraction (XRD) and scanning electron microscopy (SEM). The temperature dependences of the conductivity were investigated by impedance spectroscopy as a function of pO_2 and pH_2O. For the family of $Gd_{3-x}Me_xGaO_{6-\delta}$ (Me = Ca^{2+}, Sr^{2+}), we studied the influence of dopant nature and content on the structural and electrical properties. Results indicate that the substitution possible till 10 % of doping content. According to the SEM observations, the grain size is increased with increasing dopant content. characterized by the XRD and SEM techniques. The average grain size increased significantly with increasing amount of Y^{3+}. Conduction properties were slightly improved with the partial substitution of niobium by yttrium. The stability of $Ba_2Y_{1+x}Nb_{1-x}O_{6-\delta}$ compounds was investigated under different atmospheres and conditions. The ionic conduction in this case is quite low, which has been explained by futher molecular dynamics simulations. Finally, we studied the influence of an ZnO and NiO additives on the sintering of BZY15, being these sintering aids used to lower the sintering temperature. Zinc oxide as a sintering aid lowers the sintering temperature by 300 °C and slightly increases the bulk and total conductivity of BZY15.

Table of contents

Acknowledgements 3

Abstract 5

Résumé 6

Chapter 1 **Introduction** 10

1.1 Fuel cells: principle, types, advantages 10

1.2 Solid Oxide Fuel Cells (SOFC) and Proton Conducting Fuel Cells (PCFC): principle and components 13

1.3 Proton-conducting electrolyte materials for SOFCs 17

1.3.1 Materials 17

1.3.2 Mobility of proton defects 19

1.3.3 Hydration thermodynamics 20

1.3.4 Isotope effect 22

1.4 Objectives 25

References 27

Chapter 2 **Experimental Techniques** 30

2.1 Introduction 30

2.2 Nanopowders synthesis 30

2.2.1 Microwave-assisted citric acid combustion method 30

2.2.2 Modified citrate-EDTA complexing method 32

2.2.3 Freeze drying synthesis 34

2.3 Preparation of Ceramics 36

2.4 Chemical and structural characterization 36

2.4.1 X-Ray diffraction analysis 36

2.4.1.a Routine X-Ray diffraction analysis 36

2.4.1.b High-temperature X-Ray diffraction 36

2.4.2 Scanning electron microscopy (SEM) and Energy dispersive spectroscopy (EDS) 37

2.4.3 Dilatometry analysis 38

2.4.4 Transmission electron microscopy (TEM) 39

2.5 Conductivity measurements 40

2.5.1 Fundamentals of electrochemical impedance method 40

2.5.2 Experimental details 43

2.5.3 Controlling of the atmosphere 44
2.5.3.a Controlling of oxygen partial pressure 44
2.5.3.b The humidity controlling 44
References 45
Chapter 3 **Synthesis, structure and electrical properties of $Gd_{3-x}Me_xGaO_{6-\delta}$ ($Me=Ca^{2+}$, Sr^{2+})** 46
3.1 Introduction 46
3.2 Phase equilibrium in $Ln_2O_3 - Ga_2O_3$ binary systems 49
3.3 Objectives of the study 53
3.4 Structural properties of $Gd_{3-x}Me_xGaO_{6-\delta}$ ($Me=Ca^{2+}$, Sr^{2+}) compounds 54
3.4.1 Structural analysis of $Gd_{3-x}Me_xGaO_{6-\delta}$ ($Me=Ca^{2+}$, Sr^{2+}) powders 54
3.4.2 High temperature X-Ray diffraction and thermal expansion coefficient 56
3.4.3 Structural analysis of $Gd_{3-x}Me_xGaO_{6-\delta}$ ($Me=Ca^{2+}$, Sr^{2+}) sintered pellets 57
3.4.4 Microstructural analysis of $Gd_{3-x}Me_xGaO_{6-\delta}$ ($Me=Ca^{2+}$, Sr^{2+}) sintered pellets 62
3.4.5 Chemical stability 67
3.5 Transport and hydration properties 69
3.5.1 Impedance spectra of $Gd_{3-x}Me_xGaO_{6-\delta}$ ($Me = Ca^{2+}$, Sr^{2+}) 69
3.5.2 Transport properties of solid solutions $Gd_{3-x}Me_xGaO_{6-\delta}$ ($Me = Ca^{2+}$, Sr^{2+}) as a function of temperature 70
3.5.3 Transport properties as a function of $p(O_2)$ 74
3.6 Conclusion 77
References 79
Chapter 4 **Synthesis, structure and electrical properties of $Ba_2Y_{1+x}Nb_{1-x}O_{6-\delta}$** 81
4.1 The perovskite background 81
4.1.1 Simple perovskite structure 81
4.1.2 Double perovskite structure 83
4.1.3 Structural properties of $Ba_2LnB'X_6$ (*Ln*=lanthanide, In and Y, B'= Nb^{5+} and Ta^{5+}) 86
4.1.4 Electrical properties of $A_2LnB'X_6$ (A= Ba^{2+}, Sr^{2+}, Ca^{2+}, *Ln*=lanthanide, In and Y, B'= Nb^{5+} and Ta^{5+}) 93
4.2 Objectives of the study 98
4.3 Structural properties of $Ba_2Y_{1+x}Nb_{1-x}O_{6-\delta}$ compounds (x = 0, 0.05, …, 0.25) 99
4.3.1 Structural characterization of sintered pellets 99
4.3.2 Microstructural characterization of sintered pellets 107
4.3.3 Chemical stability 109
4.4 Transport properties 111
4.4.1 Transport properties as a function of T. Analysis of impedance spectra 111

4.4.2 Transport properties as a function of $p(O_2)$ 115
4.5 Molecular dynamics simulations 116
4.5.1 Calculations details 116
4.5.2 Results 117
4.5.2.1 Room temperature simulations 117
4.5.2.2 High temperature simulations 118
4.6 Transmission Electron Microscopy (TEM) 121
4.6.1 Objective 121
4.6.2 Description of the experiment 121
4.6.2.1 Principle of the Focus Ion Beam 121
4.6.2.2 FIB preparation for TEM 122
4.6.3 Results 122
4.7 Conclusion 125
References 127
Chapter 5 **Synthesis, structure and electrical properties of BZY15** 130
5.1 Introduction 130
5.1.1 Structure of Barium Zirconate 130
5.1.1 Chemical Stability 131
5.1.2 Conductivity properties of Doped Barium Zirconate 133
5.2 Objectives of the study 135
5.3 Structural and microstructural properties of BZY15 135
5.3.1 Enhanced Sintering of Yttrium doped Barium Zirconate by addition of ZnO and NiO 138
5.4 Transport properties 143
5.5 Conclusion 147
References 148
Chapter 6 **General conclusions and perspectives** 150
6.1 Summary 150
6.2 Perspectives 152

Chapter 1 Introduction

1.1 Fuel cells: principle, types, advantages

Renewable energy sources are an infinite resource unlike energy produced from fossil fuels. Natural phenomena such as sunlight, wind, waves, water flow, biological processes and geothermal heat are some of the renewable energy sources available to mankind. But they are site-specific and intermittent, which is not suitable for continuous energy supply. Therefore storage or energy carriers are needed [1-4]. Hydrogen and fuel cells are seen by many as key solutions for the 21st century, enabling clean efficient production of power and heat from a range of primary energy sources. Hydrogen, which is transportable and storable, could serve as an attractive option for energy carrier, as a precursor for synthetic fuels when combined with CO_2, as well as a potential clean fuel for many applications, such as for heating, electricity and vehicles [5-7]. Fuel cells will be used in a wide range of products, ranging from very small fuel cells in portable devices such as mobile phones and laptops, through mobile applications like cars, delivery vehicles, buses and ships, to heat and power generators in stationary applications in the domestic and industrial sector. Future energy systems will also include improved conventional energy converters running on hydrogen (e.g. internal combustion engines, Stirling engines, and turbines) as well as other energy carriers (e.g. direct heat and electricity from renewable energy, and bio-fuels for transport) [8].

Fuel cells are electrochemical devices that convert directly chemical energy present in fuels into electrical energy, see **Figure 1.1.** They are a promising alternative to traditional power generation with high efficiency and low environmental impact. Because the intermediate steps of producing heat and mechanical work typical of most conventional power generation methods are avoided, fuel cells are not limited by thermodynamic limitations of heat engines such as the Carnot efficiency. In principle, fuel cell works like a battery in sense that it also produces electrical energy through electrochemical processes. However, unlike a battery, a fuel cell cannot run out as long as fuel is continuously supplied. This is interesting for applications in which absolutely reliable energy supply is needed like military and health care.

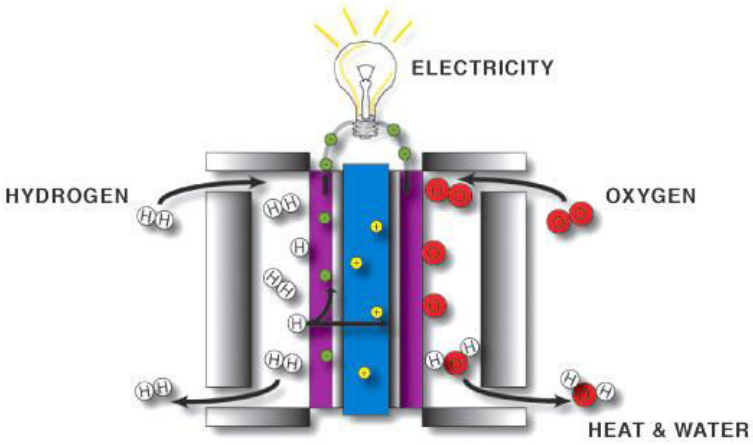

Figure 1.1 Simple scheme of working fuel cell [9]

Typically, fuel cell consists of three main sections: anode, electrolyte and cathode. A fuel and an oxidant, supplied from external sources, are introduced to the anode and cathode side, respectively. Both could be any gases capable of being electrochemically oxidised and reduced. The driving force of the operation is the chemical potential gradient of ions across the electrolyte. Direct-current electricity is consequently produced in the external circuit. In the real application, fuel cells are connected in a series of cells in order to obtain higher outlet voltage. An interconnect plate is always installed to provide the electronic contact between the anode of one cell and the cathode of the next cell [10].

Normally a fuel cell is classified by the type of working electrolyte. The electrolyte determines the chemical reactions that take place in the cell, the catalysts required, and the temperature range in which the cell operates. Fuel cells can also be divided according to their operating temperatures [11]. As seen in Table 1.1, the first three types of fuel cells may be classified as low temperature fuel cells, the remaining two being high temperature fuel cells. A key point is the relative flexibility regarding the fuel, function of the operating temperature:

✓ for low temperatures fuel cells like PEMFC, the use of hydrogen is necessary unless in the direct methanol technology.

✓ on the contrary, for high temperatures devices the use of hydrocarbons like natural gas is possible. In these cases, the high operating temperatures give the possibility to reform internally the hydrocarbons into hydrogen. Hydrocarbons being natural and quite inexpensive compared to the expensive synthesized hydrogen, this possibility are a strong asset for SOFC technology.

Table 1.1 Types of fuel cells [11]

	Type of Fuel Cell				
	PEM	AFC	PAFC	MCFC	SOFC
Electrolyte	Polymer, Proton exchange membrane	Potassium hydroxide (KOH)	Phosphoric acid	Molten salt (nitrate, carbonate…)	YSZ
Working Temperature (°C)	50-80	50-200	~ 220	~ 650	500-1000
Fuel	H_2 (from hydrocarbons or methanol)	H_2 or hydrazine	H_2 (from hydrocarbons or alcohol)	H_2, CO_2, natural gas, propane	H_2, natural gas, propane
Oxidant	O_2/Air	O_2/Air	O_2/Air	CO_2/O_2/Air	O_2/Air
Mobile Ion	H^+	OH^-	H^+	CO_3^{2-}	O^{2-}/H^+
Anode Catalyst	Platinum	Platinum	Platinum	Nickel	Nickel

Fuel cells have various advantages compared to conventional power sources, such as internal combustion engines or batteries, which feature more or less strongly for different types and lead to different applications (**Figure 1.2**).

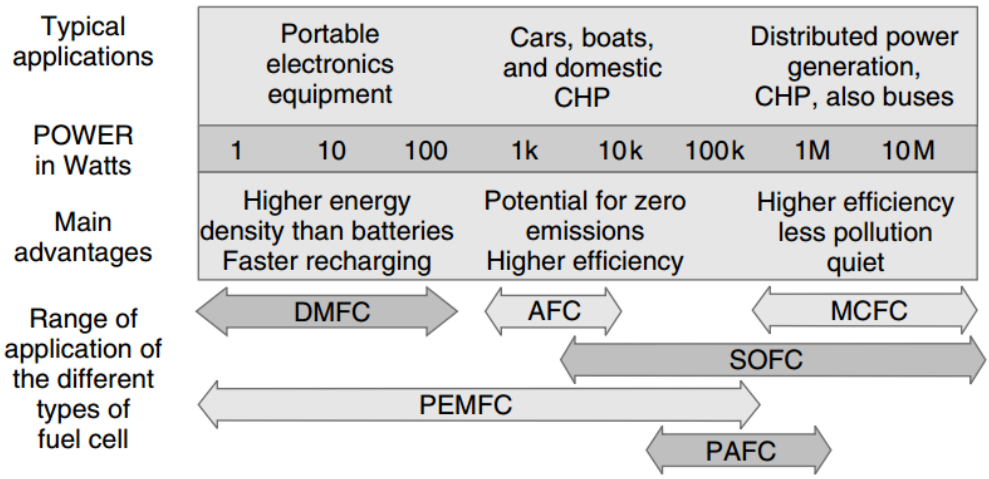

Figure 1.2 Chart to summarize the applications and main advantages of fuel cells of different types, and in different applications [11]

Although some of the fuel cells attributes are only valid for some applications, most advantages are more general [11, 12]:

✓ Fuel cells are generally more efficient than combustion engines whether piston or turbine based.

✓ Low temperature fuel cells (PEMFC, DMFC) have low heat transmission which makes them ideal for military applications. Higher temperature fuel cells produce high-grade process heat along with electricity and are well suited to cogeneration applications (such as combined heat and power for residential use).

✓ Fuel cells do not need conventional fuels such as oil or gas and can therefore reduce economic dependence on oil producing countries, creating greater energy security for the user nation.

✓ Low emissions. The by-product of the main fuel cell reaction, when hydrogen is the fuel, is pure water, which means a fuel cell can be essentially 'zero emission'. This is their main advantage when used in vehicles, as there is a requirement to reduce vehicle emissions, and even eliminate them within cities. However, it should be noted that, at present, emissions of CO_2 are nearly always involved in the production of hydrogen that is needed as the fuel.

✓ Fuel cells are very quiet, even those with extensive extra fuel processing equipment. This is very important in both portable power applications and for local power generation in combined heat and power schemes.

The most important disadvantage of fuel cells at the present time is the same for all types – the cost. Also the fact that hydrogen is the preferred fuel in fuel cells is one of their principal disadvantages as well.

1.2 Solid Oxide Fuel Cells (SOFC) and Proton Conducting Fuel Cells (PCFC): principle and components

SOFCs differ in many respects from other fuel cell technologies. First, they are composed of all-solid-state materials. Second, SOFCs operate at temperatures between 600 °C and 1000 °C where the ionic conductivities of the electrolyte materials is high enough to assure efficiently the transport of O^{2-}. Third, the solid state character of all SOFC components means that there is no fundamental restriction on the cell configuration [13]. Similar to other type of fuel cells, SOFCs require fuel such as hydrogen, and oxidant reactants such as oxygen or air to electrochemically react at high temperature and generate electrical energy. Hydrogen is normally used as the fuel since it has high electrochemical activity, but carbon monoxide can be also used as the fuel together with hydrogen. The direct use of a hydrocarbon gas instead of hydrogen or carbon monoxide is also possible when operated as internal reforming. **Figure 1.3** shows the principle of electrochemical cell for SOFC. One important challenge in improving SOFC technology is to reduce the working temperature to 500–700 °C. Such intermediate-temperature SOFCs would hasten implementation of this technology in distributed

combined heat and power (CHP) systems. In addition, lowering the working temperature is advantageous in terms of long-term operation, materials stability, cost and safety [14-18].

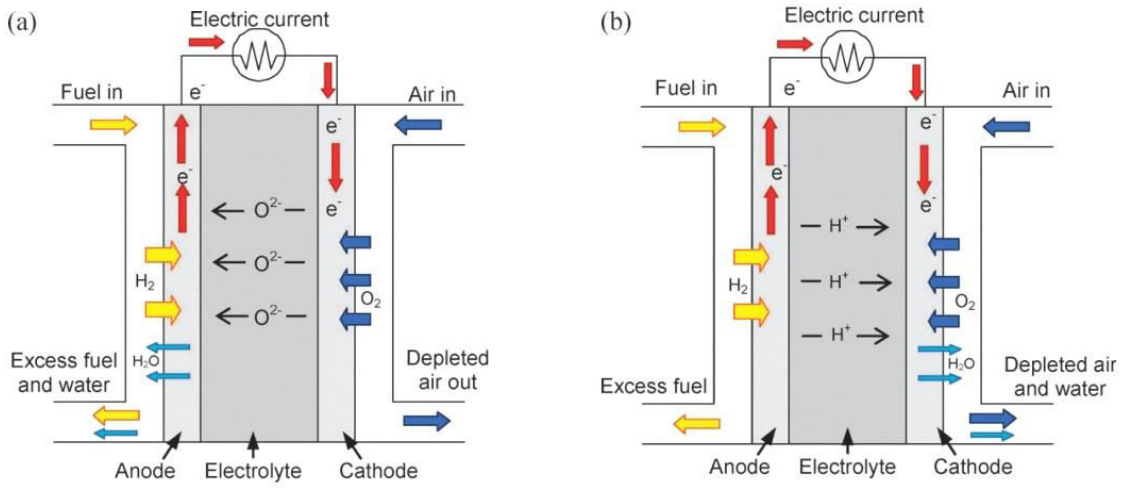

Figure 1.3 Schematic diagram of the processes taking place in a solid oxide fuel cell (SOFC) during operation; (a) oxide-ion conducting electrolyte, and (b) proton conducting electrolyte [14]

In a classical SOFC based on anion-conducting electrolyte, the reduction of oxygen occurs at the cathode and the resulting O^{2-} anion is then transported across the electrolyte till the anode side, where it will combine with H_2 gas to form gaseous water. The two half-reactions of oxidation/reduction involve exchanges of electrons that circulate in the external circuit. In Proton Conducting Fuel Cells (PCFC), hydrogen is oxidized into H^+ and this H^+ is carried out till the cathode through the proton conducting electrolyte. H^+ ions then react with O_2 gas to form gaseous water. Intrinsically, the oxide ion-conducting fuel cell produces then water vapor on the anode side, which lowers the cell voltage, and reduces fuel utilization and requires considerable fuel circulation [19]. A proton-conducting fuel cell, on the other hand, produces water at the cathode. The high air flow usually used takes care of this, while the anode fuel gas remains undiluted by water vapor, keeping the Nernst voltage high [20].

The main components of a single cell are electrolyte, cathode and anode. When single cells are stacked together to generate more power, two more cell components namely the interconnect and the sealant are required. Material specifications for SOFCs are gathered in Table 1.2. The solid electrolyte is between the electrode (anode and cathode) to conduct the ions of O^{2-} but not conduct electron, thus the current passes through the device via the external circuit. The fuel is oxidized at the anode and the oxygen is reduced at the cathode [21] according to following reactions:

Cathode Reaction: $\frac{1}{2}O_2(gas) + 2e^- \rightarrow O^{2-}$ (1.1)

Anode Reaction: $H_2(gas) + O^{2-} \rightarrow H_2O(gas) + 2e^-$ (1.2)

Overall Reaction: $H_2(gas) + O^{2-} \rightarrow H_2O(gas)$ (1.3)

Table 1.2 Main specifications for SOFC constituting materials [20]

	Material requirements	**Density**	**Ionic conductivity**	**Electronic conductivity**
Anode	Chemical stability under reducing atm. (pO_2 ~10^{-18} Atm)	Porous (20–40%) Preferably with gradient	Delocalise the electrochemical reaction	Highest (Ni-Cermet 10^3 S cm^{-1} at 800–900 °C)
Electrolyte	Chemical stability under high pO_2 gradient (10^{-18} Atm to 1 Atm)	Dense (≥ 95%)	Highest (YSZ: 10^{-1} S cm^{-1} at 1000 °C, 10^{-2} S cm^{-1} at 750 °C)	Negligible compared to ionic conductivity
Cathode	Chemical stability under oxidising atm. (pO_2 ~ 1 Atm)	Porous (20–40%) Preferably with gradient	Delocalise the electrochemical reaction	Highest (LSM ~ 10^2 S cm^{-1} at 800–900 °C)
Interconnect	Chemical stability and corrosion resistance	Dense (≥ 95%)	-	Highest (including protective coating & oxide layer)

The cathode has to be porous and stable under oxidising conditions. This layer is conducting for electrons and ideally also for ions. Different mixed ionic-electronic conductors with perovskite structure have been proposed in the last few years as potential cathode materials for SOFC, such as cobaltites, ferrites, nickelates and double perovskites. However, they usually exhibit chemical and thermal expansion incompatibilities with yttria stabilized zirconia (YSZ) electrolyte [22-24]. Sr-doped lanthanum manganites, $La_{1-x}Sr_xMnO_{3-\delta}$ (LSM), are the most common cathode material used in SOFC systems due to their high stability under oxidant atmospheres and high temperatures compared to other alternative materials [25-28]. The LSM class of compounds combines poor oxide ion conductivity with a very favorable electronic conductivity due to the partial oxidizing of Mn^{4+} in Mn^{3+}. One problem lies in the formation of $La_2Zr_2O_7$ at the interface between LSM and YSZ; on the other hand, LSC has a better ionic conductivity but presents a poor stability in presence of classical electrolytes at the working temperature [29].

The anode materials can be mixed conductors and thus typically contain transition metals to provide the electronic conductivity. Also it should be compatible (chemical and thermal expansion) with the electrolyte and provide means for transport of gas from the fuel, oxygen ions from the electrolyte and electrons to the interconnect. The catalytic properties of the anode to the fuel oxidation

reaction are also important, particularly as the operating temperature is decreased. The most widely used anode for SOFCs is a cermet of nickel and yttria-stabilized zirconia (YSZ) [30-33].

Electrolytes for SOFCs are solid and dense metal oxides. They should exhibit high ionic conductivity, however, combined with low electronic conductivity. Other requirements for the electrolyte of SOFCs are stability under both oxidation and reduction conditions, long term chemical stability and mechanical compatibility with the electrode materials [23]. Their development started in the 50's after the discovery of the crucial importance of anion vacancies in conduction mechanisms by Wagner [34]. Almost all SOFC systems currently being developed employ a stabilized zirconia (ZrO_2), especially yttria stabilized zirconia, because this material has an adequate level of oxide ionic conductivity and shows the desirable stability in both oxidizing and reducing environments, as well it is also abundant, relatively low in cost and is strong whilst being easy to fabricate. Dopant concentration is often fixed between 8 % and 10 % which prevents the formation of ordered domains of vacancies. The main disadvange is the required high temperature of use, which implies the use of ceramics as interconnects and leads to problems regarding the thermal cycling of interconnects [35, 36]. Strontium and magnesium doped lanthanum gallate (LSGM) was discovered more recently and has an ionic conductivity similar to that of doped ceria [37] and it has higher oxygen-ion conductivity than conventional YSZ between 600-800 °C and negligible electronic conductivity [38- 40]. While it is not reducible like ceria, the fact that it is a stoichiometric compound implies that the composition must be precise. LSGM is currently considered as one of the most promising electrolyte materials for intermediate temperature SOFCs [39]. But there are other materials based on different structures which are also used as electrolytes: apatites [41, 42], which present conduction channels [43], the LAMOX family [44], cuspidine-type compounds ($RE_4(Ga_2O_7)O_2$) [45] and finally, BIVEMOX materials [46]. However, none of these new compounds have yet reached a real integration into operating systems.

The interconnects form the connection between the anode of one cell and the cathode of the next in a stack arrangement. Regardless of configurations, interconnect physically separates yet electrically connects anode of one cell to the cathode of the other. The material requirements for the interconnect are the most demanding among the four components (anode, cathode, electrolyte, and interconnect). Successful development of competent and affordable interconnect is vital to the ultimate commercialization of SOFC. W.Z. Zhu *et al.* [47] give several conditions which interconnects need to fulfill:

- ✓ Excellent electrical conductivity with preferably nearly 100 % electronic conduction;
- ✓ Adequate stability in terms of dimension, microstructure, chemistry, and phase at operating temperature around 800 °C in both reducing and oxidizing atmospheres, since they are exposed to oxygen on one side and fuel on the other;
- ✓ Exceptionally low permeability for oxygen and hydrogen to minimize the direct combination of oxidant and fuel during cell operation;

✓ Thermal expansion coefficient (TEC) of interconnect should be comparable to those of electrodes and electrolyte between ambient and operating temperatures, so that the thermal stress developed during stack startup and shutdown could be minimized;

✓ Interconnect should be easy to fabricate, which plays a key role in promoting mass production.

The choice of interconnector materials is dependent on the stack design and majorly on the operating temperature. Ceramic interconnect materials which are oxides such as $LaCrO_{3-\delta}$ system, and are thus stable in oxidizing atmospheres, but typically have lower electrical conductivities as compared to metals. Lowering the operating temperature allows a switch from ceramic to metallic interconnects by effectively diminishing the oxidation rates for metals at the cathode side, showing remarkable advantages such as higher electrical and conductivity, negligible ohmic loss, low cost and easy manufacture [48-51].

1.3 Proton-conducting electrolyte materials for SOFCs

1.3.1 Materials

The search for alternative materials to YSZ has been mainly focused on oxygen-ion conducting electrolytes [52, 53]. However, in the last decade a growing interest has been directed toward high-temperature proton-conducting (HTPC) electrolytes, mainly perovskite-type oxides [50]. HTPC electrolytes show proton conductivity when exposed to hydrogen- or water-vapor-containing atmospheres, achieving suitable conductivity values in the IT range (about 10^{-2} S.cm^{-1} at 600 °C), with an activation energy that is generally smaller than that for oxygen-ion electrolytes [55-59]. These compounds should have several important requirements as electrolyte materials: high ionic conductivity with negligible electronic conductivity under working conditions, chemical stability, good sinterability and good chemical compatibility with Ni, which is the most used hydrogen electrode for both SOFCs [60]. Ceramic proton conductors have a larger ionic transport number than ceria doped gadolinia and better chemical compatibility with conventional SOFC materials than lanthanum strontium gallates (LSGM). Furthermore, these oxides can work in the temperature range 400-750 °C in dependence of their lower activation enthalpies of their conductivity, and they represent a possible alternative to the classical SOFC electrolytes based on yttria stabilized zirconia which operates only at higher temperatures [35].

The first report of protonic conduction at high temperature was given by Iwahara *et al.* [61, 62] in doped ABO_3 perovskites. After more than 20 years of active research, the perovskite-type cerates and zirconates have become well-established proton conducting systems [63-67]. A typical conductivity vs. inverse temperature curve for different proton conductors is shown in **Figure 1.4.** Doped barium cerate electrolytes show high protonic conductivity and satisfactory sinterability [55, 56] but they react with acidic gases (e.g., CO_2 and SO_2) and steam [68-70]. The use of hydrocarbons

as fuel is indeed in this case totally prohibited as it inevitably leads to the formation of CO_2. Chemically stable doped barium zirconate sintered pellets generally have a low total proton conductivity because of the large volume content of poorly conducting grain boundaries. However, electrical measurements of grain-boundary free Y-doped barium zirconate (BZY) thin films demonstrated very high bulk proton conductivity [71], indicating that the reduction of the grain-boundary content can effectively improve the BZY transport properties.

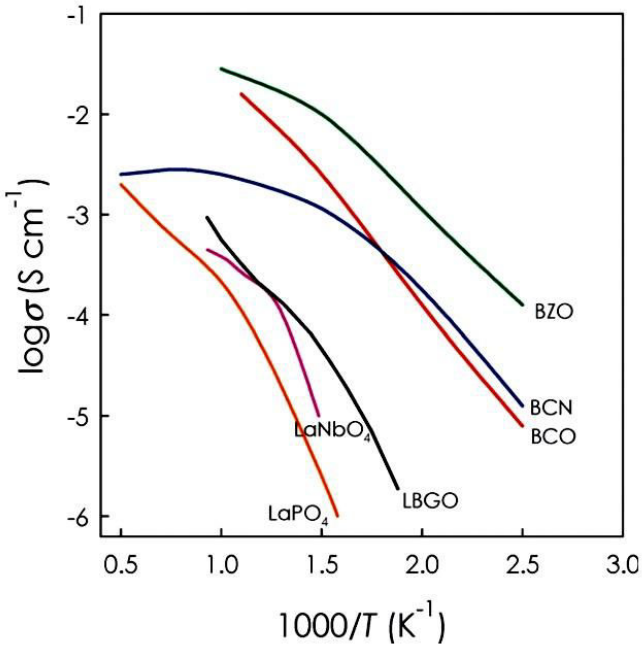

Figure 1.4 Total conductivities of some well-known proton conductors as a function of inverse temperature: $BaCe_{0.9}Y_{0.1}O_3$ (BCO); $BaZr_{0.8}Y_{0.2}O_3$ (BZO); $La_{0.9}Sr_{0.1}PO_4$; $Ba_3Ca_{1.18}Nb_{1.82}O_{8.73}$ (BCN); $La_{0.99}Ca_{0.01}NbO_4$; $La_{0.8}Ba_{1.2}GaO_{3.9}$ (LBGO) [14]

However, it is well known that non-stoichiometry, dopant nature, atmosphere, *etc.,* greatly influence defect reaction and transport properties of proton conductors. For instance, for barium cerate and barium zirconate, it has been reported that BaO evaporates easily from the surface of sintered pellets due to high sintering temperature [72], and some analysis also indicates the possible existence of an amorphous Ba-rich phase at grain boundaries [73]. Barium oxide deficiency may result in the trivalent ion residing on Ba-site. For instance, SEM analysis of Nd-$BaCeO_3$ solid solutions indicated that the solutions could be represented by a general formula $Ba_{1-x}Nd_xCe_{1-y}Nd_yO_{3-(y-x)/2}(V_O^{\cdot\cdot})_{(y-x)/2}$ in which Nd is partioned on both Ba and Ce sites [74]. The existence of Ba^{2+}-site occupation has also been proposed by theoretical calculations for large dopants such as La, Nd and Sm in doped $BaCeO_3$ [75].

$$2Ba_{Ba}^{\times} + M_2O_3 + V_O^{\cdot\cdot} \rightarrow 2M_{Ba}^{\cdot} + O_O^{\times} + 2BaO \qquad (1.4)$$

This reaction consumes oxygen vacancy instead of creating new vacancies, and thus might lower the protonic conductivity.

1.3.2 Mobility of proton defects

The proton conduction is based on the existence of a proton defect in the oxide that is created when the oxide, containing oxygen vacancies, dissociates and absorbs water from a surrounding wet atmosphere, see **Figure 1.5**.

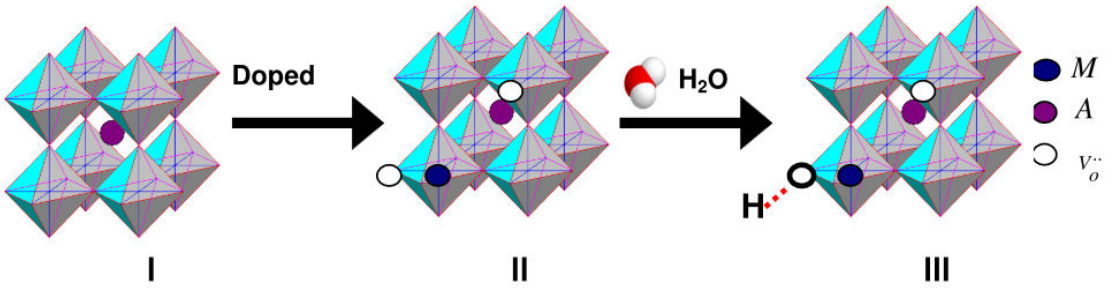

Figure 1.5 Formation of proton defect, from the ideal perovskite to the hydrated one [76]:
I) Perfect lattice, II) Introduction of oxygen vacancies, III) Formation of proton defect

The process can be written according to the following equation [20]:

$$O_O^{\times} + V_O^{\cdot\cdot} + H_2O(\text{vapour}) \leftrightarrow 2(OH)_O^{\cdot} \qquad (1.5)$$

Currently exist two principal mechanisms well recognized to describe the transport of proton: the vehicle mechanism and the Grotthuss mechanism [19, 79, 82, 83]. For the vehicle mechanism, the proton moves together with a "vehicle" as a passenger on a larger ion (H_3O^+ , NH_4^+ , OH^- , *et al.*). This mechanism is mainly observed in aqueous solution, other liquids/metal, and compounds with loose bonded small molecules, which is usually restricted to materials with open structures (i.e. channels, layers) to allow the passage for the large ions and molecules. The other mechanism is the so-called Grotthuss mechanism. This was proposed to explain the high diffusivity of H^+ ions in water and involves the protons tunneling from one water molecule to the next via hydrogen bonding. This mechanism is thought to be at the origin of the high proton mobility in solid acid salts and proton conducting oxides. The proton-conduction mechanism between fixed oxygen sites occurs mainly by rotational diffusion of a proton around an oxygen ion, followed by proton transfer toward a neighbouring oxide ion [77].

Figure 1.6 shows a scheme for a possible proton-conduction mechanism as it was described by E. Traversa *et al.* [54]. To move from the oxygen ion A to the oxygen ion B, firstly, the bond between the cation (red sphere) and the oxygen A should bend. Shortening the bond length between A and B reduces the energetic barrier for proton transfer, so that the proton can form a bond with the oxygen

atom B (from position 1 to position 2). In this position the proton can move towards another oxygen ion likely by means of rotational motion around the oxygen ion B (from 2 to 3) and repeating, then, the same processes as described.

The proton exhibits thermal rotations, stretching vibrations and jumps, and the combination of these processes leads to proton transport:

- ✓ the diffusion of the proton set up the hydrogen bond OH-O between two oxide ions;
- ✓ the distance between these oxide ions decreases;
- ✓ the proton transfers toward the adjacent oxygen ion via the stretching vibrations.

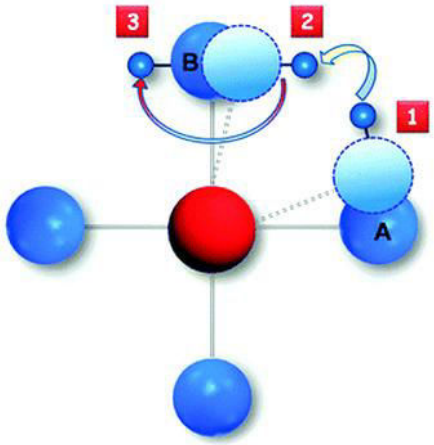

Figure 1.6 Sketch of a possible proton transfer mechanism from the oxygen ion A to oxygen ion B in perovskite oxides [54]

The literature reports contradictory experimental and computational data concerning whether transfer or rotation is the rate-determining step. Several experiments [78, 79] and quantum molecular dynamics simulations [80, 81] indicated proton transfer reaction to be the rate-limiting step and the proton rotational diffusion being the faster reaction with lower activation energy. In contrast, infrared spectral analysis suggested proton transfer as the favourite faster reaction step [82]. A more recent re-analysis [77] of quantum MD simulations, suggested that the two elemental features of the Grotthuss-type conduction mechanism have similar probabilities to occur. Distortions of the perovskite structure can influence the activation energy for proton conduction. In particular, deviations from the ideal cubic perovskite structure mainly lead to a larger activation energy [54].

1.3.3 Hydration thermodynamics

Thermodynamic parameters associated with Equation 1.5 are essential to understand the protonic behaviour of materials. It gives a description of the ability of the material to hydrate and at which temperature this phenomenon occurs. These parameters can be determined either experimentally, via thermogravimetry or conduction measurements, or theoretically using ab-initio or

semi-empirical calculations. From an experimental point of view, it is easy to correlate the thermodynamic parameters of Equation 1.5 to the amount of water incorporated in the material at a given temperature (more detailed calculations are given in the last section of this introduction). Then thermogravimetric measurements are one the most widely used methods to determine the parameters of hydration and **Figure 1.7** presents major results compiled by Kreuer [83].

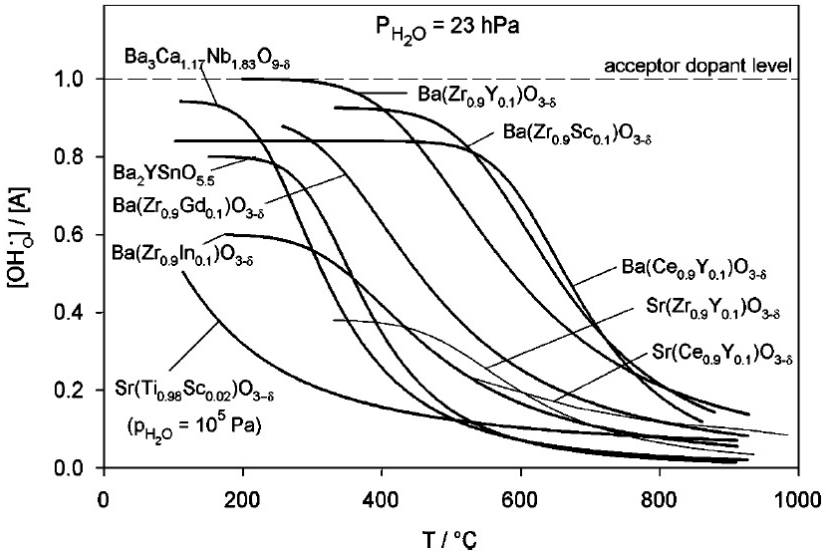

Figure 1.7 Hydration isobars of some doped compounds from Kreuer [83]

Hydration thermodynamic parameters are important in that they determine whether at a given temperature the material is primarily dominated by oxygen vacancies or protons. The enthalpy of hydration (Eq. 1.5) varies considerably, with some apparent correlation to materials properties. Norby e*t al.* [84, 85] reported that the enthalpy of hydration for rare earth sesquioxides becomes more negative as the oxide gets more stable, i.e., as the enthalpy of formation gets more negative, the stable Y_2O_3, Er_2O_3 and Yb_2O_3 thus contain protons up to very high temperatures, while less stable La_2O_3 dehydrates even at very moderate temperatures. However, the mobility of protons decreases as their stability in the oxide increases, the highest proton conductivity being thus obtained as a compromise in the middle of the series, for Gd_2O_3. In perovskite-related oxides, Kreuer *et al.* [83] suggested that the enthalpy of hydration reaction tends to become more negative with decreasing electronegativity of cations interacting with the lattice oxygen, i.e., with decreasing Bronsted basicity of the oxide. Norby *et al.* [84] have developed a correlation between the hydration enthalpy and the difference $\Delta X_{B\text{-}A}$ in electronegativity between the cations populating the B-site and the A-site of the perovskite. A linear trend from the enthalpies can be presented roughly as:

$$\Delta H \text{ (kJ/mol)} = -173(9) + 370(42)\, \Delta X_{B\text{-}A} \qquad (1.6)$$

where $\Delta X_{B\text{-}A}$ is the difference of Allred-Rochow electronegativities of A and cations.

The standard entropies of hydration reaction are usually between -160 $J.mol^{-1}K^{-1}$ and -80 $J.mol^{-1}K^{-1}$. These values are in good agreement with the -188 $J.mol^{-1}K^{-1}$ expected from the loss of one gas molecule per unit reaction. Nevertheless, some perovskites, such as $BaCeO_3$, have large negative values (exothermic) of more than -150 J/mol, and they are thus dominated by protons in wet atmospheres, and suppose a high temperature to shift the equilibrium to the left. Others, such as $SrTiO_3$, have moderate negative entropies and are dominated by protons only at relatively low temperatures [86].

1.3.4 Isotope effect

The isotope effect has been investigated in many of the proton-conducting perovskite-structured oxides. The proton is an ideal candidate for isotope effect studies because of the 2 : 1 mass ratio of the deuteron to the proton. Isotope effects are the changes in the physical or chemical properties resulting from isotopic substitution. HTPCs offer several illustrations of such effects, including changes in the concentration and ionic mobility of the protons and in the electrode kinetics of hydrogen oxidation.

Different theories have been developed to understand the mechanism of isotope effect and protonic conduction. They have been described in an important paper by Nowick and Vaysley [87]. The classical theory is adopted first to describe the isotope effect due to influence of the pre-exponential term of conductivity. If protons are fully replaced by deuterons, classical theory predicts the following relationship between conductivity (u) and mass (m) [88]:

$$\sigma (H^+) / \sigma (D^+) \approx [m (D^+) / m (H^+)]^{1/2} = \sqrt{2} \tag{1.7}$$

For an ionic conductor, the conductivity has an Arrhenius form described by:

$$\sigma = \frac{A}{T} \exp\left(-\frac{E_a}{kT}\right) \tag{1.8}$$

where A is a pre-exponential term, T is the absolute temperature, k is Boltzmann constant and E_a is the activation energy.

Using the experimental value of the conductivity preexponential term for the H_2O-treated sample may be calculated from the following formula [88]:

$$A_H = z\lambda^2 q^2 \omega_0 c_H / 6vk \tag{1.9}$$

where z is the number of directions in which the conductivity jump may occur, λ is the jump distance (taken as the oxygen-oxygen separation), q is the charge of the hopping ion, ω_0 is the frequency factor (taken as the frequency of the OH stretch mode in IR analysis), v is the unit cell volume (of the pseudocubic cell) and k is the Boltzmann constant. Classical theory predicts no difference in the activation energies of migration for protons and deuterons.

The semi-classical theory was firstly described by Nowick and Vaysley [87] and recently improved by N. Bonanos *et al.* [89]. This theory modifies the above model by considering the zero-

point energy of the H/D species in the potential well in which they reside (**Figure 1.8**). The zero-point energies are given by following equations (1.10) and (1.11), in which ν_H and ν_D are vibrational frequencies.

$$E_{0,H} = \frac{1}{2} h\nu_H \tag{1.10}$$

$$E_{0,D} = \frac{1}{2} h\nu_D \tag{1.11}$$

The higher vibrational frequency of H results in a higher zero-point energy and, consequently, a lower energy barrier. As for the pre-exponentials of the conductivity, these should be higher for protons than deuterons by a factor of 1.374 to 1.414, the latter value being usually quoted.

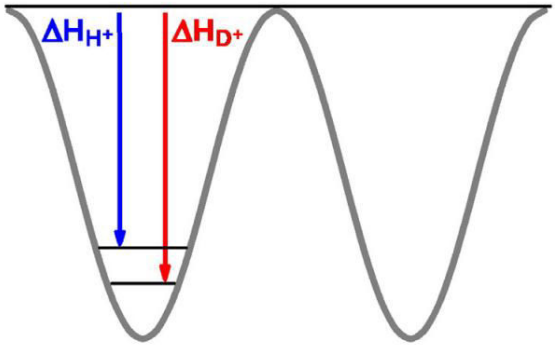

Figure 1.8 Semi-classical picture of proton and deuteron in a finite potential well. The different zero-point energies of the two species results in an activation energy for D^+ migration that is higher than that for H^+ [89]

The conductivity plots for several materials presented on the **Figure 1.9.** It shows that they differ substantially in conductivity values. In all cases the Arrhenius relation for the conductivity is well obeyed, with no breakaway at lower temperatures. Also in all cases E_D is greater than E_H [87].

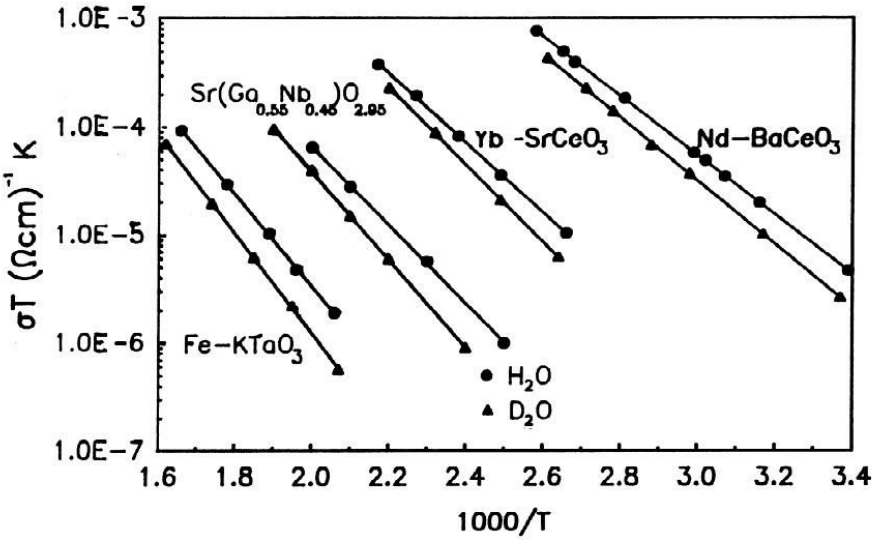

Figure 1.9 Isotope effect on ionic conductivity for four different perovskite structured materials. Data for samples treated in H_2O and D_2O are, respectively, shown as circles and triangles [87]

For the OH-ion in perovskite oxides, the OH stretching frequency ν_H is close to 10^{14} s^{-1} [90], and with $\nu_D / \nu_H = 1 / \sqrt{2}$, we obtain $E_D - E_H \cong 0.055$ eV. If the proton is the dominating charge carrier, the isotope effect will be clearly observable first from conductivities values, then from activation energies. Otherwise it can be concluded that the conductivity mechanism is not protonic.

1.4 Objectives

Families of $Gd_{3-x}Me_xGaO_{6-\delta}$ (Me = Ca^{2+}, Sr^{2+}) and $Ba_2Y_{1+x}Nb_{1-x}O_{6-\delta}$ materials could be an interesting alternative to the yttria-stabilized zirconia. Materials whose structure contains tetrahedral units, such as $Gd_{3-x}Me_xGaO_{6-\delta}$, have attracted significant recent interest because of good stability in atmospheres containing CO_2 and H_2O. Concerning the physical properties, this group of materials can exhibit interesting luminescent properties. These materials would be potentially good candidates for field emission displays (FEDs), and also currently developing technology of the devices (LCD, PDP, OLED) transmission of the image. Among many gallate-based phosphors, Gd_3GaO_6 was recently reported as a host material for the rare earth doping. Rare-Earth oxides usually present a strong affinity toward water uptake which would makes acceptor-doped RE_3GaO_6 materials potential proton conductors to be used as electrolytes materials. This lack of electronic conductivity, required for electrolyte application in SOFC, contributed to the interest in this type of compound.

On the other hand, it is well known that many perovskite-type oxides show high proton conductivity when exposed to wet atmospheres, for example BCN18. It has been recently discovered that dopants in the Nb sites can improve proton conductivity without sacrificing the chemical stability. Other similar compounds could be of great interest, such as $Ba_2Y_{1+x}Nb_{1-x}O_{6-\delta}$ materials. But the information about the structural and electrical properties of them is still not complete and consistent. According to the literature, establishing the correct symmetry in perovskites can be problematic. There are numerous examples of materials being assigned different symmetries, with Ba_2YNbO_6 being a case in point. The degree of Y–Nb ordering and local symmetry is sensitive to the preparative conditions and that low temperature synthetic methods favour highly distorted structures. The aim of this work was, firstly, to determine how the structure evolves as Nb is replaced by Y and check the possibility of ordering and existence of superstructure. Secondly, to investigate the stability and conductivity properties of samples.

$BaZr_{0.85}Y_{0.15}O_{3-\delta}$ (BZY15) appears to be a promising electrolyte, since it was demonstrated that this material was a thermodynamically stable material with high chemical stability in CO_2 containing and humidified atmospheres. However, experimental results show obvious discrepancies and a very low total conductivity. The results from impedance spectroscopy measurements showed that if the grain interior is highly conductive, the grain boundaries are highly resistive and limit the overall conductivity. Thus, strategies for improving total grain boundary conductivity are required. The development of these materials passes through the optimization of their composition, microstructure and understanding of the oxide ion and proton conduction mechanism in the structure. It is in this perspective that this thesis is inscribed. Based on the foregoing, following thesis organized into six chapters.

The **Chapter 1** briefly presents the fuel cells and particularly SOFC and Proton Conducting Fuel Cells (PCFC) and the specifications of the electrolyte material. Also specific of proton conduction mechanism and hydration thermodynamics.

The **Chapter 2** is devoted to the synthesis, instruments and methods for characterization of proton conductors.

In **Chapter 3** we will discuss about doped gadolinium gallates $Gd_{3-x}Me_xGaO_{6-\delta}$ (Me = Ca^{2+}, Sr^{2+}) synthesized by microwave-assisted citric acid combustion method. The objective of this part is the description of the structural and physical properties of a new proton conductors family. Initially, the influence of the oxygen stoichiometry and cationic substitutions was studied to identify the compositions leading to the best conductivities. Then, the sintering conditions of the materials were changed to selected compositions to determine the influence of the microstructure (grain size) on properties. A description of the protonic behavior is given as a function of the content of alkaline earth metals. Also we will present a stability studies under different conditions.

Chapter 4 is devoted to the yttium doped barium niobates $Ba_2Y_{1+x}Nb_{1-x}O_{6-\delta}$ prepared by freeze-drying synthesis. The effects of introducing some oxygen vacancies are presented. Structural and microstructural properties characterized by X-Ray diffraction, scanning electron microscopy (SEM) and transmission electron microscopy (TEM). Conductivity properties are studied under different conditions by varying the temperature (T) and pO_2. The suitability of these materials under operating conditions is presented.

Chapter 5 provides a set of data i.e. microstructure, crystallography, and conductivity for yttrium-doped barium zirconate. The results are compared to the literature values. Optimization of sintering of yttrium-doped barium zirconate through ZnO and NiO additions. Characterize the effects of the sintering aid on sintering, microstructure and electrical properties.

Finally, **Chapter 6** integrates the results of the studies described in the thesis and presents future perspectives.

Each chapter is written with self-contained data along with discussion of the results.

References:

[1] L. Bi, S. Boulfrad, E. Traversa, *Chem. Soc. Rev*., **2014**, 1-16.

[2] N. Armaroli, V. Balzani, *Energy Environ. Sci.,* **2011**, 4, 3193–3222.

[3] K. Christopher, R. Dimitrios, *Energy Environ. Sci.*, **2012**, 5, 6640–6651.

[4] J. Graetz, *Chem. Soc. Rev.*, **2009**, 38, 73–82.

[5] Y. Z. Voloshin, A. V. Dolganov, O. A. Varzatskii, Y. N. Bubnov, *Chem. Commun*., **2011**, 47, 7737–7739.

[6] B. Coelho, A. C. Oliveira and A. Mendes, *Energy Environ. Sci*., **2010**, 3, 1398–1405.

[7] M. Bechelany, A. Abou Chaaya, F. Frances, O. Akdim, D. Cot, U. B. Demirci and P. Miele, *J. Mater. Chem. A*, **2013**, 1, 2133–2138.

[8] Hydrogen Energy and Fuel Cells – A vision of our future, *European Commission*, **2003**.

[9] http://www.greenspec.co.uk/building-design/fuel-cells/

[10] N. Q. Minh, "Ceramic Fuel Cells," *J. Amer. Cer. Soc*., **1993**, 76, 563-588.

[11] J. Larminie, A. Dicks, "Fuel Cell Systems Explained", *Chichester: John Wiley & Sons Ltd*, **2001.**

[12] http://www.fuelcelltoday.com/about-fuel-cells/benefits#sthash.3xfCP8XF.dpuf

[13] A. B. Stambouli, E. Traversa, *Renewable and Sustainable Energy Reviews*, **2002**, 6, 433-455.

[14] L. Malavasi, Craig A. J. Fisher, M. Saiful Islam, *Chem. Soc. Rev.,* **2010**, 39, 4370–4387.

[15] B. C. H. Steele, A. Heinzel, *Nature*, **2001**, 414, 345.

[16] S. M. Haile, *Acta Mater.,* **2003**, 51, 5981.

[17] A. Orera, P. R. Slater, *Chem. Mater*., **2010**, 22, 675.

[18] V. V. Kharton, F. M. B. Marques, A. Atkinson, *Solid State Ionics*, **2004**, 174, 135.

[19] N. Bonanos, *Solid State Ionics,* **1992**, *53-56*, 967.

[20] F. Lefebvre-Joud, G. Gauthier, J. Mougin, *J. Appl. Electrochem*., **2009,** 39:535–543.

[21] N. Laosiripojanaa , W. Wiyaratnb , W. Kiatkittipongc, *Engineering J.*, **2009**, 13, 65-83.

[22] R. Moriche, D. Marrero-López, F.J. Gotor, M.J. Sayagués, *J. Power Sources,* **2014**, 252, 43-50.

[23] A.J. Jacobson, *Chem. Mater*., **2010**, 22, 660–674.

[24] J.X. Wang, Y.K. Tao, J. Shao, W.G. Wang, *J. Power Sources*, **2009**, 186, 344–648.

[25] S.B. Adler, J.A. Lane, B.C. Steele, *J. Electrochem. Soc*., **1996**, 143, 3554.

[26] S.B. Adler, *Solid State Ionics*, **1998**, 111, 125.

[27] J. Fleig, *Annu. Rev. Mater. Res.,* **2003**, 33, 361.

[28] E. Siebert, A. Hammouche, M. Kleitz, *Electrochim. Acta*, **1995**, 40, 1753.

[29] M.A. Schubert, S. Senz, D. Hesse, *Solid State Ionics*, **2008**, 179, 453–457.

[30] S.P. Jiang, S.H. Chan, *J. Mater. Sci.,* **2004,** 39, 4405.

[31] W.Z. Zhu, S.C. Deevi, *Mater. Sci. Eng*., A, **2003,** A362, 228.

[32] A. McEvoy, S.C. Singhal, K. Kendall (Eds.), *Elsevier Ltd, Oxford, UK,* **2003**, 149.

[33] A. Atkinson, S. Barnett, R.J. Gorta, J.T.S. Irvine, A. McEvoy, M. Mogensen, S.C. Singhal, J. Vohs, *Nat. Mater.,* **2004**, 3 (1), 17.

[34] C. Wagner., *Naturwissenschaften*, **1943**, 31(23), 265–268.

[35] M. Lo Faro, D. La Rosa, V. Antonucci, A. S. Arico, *J. Ind. Inst. Sci*., **2009**, 89:4.

[36] O. Yamamoto, Y. Arati, Y. Takeda, N. Imanishi, Y. Mizutani, M. Kawai, Y. Nakamura, *Solid State Ionics*, **1995**, 124, 137.

[37] Sylvia Baron, *Intermediate Temperature (500-850 °C) Solid Oxide Fuel Cell Today*, **2004**.

[38] Uday B. Pal, S. Gopalan, *J. Electrochem. Soc*., **2005**, 152, 9, 1890-1895.

[39] X.Q. Ma, S. Hui, H. Zhang, J. Dai, J. Roth, T.D. Xiao, D.E. Reisner, *J. Therm. Spray Tech.,* **2005,** 14, 1.

[40] P. Ravi Chandran, *Int. J. Chem.Tech. Res.*, **2014**, 07(01), 488-497.

[41] S. Nakayama, M. Sakamoto, M. Highchi, K. Kodaira, *J. Mat. Sci. Let.,* **2000**, 19(2):91–93.

[42] S. Nakayama, T. Kageyama, H. Aono, Y. Sadaoka. *J. Mat. Chem.*, **1995,** 5(11):1801–1805.

[43] A. Orera, P.R. Slater. *Chem. Mat*, **2009**, 22(3):675–690.

[44] S. Georges, F. Goutenoire, O. Bohnke, MC Steil, SJ Skinner, H.D. Wiemhoefer, P. Lacorre. *Chem. Inform.*, **2004,** 35(49).

[45] A. Chesnaud, O. Joubert, M.T. Caldes, S. Ghosh, Y. Piffard, L. Brohan. C*hem. Mater.*, **2004,** 16(25):5372–5379.

[46] R.N. Vannier, S.J. Skinner, R.J. Chate.r, J.A Kilner, G. Mairesse, *Solid State Ionics*, **2003,** 160(1-2):85–92.

[47] W.Z. Zhu, S.C. Deevi, *Mater. Sci. Eng.,* **2003,** A348, 227-243.

[48] Steele, B. C. H. *Journal of Materials Science* **2001**, *36*, 1053-1068.

[49] Fergus, J. W. *Solid State Ion.* **2004**, *171*, 1-15.

[50] Yang, Z.; Weil, K. S.; Paxton, D. M.; Stevenson, J. W. *J. Electrochem. Soc.* **2003**, *150*, A1188-A1201.

[51] Kurokawa, H.; Kawamura, K.; Maruyama, T. *Solid State Ion.* **2004**, *168*, 13-21.

[52] B. C. H. Steele, *Solid State Ionics,* **2000**, 129, 95–110.

[53] T. Hibino, A. Hashimoto, T. Inoue, J. Tokuno, S. Yoshida, M. Sano, *Science,* **2000**, 288, 2031.

[54] E. Fabbri, D. Pergolesi, E. Traversa, *Chem. Soc. Rev.,* **2010**.

[55] K. Katahira, Y. Kohchi, T. Shimura, H. Iwahara, *Solid State Ionics,* **2000**, **138**, 91.

[56] D. Shima, S. M. Haile, *Solid State Ionics,* **1997**, **97**, 443.

[57] Y. Yamazaki, R. Hernandez-Sanchez, S. M. Haile, *Chem. Mater.,* **2009**, **21**, 2755.

[58] C. Zuo, S. Zha, M. Liu, M. Hatano, M. Uchiyama, *Adv. Mater.,* **2006**, **18**, 3318.

[59] E. Fabbri, Lei Bi, H. Tanaka, D. Pergolesi, E. Traversa, *Adv. Funct. Mater*. **2011**, 21, 158–166.

[60] L. Bi, E. Fabbri, Z. Q. Sun and E. Traversa, *J. Electrochem. Soc.*, **2011**, 158, B797–B803.

[61] H. Iwahara, T. Esaka, H. Uchida, N. Maeda. *Solid State Ionics*, **1981**, 3:359–363.

[62] H. Iwahara., *J. Electrochem. Soc.J. Electrochem. Soc.*, **1988**, 135(2):529.

[63] T. Yajima, H. Kazeoka, T. Yogo and H. Iwahara, *Solid State Ionics*, **1991**, 47, 271.

[64] T. Yajima, H. Suzuki, T. Yogo and H. Iwahara, *Solid State Ionics*, **1992**, 51, 101.

[65] H. Iwahara, *Solid State Ionics*, **1992**, 52, 99.

[66] H. Iwahara, T. Yajima, T. Hibino, K. Ozaki, H. Suzuki, *Solid State Ionics*, **1993**, 61, 65.

[67] H. Iwahara, *Solid State Ionics*, **1996**, 86–88, 9–15.

[68] N. Zakowsky, S. Williamson, J. T. S. Irvine, *Solid State Ionics,* **2005**, 176, 3019.

[69] S. V. Bhide, A. V. Virkar, *J. Electrochem. Soc.,* **1999**, 146, 2038–2044.

[70] F. Chen, O. T. Sørensen, G. Meng, D. Peng, *J. Mater. Chem.*, **1997**, 7, 481.

[71] D. Pergolesi, E. Fabbri, A. D'Epifanio, E. Di Bartolomeo, A. Tebano, S. Sanna, S. Licoccia, G. Balestrino, E. Traversa, *Nat. Mater.,* **2010**, 9, 846.

[72] P. Babilo, T. Uda, S. M. Haile, *Journal of Materials Research* **2007**, *22*, 1322.

[73] J. Wu, L. P. Li, W. T. P. Espinosa, S. M. Haile, *J. Mat. Res.* **2004**, 2366.

[74] D. Makovec, Z. Samardzija, D. Kolar, *Journal of the American Ceramic Society,* **1997**, 80, 3145.

[75] R. Glockner, M. S. Islam, T. Norby, *Solid State Ionics,* **1999**, *122*, 145.

[76] M.-D. Braida, Nouveaux conducteurs protoniques de structure fluorite, *PhD thesis*, **2010**.

[77] K. D. Kreuer, *Solid State Ionics*, **2000**, 136–137, 149–160.

[78] M. Pionke, T. Mono, W. Schweika, T. Springer and T. Schober, *Solid State Ionics*, **1997**, 97, 497–504.

[79] K. D. Kreuer, A. Fuchs and J. Maier, *Solid State Ionics*, **1995**, 77, 157–162.

[80] W. Münch, G. Seifert, K. D. Kreuer and J. Maier, *Solid State Ionics*, **1997**, 97, 39–44.

[81] W. Münch, G. Seifert, K. D. Kreuer and J. Maier, *Solid State Ionics*, **1996**, 86–88, 647–652.

[82] K. D. Kreuer, *Solid State Ionics*, **1997**, 97, 1–15.

[83] K.D. Kreuer, *Annu. Rev. Mater. Res*. **2003**, 33, 333–59.

[84] T. Norby, M. Widerøe, R. Glöckner, *Dalton Trans,* **2004**, 3012.

[85] Y. Larring, T. Norby, *Solid State Ionics,* **1995**, 77, 147.

[86] T. Ishihara, Perovskite Oxide for Solid Oxide Fuel Cells (Fuel Cells and Hydrogen Energy), *Springer*, **2009**.

[87] A.S. Nowick, A.V. Vaysleyb, *Solid State Ionics*, **1997**, 97, 17–26.

[88] T. Scherban, Y. M. Baikov, E. K. Shalkova, *Solid State Ionics*, **1993**, 66, 159.

[89] N. Bonanos, A. Huijser , F.W. Poulsen, *Solid State Ionics,* **2015**.

[90] A. S. Nowick, Y. Du, *Solid State Ionics*, **1995**, 77, 137.

Chapter 2 Experimental Techniques

2.1 Introduction

The following experimental chapter outlines the procedures and techniques used for the preparation and characterization of the different materials used for SOFCs: soft chemistry synthesis, structural characterization by X-Ray diffraction, scanning electron microscopy (SEM), dilatometry and *ac* impedance spectroscopy.

2.2 Nanopowders synthesis

There are several methods to synthesis oxide ceramic nanopowders: solid-solid solid-gas processes or solution based reactions. These techniques are a promising alternative comparing with the solid-state reactions and have a lot of advantages like high purity powders with fine particle sizes, homogeneous materials and low costs of production process [1-3]. For this work, three synthesis routes have been used to prepare nanopowders: microwave-assisted citric acid combustion method, modified citrate-EDTA complexing method and freeze-drying synthesis.

2.2.1 Microwave-assisted citric acid combustion method

Microwave-assisted citric acid combustion synthesis (MWCS) is an effective method for the fabrication of nanoscale materials. In this process material is directly heated by radiation instead of indirect heating by thermal sources leading to higher temperature homogeneity in the reaction mixture. Microwave heating can be more advantageous than conventional heating because of short processing time and volumetric heating. In this process of heating, microwave radiation interacts with the polar molecules possessing dipole moment and makes them reorient through rotation [4].

As starting materials, we have used commercial nitrates: $Me(NO_3)_2$ (Me = Ca^{2+}, Sr^{2+}, SIGMA, 99,9%), $Ga(NO_3)_3$*nH_2O and $Gd(NO_3)_3$*nH_2O (Strem chemicals, 99.9%). Quantities of all precursors were calculated according to the Equations 2.1 and 2.2. All nitrates were dissolved in 150 ml of deionized water until a transparent solution was obtained. Then, citric acid was added as a chelating agent. Solution was heating up under continuous stirring to obtain a viscous gel. After further heating, the viscous gel was put into a domestic microwave for 2 h and converted into a brown ash. The precursor powders were ground into an agata mortar and calcined at 900 °C for 5 h to obtain a single crystalline phase. The experimental process is presented in **Figure 2.1.**

$$3Gd(NO_3)_3 \cdot 6H_2O + Ga(NO_3)_3 \cdot 7H_2O \rightarrow Gd_3GaO_6 + 12HNO_3 + 19H_2O \qquad (2.1)$$

$$(3-x)\mathrm{Gd(NO_3)_3 \cdot 6H_2O} + \mathrm{Ga(NO_3)_3 \cdot 7H_2O} + x\mathrm{Me(NO_3)_2 \cdot yH_2O} \rightarrow \mathrm{Gd_{3-x}Me_xGaO_{6-\delta}} \qquad (2.2)$$

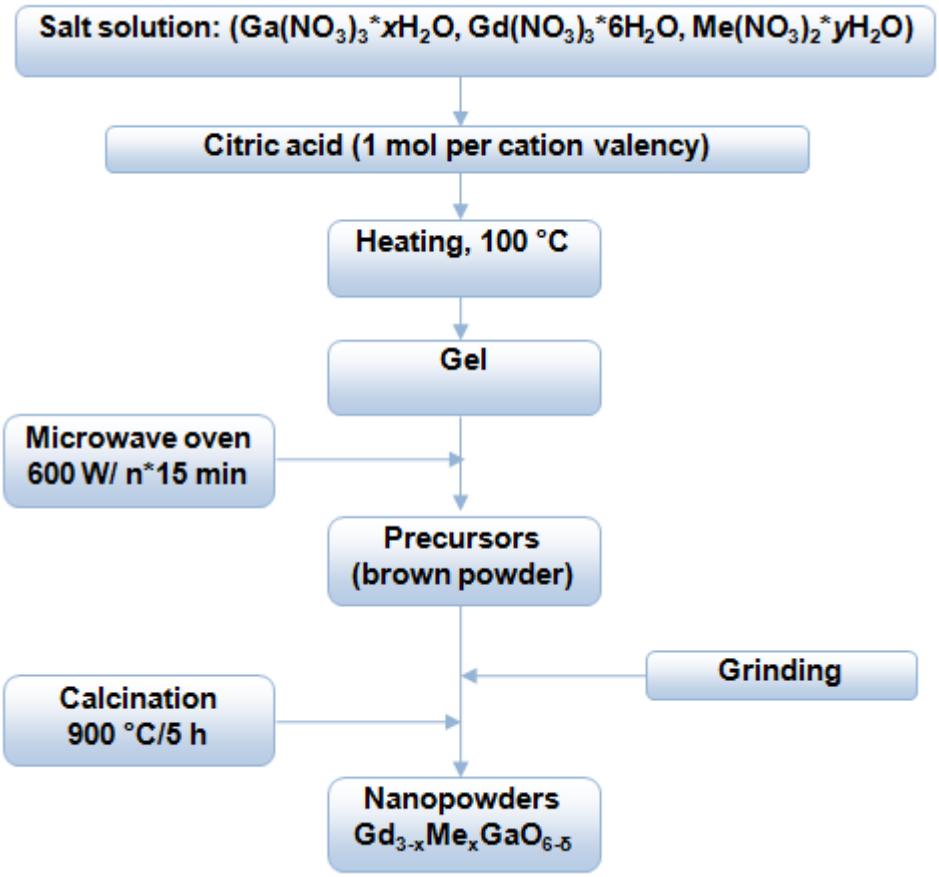

Figure 2.1 Synthesis process of a microwave-assisted citric acid combustion method

Scanning electron microscopy (SEM) micrographs of Gd_3GaO_6 powder obtained by MWCS at 900 °C shows that it consists of small spherical particles of about 100 nm (**Figure 2.2**). The SEM pictures for all Gd_3GaO_6 - based materials have reflected the same kind of powder morphology.

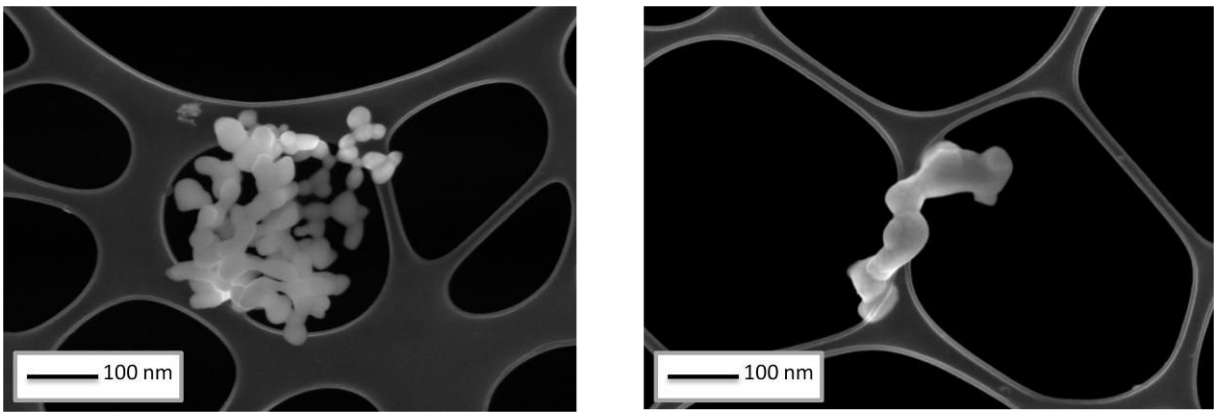

Figure 2.2 SEM picture of Gd_3GaO_6 powder prepared by microwave-assisted citric acid combustion method and calcinated at 900 °C for 5 h

Compared to the gel combustion method, the productivity has been effectively improved through this citric acid combustion route. Due to a unique complexing agent and the rapid heating rate in microwave, the dehydration of solution, swelling and combustion of viscous gel could be accomplished in a short reaction time (~ 2 h), without ignition or visible flame. The volume of residual precursors of citric acid combustion after microwave step is much smaller than that of gel combustion method, which significantly facilitates the following calcination steps by obtaining much larger amount of synthesized powders, in spite of limitation on the size of available crucibles [5].

2.2.2 Modified citrate-EDTA complexing method

$BaZr_{0.85}Y_{0.15}O_{3-\delta}$ (BZY15) was prepared using modified citrate-EDTA complexing method. Chelating agents such as citric acid and EDTA play an important role in synthesizing of ceramics powder. The combined citrate-EDTA method is particularly useful for synthesizing ultrafine powders of complex oxide compositions [6]. It can also eliminate the occurrence of unbound metal cations so as to ensure the complexation of all metal cations to give homogenous precursors [7, 8].

The necessary amounts of nitrates $Ba(NO_3)_2$ (Strem chemicals, 99.95%), $Y(NO_3)_3$*$6H_2O$ (Alfa Aesar, 99.9%) and $ZrO(NO_x)$*yH_2O (Alfa Aesar, 99.9%) were dissolved in 100 ml of deionized water with magnetic stirring until a transparent solution was obtained. Quantities of all precursors were calculated according to the Equation 2.3. Then, citric acid and EDTA were added as chelating agents. During this process, besides citrates as primary coordinate agent, a suitable amount of EDTA was used as a secondary coordinate agent, which has comparatively stronger complexing ability. The cooperation of citrate and EDTA would allow to obtain more stable chelate complex [8]. The mole ratio of (EDTA acid): (citric acid) : (total metal ions) was controlled around 1.5:1.5:1. Aqueous ammonia was then added to the beaker to facilitate the dissolution of EDTA, forming a water-soluble ammonium salt. The pH value was adjusted to about 7 by controlling with pH-meter. EDTA-$NH_3 \cdot H_2O$ and citrate formed a buffering solution, so the pH value of the system was successfully sustained during the whole water-evaporation process.

Solution was heating up under continuous stirring to obtain a viscous gel. The black porous sponge-puffy stuff as the precursor was obtained from the dry gel combustion in the domestic microwave. The precursor powders were ground into an agata mortar and calcined at 1000 °C for 5 h to obtain a single crystalline phase. The experimental process is presented in **Figure 2.3.**

$$Ba(NO_3)_2 + 0.15Y(NO_3)_3 \cdot 6H_2O + 0.85ZrO(NO_x) \cdot yH_2O \rightarrow BaZr_{0.85}Y_{0.15}O_{3-\delta} \quad (2.3)$$

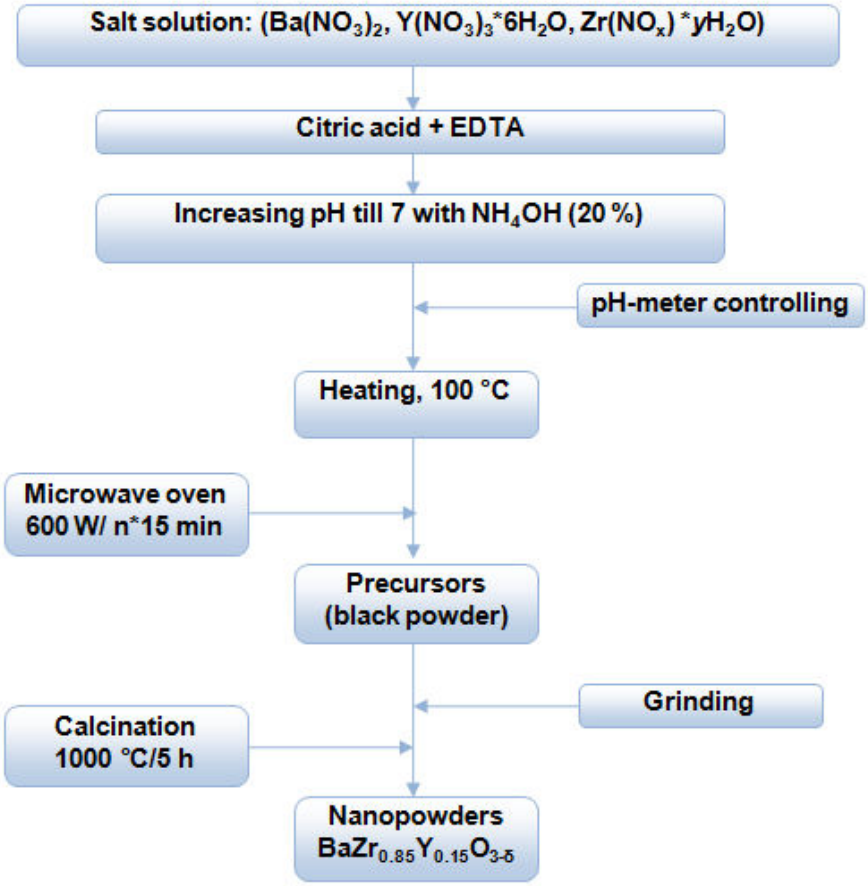

Figure 2.3 Synthesis process of modified citrate-EDTA complexing method

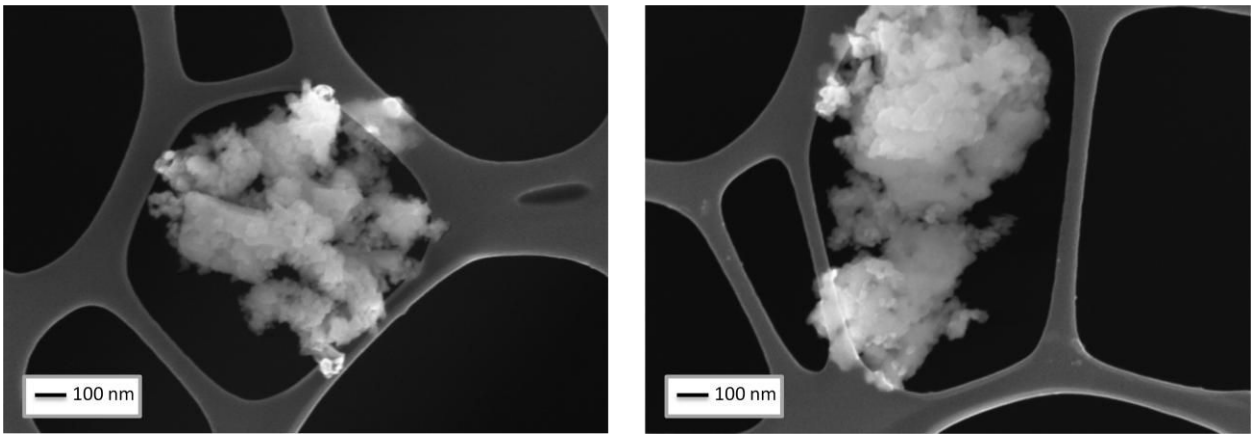

Figure 2.4 SEM picture of morphology BZY15 powder prepared by modified citrate-EDTA complexing method and calcinated at 1000 °C for 5h

Typical images of BZY15 powder obtained by scanning electron microscopy (SEM) are shown **Figure 2.4.** The powders calcined at 1000 °C were strongly agglomerated with particles size about 20-50 nm.

2.2.3 Freeze drying synthesis

Freeze-drying is a particularly interesting technique for powder preparation. This method is relatively simple and allows the preparation of high purity powders with carefully controlled compositions. It requires only low cost starting chemicals, low energy efficiency in comparison with other ordinary drying technologies such as rotary drying, fluid bed drying, spray drying, etc. In addition, the method is easily adaptable to new oxide compositions. The freeze-drying technique consists in the preparation of a solution of soluble salts of the desired cations, the spraying and freezing of this solution, the drying in a freeze-dryer to sublime water, and calcination to remove volatile species [9]. Quantities of all precursors were calculated according to the Equation 2.4.

Firstly, EDTA (VWR Chemicals) and ammonium hydroxide (20.5%, VWR Chemicals) were dissolved in deionised water with stirring. Then stoichiometric quantities of barium acetate ($C_4H_6BaO_4$, 99%, Sigma-Aldrich), yttrium acetate tetrahydrate ($(CH_3CO_2)_3Y*4H_2O$, 99.9%, Alfa Aesar) and peroxo-citrato-niobium complex were successively added. Last component was prepared according to the previous work [10]. The solution was clear after each addition of the precursors, the pH was around 5-6. After that the solution was sprayed in liquid nitrogen (**Figure 2.5 (a)**). Then, the frozen mass was put on a plate in a freeze-dryer (ALPHA 2–4, Christ) under vacuum (0.030 mbar) (arrow 2 in **Figure 2.5 (b)**). By maintaining the temperature of the product at −30 °C for 48 h and the vacuum as low as possible, water was removed by sublimation (arrow 3 in **Figure 2.5 (b)**). At the end of the process (arrow 4 in **Figure 2.5 (b)**), the product was warmed up to 30 °C to get rid of the adsorbed H_2O. A fluffy powder was obtained. If water had remained in it, the solid would have melted when returning to ambient temperature and pressure [11]. The powders were ground and calcinated at 900°C for 30 min. The samples were ground, pelleted and sintered for 24 hours at 1450 °C.

$$2Ba(CH_3COO^-)_2 + \frac{(1+x)}{2} Y_2O_3 + \frac{(1-x)}{2} Nb_2O_5 \rightarrow Ba_2Y_{(1+x)}Nb_{(1-x)}O_{6-\delta} \qquad (2.4)$$

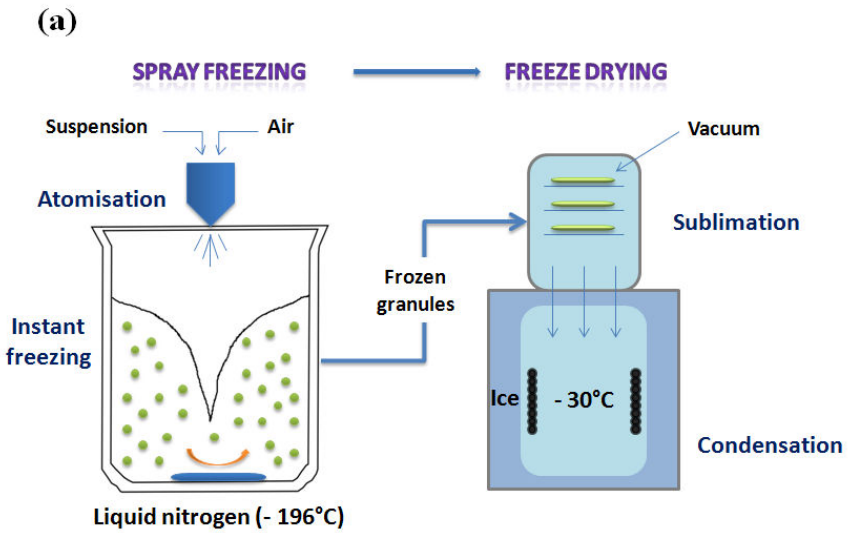

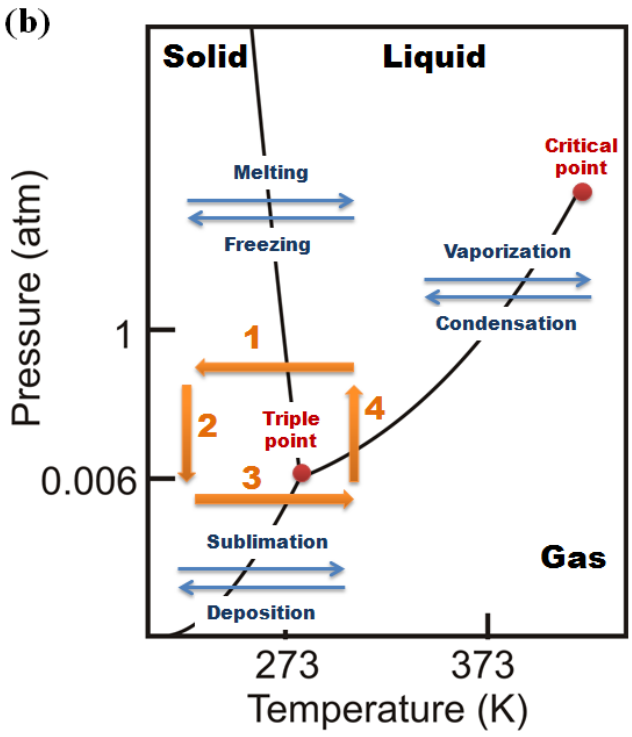

Figure 2.5 (a) Schematic of the freeze granulation/freeze drying process; (b) Temperature–pressure diagram of water and representation of a freeze-drying cycle by orange arrows from 1 to 4

Figure 2.6 exhibits the natural surface of pure Ba_2YNbO_6. It can be seen that the as-prepared powders are agglomerated and essentially consist of some irregularly cubic particles. The average particle size is about 50 nm.

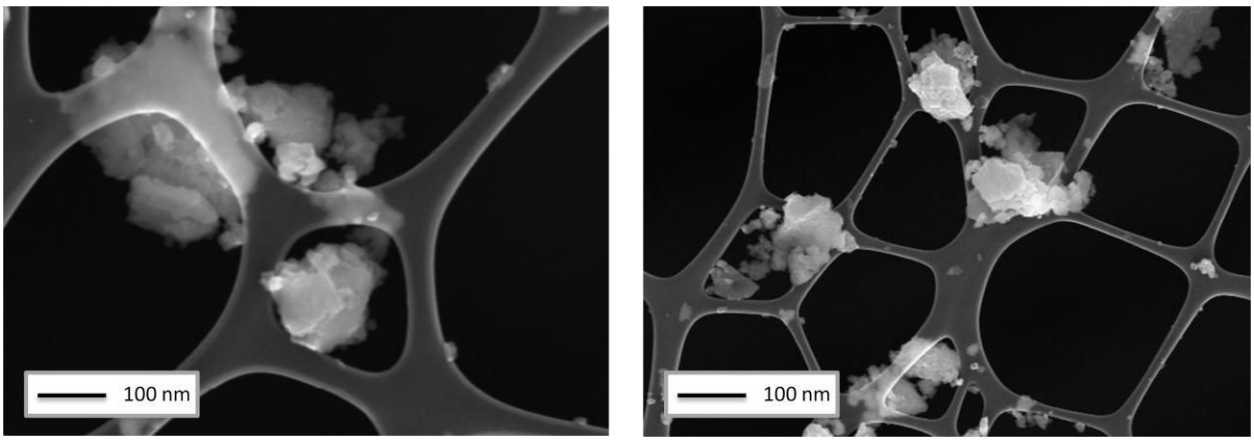

Figure 2.6 SEM picture of morphology Ba_2YNbO_6 powder prepared by freeze drying process and calcinated at 900 °C for 30 min

2.3 Preparation of Ceramics

Samples were prepared in the form of pellets with a diameter of 8-10 mm with a thickness of around 2 mm. Pressing was performed on a manual hydraulic press under a pressure of 2 $T.cm^{-1}$ and then on isostatic press at 750 MPa during 10 min. Sintering temperatures are shown in Table 2.1. In all cases $T_{sintering}$ was chosen to ensure phase purity, high density and non nanometric grain size.

Table 2.1 Temperature mode for sintering compositions

Solid solution	Gd_3GaO_6, $Gd_{3-x}Me_xGaO_{6-\delta}$	$BaZr_{0.85}Y_{0.15}O_{3-\delta}$	$BaZr_{0.85}Y_{0.15}O_{3-\delta}$ using ZnO, NiO	Ba_2YNbO_6, $Ba_2Y_{1+x}Nb_{1-x}O_{6-\delta}$
$T_{sintering}$	1450 °C - 10 h	1600 °C - 24 h	1300 °C - 24 h	1450 °C - 24 h

2.4 Chemical and structural characterization

2.4.1 X-Ray diffraction analysis

2.4.1.a Routine X-Ray diffraction analysis

The Xray diffraction analysis was performed in order to control the phase purity and homogeneity of the synthesis products. Intensities were obtained at room temperature using Bruker Advance D2 diffractometer in CuKα - radiation in the 2θ range 20 ÷ 80 ° with a step size of 0.02 ° and exposition time 5 sec per point. To determine the sample composition at the stage of synthesis, we used the EVA 2 [27] database. For more specific structural studies in particular for single-phase materials, refinement of the crystal structure of a series of compounds was carried out according to the X-ray diffraction Rietveld full-profile analysis method [12] using the computer program FullProf [28]. From this analysis we could extract information about atom positions and bond lengths.

2.4.1.b High-temperature X-Ray diffraction

Measurement of the linear thermal expansion coefficient (TEC) of ceramic materials necessary to determine the possibility of obtaining a lasting contact is high-temperature electrochemical devices (such components are electrolytes, electrodes, sealants, etc.). Measurements were carried out at high resolution goniometer associated with a rotating anode (Rigaku RA-HF18) with a power 15kW using CuKα radiation in the air condition (**Figure 2.7**). 2θ range was 20 ÷ 80 ° with a step size of 0.02° and exposition time 5 sec per point. Temperature range was 295 – 995 K. Profile matching of the XRD pattern was perfomed using FullProf program.

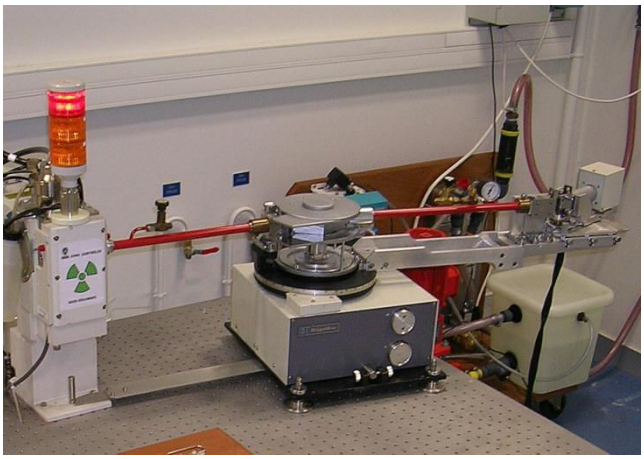

Figure 2.7 General view of the rotating anode Rigaku RA-HF18

Isobaric linear coefficient of thermal expansion (TEC) was determined according to the equation:

$$TEC = \sqrt[3]{\alpha_p} = \sqrt[3]{\frac{1}{V_0}\left(\frac{\partial V}{\partial T}\right)_p} = \frac{1}{L_o}\left(\frac{\partial L}{\partial T}\right)_P \quad (2.5),$$

from the slope of experimental curves $\Delta L/L = f(T)$, where α_p - thermal expansion coefficient, L_o - sample cell parameter or volume at room temperature, ΔL - current change of the sample cell parameter or volume, T - temperature.

2.4.2 Scanning electron microscopy (SEM) and Energy dispersive spectroscopy (EDS)

The scanning electron microscope (SEM) uses a focused beam of high-energy electrons to generate a variety of signals at the surface of solid specimens. The signals that derive from electron-sample interactions reveal information about the sample including external morphology (topography), chemical composition, and with special analysis the crystalline structure and orientation of crystallites [13]. The microstructure and chemical composition of powders and sintered samples were investigated by means of scanning electron microscopy (FEG LEO 1530) in conjunction with EDS (Energy Dispersive X-ray Spectroscopy). Powder samples for SEM investigations were mounted on aluminium sample holders using a carbon conductive scotch tape and TEM copper grid as shown on the **Figure 2.8.**

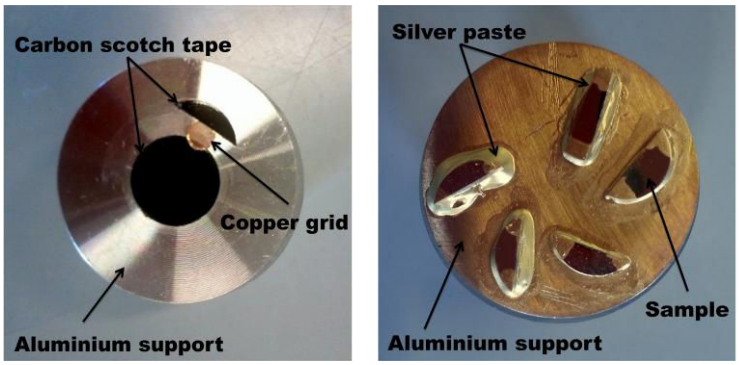

Figure 2.8 Powder and pellet **s**ample preparation (respectively) for the SEM analysis

Sintered samples were previously polished using waterproof silicon carbide paper (#2400 and #4000, Struers) and then using cloth with short synthetic nap with diamond paste (1 μm and ¼ μm, DP-Paste P). After polishing samples were thermally etched at the $T_{thermal\ etching} = (T_{sintering} - 100\ °C)$ in the furnace during 3 hours and then were mounted on aluminium sample holder using a silver conductive paste. For a better observation and to avoid sample charging, thin layer of gold was deposit using a plasma sputerring device PLASSYS (**Figure 2.8**).

2.4.3 Dilatometry analysis

Dilatometry is a thermoanalytical technique used to measure the expansion or shrinkage of solids, powders, pastes and liquids under negligible load when subjected to a controlled temperature/time program. A precise understanding of this behavior can provide insight into firing processes, the influence of additives and raw materials, densification and sintering properties, reaction kinetics, phase transitions, and thermal shock [14]. The working principle of a dilatometer consists in applying a constant force to the sample along a controlled temperature program and in measuring the displacement of the pushrod due to resulting contraction or expansion of the sample. As the dilatometer components expand under the heating program, a control run is needed to cancel its contribution.

In the present work dilatometry was used to investigate the sintering behaviour of compacted powder of Gd_3GaO_6. Experimental work was carried on a Netzch dilatometer Dil 420C in collaboration with Ecole de Mines Paristech. Before dilatometric studies, samples were isostatically pressed into pellets of 6 mm in diameter. The samples were heated in the furnace and length changes were measured via a pushrod positioned on the cold part of the dilatometer, see **Figure 2.9.**

As an example of thermal scenario would be:

RT (2 °C/min) → 35 °C (120 min) → 1570 °C (5 °C/min).

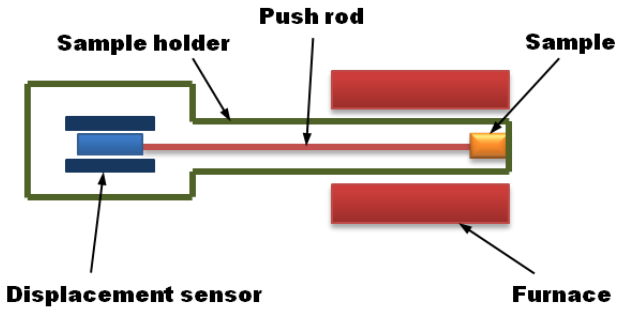

Figure 2.9 Schematic diagram of a horizontal dilatometer [15]

Figure 2.10 shows the linear shrinkage rate as a function of temperature. There is no clear on-set temperature of shrinkage was found. Sintering temperature was between 1128-1166 °C. Particles continued to shrink up to 1600 °C, which was the maximum temperature of our heater.

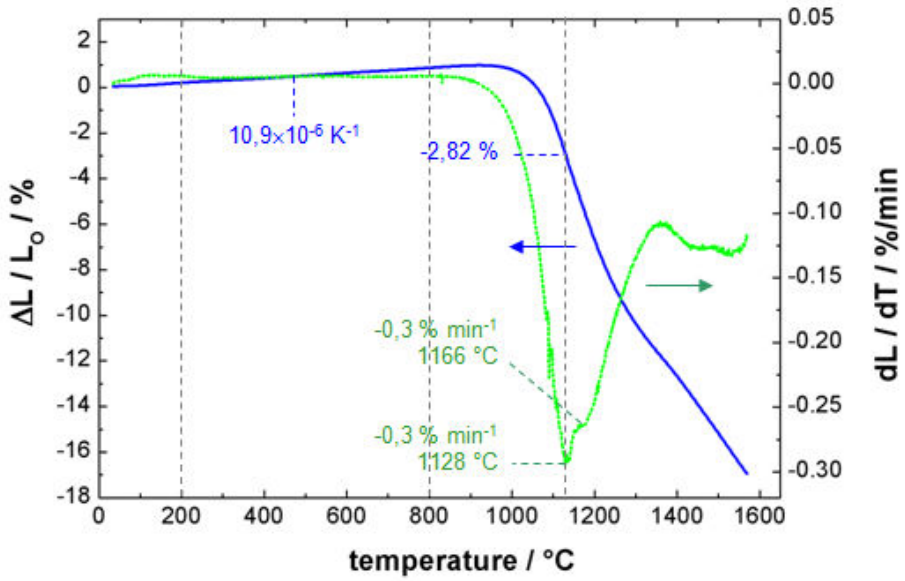

Figure 2.10 Typical dilatometer data for Gd_3GaO_6 sample

2.4.4 Transmission electron microscopy *(TEM)*

Transmission electron microscopy (TEM) is performed on dense sintered specimen. HRTEM and STEM images were recorded using a FEI Cs-corrected Titan microscope of MSSMAT laboratory. High Resolution TEM and STEM images were obtained by using a FEI Titan^3 Cubed G2 60-300. This microscope is equipped with a high brightness source X-FEG Schottky and a Cs probe corrector (DCOR). The chemical mapping EDS is acquired with Super-X detector system based on 4 windowless Silicon Drift Detector (SDD), which enhanced acquisition efficiency and spatial resolution. The observations were performed at 200 kV high tension on the nickel or copper TEM grids with carbon films (300 mesh).

2.5 Conductivity measurements

2.5.1 Fundamentals of electrochemical impedance method

This method is based on measuring the impedance of an alternating current circuit in a wide range of frequencies. The amount of current flowing through the resistor R by a field U, defined by Ohm's law:

$$\tilde{I}=\tilde{U}/R \tag{2.6}$$

and does not depend on a frequency of the field. The capacitor blocks the direct current; an alternating current passing through it by the following formula:

$$\tilde{I}=i\omega C\tilde{U}, \tag{2.7}$$

ω - where the angular frequency, i - imaginary unit. These relations for R and C can be written as:

$$\tilde{I}=\tilde{U}/\ Z^*(\omega), \tag{2.8}$$

Z * (ω) - impedance of the chain, which includes real and imaginary parts:

$$Z^*(\omega) = Z^{I} - iZ^{II} \tag{2.9}$$

When connecting the resistance and capacitance is given by:

$$Z^*(\omega) = R+1/i\omega C = R - i/\omega C \tag{2.10}$$

In parallel connection of R and C are summed reciprocals of ohmic and capacitive impedance. And then calculated reciprocal of the impedance - admittance circuit A*. The impedance at the same time is as follows:

$$Z^*(\omega) = (A^*) - 1= R/[1+(i\omega RC)^2] - R(\omega RC/[1+(i\omega RC)^2]) \tag{2.11}$$

Here three representations which are relevant to this work are introduced [22]. The basic representation is the plot of Z' and Z'' against log (f) (**Figure 2.10, a**). The arcs (peaks) in the plot of Z'' against log(f) reveal the relaxation frequencies f_{el}, f_{gb} and f_b.

The range of frequencies for each process is known and is presented in **Table 2.2** from [23].

Table 2.1 Typical capacitance values with their interpretation [23]

Capacitance F	Phenomenon
10^{-12}	Bulk
10^{-11}	Second phase
10^{-11} - 10^{-8}	Grain boundary 10^{-4}
10^{-9} - 10^{-7}	Surface layer
10^{-7} - 10^{-4}	Sample-electrode interphase
10^{-4}	Electrochemical reactions

Another popular representation is the Nyquist plot which is a plot of Z'' against Z' (**Figure 2.10, b**). In an electrically inhomogeneous sample, which contains several components (bulk, grain boundary, electrode *etc.*), each semicircle corresponds to the grain, grain boundary and electrode contributions respectively, which may be represented by a parallel *RC* element, where *R* is the resistance and *C* the capacitance. [18-23].

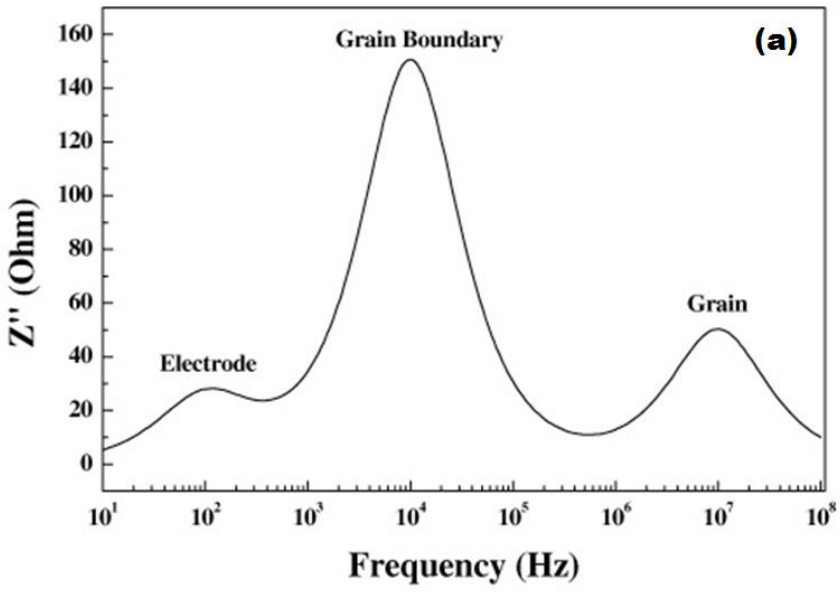

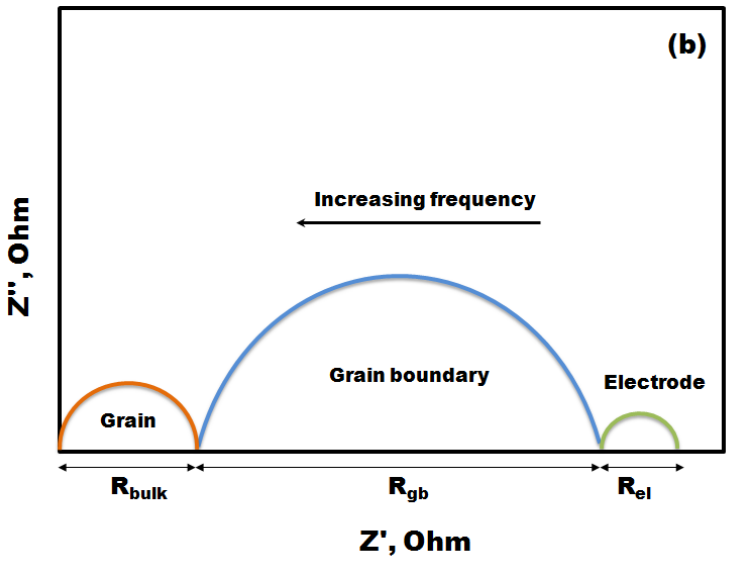

Figure 2.10 Typical representations of impedance spectroscopy:
(a) Basic one of Z'' against f [22]; (b) Nyquist plot of Z'' against Z'

ZView software [24] was used to fit the acquired impedance data to equivalent circuits assuming "block-layered" model sample, see **Figure 2.11**. Depending on the complex impedance plane plot shape, different equivalent circuits were used.

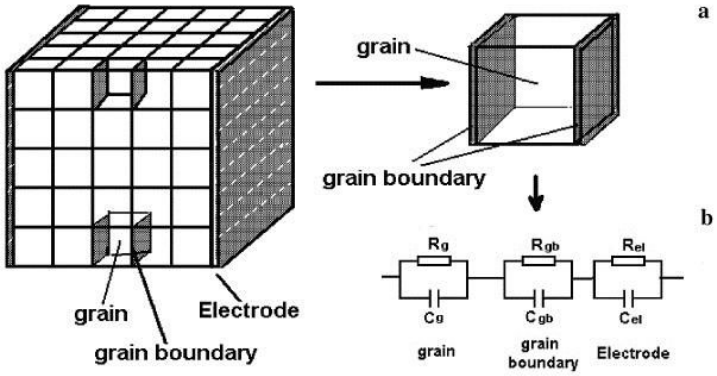

Figure 2.11 (a) Brick layer model of polycrystalline sample; (b) Equivalent circuit to model a three-process system [22]

Frequently, the experimental data for many systems give complex plane diagrams that form circular arcs with center lying below the axis (that is a depressed semicircle). This is the so-called dispersing phenomenon. In the case of the dispersing effect, the double-layer capacitance and pseudo-capacitance involved in electrochemical reactions do not function as pure capacitors, but as constant phase elements (CPEs), whose admittance and impedance, respectively, are defined as:

$$Y_{CPE} = Y_0(j\omega)^a \qquad (2.12)$$

$$Z_{CPE} = \frac{1}{Y_0(j\omega)^a} \tag{2.13}$$

Where Y_o is the admittance magnitude and *a* the exponential term, *a* =1 in a perfect capacitor and *a* = 0 for a pure resistor. Capacitors should be substituted by CPEs in the equivalent circuits to result in a better fit when the dispersing impedance data are encountered [25].

2.5.2 Experimental details

The conductivity of the samples was investigated by electrochemical impedance spectroscopy. Measurements were performed using ProboStat™ cell and an impedance spectrometer Solartron 1260 within the frequency range of 1 Hz ÷ 1 MHz at temperatures 200 - 900 °C. Temperature change rate was 30 °C / hour for dry atmosphere and 12 °C / hour for wet atmosphere and a stabilization time for of 15 – 30 min for each temperature.

In the Probostat A™ cell [16], the sample is placed on a long support alumina tube as schemed in **Figure 2.12**. The sample is contacted with 2 electrodes made out of platinum. A spring-loaded alumina assembly holds the sample and electrodes in place. A thermocouple is used to measure the temperature close to the sample position. Electrical connections are made via standard multiconnectors, coax cables suitable for standard impedance spectrometer connectors, and standard thermocouple compensation cables. Gases can be fed in single or dual chamber mode directly onto electrodes. The furnace sets the temperature around the sample. It is a vertical tubular furnace, which covers the closed outer tube of the Probostat A™. The sample position is located in the centre of the hot zone of the oven [17]. For the electrical conductivity measurements both sides of sintered pellet were coated with platinum paste (Pt ink 6082, Metalor Technologies UK Lt) and gold paste (Gold M-0034, Metalor Technologies UK Lt) and fired at 900 °C and 850 °C respectively for 2 hours in the air.

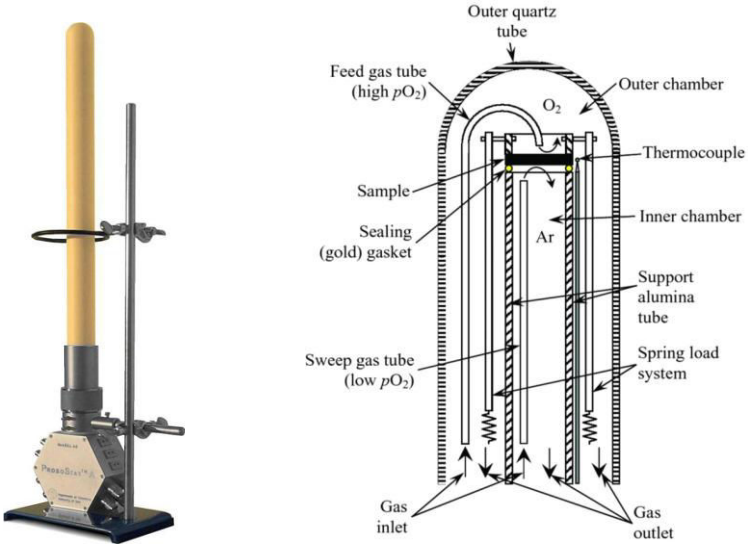

Figure 2.12 ProboStat™ cell and scheme of the specimen placed in it (figure reproduced from www.norecs.com)

Calculation of conductivity values was performed according to the formula:

$$\sigma = \frac{1}{R} * \left(\frac{h}{S} \right) \tag{2.14}$$

where σ - total electrical conductivity ($Ohm^{-1}cm^{-1}$); h - height of sample (cm); S - square surface sample (cm^2); R - resistance of the sample (Ohm).

2.5.3 Controlling of the atmosphere

2.5.3.a Controlling of oxygen partial pressure

Equipment for measuring the electrical conductivity allows the measurement in the range of oxygen partial pressures 0.21 - 10^{-20} atm. Oxygen partial pressure was differently controlled depending on the desired oxygen partial pressure: above 1000 ppm, mixtures of argon, air and oxygen were used. Between 1 ppm and 1000 ppm, the oxygen partial pressure was monitored using a Zirox SGM5 EL [26], which combines an electrolysis cell with a potentiometric measuring cell. The scheme of the device is presented **Figure 2.13**.

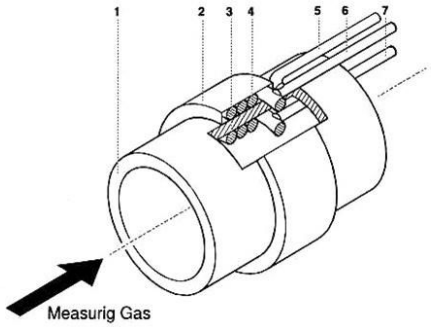

1 Ceramic Tube
2 Ceramic Cover of the Reference Electrode
3 Measuring Electrode
4 Reference Electrode
5 Thermocouple
6 Reference Electrode Connection
7 Measuring Electrode Connection

Figure 2.13 Electrolysis and analysis cell [26]

For low oxygen partial pressure, we used a mixture of pure argon and argon (95 %)/ hydrogen (5 %). Then the oxygen partial pressure is determined using the high temperature equilibrium between H_2, O_2 and H_2O (http://navier.engr.colostate.edu/tools/equil.html).

2.5.3.b The humidity controlling

Conductivity was performed by varying humidity of atmosphere.

The partial pressure of water vapor set as follows:

- Dry atmosphere ($pH_2O = 10^{-5}$ atm): circulation of air passed through the ultra-high capacity moisture filter cartridges (Restek Super Clean);

- Humid atmosphere ($pH_2O = 2.4 \cdot 10^{-2}$ atm.): gasflow bubbling through room temperature H_2O.

References:

[1] M. Niederberger, N. Pinna, J. Polleux, M. Antonietti *Angew. Chem. Int. Ed*., **2004**, 43, 2270–2273.

[2] M. Liu, D. Xue *Mater. Lett.,* **2005**, 59, 2908–2910.

[3] E.R. Camargo, M. Kakihana *Chem. Mater.,* **2001**, 13, 1905–1909.

[4] Akrati Verma, Reena Dwivedi, R. Prasad,K. S. Bartwal, *Journal of Nanoparticles,* **2013**, 480-491.

[5] Y. HU, Study of $GdBaCo_{2-x}M_xO_{5+\delta}$ (M=Ni, Fe; x = 0, 0.1, 0.2, …) as new cathode materials for IT-SOFC application, *Thesis work*, **2011**.

[6] Y. Tao, J. Shao, J. Wang, W. G. Wang, *Journal of Power Sources*, **2008**, V. 185, 2, 609–614.

[7] J. Shao, Y. Tao, J. Wang, C. Xu, W. G. Wang, *Journal of Alloys and Compounds*, **2009**, V. 484, 1-2, 263–267.

[8] N. A. Abdullah, S. Hasan, N. Osman *Journal of Chemistry*, **2013**, 1-7.

[9] S. M. Johnson, M. I. Gusman, D. L. Hildenbrand, *Mat. Res. Soc. Symp. Proc.* , **1988**, Vol. 12, 413-420.

[10] Y. Narendar, G. L. Messing, *Chem. Mater*., **1997**, 9, 580-587.

[11] Y. Rabinovitch, C. Bogicevic, F. Karolak, D. Tetard , H. Dammak *J. Mater. Proc. Techn.* **2008**, 199, 314–320.

[12] Rietveld H.M. *J. Appl. Cryst*., **1969**., V.2., 65-71.

[13] http://serc.carleton.edu/research_education/geochemsheets/techniques/SEM.html

[14] Netzsch, *Dilatometry. Method, Instruments, Applications – From -180°C to 2800°C.*

[15] http://www.ceramicindustry.com/articles/92598-dilatometer-technology.

[16] Probostat, Manual Version A-4, **2004**.

[17] S. Duval, *Y-substituted barium zirconate, a proton conducting electrolyte for applications at intermediate temperatures*, PhD thesis, Munich, **2008.**

[18] Z.B. Stoynov, *The electrochemical impedance*, Nauka, **1991**, 335.

[19] N.G. Bukun, *Electrochemistry*, **1993**, V. 29, 110-116.

[20] V.M. Zhukovsky, *Impedance spectroscopy of solid electrolyte materials*, **2000**, 35.

[21] A. R. West, *Solid State Chemistry. Theory and Applications*, Mir, **1988**.

[22] S.Song, F. Placido, *J. Stat. Mech.: Theor. Exp*. **2004**, 1-14.

[23] D.C. Sinclair, F.D. Morrison, A.R. West. *Int. Ceram.*, (2), **2000**, 33–34.

[24] D. Jonhson. Software Zview–v. 2, 3d, Scribner Associates, **2000.**

[25] Y. Wang, *Synthesis and characterisation of acceptor-doped $BaSnO_3$ compounds as proton conductors*, PhD thesis, **2009**.

[26] Zirox electrolysis device SGM5-EL, Operational manual, **2003**, 16.

[27] EVA 2, Bruker AXS inC., **2001**.

[28] http://www.ill.eu/sites/fullprof/

Chapter 3 Synthesis, structure and electrical properties of $Gd_{3-x}Me_xGaO_{6-\delta}$ ($Me=Ca^{2+}$, Sr^{2+})

3.1 Introduction

During the last decades intensive search for materials in the field of SOFC has led to the discovery of several new classes of materials with excellent ion conducting properties. Several conventional materials with good ionic conductivity are known and some are already in practical use, such as yttria-stabilized zirconia (YSZ) and cerium dioxide, CeO_2. However, several drawbacks, such as high operating temperatures, partial electronic conductivity and/or poor chemical stability, still limit their widespread applications. These issues have motivated researchers in the solid-state ionics community to develop new materials with improved properties.

Well-known groups of solid state ionic conductors include perovskite and fluorite structures. For example, yttria-stabilized zirconia (YSZ) has a stable ionic conductivity in a large range of oxygen partial pressure and its electronic conductivities negligible with respect to the ionic one. However, zirconia has some disadvantages: at operating conditions of about 1000 °C, a degradation of zirconia's ionic conductivity is observed after less than 1000 h [1]. Another potential candidate is cerium dioxide, CeO_2. It has a fluorite structure and presents higher oxygen-ion conductivity. Doped ceria is also chemically stable towards potential electrode materials. Its transport properties can be improved by doping with rare earth cations that will reach a maximum between 10 % and 20 % of dopant on Ce site depending on the dopant's ionic radius [2-4]. These materials have, however, drawbacks related to the low stability of the cerium ion that changes its valence from Ce^{4+} to Ce^{3+} in reducing atmospheres becoming mixed conductors which can lead to the short-circuit of the cell. Such problem can be overcome by reducing the operating temperature of the system to < 550 °C [5]. This has triggered a huge amount of research aimed not only at improving the efficiency but also at understanding phenomena on a fundamental level by experimental and theoretical methods.

Recently another class of oxides has been reported whose structure contains tetrahedral units, for example, apatites [6-8], rare-earth ortho-tantalates and ortho-niobates [9], lanthanium barium gallates $La_{1-x}Ba_{1+x}GaO_{4-x/2}$ [10-11] and lanthanide monogallates Ln_3GaO_6 [12]. The alternative structures exhibit defect association and migration that may vary from conventional types. $LaMO_4$ (M = P, Nb, and Ta) and $LaBaGaO_4$ materials have attracted significant recent interest because of high temperature proton conductivity. Increasing the barium over lanthanum ratio in $LaBaGaO_4$ results in oxygen vacancies, and, as with the perovskite systems, protons are incorporated *via* water dissociation. Thus, significant proton conductivity (~ 10^{-4} $S.cm^{-1}$ at 600 °C) has been reported in $La_{0.8}Ba_{1.2}GaO_{3.9}$

[10]. A detailed understanding of the atomic-scale ionic and protonic conduction process is needed for optimization and development of new materials [13]. E. Kendrick et *al*. [39, 40] were the first ones who clarified the atomic scale oxygen conduction mechanism in one of these systems using a combination of experimental and computational modelling methods. **Figure 3.1.1** shows the structure of $LaBaGaO_4$, which contains gallium in a distorted tetrahedral environment and ordered alternating layers of lanthanum and barium. The gallate tetrahedra are identified as isolated moieties within the lattice. It was shown that both methods successfully reproduced the distorted nature of the GaO_4 tetrahedron, where the O–Ga–O bond angles have values between 98° and 132°. The defect properties of this material were then investigated, enabling detailed analysis of the oxygen vacancy defects and oxygen diffusion pathways, as well as proton incorporation and migration [40].

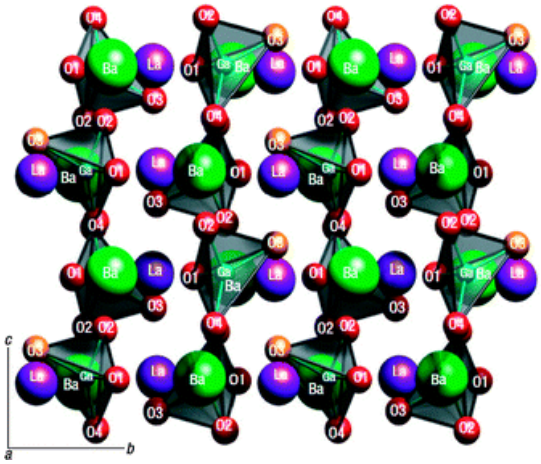

Figure 3.1.1 Crystal structure of $LaBaGaO_4$ [40]

Upon removal of an oxygen from a GaO_4 unit, rather than producing a three-coordinate Ga unit, considerable relaxation of a neighbouring GaO_4 unit takes place. A Ga_2O_7 group is formed, such that each Ga retains a tetrahedral coordination, sharing one apical oxygen between two tetrahedral (**Figure 3.1.2** (a) and (b)). This creation of Ga_2O_7 units therefore means that even with the introduction of oxygen vacancies, all the Ga sites maintain their tetrahedral coordination. Thereby, based on recent studies proton conductors containing tetrahedral units [39, 42, 43] we may suggest that oxide ion vacancies are accommodated by the creation of Me_2O_7 units.

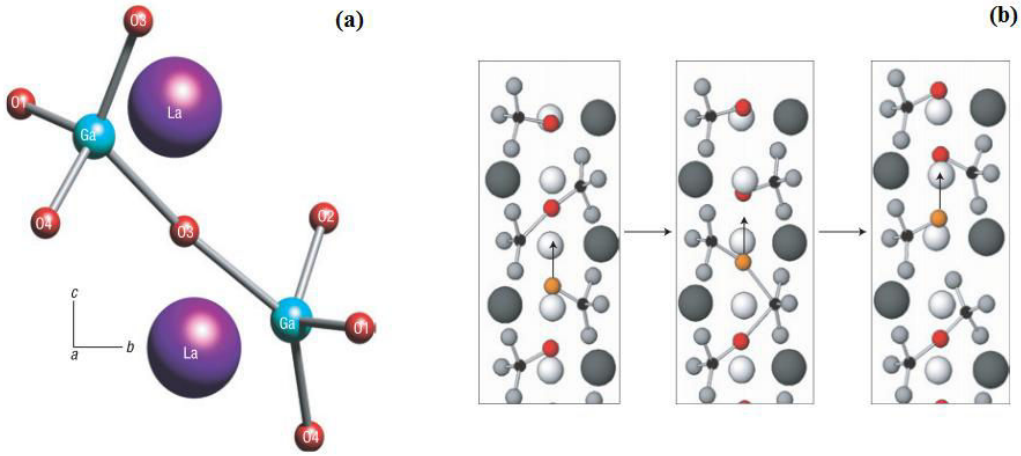

Figure 3.1.2 (a) Local structure around an oxide-ion vacancy defect in the $LaBaGaO_4$ system; (b) Oxygen vacancy migration pathway in $La_{1-x}Ba_{1+x}GaO_{4-x/2}$ [39]

In order to investigate the location of protons in $La_{1-x}Ba_{1+x}GaO_{4-x/2}$, the group of P. Slater [40] performed atomistic (potential-based) and DFT calculations. Both techniques gave similar energies for proton defects at every oxygen position, indicating a range of possible proton sites (given in Table 3.1). Proton conduction appears at low temperatures and water incorporation leads to the break-up of the Ga_2O_7 according to the Equation 3.1:

$$Ga_2O_7^{-8} + H_2O \rightarrow 2GaO_4H^{4-} \qquad (3.1)$$

Table 3.1 Activation energies for proton migration around a GaO_4 unit (intra-tetrahedron) and between two adjacent GaO_4 tetrahedra (inter-tetrahedra) determined from DFT calculations [40]

	Ea, eV
Intra-tetrahedron	
O1 to O3	0.75
O2 to O4	0.68
O4 to O1	0.55
O4 to O2	0.45
Inter-tetrahedra	
O1 to O2	0.07
O3 to O3	0.07

As it shown at the **Figure 3.1.3** (a) and (b) the proton follows a curved path between two intra-tetrahedral oxide ions probably owing to repulsive interactions with adjacent large cations. There is also significant local ion movement with the O–O separation contracting to about 2.5 Å to facilitate

the proton transfer process. In contrast to the oxide-ion conduction mechanism, which seems to be dominated by correlated diffusion along the direction defined by the Ga_2O_7 units, proton conduction is expected to be isotropic, with the H-bonding-mediated transfer of protons between GaO_4 units within a layer and between layers being equally favorable [40].

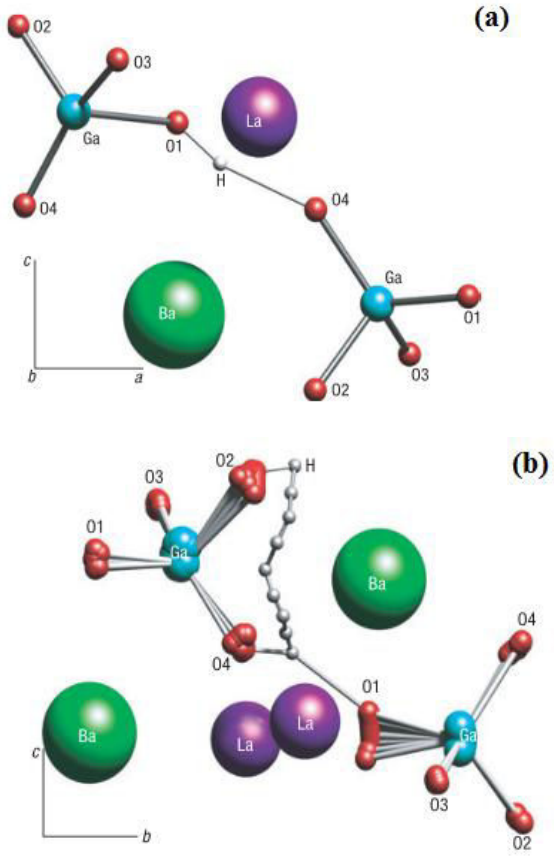

Figure 3.1.3 (a) Calculated relaxed configuration of a proton from static lattice simulations; (b) Proton migration pathway around a GaO_4 tetrahedron from DFT calculations [40].

Based on the foregoing similar mechanisms of oxide-ion and proton transport can be possibly applied for another systems containing tetrahedral moieties. Nevertheless the foregoing further work is required to investigate there new class of materials.

3.2 Phase equilibrium in Ln_2O_3 – Ga_2O_3 binary systems

Firstly the equilibrium phase diagrams of Gd_2O_3 – Ga_2O_3 and Sm_2O_3 – Ga_2O_3 were reported by S.J. Schneider et al. in 1961 [14] and then by J. Nicolas et al. in 1984 [15]. **Figure 3.2.1** shows that exist at least four different compounds $Ln_3Ga_5O_{12}$, $Ln_4Ga_2O_9$, $LnGaO_3$ and Ln_3GaO_6.

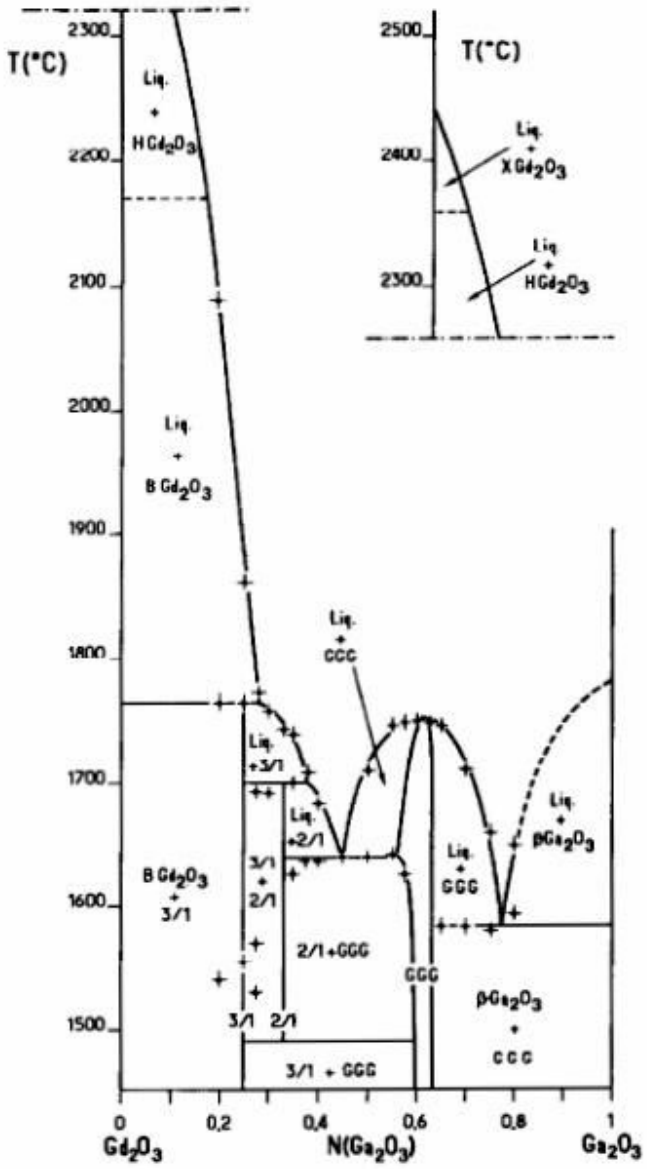

Figure 3.2.1 Gd_2O_3 – Ga_2O_3 phase diagram [15]

Single crystals of gallium garnet $Ln_3Ga_5O_{12}$ has a space group cubic *Ia*-3*d* [16]. As reported in [17-19], garnets are used as substrate material for yttrium iron garnets (YIG) film. The monoclinic phase of $Ln_4Ga_2O_9$ (*Ln*=La, Nd, Sm, Eu and Gd) are isostructural with $Eu_4Al_2O_9$[20]. The $Gd_4Ga_2O_9$ is stable only at high temperature (T >1490 °C) and melts incongruently, whereas $Sm_4Ga_2O_9$ is synthesized above 1200 °C [15]. $Ln_3Ga_5O_{12}$ was found in most of the *Ln*–Ga oxides pseudo-binary system, while $LnGaO_3$ compounds were reported only in *Ln*=La, Ce, Pr, Nd, with distorted perovskite structure. Nicolas et al. [15] reported that short melting and overheating of the melt using the laser device yield pure $SmGaO_3$ and $GdGaO_3$ isostructural with $GdFeO_3$ (*Pbnm*). According to the phase diagrams of Sm_2O_3–Ga_2O_3 and Gd_2O_3–Ga_2O_3, Sm_3GaO_6 and Gd_3GaO_6 have non-congruent melting points at 2018 K and 2033 K, respectively, and melt to Ln_2O_3 and liquid. Previously, three phases in

Ln_3GaO_6 group (Ln = Nd, Sm, Gd) were reported by S.J. Schneider et al. [14] and Carruthers et al. [21]. Several years ago F.S. Liu et al. [12] presented a systematical study of Ln_3GaO_6. The compounds of Ln_3GaO_6 (*Ln* = Nd, Sm, Gd, Tb, Dy, Ho and Er) were prepared by solid state reaction method. These phases were assigned with the orthorhombic unit cell with space group $Cmc2_1$. The XRD confirmed that all compositions are iso-structural with Gd_3GaO_6. **Figure 3.2.2** represents a typical structure for this group. For the Ln_3GaO_6 phase, *Ln* atoms located are on two different asymmetrical sites of sevenfold coordination LnO_7. Ga atoms are in distorted oxygen tetrahedral which are elongated along the *c* axis. The Ga–O bond lengths are in the range 1.83-1.89 Å and the average length of 1.85 Å is equal to the Ga–O bond length for the GaO_4 tetrahedron in the structure of $Gd_3Ga_5O_{12}$ [22-23].

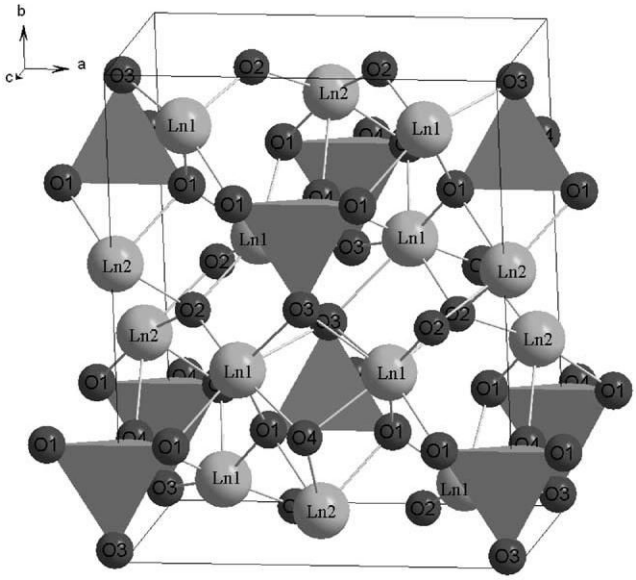

Figure 3.2.2 The structure of Ln_3GaO_6 showing GaO_4 tetrahedra [12]

For the rare earth elements with ionic radius larger than that of Nd or smaller that of Er, an Ln_3GaO_6 cannot form. The unit cell parameters for all compositions are listed in Table 3.2. The parameters a, b and c increases linearly with the size of the rare earth in accordance with a decrease of the covalently Ln-O bonds. J.K. Liang et al. [12] have also shown that the average distances Ln-O bonds are particularly sensitive to the size of the rare earth. They increase with the radius of Ln^{3+} and reach a maximum value if Ln = Nd.

Table 3.2 Unit cell parameters of Ln_3GaO_6 [24]

Compound	*a*, Å	*b*, Å	*c*, Å	Volume, Å^3	Ref.
Nd_3GaO_6	9.1820(1)	11.5396(1)	5.5748(1)	590.690(4)	[12]
Sm_3GaO_6	9.0743(1)	11.4070(1)	5.5181(1)	571.183(3)	[12]
Eu_3GaO_6	9.0264(3)	11.3385(3)	5.4941(2)	562.297(1)	[24]
Gd_3GaO_6	8.9111(1)	11.2801(1)	5.4796(1)	555.746(4)	[12]
Tb_3GaO_6	8.9332(6)	11.2122(7)	5.4432(3)	545.189(3)	[24]
Dy_3GaO_6	8.8848(3)	11.1474(4)	5.4206(2)	536.863(2)	[24]
Ho_3GaO_6	8.8410(3)	11.0882(4)	5.4011(2)	529.475(2)	[24]
Er_3GaO_6	8.8002(4)	11.0320(5)	5.3796(3)	522.273(3)	[24]

Concerning the physical properties, this group of materials can exhibit interesting luminescent properties. These materials would be potentially good candidates for field emission displays (FEDs), and also currently developing technology of the devices (LCD, PDP, OLED) transmission of the image. Among many gallate-based phosphors, Gd_3GaO_6 was recently reported as a host material for the rare earth doping, because it's proper low voltage cathodoluminescence is imperative for improving the performance of field emission display [12, 24-27]. But despite this, we have not found many relevant information about the electrical properties of these materials. The electrical resistance of these rare earth monogallates, as measured by the standard four-point technique, present values above 200 MΩ.cm [12]. This characterizes these compound as insulating materials. This lack of electronic conductivity, required for electrolyte application in SOFC, contributed to the interest in this type of compound. Acceptor-doped Nd_3GaO_6 compounds have been presented recently as good oxygen ion conductors in spite of very low doping levels [28]. Rare-Earth oxides usually present a strong affinity toward water uptake which would makes acceptor-doped RE_3GaO_6 materials potential proton conductors to be used as electrolytes materials. As it can be seen on **Figure 3.2.3 (a)** and **(b)** that the creation of a small rate of oxygen vacancies in the Nd_3GaO_6 structure, concomitant with substitutions of Ca^{2+} and Sr^{2+} for Nd^{3+}, induces a significant increase of the anionic conductivity which reaches 6×10^{-3} and 7×10^{-3} S.cm^{-1}, at 800 °C, for $Nd_{2.91}Ca_{0.09}GaO_{5.955}$ and $Nd_{2.955}Sr_{0.045}GaO_{5.9775}$, respectively. These values are comparable with already known oxygen-ion conductors, for instance 2×10^{-3} S.cm^{-1} at 800 °C for 10 mol % YSZ [47-48]. Activation energies for these Ca and Sr substituted compounds, 0.97 and 1.06 eV, respectively, are, as expected, rather close to those of other Nd_3GaO_6-based materials [28].

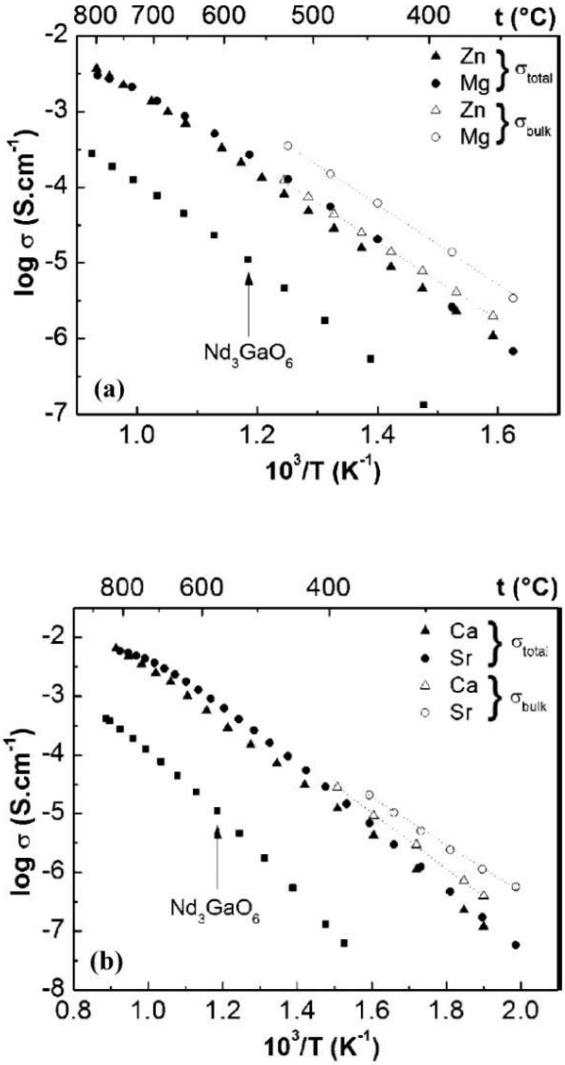

Figure 3.2.3 Arrhenius plots for: (a) $Nd_3O_2GaO_4$ and $Nd_3Ga_{0.97}M_{0.03}O_{5.985}$ (M = Zn^{2+}, Mg^{2+}) and (b) $Nd_3O_2GaO_4$, $Nd_{2.91}Ca_{0.09}GaO_{5.955}$ and $Nd_{2.955}Sr_{0.045}GaO_{5.9775}$ [28]

3.3 Objectives of the study

In connection with the foregoing, the objectives of this chapter are:

- Synthesis of solid solutions $Gd_{3-x}Me_xGaO_{6-\delta}$ (Me=Ca^{2+}, Sr^{2+}) by modified sol-gel combustion method and characterization of their crystal structure;

- The study of the transport properties in the range of temperatures 300 – 900 °C, in different atmospheres with different oxygen partial pressures;

- Investigation of these phases on a possibly proton transfer;

- Examine its stability under operating conditions.

3.4 Structural properties of $Gd_{3-x}Me_xGaO_{6-\delta}$ (Me=Ca^{2+}, Sr^{2+}) compounds

3.4.1 Structural analysis of $Gd_{3-x}Me_xGaO_{6-\delta}$ (Me=Ca^{2+}, Sr^{2+}) powders

In general, rare-earth monogallates are synthesized by the solid-state reaction at high temperature. However, this method requires a long processing time, a high processing temperature, repeated milling and washing with chemicals. All the powders of $Gd_{3-x}Me_xGaO_{6-\delta}$ (Me=Ca^{2+}, Sr^{2+}) have been synthesized by a microwave-assisted citric acid combustion method as described in the **Chapter 2**. The citrate/nitrate ratio was chosen equal to 1 which provided a suited morphology of the powder.

Firstly we synthesized the pure Gd_3GaO_6 compound, which was used as a basis for the formation of solid solutions. Synthesis of the sample was performed according to the modified combustion method. The sample was calcinated in ambient atmosphere at 900 °C for 5 h. XRD diagram could be indexed in non-centrosymmetric orthorhombic structure with lattice parameters a = 8.9891(2) Å, b = 11.2804(3) Å, c = 5.4753(1) Å, $\alpha = \beta = \gamma = 90°$ (space group $Cmc2_1$). The lattice parameters of Gd_3GaO_6 determined in the present work agree well with the former reported data [12, 15]. The as-synthesized white powders of $Gd_{3-x}Me_xGaO_{6-\delta}$ were characterized by X-Ray diffraction. All samples of $Gd_{3-x}Me_xGaO_{6-\delta}$ were calcinated at 900 °C for 5 h in ambient atmosphere. Data were collected over the angular range from 20° to 80° with step of 0.02°. **Figure 3.3.1** shows an evolution of the XRD patterns of solid solutions with increasing content of Ca and Sr. All the compositions in the range $0 \leq x \leq 0.10$ have a single phase and are isostructural with pure Gd_3GaO_6 (non-centrosymmetric orthorhombic structure, space group $Cmc2_1$). For the compositions with $x > 0.10$, we noticed the presence of Gd_2O_3 impurity phase. These samples have not been investigated further.

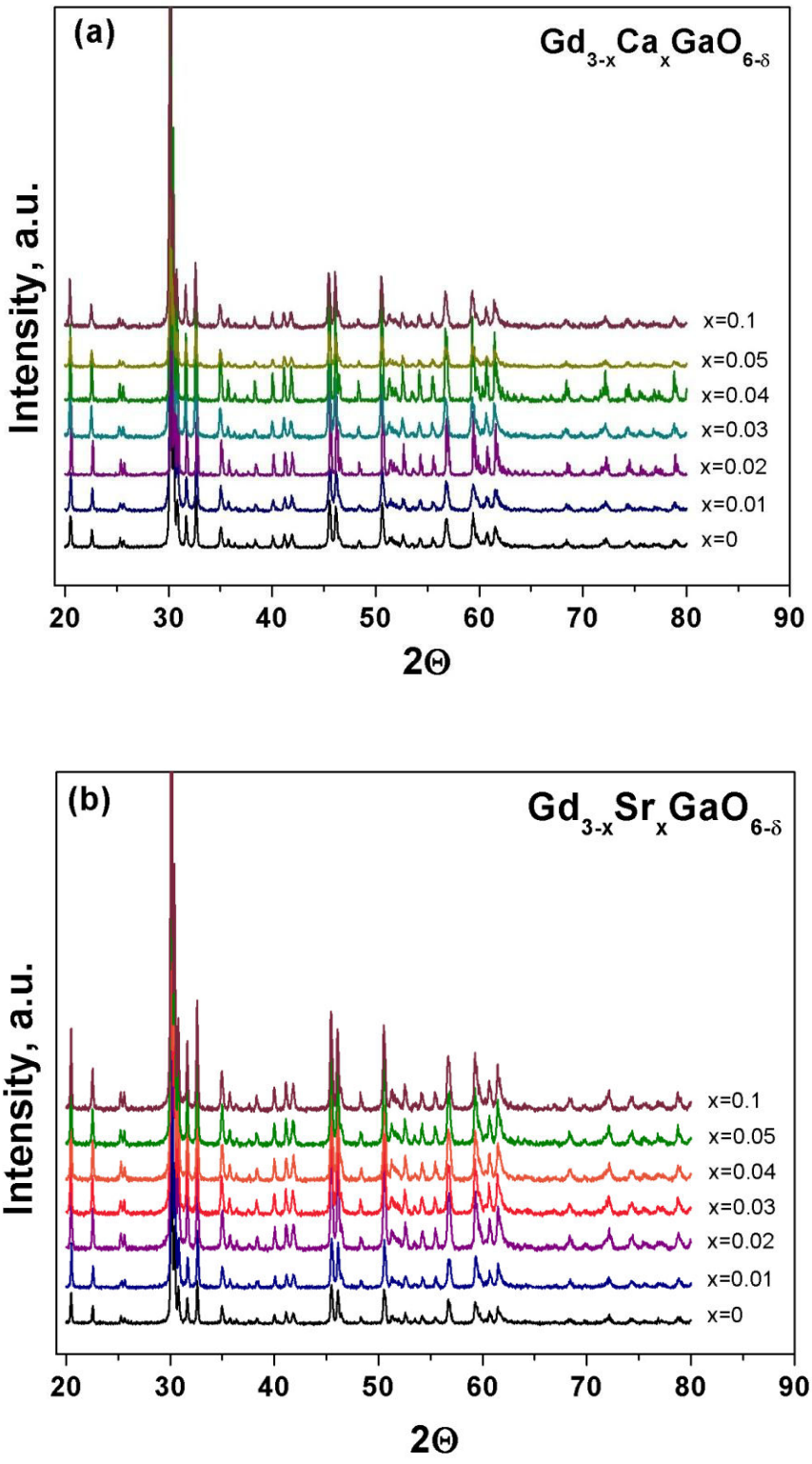

Figure 3.3.1 X-Ray diffraction pattern of (a) Gd_{3-x} $Ca_xGaO_{6-\delta}$ and (b) Gd_{3-x} $Sr_xGaO_{6-\delta}$ powders calcined at 900 °C for 5 h

3.4.2 High temperature X-Ray diffraction and thermal expansion coefficient

Thermal expansion coefficient (TEC) is an important property of ceramics materials when they are used under conditions of thermal stress and its combination with other materials. Since ceramics are polycrystalline materials, even if the thermal expansion of the constitutive crystal is anisotropic, the materials as a whole will exhibit an averaged isotropic expansion. In such a case, the average linear expansion coefficient for the polycrystalline substance will be one-third of the coefficient of volume expansion of the constituent crystal [29]. X-Ray diffraction experiments were performed on the powders in air from 295 K to 995 K, see **Figure 3.3.2.** Profile matching of the XRD pattern was performed using Fullprof suite program using LeBail fitting. Atomic positions were thus not refined. The indexations of the peaks are always done considering a structure with space group $Cmc2_1$. The evolution of the cell parameters with temperature is presented in **Figure 3.3.3**. It shows that even at high temperature doped Gd_3GaO_6 compounds do not present any structural transition. Thermal expansion coefficients for Ca and Sr-doped samples are shown in the **Table 3.3.1**. The results show no evidence for TEC evolution with dopant nature and content.

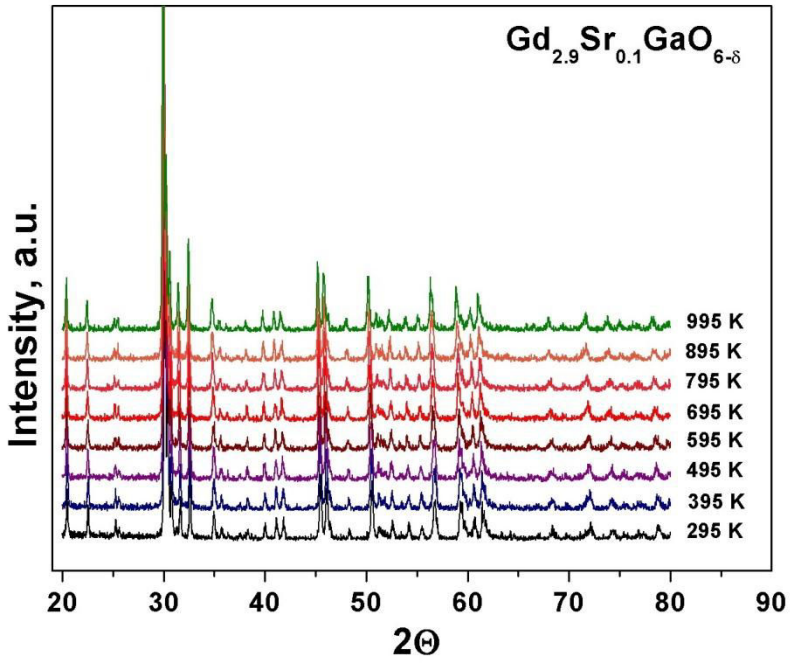

Figure 3.3.2 X-Ray diffraction of $Gd_{2.9}Sr_{0.1}GaO_{6-\delta}$ at different temperatures

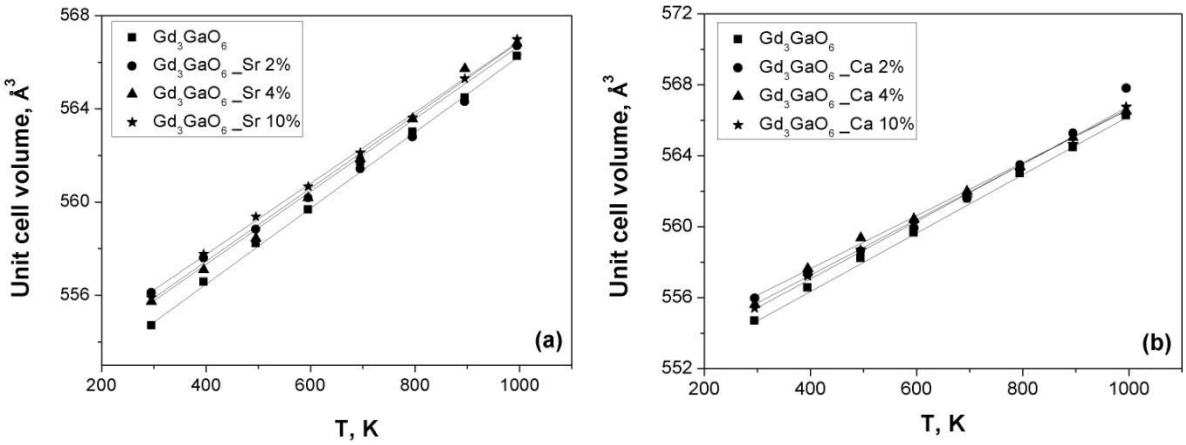

Figure 3.3.3 Unit cell volume of $Gd_{3-x}Sr_xGaO_{6-\delta}$ (a) and $Gd_{3-x}Ca_xGaO_{6-\delta}$ (b) at different temperatures

Table 3.3.1 Linear thermal expansion coefficient of $Gd_{3-x}Ca_xGaO_{6-\delta}$ and $Gd_{3-x}Sr_xGaO_{6-\delta}$ sintered at 1450 °C for 10 h

Me dopant content, %	**TEC, K^{-1} $Gd_{3-x}Ca_xGaO_{6-\delta}$**	**TEC, K^{-1} $Gd_{3-x}Sr_xGaO_{6-\delta}$**	**Temperature range, K**
0	9.79E-6 (±0.01)	9.79E-6 (±0.01)	295 - 995
2	9.87E-6 (±0.01)	8.62E-6 (±0.01)	295 – 995 (*)
4	9.74E-6 (±0.01)	9.83E-6 (±0.01)	295 - 995
10	9.38E-6 (±0.01)	9.23E-6 (±0.01)	295 - 995

* 295-895K for $Gd_{3-x}CaGaO_{6-\delta}$

From the literature data, we can notice that these values are close to those of typical electrolytes ($10.9*10^{-6}$ K^{-1} for 8YSZ, $12.5*10^{-6}K^{-1}$ for CGO and $10.4*10^{-6}$ K^{-1} for LSGM [30]). The values reported in this work are thus in the usual range for fuel cell applications and comparable with typical electrolyte values.

3.4.3 Structural analysis of $Gd_{3-x}Me_xGaO_{6-\delta}$ (Me=Ca^{2+}, Sr^{2+}) sintered pellets

The cell parameters, volume and relative densities of sintered compounds depends on quantity of dopant as shown in Table 3.3.2 (a) and (b). As we could see the partial substitution of Gd^{3+} for Ca^{2+} or Sr^{2+} improves the sinterability of Gd_3GaO_6, which could be explained by that fact that ionic radius of dopant closer to Gd are favourable to sintering.

Table 3.3.2 Cell parameters, volume and relative densities of compounds sintered at 1450 °C for 10 h:

(a) $Gd_{3-x}Ca_xGaO_{6-\delta}$

x (Ca)	*a*, Å	*b*, Å	*c*, Å	Unit cell volume, Å^3	Space group	Relative density, %
0	8.9903(2)	11.2816(3)	5.4761(1)	555.411	$Cmc2_1$	83
0.01	8.9885(1)	11.2793(2)	5.4761(1)	555.182	$Cmc2_1$	70
0.02	8.9894(1)	11.2815(1)	5.4751(3)	555.261	$Cmc2_1$	90
0.03	8.9896(3)	11.2797(2)	5.4771(1)	555.367	$Cmc2_1$	91
0.04	8.9905(2)	11.2786(4)	5.4781(1)	555.480	$Cmc2_1$	93
0.05	8.9908(1)	11.2779(3)	5.4787(2)	555.525	$Cmc2_1$	94
0.1	8.9911(2)	11.2788(1)	5.4791(1)	555.618	$Cmc2_1$	94

(b) $Gd_{3-x}Sr_xGaO_{6-\delta}$

x (Sr)	*a*, Å	*b*, Å	*c*, Å	Unit cell volume, Å^3	Space group	Relative density, %
0	8.9903(2)	11.2816(3)	5.4761(1)	555.411	$Cmc2_1$	83
0.01	8.9908(3)	11.2798(4)	5.4771(1)	555.459	$Cmc2_1$	85
0.02	8.9922(2)	11.2825(3)	5.4788(1)	555.846	$Cmc2_1$	88
0.03	8.9930(2)	11.2832(2)	5.4777(1)	555.826	$Cmc2_1$	91
0.04	8.9941(2)	11.2827(3)	5.4799(1)	556.090	$Cmc2_1$	92
0.05	8.9956(2)	11.2836(2)	5.4803(2)	556.267	$Cmc2_1$	92
0.1	8.9973(1)	11.2855(2)	5.4815(2)	556.581	$Cmc2_1$	96

The lattice parameter evolution as a function of dopant concentration is presented in **Figure 3.3.4**. As can be seen, the parameter *b* changed nonlineary, while the parameters *a*, *c* and the cell volume increases slightly with increasing dopant concentration. Hereinafter interval of measurement error included in the diameter of plotted points and therefore cannot be specified. From a simple consideration of ionic radii (r^{VII} (Ca^{2+}) =1.06 Å and r^{VII} (Sr^{2+}) =1.21 Å), the Sr-doped samples would be expected to have bigger lattice parameters and cell volume compared to Ca-doped samples.

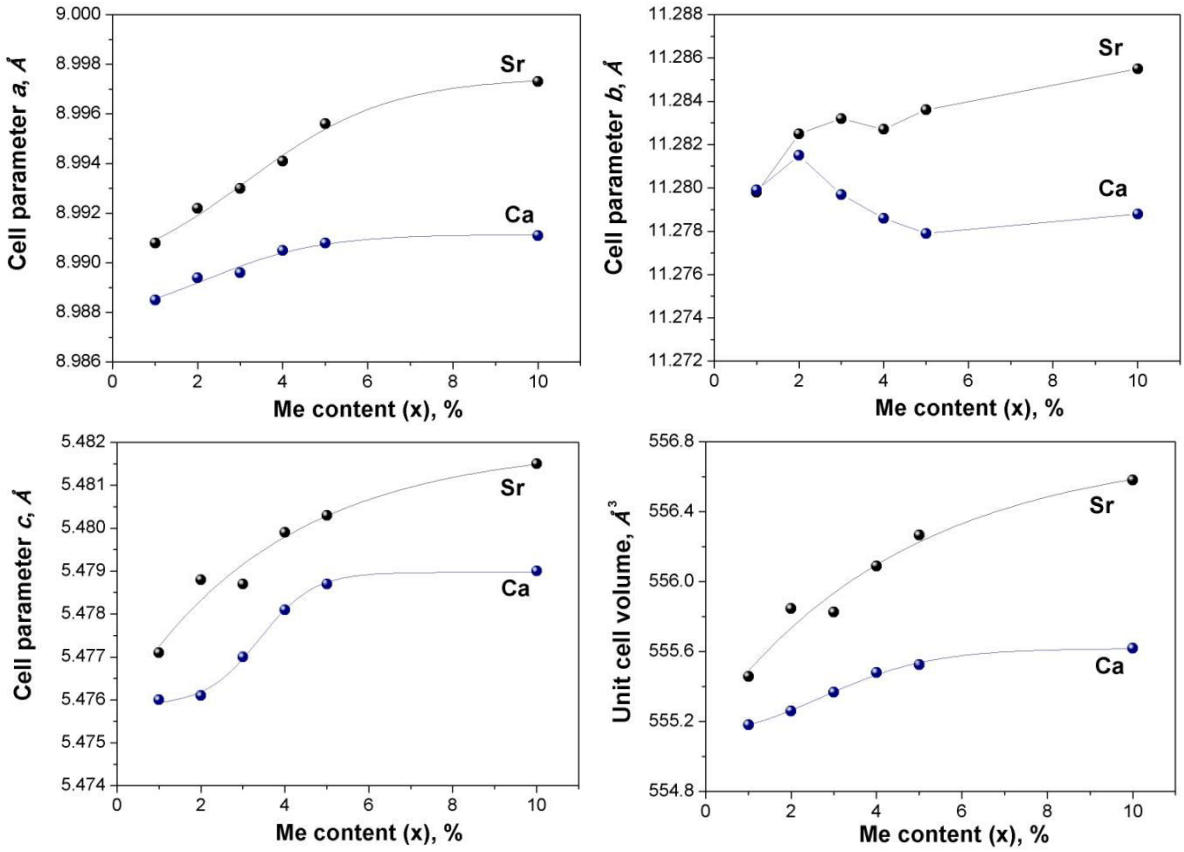

Figure 3.3.4 Evolution of cell parameters and volume as a function of dopant content of $Gd_{3-x}Me_xGaO_{6-\delta}$ compounds

In order to obtain more detailed structural information, Rietveld refinement has been applied to analyze all XRD data. **Figure 3.3.5** presents a typical fit for pure Gd_3GaO_6 and $Gd_{2.97}Sr_{0.03}GaO_{5.985}$. In the pictures red dots and solid black lines corresponded with experimental data and calculated curve, respectively, while the blue solid lines being their difference in the bottoms. The blue vertical bars indicate the Bragg angle positions corresponding to the structure. Refined atomic coordinates and agreement factors are given in Table 3.3.3 for $Gd_{2.97}Sr_{0.03}GaO_{5.985}$. The lengths of characteristic bonds are summarized in Table 3.3.4. In the present simulation, oxygen content was set to 5.985 for the formula unit, when vacancies an equally spread on all oxygen atoms.

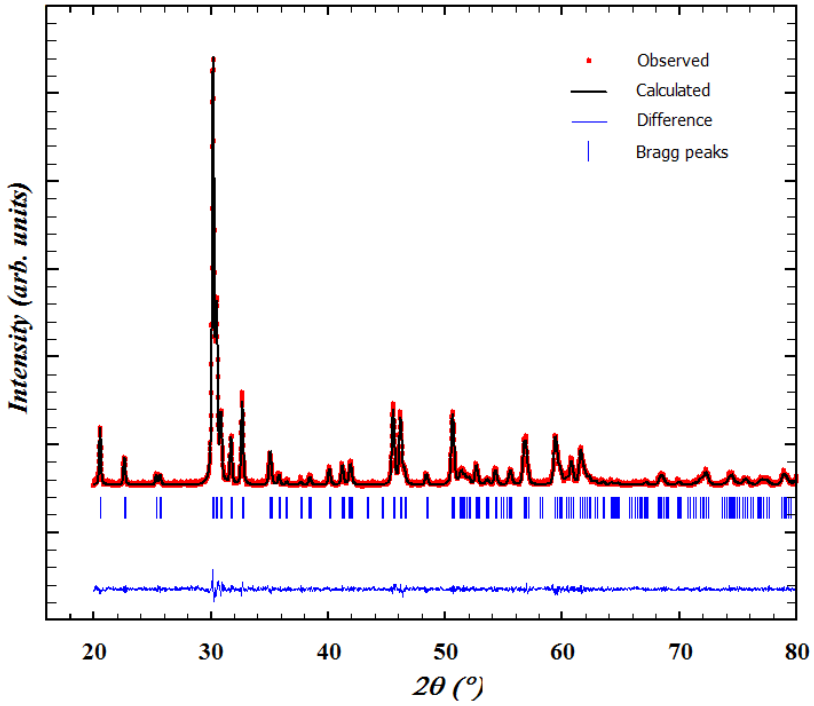

(a) Gd_3GaO_6 : R_{Bragg} = 1.28, R_f = 1.33, R_p = 9.04, R_{wp} = 10.8

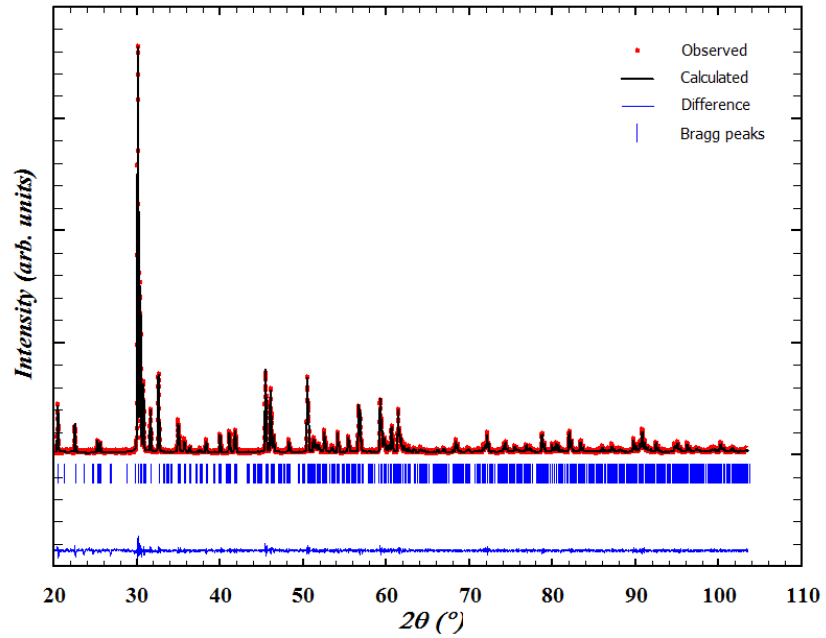

(b) $Gd_{2.97}Sr_{0.03}GaO_{5.985}$: R_{Bragg} = 2.58, R_f = 2.37, R_p = 9.88, R_{wp} = 9.2

Figure 3.3.5 Diagram of XRD powder diffraction data for (a) Gd_3GaO_6 and (b) $Gd_{2.97}Sr_{0.03}GaO_{5.985}$ refined by Rietveld method. Reliability factors are listed below each pattern

Table 3.3.3 Structural parameters and reliability factors for the Rielveld refinement of $Gd_{2.97}Sr_{0.03}GaO_{5.985}$

x = 0.03	**$Gd_{2.97}Sr_{0.03}GaO_{5.985}$**	
Cell parameters **Space group**	a = 8.9930(2) Å, b = 11.2832(2) Å, c = 5.4777(1) Å *$Cmc2_1$*	
Atom	**Wyck**	**x, y ,z positions**
Gd(1) Occupation of site	*8b*	x = 0.19429 , y = 0.11044, z = 0.46084 Gd = 97%, Sr = 3%
Gd(2)	*4a*	x = 0, y = 0.39376, z = 0.42089
Ga	*4a*	x = 0, y = 0.20005, z = 0
O(1)	*8b*	x = 0.08718, y = 0.12838, z = 0
O(2)	*8b*	x = 0.33372, y = 0.42151, z = 0
O(3)	*4a*	x = 0, y = 0.02731, z = 0.22782
O(4)	*4a*	x = 0, y = 0.22992, z = 0.65631
R_{Bragg}, R_f	R_{Bragg} = 2.58, R_f = 2.37	

Table 3.3.4 Interatomic distancies (Å) of Gd to O after the Rietveld refinements for the $Gd_{2.97}Sr_{0.03}GaO_{5.985}$ compound

Gd(1)-O(1)	2.7095	2.7688
Gd(1)-O(2)	2.3286	2.3133
Gd(1)-O(3)	2.7079	2.7576
Gd(1)-O(4)	2.5523	2.6850
Gd(2)-O(1)	2.8589	2.7449
Gd(2)-O(2)	2.4967	2.5784
Gd(2)-O(4)	2.5536	

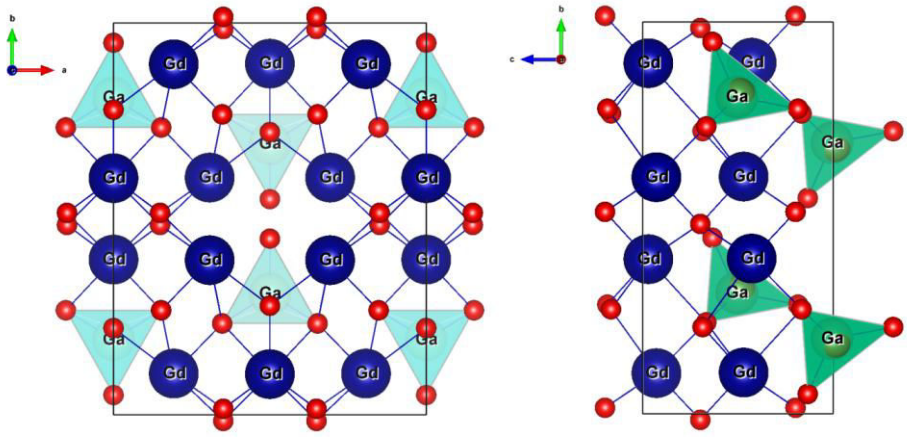

Figure 3.3.6 View of the structure Gd_3GaO_6 in the directions (a) [001] and (b) [100] showing GaO_4 tetrahedra, Gd and O atoms (small red circles)

Figure 3.3.6 represents a view of the structure Gd_3GaO_6 in the different directions. As starting model for the refinement of the structure, was used a structural information given by Liu *et al* [12]. There are four formula units per unit cell, *i.e.*, the unit cell contains $12Gd + 4Ga + 24O$. The ions Gd, Ga and oxygens occupy 8(*b*) + 4(*a*), 4(*a*) and two 8(*b*) + two 4(*a*) sites respectively. Because all of the *z* coordinates of atoms are variable, so we fix the *z* coordinate of Ga to zero. There are two sites of seven-fold coordination for Gd atoms with oxygens (Wyckoff position 8*b* for *Gd*1 and 4*a* for *Gd*2). Ga atoms are in oxygen tetrathedra which are distorted and elongated along *c*-axis. The average lengths of the Ga–O bonds are in the range 1.78–1.85 Å. Oxygen atoms on O(2) site coordinate only to Gd atoms, and the Gd–O distance for the combination of atoms Gd(1)–O(2) is 2.32 Å.

3.4.4 Microstructural analysis of $Gd_{3-x}Me_xGaO_{6-\delta}$ ($Me=Ca^{2+}$, Sr^{2+}) sintered pellets

The powder after synthesis was ground in an agate mortar and then pressed in the form of pellet of 10 mm in diameter under a pressure of 750 MPa. The sintering was performed under air at a temperature of 1450 °C for 10 hours, with heatting speed 200 °C/ h. Sintering temperature was higher than previously reported in [28]. But at higher heating temperature, we could be able to increase the grain size and as a consequence increase the conductivity values. **Figure 3.3.7** presents a color change of the samples for the series of Sr-doped Gd_3GaO_6 samples. For the series of Ca-doped Gd_3GaO_6 samples, we did not observe any change in color.

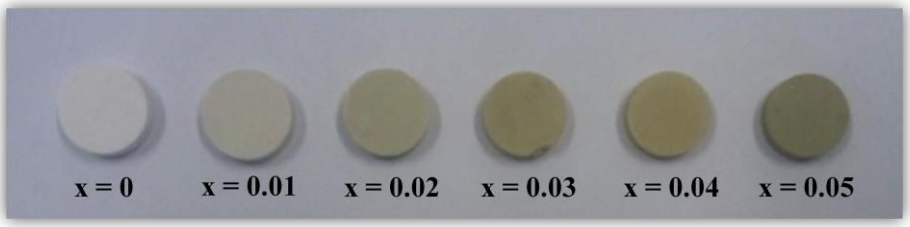

Figure 3.3.7 The color change of the $Gd_{3-x}Sr_xGaO_{6-\delta}$ samples depends on the dopant concentration

The morphology of the surface of the sintered samples was investigated using scanning electron microscopy (SEM). **Figure 3.3.8, Figure 3.3.9, Figure 3.3.10** show typical micrographs for pellet surface and particle size distribution of Gd_3GaO_6 and $Gd_{3-x}Me_xGaO_{6-\delta}$. As can be seen the doped samples consist of small and large grains with clean grain area and a size of about 300 nm and 4-5 µm respectively. Grain size changes slightly with quantity of dopant. In the case of pure Gd_3GaO_6, the grain size is more inconstant with small crystallites.

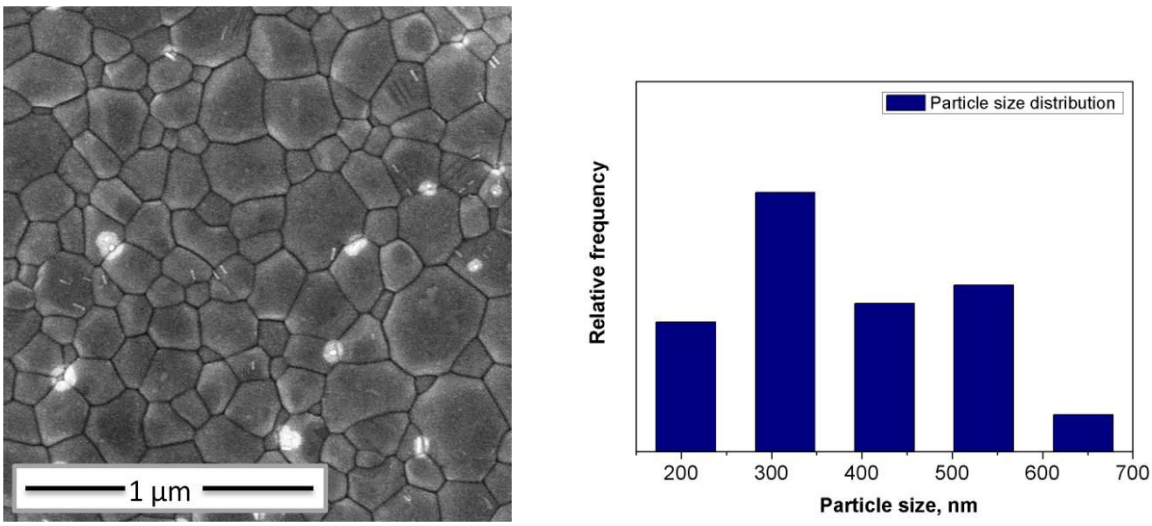

Figure 3.3.8 SEM pictures of a fracture surface of a dense pellet of Gd_3GaO_6 compound sintered 1450 °C for 10 h and particle size distribution

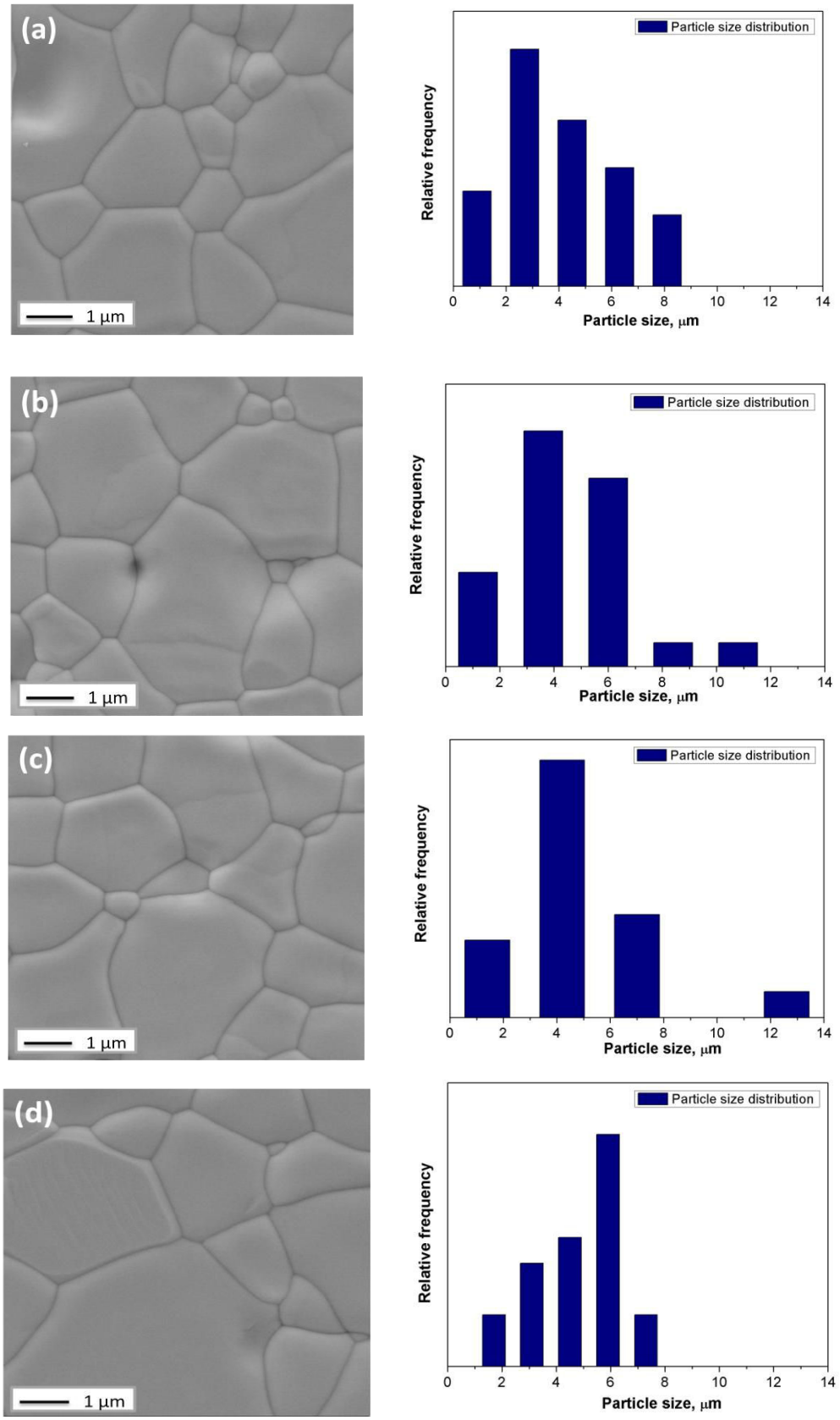

Figure 3.3.9 SEM pictures and particle size distribution of $Gd_{3-x}Ca_xGaO_{6-\delta}$ compounds sintered at 1450 °C for 10 h: a, b, c, d represent fracture surface of Ca-doped samples (2, 3, 4, 5% of doping respectively)

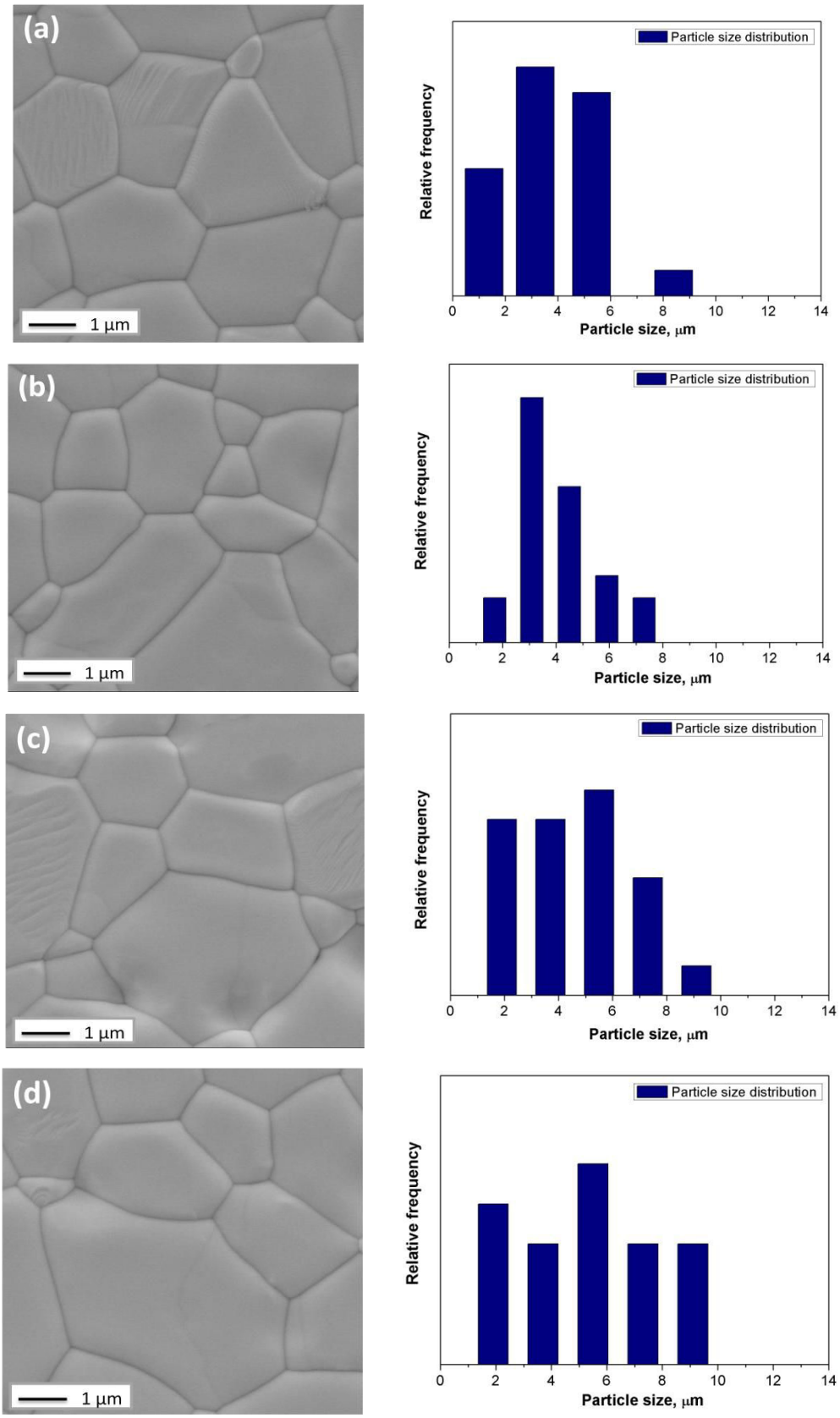

Figure 3.3.10 SEM pictures and particle size distribution of $Gd_{3-x}Sr_xGaO_{6-\delta}$ compounds sintered at 1450 °C for 10 h: a, b, c, d represent fracture surface of Sr-doped samples (2, 3, 4, 5% of doping respectively)

To determine the homogeneity of chemical composition several pictures were taken in secondary electrons, and the corresponding X-Ray line profile of the sample. For all samples with low substitution rates ($x < 0.05$), EDX is not a sufficiently sensitive analytical technique for quantifying the content of dopant. **Figure 3.3.11** shows an image of the surface of the pellet surface of $Gd_{2.9}Ca_{0.1}GaO_{6-\delta}$. To obtain the dependence of the intensity of the characteristic X-ray lines of Gd, Ca, Ga, O, an EDX aquisition was carried out by scanning the sample surface. Despite the fact that the quantification of the elements is poor, the presence of Ca could be clearly seen by EDX. **Figure 3.3.12** indicates the distribution of Ga, Gd, Ca and O (K, L-lines) in the sample's volume. The color scale corresponds to the content element at a given point in the surface at. %. It can be seen a uniform distribution of all components in the polycrystalline sample. The EDX study was conducted and there was no evidence of segregation of elements.

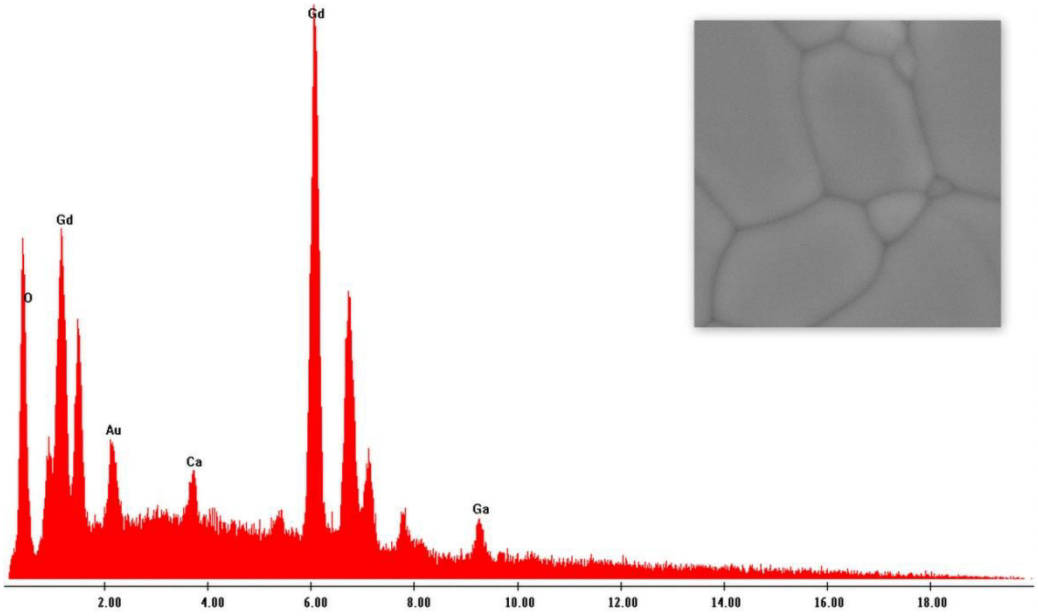

Figure 3.3.11 Energy-dispersive analysis of pellet surface of $Gd_{2.9}Ca_{0.1}GaO_{6-\delta}$ and characteristic shape of the spectrum

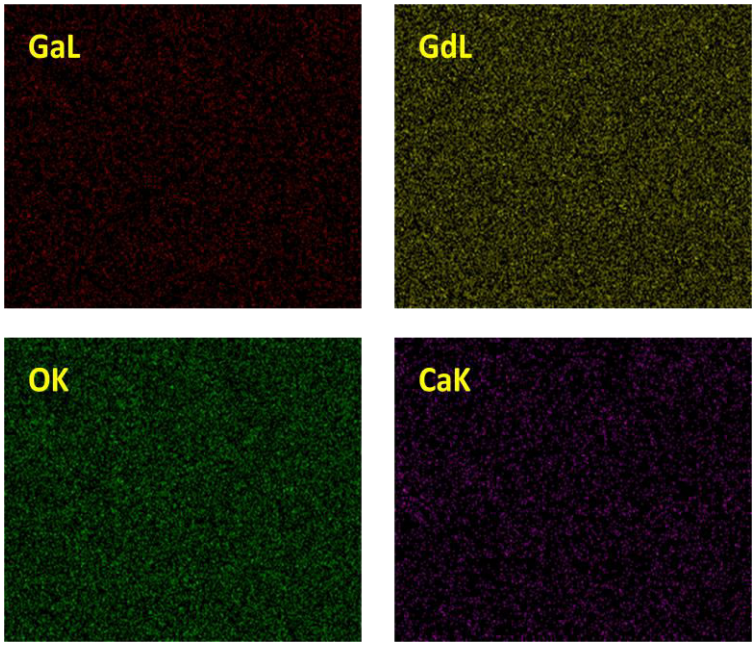

Figure 3.3.12 Distribution of Ga, Gd, Ca and O (K, L-lines) in the sample's volume

3.4.5 Chemical stability

One of the important characteristics of ceramic materials for SOFC electrolyte applications is their phase stability in both oxidizing and reducing conditions. Below we present some stability tests on Gd_3GaO_6 and $Gd_{3-x}Sr_xGaO_{6-\delta}$ compounds put under severe conditions such as boiling water, wet CO_2 and Ar + 5% H_2. Despite the fact that boiling water is not a usual environment for an electrolyte, this test was successfully used in the case of barium cerates [31, 32, 33]. Such type of treatment is very fast and valuable to test the stability of materials in humid atmosphere. Oxygen vacancies in protonic materials can be filled by water molecules according to Equation (3.2).

$$H_2O\ (g) + V_o^{\cdot\cdot} + O_o^x <=> 2OH_o \qquad (3.2)$$

X. Guo in [34] well described an incorporation of water molecules into the structure by filling oxygen vacancies, which leads to the formation of proton defects. The steps are following: 1) chemical absorption of H_2O on the material surface, 2) reaction of H_2O with O^{2-} on the material surface to form hydroxyl ions OH^-, 3) penetration of OH^- into the inner part by grain boundary diffusion, 4) filling of oxygen vacancies by OH^- ions, and therefore the formation of proton defects. When water is boiling, her transport through the porous layer is expected to be much faster than the transport of oxygen ions and proton defect through the lattice [35]. **Figure 3.3.13** shows XRD patterns of powders of Gd_3GaO_6 and $Gd_{3-x}Sr_xGaO_{6-\delta}$ after a treatment in boiling water for 10 h. From X-Ray diffraction, we did not find any change in the composition nor change in the structure of tested compounds.

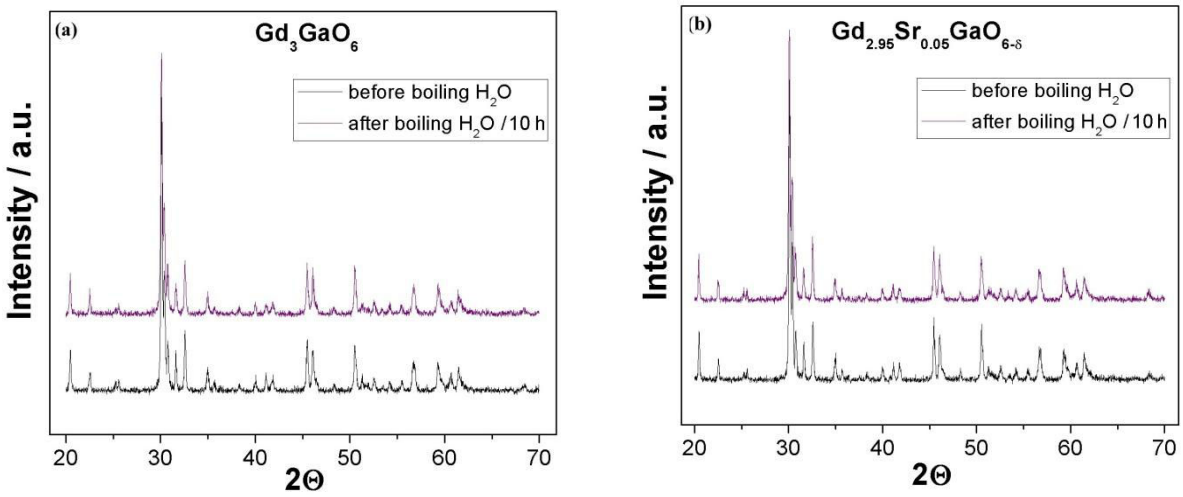

Figure 3.3.13 XRD patterns of powders of Gd_3GaO_6 (a) and $Gd_{3-x}Sr_xGaO_{6-\delta}$ (b) in boiling water for 10 h

Pellets of all compositions were treated thermally at 600 °C for 50 h under wet 5% H_2/Ar and 600 °C for 50 h under wet CO_2. The X-ray diffraction patterns are shown in **Figure 3.3.14** and **Figure 3.3.15**, respectively. No extra-phases, phase or color changes were observed on these diffractograms.

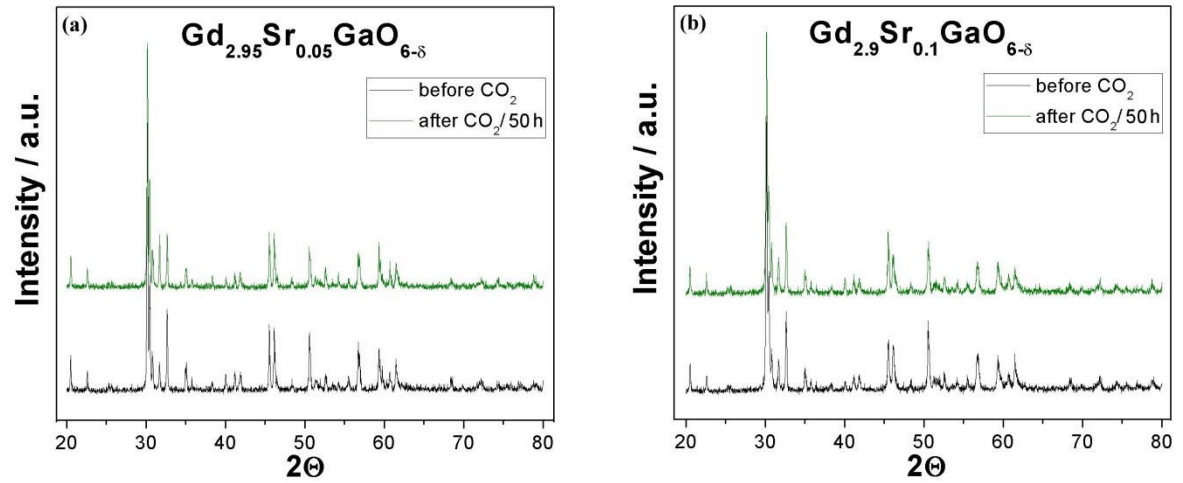

Figure 3.3.14 XRD patterns of pellet surface of (a) $Gd_{2.95}Sr_{0.05}GaO_{6-\delta}$ and (b) $Gd_{2.9}Sr_{0.1}GaO_{6-\delta}$ in wet CO_2 at 600 °C for 50 h

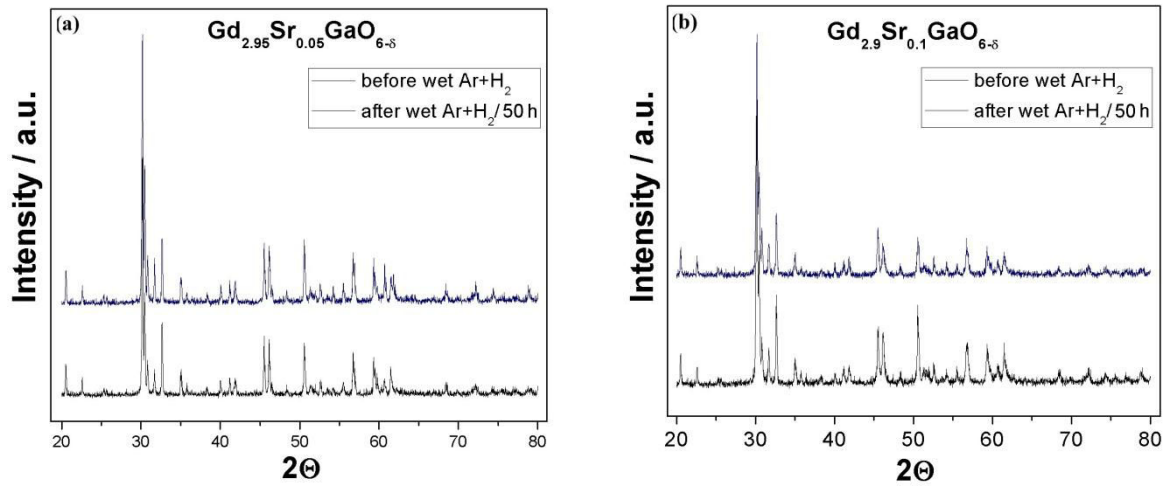

Figure 3.3.15 XRD patterns of pellet surface of (a) $Gd_{2.95}Sr_{0.05}GaO_{6-\delta}$ and (b) $Gd_{2.9}Sr_{0.1}GaO_{6-\delta}$ in wet $Ar+H_2$ at 600 °C for 50 h

3.5 Transport and hydration properties

This section presents the results of the study of the electrical properties of the $Gd_{3-x}Me_xGaO_{6-\delta}$ (Me = Ca^{2+}, Sr^{2+}) phases by varying environmental parameters (T, pO_2).

3.5.1 Impedance spectra of $Gd_{3-x}Me_xGaO_{6-\delta}$ (Me = Ca^{2+}, Sr^{2+})

Figure 3.4.1 shows the typical impedance plots of $Gd_{3-x}Ca_xGaO_{6-\delta}$ in atmospheres of different humidity levels at different temperatures. It shows that over the temperature range 300 °C – 800 °C, up to 3 contributions can be identified. Below 500 °C, one contribution appears at high frequencies which is thought to correspond to bulk and a second one at low frequencies which could be attributed to grain boundary. By increasing the temperature from 500 °C to 800 °C, the first contribution cannot be seen anymore. At 600 °C, a third contribution starts to appear at the low frequency end. The modeling of the impedance spectra was done by using ZView software. It gives access to the precise values of conductivity for the different contributions. The overall equivalent circuit used in the present work to model the behavior of the bulk and the grain boundaries. Over the temperature range 300 °C – 500 °C it corresponds to two RC circuits (a parallel arrangement of resistor and capacitance), one attributed to the bulk and one to the grain boundary contribution to the impedance, in series. At higher temperatures (over than 500 °C) equivalent circuit corresponds to a resistance in series with two RC circuits. When the temperature was further increased, the semicircle corresponding to the bulk conduction response can no longer be well defined and the bulk resistance can be then derived from the high frequency intercept of the intermediate frequency semicircle with the real axis. The analysis is performed according to the "brick layer model" as described in Chapter 2. The calculations used the resistance value of the sample obtained by fitting the semi-circles. It can be noticed that under the 600 °C impedance of samples in wet argon diminishes strongly as compared to dry atmosphere. Sensitivity

of the electric conductivity values to the presence of water vapor in the gas phase indicates the appearance of proton conduction contribution.

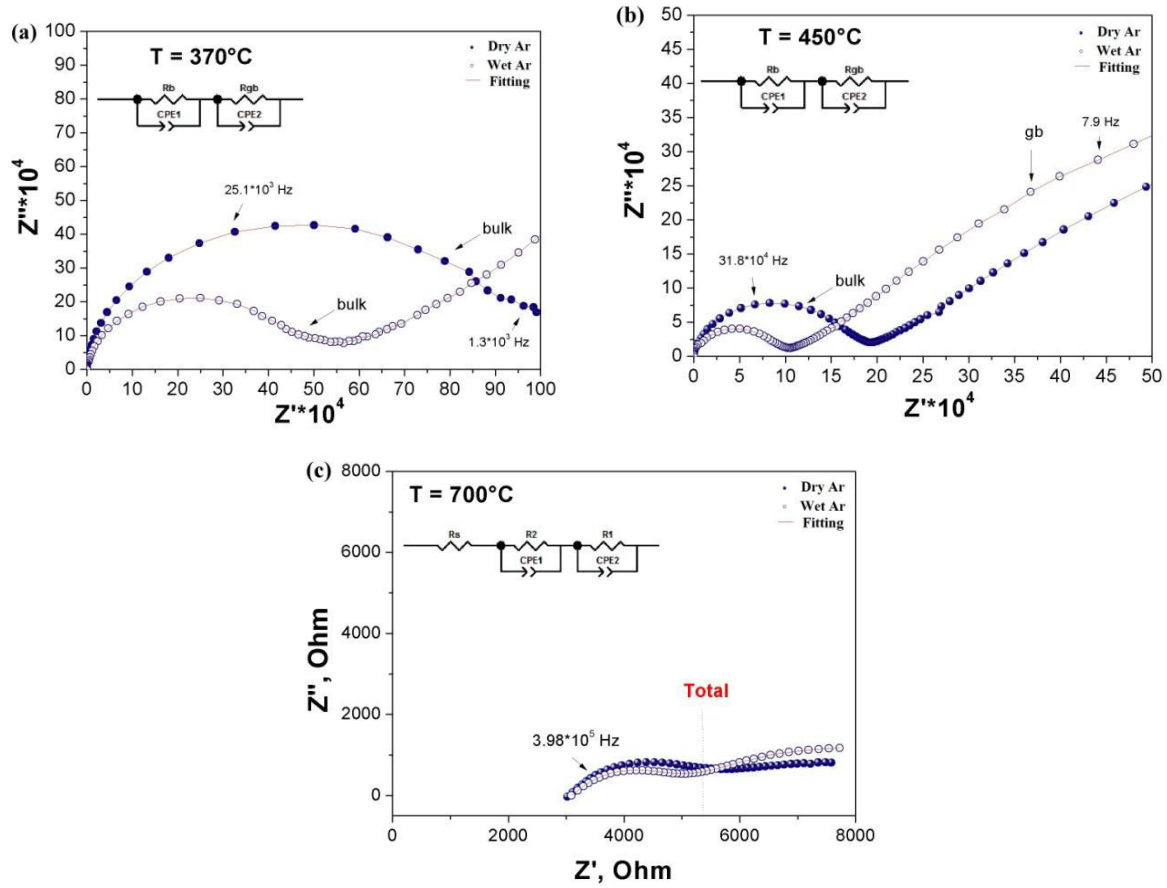

Figure 3.4.1 The Nyquist plots of $Gd_{3-x}Ca_xGaO_{6-\delta}$ in dry and humidified Ar at different temperatures: 370 °C (a), 450 °C (b) and 700 °C (c)

3.5.2 Transport properties of solid solutions $Gd_{3-x}Me_xGaO_{6-\delta}$ (Me = Ca^{2+}, Sr^{2+}) as a function of temperature

All conductivity measurements were carried out under different atmospheres in a wide range of temperatures. **Figure 3.4.2** and **Figure 3.4.3** show dependences of electrical conductivity for both series of samples. As it can be seen all conductivity curves reflect an Arrhenius type of behavior. Pure Gd_3GaO_6 has quite low conductivity at all temperatures. This result can be in great part related to its small grain size, its low density (83 %) and, of course, to the absence of dopant. With increasing humidity, the total conductivity Gd_3GaO_6 varies little. In both atmospheres conductivity curves have a slope with an activation energy 1.30 eV which is a little bit higher than for pure Nd_3GaO_6 – 1.2 eV [28]. With increasing percentage of alkaline earth metals in $Gd_{3-x}Me_xGaO_{6-\delta}$ we could see a significant increase in conductivity values as expected from the increased number of oxygen vacancies with the

substitution level. In the high temperature (HT, above 600 °C) and low temperature (LT, below 600 °C) ranges conductivity curves can be approximated by straight lines with activation energies gathered in Table 3.4.1 and Table 3.4.2. In a humid atmosphere we observed an increase in conductivity at temperatures below 600 °C. The difference in the values of the conductivity can reach 1 order of magnitude, probably due to the presence of protons contribution. For the case of $Gd_{2.9}Sr_{0.1}GaO_{6-\delta}$, in dry atmosphere and temperature above ~ 600 °C can be noticed a change of activation energy from 0.92 eV to 0.74 eV. It indicates the presence of the electronic component of conductivity (p-type).

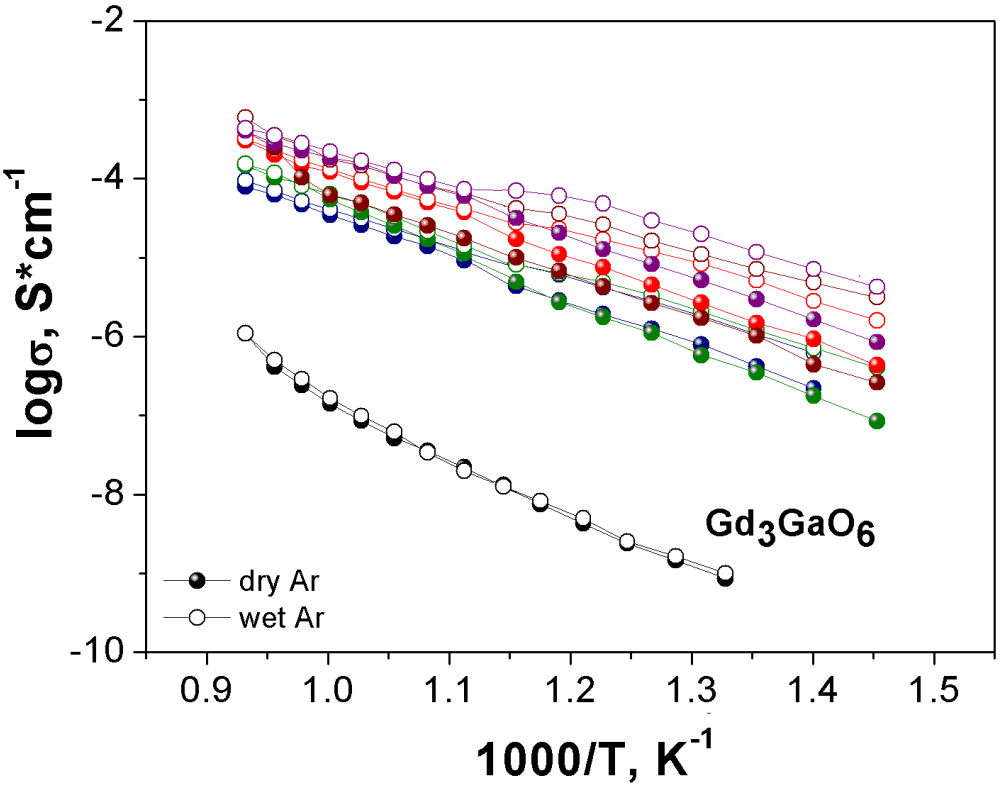

Figure 3.4.2 Arrhenius plots of total conductivities in dry and wet Ar of $Gd_{3-x}Ca_xGaO_{6-\delta}$: $Gd_{2.98}Ca_{0.02}GaO_{6-\delta}$ (●- dry Ar, ○- wet Ar), $Gd_{2.97}Ca_{0.03}GaO_{6-\delta}$ (●- dry Ar, ○- wet Ar), $Gd_{2.96}Ca_{0.04}GaO_{6-\delta}$ (●- dry Ar, ○- wet Ar), $Gd_{2.95}Ca_{0.05}GaO_{6-\delta}$ (●- dry Ar, ○- wet Ar), $Gd_{2.9}Ca_{0.1}GaO_{6-\delta}$ (●- dry Ar, ○- wet Ar)

Table 3.4.1 Activation energy for total conductivity of $Gd_{3-x}Ca_xGaO_{6-\delta}$ compounds under Ar atmosphere

Composition	HT range, eV		LT range, eV		Ea ref, eV [28]
	Dry Ar	Wet Ar	Dry Ar	Wet Ar	
Gd_3GaO_6	1.30	1.30	1.30	1.30	1.2
$Gd_{2.98}Ca_{0.02}GaO_{6-\delta}$	1.05	1.05	1.05	0.79	-
$Gd_{2.97}Ca_{0.03}GaO_{6-\delta}$	1.02	1.02	1.02	0.76	-
$Gd_{2.96}Ca_{0.04}GaO_{6-\delta}$	1.04	1.04	1.04	0.68	-
$Gd_{2.95}Ca_{0.05}GaO_{6-\delta}$	1.00	1.00	1.00	0.71	-
$Gd_{2.9}Ca_{0.1}GaO_{6-\delta}$	0.98	0.98	0.98	0.70	0.97

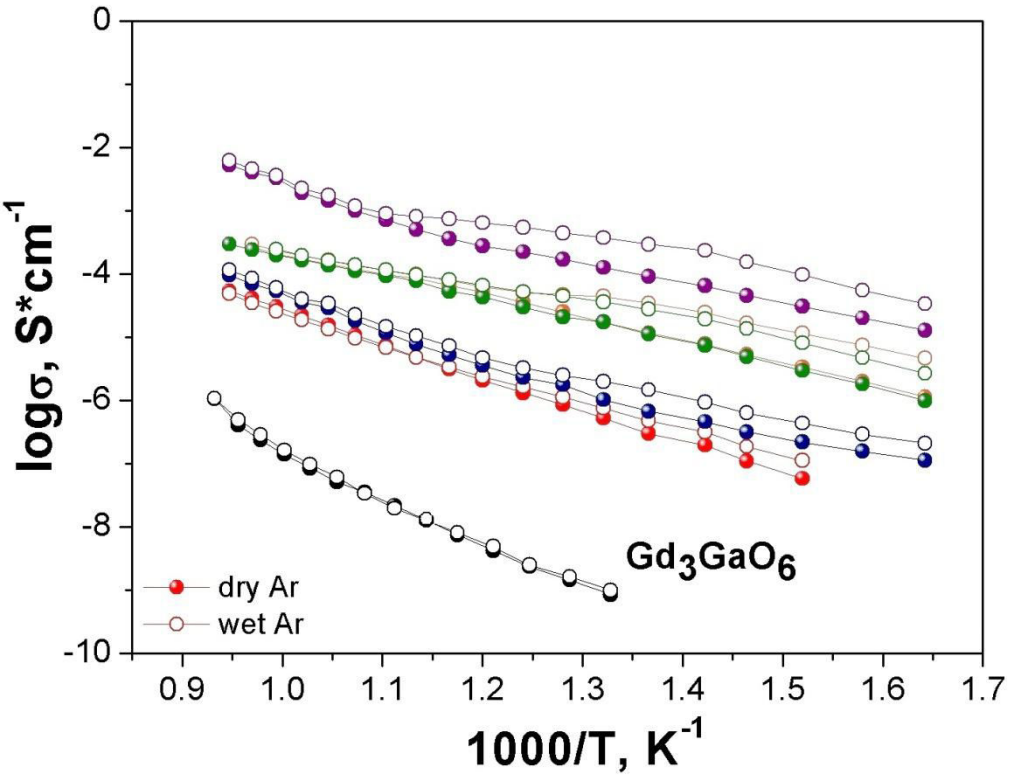

Figure 3.4.3 Arrhenius plots of total conductivities in dry and wet Ar of $Gd_{3-x}Sr_xGaO_{6-\delta}$: $Gd_{2.98}Sr_{0.02}GaO_{6-\delta}$ (●- dry Ar, ○- wet Ar), $Gd_{2.97}Sr_{0.03}GaO_{6-\delta}$ (●- dry Ar, ○- wet Ar), $Gd_{2.96}Sr_{0.04}GaO_{6-\delta}$ (●- dry Ar, ○- wet Ar), $Gd_{2.95}Sr_{0.05}GaO_{6-\delta}$ (●- dry Ar, ○- wet Ar), $Gd_{2.9}Sr_{0.1}GaO_{6-\delta}$ (●- dry Ar, ○- wet Ar)

Table 3.4.2 Activation energy for total conductivity of $Gd_{3-x}Sr_xGaO_{6-\delta}$ compounds under Ar atmosphere

Composition	HT range, eV		LT range, eV		Ea ref, eV [28]
	Dry Ar	Wet Ar	Dry Ar	Wet Ar	
Gd_3GaO_6	1.30	1.30	1.30	1.30	1.2
$Gd_{2.98}Sr_{0.02}GaO_{6-\delta}$	0.98	0.98	0.98	0.90	-
$Gd_{2.97}Sr_{0.03}GaO_{6-\delta}$	0.87	0.87	0.87	0.79	-
$Gd_{2.96}Sr_{0.04}GaO_{6-\delta}$	0.79	0.79	0.79	0.67	-
$Gd_{2.95}Sr_{0.05}GaO_{6-\delta}$	0.79	0.79	0.79	0.65	-
$Gd_{2.9}Sr_{0.1}GaO_{6-\delta}$	0.92	0.92	0.74	0.64	-

The grain boundary conductivity decreases with dopant content which has to be related to the grain size of the samples, which was shown also to slightly increase with Ca and Sr content (see **Figure 3.3.9** and **Figure 3.3.10**). **Figure 3.4.4** represents some Arrhenius plots of total and bulk conductivities which demonstrated in the temperature range where it could be separated accurately. This picture is representative of all series of samples.

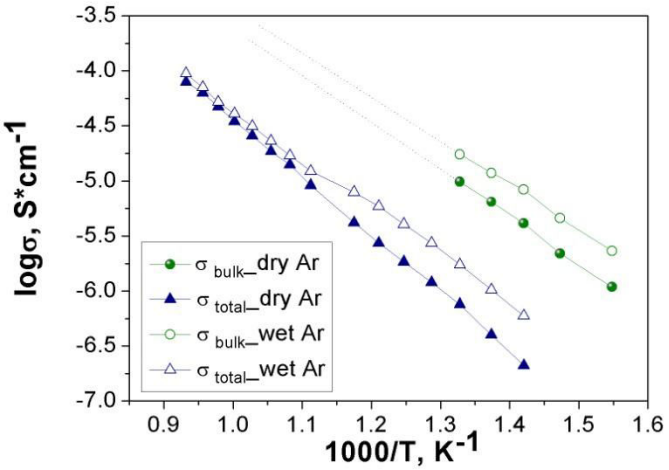

Figure 3.4.4 Conductivity data of $Gd_{3-x}Ca_xGaO_{6-\delta}$ in dry and wet argon at different temperatures

Figure 3.4.5 (a) and **(b)** shows the concentration dependence of the total conductivity of solid solutions $Gd_{3-x}Ca_xGaO_{6-\delta}$ and $Gd_{3-x}Sr_xGaO_{6-\delta}$. It is evident that the creation of small rate of oxygen vacancies in the Gd_3GaO_6 structure by doping induces a significant increase of the ionic conductivity which reaches 3.2×10^{-3} S.cm^{-1} and 4.1×10^{-4} S.cm^{-1} at 800 °C for 10 % of dopant for Sr and Ca-doped Gd_3GaO_6 respectively. In the **Figure 3.4.5 (c)** we plot the evolution of conductivity with dopant level and atmosphere at 500 °C. The maximum difference between dry and wet atm observed for the

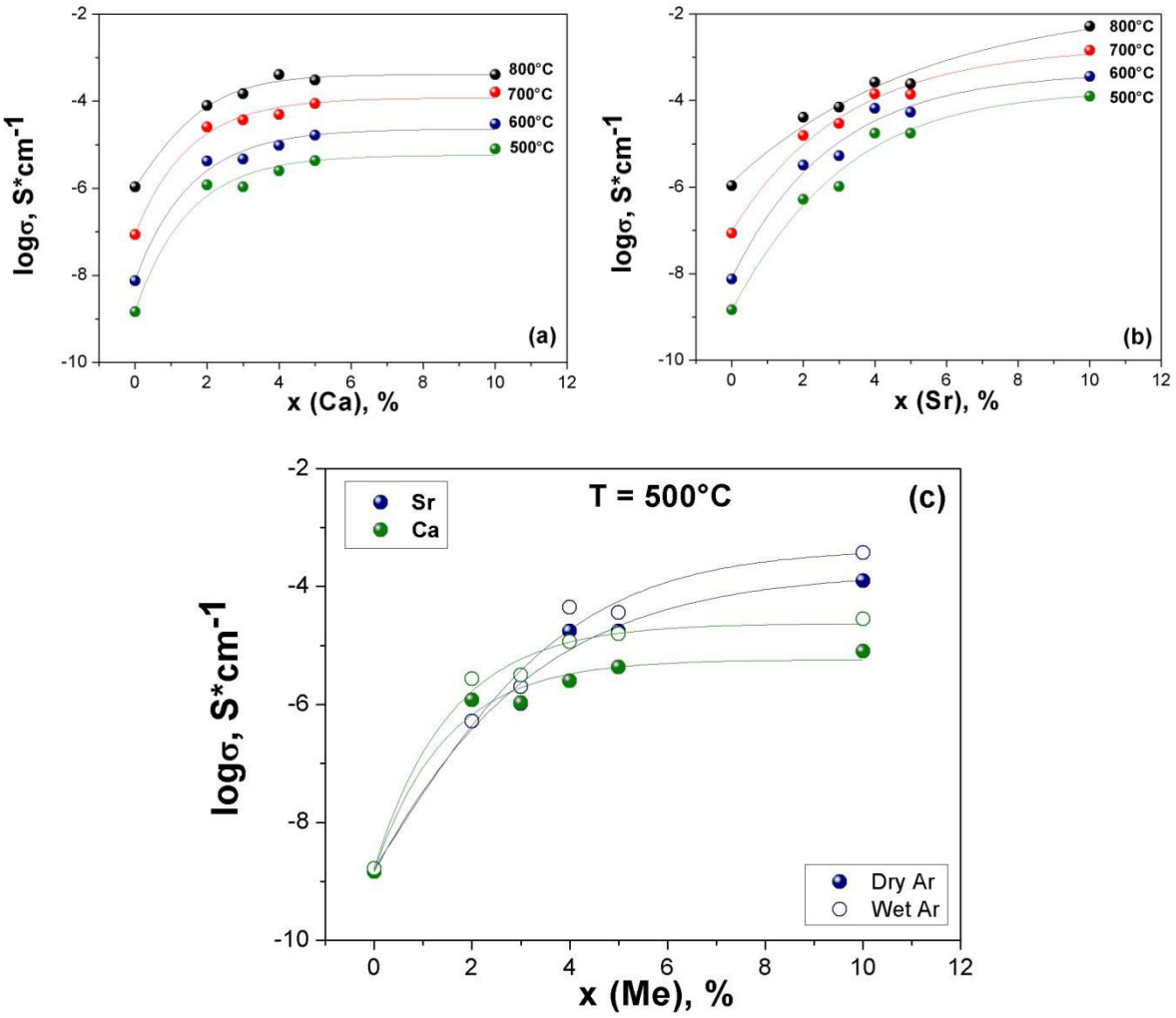

Figure 3.4.5 Evolution of total conductivity values of $Gd_{3-x}Ca_xGaO_{6-\delta}$ and $Gd_{3-x}Sr_xGaO_{6-\delta}$ with temperature in dry Ar (a, b) and in wet Ar (c) at 500 °C

3.5.3 Transport properties as a function of $p(O_2)$

Conductivity has been measured for all samples as a function of oxygen partial pressure between Argon/hydrogen (5 %) and pure O_2 in the 500 – 800 °C range of temperatures. During these measurements, the stabilization time was around 1-2 h at 800 °C and adjusted depending on the evolution of the impedance spectrum at lower temperature. All these measurements were done bubbling throughout H_2O to ensure a constant pH_2O of 0.024 atm. **Figure 3.4.6**, **Figure 3.4.7** and **Figure 3.4.8** show the dependency of the samples conductivity at 700 °C. The results for all compounds were very similar. At high pO_2 range ($pO_2 > 10^{-4}$ atm) curves have a positive slope characterizing the contribution of electronic conductivity of *p*-type. The process of formation of holes

carriers are generally described by the following Equation:

$$V_O^{\cdot\cdot} + \frac{1}{2}O_2 \leftrightarrow O_o^x + 2h^{\cdot} \quad (3.3)$$

In the intermediate and low pO_2 ($pO_2 < 10^{-4}$ atm), we observe big plateau of conductivity with pO_2 independence, which usually correspond to dominant ionic conductivity.

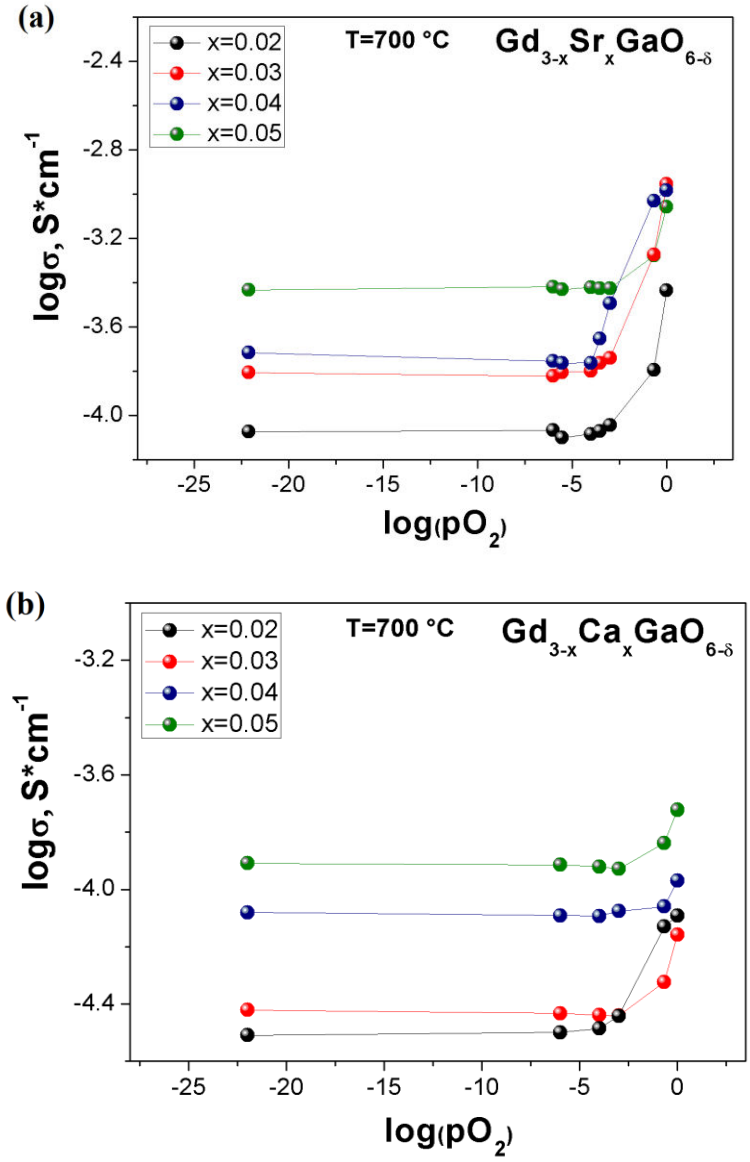

Figure 3.4.6 Log (pO_2) dependency at 700 °C for various compounds of (a) $Gd_{3-x}Sr_xGaO_{6-\delta}$ and (b) $Gd_{3-x}Ca_xGaO_{6-\delta}$

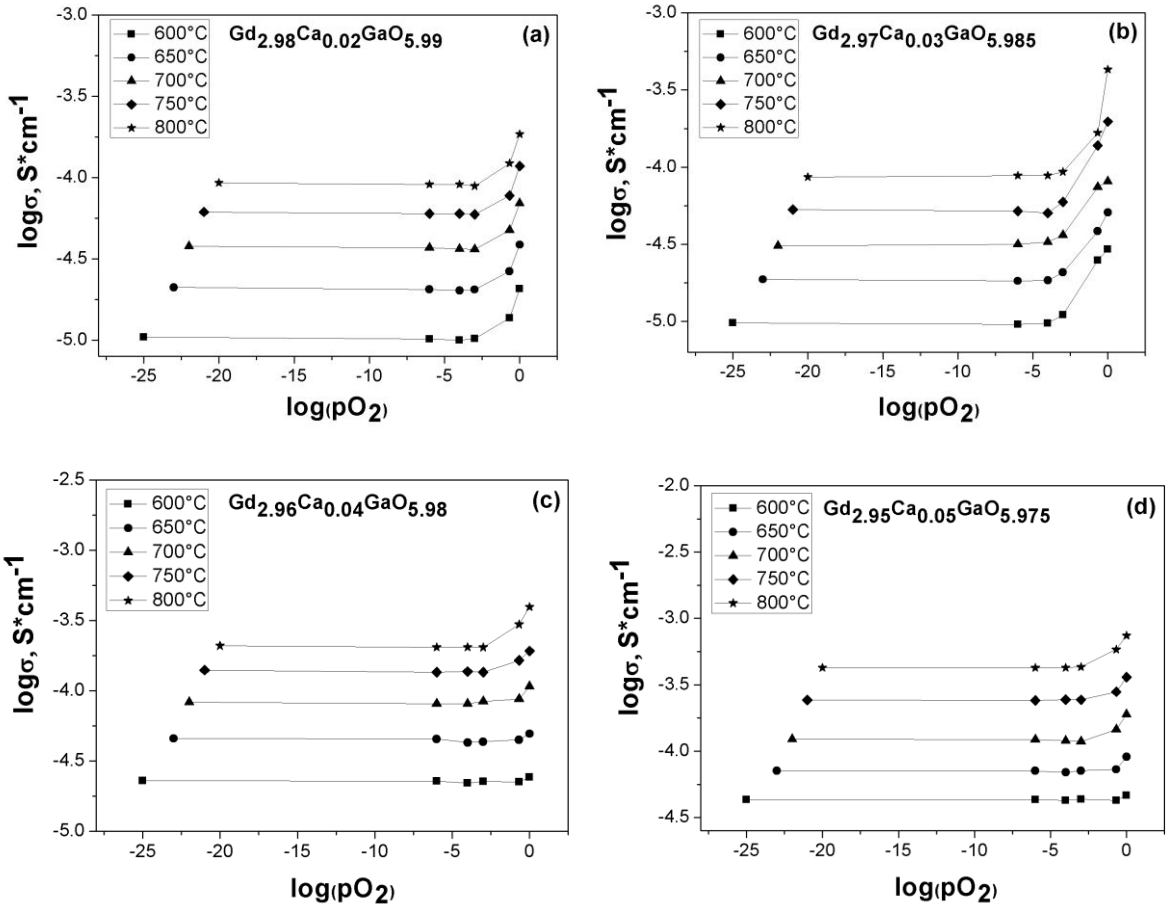

Figure 3.4.7 (a, b, c, d) IS measurements as a function of pO_2 in wet Ar by varying the temperature for $Gd_{3-x}Ca_xGaO_{6-\delta}$

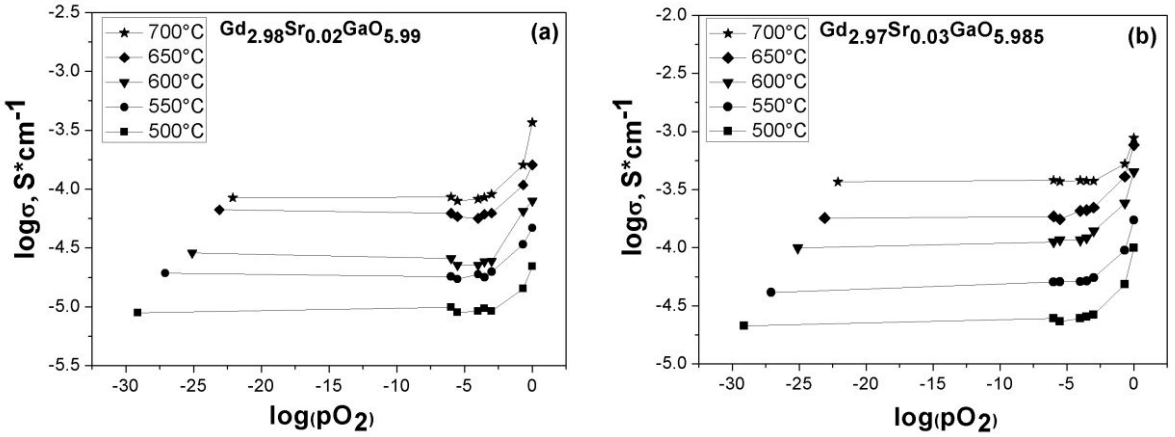

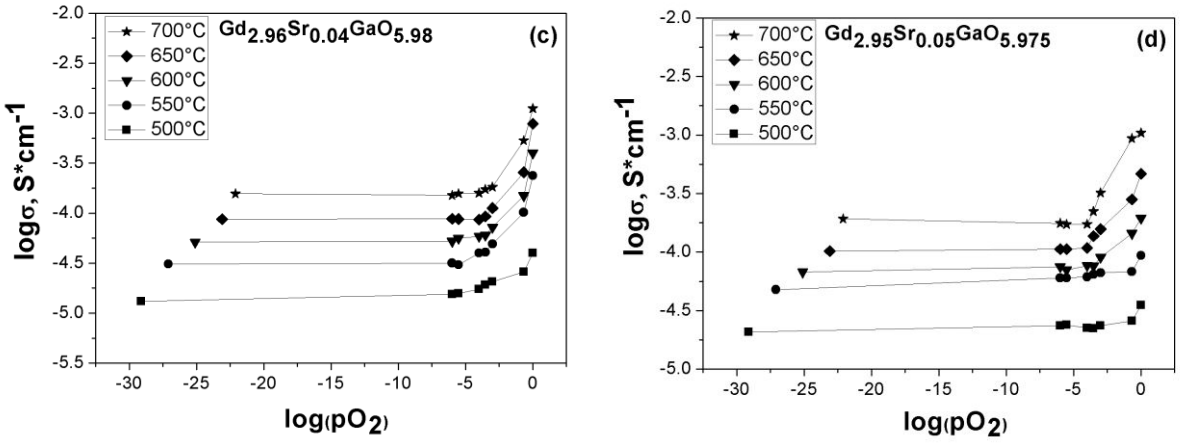

Figure 3.4.8 (a, b, c, d) IS measurements as a function of pO_2 in wet Ar by varying the temperature for $Gd_{3-x}Sr_xGaO_{6-\delta}$

3.6 Conclusion

In this chapter we have synthesized successfully two series of $Gd_{3-x}Me_xGaO_{6-\delta}$ (Me = Ca^{2+}, Sr^{2+}) dense compounds by microwave-assisted citric acid combustion method. All materials present a non-centrosymmetric orthorhombic structure with cell parameters following the evolution of dopant content. Highest density of samples found for 10 % of dopant content and it reaches 94 % for $Gd_{2.9}Ca_{0.1}GaO_{6-\delta}$ and 96 % for $Gd_{2.9}Sr_{0.1}GaO_{6-\delta.}$ The pure Gd_3GaO_6 compound shows as expected a low conductivity and the absence of proton conduction. In such a way based on the analysis of the concentration dependences of the conductivity of alkaline earth-substituted solid solutions based on Gd_3GaO_6, it can be concluded that the introduction of small amounts of Ca^{2+} and Sr^{2+} in the matrix gadolinium gallate leads to a sharp increase in the values of electrical conductivity. The best conduction properties are observed for higher Ca^{2+} and Sr^{2+} contents, 7.1×10^{-5} $S.cm^{-1}$ and 7.5×10^{-4} $S.cm^{-1}$ at 600 °C in wet argon respectively. Proton conduction is observed at low temperature, in humid atmosphere for all doped compounds. Table 3.5.1 presents a comparison of conductivity values of different electrolyte materials as reported in the literature. As we can see our compounds have the same level of conductivity comparing with materials whose structure contains tetrahedral units, such as $La_{0.99}Ca_{0.01}NbO_4$. All doped compounds are oxygen ion conducting at high temperature and present a mixed anion-hole behavior in the range 10^{-29} - 1 atm of oxygen partial pressure. The figures evidence an evolution of conductivity with $p(O_2)$ similar to that of other proton conductors such as barium zirconates or cerates. Indeed, the material changes from pure anion conducting compound with no evolution of conductivity with $p(O_2)$ to a p-type conducting behavior with an evolution of conductivity $p(O_2)$ following a ¼ power law.

Table 3.5.1 Conductivity of different electrolyte materials as reported in the literature comparing with $Gd_{3-x}Me_xGaO_{6-\delta}$

Composition	**Conductivity at 600°C, S/cm**	**Conductivity measurement conditions**	**Ref.**
$La_{0.99}Ca_{0.01}NbO_4$	4.1×10^{-4} 7.6×10^{-4}	Dry O_2 ($pH_2O = 3*10^{-5}$ atm) Wet O_2 ($pH_2O = 0.025$ atm)	36
$La_{1-x}Ba_{1+x}GaO_{4-x/2}$	1×10^{-4}	Wet O_2 ($pH_2O = 0.025$ atm)	37, 38
$BaZr_{0.93}Y_{0.07}O_{3-x}$	3.8×10^{-3} 4.2×10^{-3}	Wet N_2 ($pH_2O = 0.023$ atm) Wet air ($pH_2O = 0.025$ atm)	46
$BaZr_{0.95}In_{0.05}O_{3-x}$	1.2×10^{-2}	Wet H_2	45
$Gd_{2.9}Ca_{0.1}GaO_{6-\delta}$	3.1×10^{-5} 7.1×10^{-5}	Dry Ar ($pH_2O = 10^{-5}$ atm) Wet Ar ($pH_2O = 0.023$ atm)	This work
$Gd_{2.9}Sr_{0.1}GaO_{6-\delta}$	3.6×10^{-4} 7.5×10^{-4}	Dry Ar ($pH_2O = 10^{-5}$ atm) Wet Ar ($pH_2O = 0.023$ atm)	This work
$Nd_{2.955}Sr_{0.045}GaO_{6-\delta}$	1×10^{-3}	Dry air	28
$Nd_{2.91}Ca_{0.09}GaO_{6-\delta}$	9×10^{-4}	Dry air	28
Ca-doped $LaPO_4$ Sr-doped $LaPO_4$ Ba-doped $LaPO_4$	5×10^{-4} 4×10^{-4} 2×10^{-4}	Wet O_2 Wet O_2 Wet O_2	44

Also chemical stability was investigated of pure Gd_3GaO_6 and Sr-doped Gd_3GaO_6 under different atmospheres and conditions. No extra-phases or phase changes were observed. All materials show an excellent stability against reducing and humid atmospheres.

References:

[1] L. Malavasi, C. A. J. Fisher, M. S. Islam, *Chem. Soc. Rev.* **2010**, *39*, 4370-4387.

[2] B.C.H. Steele, *Solid State Ionics*, **2000**, 129, 95-110.

[3] M. Mogensen, N.M. Sammes and G.A. Tompsett, *Solid State Ionics*, **2000**, 129, 63-94.

[4] J. Faber, C. Geoffrey, A. Roux, A. Sylvestre, and P. Abelard. *Applied Physics*, **1989,** A49:225.

[5] V.V. Kharton, F.M.B. Marques, and A. Atkinson., *Solid State Ionics*, **2004**, 174:135–149.

[6] Nakayama, S.; Aono, H.; Sadaoka, Y. *Chem. Lett.* **1995**, *24*, 431−432.

[7] Slater, P. R.; Sansom, J. R.; Tolchard, J. R. *Chem. Rec.* **2004**, *4*, 373−384.

[8] Kendrick, E.; Islam, M. S.; Slater, P. R. *J. Mater. Chem.* **2007**, *17*, 3104−3111.

[9] Haugsrud, R.; Norby, T. *Nat. Mater.* **2006**, *5*, 193−196.

[10] Li, S.; Schönberger, F.; Slater, P. *Chem. Commun.* **2003**, *21*, 2694−2695.

[11] Schönberger, F.; Kendrick, E.; Islam, M. S.; Slater, P. *Solid State Ionics* **2005**, *176*, 2951−2953.

[12] F.S. Liu, Q.L. Liu, J.K. Liang, L.T. Yang, G.B. Song, J. Luo, and G.H. Rao, *J. Solid State Chem*., **2004**, 177, 1796-1802.

[13] N. Jalarvo, O. Gourdon, Z. Bi, D. Gout, M. Ohl, M. P. Paranthaman, *Chem. Mater.* **2013**, 25, 2741-2748.

[14] S.J. Schneider, R.S. Roth and J.L. Waring, *J. Res. Nat. Bur. Stand. Sect.*, **1961**, A 65, 345.

[15] J. Nicolas, J. Coutures, J.P. Coutures, Journal of Solid State Chemistry, **1984**, 52, 101-113.

[16] H. Sawada, *J. Solid State Chem*. **1997**, 132, 300–307.

[17] J.E. Mee, G.R. Pulliam, J.L. Archer, P.J. Besser, *IEEE Trans.Magn.* **1969**, MAG-5, 717.

[18] R.C. Linares, *J. Crystal Growth,* **1969**, 3 (4), 443.

[19] C.D. Brandle, A.J. Valentino, *J. Crystal Growth*, **1972**, 12 3–8.

[20] C.D. Brandle, H. Steinfink, *Inorg. Chem.,* **1969**, 8 (6), 1320–1324.

[21] J. R. Carruthers, M. Kokta, R. L. Barns, and M. Grasso, *J. Cryst. Growth,* **1973***,* 19, 204.

[22] W.G. Zeier, Irina P. Roof, M.D. Smith, H.-C. zur Loye, *Solid State Sciences,* **2009***,* 11, 1965–1970.

[23] H. Yamane, T. Sakamoto, S. Kubota, M. Shimada, *Acta Cryst.,* **1999**, C55, 479-481.

[24] P.Guo, G. Li, F. Zhao, F. Liao, S. Tian, X. Jing *, J. Electrochem. Soc.*, **2003**, 150 (9) H201-H204.

[25] F.S. Liu, Q.L. Liu, J.K. Liang, L.T. Yang, G.B. Song, J. Luo, and G.H. Rao, *J. Alloy Comp*., **2006**, 425, 278.

[26] J.C.Boyer, F.Vetrone, J.A.Capobianco, A.Speghini, M.Bettinelli, *Chem. Phys. Lett.* **2004**, 390, 403–407.

[27] P. Guo, G. Li, F. Zhao, S. Tian, X. Jing, *J. Electrochem. Soc*., **2004**, 9, 115–119.

[28] A. Chesnaud. Rare-earth oxy-gallates and oxy-germanates oxide-ion conductors, PhD thesis, University of Nantes, **2005.**

[29] Shigeyuki Somiya, *Advanced Technical Ceramics*, **2012**, 96.

[30] F. Tietz. Thermal expansion of SOFC materials. *Ionics*, **1999**, 5(1):129–139.

[31] S.V. Bhide and A.V. Virkar, *J. Electrochem. Soc*, **1999**, 146, 2038.

[32] Z. Zhong. *Solid State Ionics,* **2007***,* 178 (3-4), 213-220.

[33] M.-D. Braida, Nouveaux conducteurs protoniques de structure fluorite, PhD thesis**, 2010**, 64-66.

[34] X. Guo, *Chemistry of Materials* **2004**, *16*, 3988.

[35] S. V. Bhide, A. V. Virkar, *Journal of The Electrochemical Society* **1999**, *146*, 2038.

[36] R. Haugsrud, T. Norby, *Solid State Ionics,* **2006**, 177 , 1129–1135.

[37] S. Li, F. Schonberger, P. Slater, *Chem. Comm.* **2003,** 21, 2694–2695.

[38] F. Schonberger, E. Kendrick, M. S. Islam, P. Slater, *Solid State Ionics.* **2005,** 176, 2951–2953.

[39] E. Kendrick, J. Kendrick, A. Orera, P. Panchmatia, M. S. Islam, P. R. Slater *Fuel cells,* **2011**, 11, 1, 38–43.

[40] E. Kendrick, J. Kendrick, K. Knight, M. S. Islam, P. R. Slater *Nature materials,* **2007**, 6, 871- 875.

[41] A. Chroneos, B. Yildiz, A. Taranc´on, D. Parfit and J. A. Kilner *Energy Environ. Sci.*, **2011**, 4, 2774–2789.

[42] A. Kuwabara, R. Haugsrud, S. Stolen, T. Norby, *Phys. Chem. Chem. Phys.* **2009**, *11*, 5550.

[43] N. Kitamura, K. Amezawa, Y. Tomii, *J. Electrochem. Soc.* **2005**, *152*, A658.

[44] K. Amezawa et al., *Solid State Ionics*, **2005,** 176, 135–141.

[45] H. Iwahara, T. Yajima, T. Hibino, K. Ozaki, and H. Suzuki, *Solid State Ionics*, **1993**, 61, 65.

[46] V.P. Gorelov, V.B. Balakireva, Y.N. Kleshchev, V.P. Brusentsov, *Inorg. Mater.* **2001**, 37, 535.

[47] B.C.H. Steele, *Cur. Op. Sol. St. and Mat. Sci.*, **1996**, 1, 684-691.

[48] H. Yanagida, K. Koumoto, M. Miyayama, *John Wiley & Sons*, **1996**.

Chapter 4 Synthesis, structure and electrical properties of $Ba_2Y_{1+x}Nb_{1-x}O_{6-\delta}$

4.1 The perovskite background

Perovskite form is a relatively simple system to study with greatly varying structural, electronic and magnetic properties. They may be insulators with a wide range of band-gap values, metals, half-metals ($La_{1-x}Ca_xMnO_3$, A_2CoWO_6 (A = Sr, Ba, Ca)) [1,2] or even superconductors ($LaBaCuO_4$, $YBa_2Cu_3O_{7-\delta}$) [3]. They exhibit magnetic orderings ranging from antiferromagnetic to ferri- and ferromagnetic ($BaLaZnRuO_6$, $BaTiO_3$) [4, 5], but can also show magnetic frustration with no apparent long-range spin order ($BaLaNiRuO_6$, Sr_2FeRuO_6) [6, 7]. Perovskites may also show high ionic conductivities ($BaCeO_3$, $BaZrO_3$, $LaGaO_3$, $Na_{0.5}Bi_{0.5}TiO_3$) [8] and good catalytic properties ($Cs_{2.5}H_{0.5}PW_{12}O_{40}$, $La(Fe,Co)_{0.9}Pd_{0.1}O_3$) [9]. As a result, perovskite materials are of great technological interest, with a range of possible applications such as dielectrics or magnetic memory components in electronics [3], electrode and electrolyte materials for fuel cells ($La_{0.8}Sr_{0.2}Ga_{0.83}Mg_{0.17}O_{2.815}$, $Sr_2Mg_{1-x}Mn_xMoO_{6-\delta}$) [10], photocatalysts for water splitting [9], and as recently discovered, components for solar cells ($CH_3NH_3PbBr_3$) [11], to name just a few.

4.1.1 Simple perovskite structure

Perovskites have the general formula ABX_3, in which A represents a large electropositive cation in 12-coordinate sites, B represents a small transition metal or main group ion, and X is commonly an oxide or halide ion (**Figure 4.1.1**). The space group for ideal cubic perovskites is $Pm\bar{3}m$ (221) [12]; the equivalent positions of the atoms are detailed in **Table 4.1**. In an idealised cubic perovskite constructed of rigid spheres, each cation has the perfect size to be in contact with an oxygen anion, themselves forming a compact array of spheres.

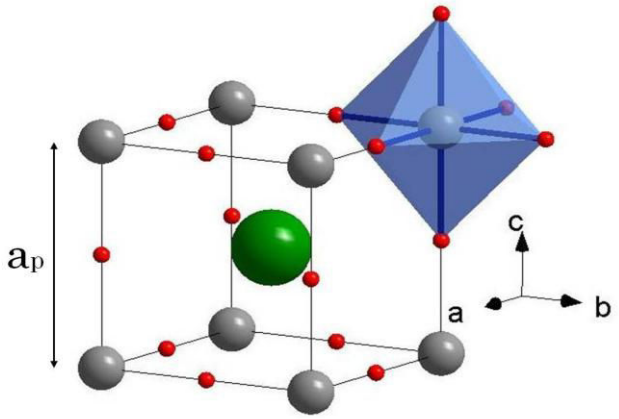

Figure 4.1.1 The schematic representation of the ABO_3 ideal perovskite structure, where the green, grey and red spheres represent, *A*, *B* and oxygen cations, respectively [13]

Table 4.1: Atomic positions in cubic perovskites [14]

Site	Location	Co-ordinates
A cation	(1a)	(0, 0, 0)
B cation	(1b)	(½, ½, ½)
O anion	(3c)	(½, ½, 0), (½, 0, ½), (0, ½, ½)

The compositional flexibility of the perovskite structure is especially notable in the case of cation substitution. Both the *A* and *B* cations can be partially substituted with either iso- or aliovalent cations, resulting in a large number of possible mixed compositions. What is more, chemical ordering of the substituted cations is possible, and can happen either at the *A* or *B* site, or at both simultaneously. The perovskite structure allows a rather large mismatch of ionic radii. This *A* and *B* cation size mismatch is often described by the Goldschmidt tolerance factor [15]. With decreasing A cation size, a point will be reached where the A-cations will be too small to remain in contact with the anions in the cubic structure. In this case the B-O-B bonds bend slightly, tilting the BO_6 octahedra to bring some anions into contact with the A cations [16]. To better describe the property of perovskite structure toward this for this distortion, a constant, ***t***, is introduced with the expression (4.1):

$$t = (r_A + r_O)/\sqrt{2(r_B + r_O)} \tag{4.1}$$

where t – the Goldschmidt tolerance factor, r_A, r_B, and r_O are the ionic radii of *A*, *B* and O, respectively. Each distortion of the cubic structure means ***t*** deviation from its ideal value equal to 1. Depending on the value of the tolerance factor, we can distinguish several situations, shown in the Table 4.2. Therefore, the closer to cubic, the closer the value of the tolerance factor is to unity. The BX_6 octahedra can expand, contract or tilt in order to compensate non-ideal ionic size ratios of the

different cations, and in case of electronic instabilities, the octahedra can distort or the cations may shift from their ideal positions. One important feature of this structure is a possibility to make partial substitutions or to create vacancies at any of the three sites of the structure. As a result of this flexibility, the perovskite structure can accommodate almost all of the elements of the periodic table.

Table 4.2 Evolution of crystal structures depending on the value of the tolerance factor [17]

	0.75 < *t* < 1.06 **Perovskite**			
t < 0.75				*t* > 1.06
Ilmenite	0.75 < *t* < 0.96 *orthorhombic distortion*	0.96 < *t* < 0.99 *rhombohedral distortion*	0.99 < *t* < 1.06 *cubic*	**Hexagonal**

All perovskite distortions that maintain the A and B site oxygen coordinations involve the tilting of the BO_6 octahedra and an associated displacement of the A cation. For the orthorhombic structure, these octahedra tilt about the *b* and *c* axes, while in the rhombohedral structure the octahedra tilt about each axis [18].

4.1.2 Double perovskite structure

The study of double perovskites was initiated in the early 1950s [19, 20] and expanded in the late 1950s [21, 22]. From the late 1950s to the mid 1970s, many of the double perovskites currently known were discovered and studied [23-30]. The double perovskite general formula is $A_2B'B''X_6$ or $A'A'B_2O_6$, where A'- and A''- cations, and B'- and B''- cations can be the same or different type.

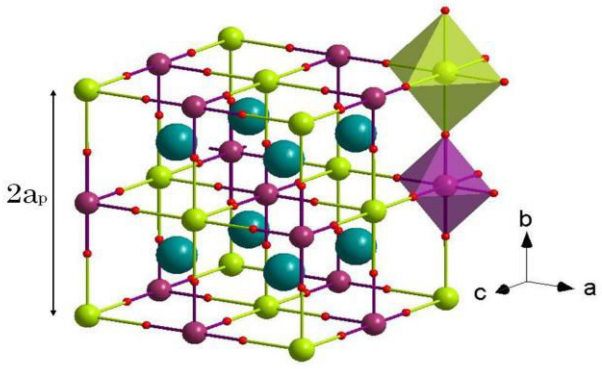

Figure 4.1.2 The schematic representation of the $A_2B'B''X_6$ ideal double perovskite structure; where *B'*-cation and *B'O*$_6$ octahedra are represented in purple, *B''*-cation and *B''O*$_6$ octahedra in green, *A* -cations in blue, and oxygens in red [13]

There are three B-cation sublattice types known for double perovskites: rock salt, columnar and layered, see **Figure 4.1.3.** For example, order-disorder effects are most often encountered when the charge difference between B' and B" is two or less. Rock-salt (1:1) ordering also known as the elpasolite structure, after the mineral K_2NaAlF_6. This type of ordering of the octahedral-site cations doubles the unit cell of the simple undistorted ABX_3 perovskite, changing the space-group symmetry from $Pm\bar{3}m$ to $Fm\bar{3}m$. The *B*-site cations may also form a layered order, where the cations alternate only in one direction, as presented in **Figure 4.1.3.** This ordering is stabilized only in rare cases where one of the *B*-site cations is a Jahn-Teller (JT) active ion and the difference in *B*-site cation radii is great. A columnar order of the *B*-site cations is also possible, with cations alternating in two directions, as shown in **Figure 4.1.3**. The three B-cation sublattice types and common cell sizes, crystal systems, and space groups are shown in **Table 4.3.**

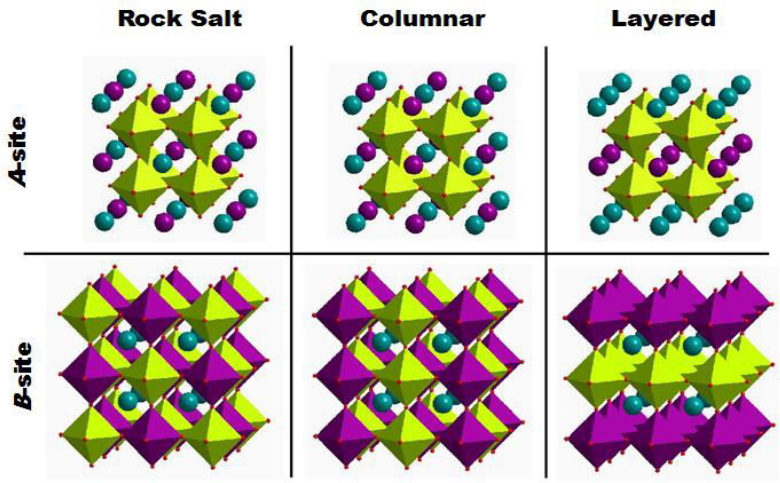

Figure 4.1.3 Cation ordering schemes in perovskites. From left to the right: 0D (rock salt), 1D (columnar ordering), and 2D (layered ordering) are shown for *A*-site ordering in $AA'B_2O_6$ perovskites (top) and for *B*-site ordering in $A_2B'B''O_6$ perovskites (bottom) [13]

Table 4.3 Crystallographic information for common double perovskites [31]

Sublattice type	Cell size	Crystal system	Space group
Random	$1a_p \times 1a_p \times 1a_p$	Cubic	$Pm\bar{3}m$
	$\sqrt{2}\ a_p \times \sqrt{2}\ a_p \times 2a_p$	Orthorhombic	$Pbnm$
Rock-salt	$2a_p \times 2a_p \times 2a_p$	Cubic	$Fm\bar{3}m$
	$\sqrt{2}\ a_p \times \sqrt{2}\ a_p \times 2a_p$	Monoclinic	$P2_1/n$
Layered	$2a_p \times 2a_p \times 2a_p$	Monoclinic	$P2_1/m$

The possibility of cation ordering adds to the complexity and modifiability of the perovskite compounds. Such order-disorder phenomena are of fundamental interest by themselves, but the ordering also affects many of the physical properties of these compounds. If an ordered arrangement between B' and B'' occurs, the symmetry and the size of sites are changed. One way to define the tolerance factor for $A_2B'B''O_6$ doubles perovskites as in equation 4.2 [15]:

$$t = (r_A + r_O) / \sqrt{2}(\bar{r}_{(B'B'')} + r_O) \tag{4.2}$$

where t – the Goldschmidt tolerance factor, $\bar{r}_{(B',\ B'')}$ is the averaged ionic radius of B-cation, considering B' and B'' cations.

Based on the work of M. Anderson *et al.* [31], there are several factors which influence the ordering:

✓ The difference in charge between *B*' and *B*''- cations. If the difference in the oxidation state is two or less, all of the ordering arrangements listed above are possible, dominated by completely disordered and partially ordered arrangements. If the difference is greater than two, highly ordered compounds are generally observed [13].

✓ The size difference of the *B*-site cations. Generally, bigger differences in ionic radii ($\Delta r_{B'/B''} = |r_{B'} - r_{B''}|$) is related to higher degrees of cation ordering. For instance, Sr_2MTaO_6 where M^{3+} = Sc,Cr,Fe [32,33], have a *M*-cation charge difference of +2, but Sr_2ScTaO_6 ($\Delta r_{Sc/Ta}$=0.105 Å) is fully ordered, Sr_2CrTaO_6 ($\Delta r_{Cr/Ta}$=0.025 Å) is partially ordered (0.8/0.2 proportion), and Sr_2FeTaO_6 ($\Delta r_{Fe/Ta}$=0.005 Å) is completely disordered.

✓ The method of preparation used and the final synthesis temperature. Woodward [34] examined this factor in the cubic compounds Sr_2AlTaO_6 and Sr_2AlNbO_6. The ordering generally increased as synthesis temperature increased. However, in this example for Sr_2AlNbO_6 material, the ordering reached a thermodynamic equilibrium at 1673 K and subsequent annealing at higher temperatures decreases the Al/Nb grade of ordering.

If there is mismatch between the A-X and the averaged (B',B'')-X bond lengths, i.e. $t > 1$or $t <$, the structure of the double perovskite distorts from the cubic symmetry. The most common occurred distortions in $A_2B'B''O_6$ are due to the tilting of the $B'O_6$/ $B''O_6$ octahedra. Glaser et al. [35] was the first who described the various types of octahedral tilting distortions. In 1997 Woodward summarized Glazers' work for ordered double perovskite structures ($A'A''B'B''O_6$) [36]. The generalization process consists on the search of space groups for each 23 Glazer tilts, that allow B' and B''- cation ordering and maintain rigid octahedra. 14 possible space groups were searched for 1:1 ordered double perovskites. Several years ago Howard et al. [37] presented a precise work concerning the group-theoretical analysis and specially considered octahedral tilting in rock-salt ordered perovskites and discussed some approaches and possible pitfalls to the structure determination process. Howard reduced the number of possible space groups to 15, and of these six are commonly observed with a

single *A*-site cation.

4.1.3 Structural properties of $Ba_2LnB'X_6$ (*Ln*=lanthanide, In and Y, B'= Nb^{5+} and Ta^{5+})

The series of the compounds Ba_2LnNbO_6 firstly were synthesized and reported by Brixner [38] to have a simple cubic perovskite structure with the exception of Ba_2LaNbO_6, which was described as a tetragonally distorted perovskite. But, at the same time for this compound was also reported a rhombohedral distortion [39]. Later Galasso *et al.* [40] presented a study concerning $Ba(M_{0.5}Nb_{0.5)}O_3$ (M=Rare Earth, indium). This study is in contrast with the observations which were reported by Brixner. Brixner indicates that in these barium-rare earth niobates, the rare earth ions and niobium ions are arranged randomly in the B-sites while the Galasso *et al.* found ordered arrangement in all series of $Ba(M_{0.5}Nb_{0.5)}O_3$ (M=Rare Earth, indium), see Table 4.4. Von Wittmann *et al.* [41] referred the unit cell of Ba_2LaNbO_6 as monoclinic and that of Ba_2GdNbO_6 as tetragonal, respectively. Evdokimov and Men'shenina [42] determined the monoclinic unit cells for Ln = La–Sm, the tetragonal unit cells for Ln = Eu–Tb, and double cubic unit cells for Ln = Dy–Lu and Y. However, in all the studies mentioned above, the authors did not show any information about space group symmetry and any structural details.

Table 4.4 Structure data for the $Ba(M_{0.5}Nb_{0.5)}O_3$ compounds [40]

Compound	**Cell size[a], Å**	**Arrangement of B ions**	**Diff. in ionic radii of B ions, Å**
$Ba(La_{0.5}Nb_{0.5)}O_3$	a = 8.607 c = 8.690	Ordered	0.45
$Ba(Nd_{0.5}Nb_{0.5)}O_3$	8.540	Ordered	0.35
$Ba(Sm_{0.5}Nb_{0.5)}O_3$	8.518	Ordered	0.31
$Ba(Eu_{0.5}Nb_{0.5)}O_3$	8.507	Ordered	0.29
$Ba(Gd_{0.5}Nb_{0.5)}O_3$	8.496	Ordered	0.28
$Ba(Dy_{0.5}Nb_{0.5)}O_3$	8.437	Ordered	0.23
$Ba(Ho_{0.5}Nb_{0.5)}O_3$	8.434	Ordered	0.22
$Ba(Er_{0.5}Nb_{0.5)}O_3$	8.427	Ordered	0.20
$Ba(Tm_{0.5}Nb_{0.5)}O_3$	8.408	Ordered	0.18
$Ba(Yb_{0.5}Nb_{0.5)}O_3$	8.374	Ordered	0.17
$Ba(Lu_{0.5}Nb_{0.5)}O_3$	8.364	Ordered	0.16
$Ba(In_{0.5}Nb_{0.5)}O_3$	8.279	Ordered	0.12
a – data from Brixner [35]			

Lately, Hemni *et al.* [43] performed a Rietveld analysis of the X-Ray diffraction data and described the structure of Ba_2LnNbO_6 (Ln = La– Lu), all in the space group $P2_1/n$ (tilt system $(a^-a^-c^+$ according to Glaser [35] notation)) with the unit cell of $a \approx b \approx \sqrt{2}a_p$, $c \approx 2a_p$, and $b \approx 90°$, where a_p denotes the lattice constant of the primitive cubic perovskite. This space group allows two crystallographically distinct octahedral sites in the perovskite structure, thus permitting 1: 1 positional ordering between the B site ions, Ln^{3+}, and Nb^{5+} ions. These ions are arranging alternately and they have a rock salt sublattice [42]. The crystal structures of these compounds are derived from the perovskite structure with different distortions. Ba_2LnNbO_6 crystal structure is shown in **Figure 4.1.4 (a)** and the variation of lattice parameters for Ba_2LnNbO_6 with the ionic Ln^{3+} radius in **Figure 4.1.4 (b).**

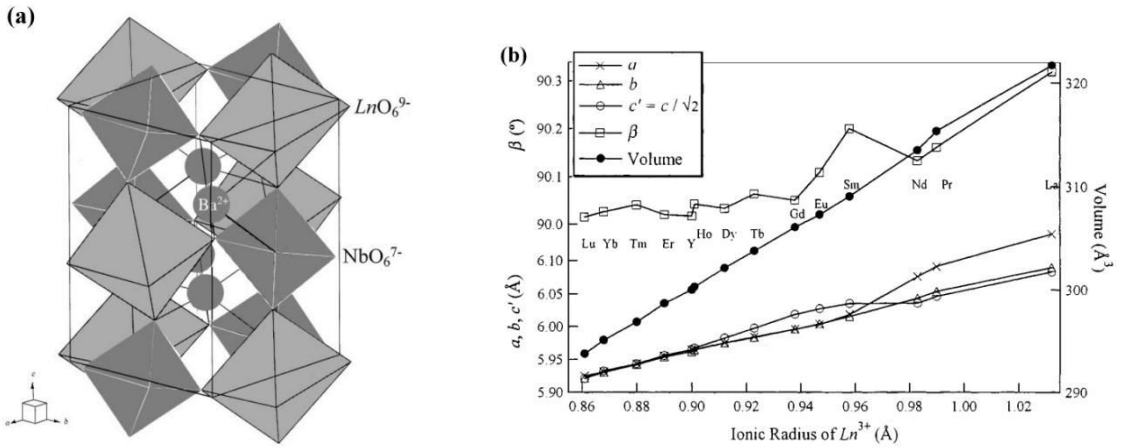

Figure 4.1.4 (a) Crystal structure of Ba_2LnNbO_6 and (b) Variation of lattice parameters for Ba_2LnNbO_6 with the ionic Ln^{3+} radius [43]

The average *Ln*-O bond length increases with the ionic radius of Ln^{3+}, the average Nb-O bond length is nearly constant (~ 1.94 Å) for all the Ba_2LnNbO_6**.** This value is shorter than the Nb-O bond length calculated from using Shannon's ionic radii, 2.04 Å. This result indicates the existence of the covalency in the Nb-O bond in these Ba_2LnNbO_6 [43].

In 2004 Ting *et al.* [44, 45] presented a detailed structural analysis of A_2InNbO_6 materials by using neutron powder diffraction, electron diffraction and bond valence calculations. In the first report [41], authors concluded that Ba_2InNbO_6 occurs in the $Fm\bar{3}m$ elpasolite-type structure, whereas Sr_2InNbO_6 shows a $P2_1/n$ monoclinic perovskite-related superstructure. In the conclusion, authors proposed an additional Rietveld refinement through neutron diffraction data in order to increase reliability of the oxygen ions positions determination. This procedure was conducted and reported by the same authors in a subsequent work [44]. In principle, this reduction of symmetry can have three different effects on the diffraction patterns: splitting of the peaks, introduction of unobserved peaks and/or changes in the peaks intensities. In **Figure 4.1.5** is shown the effect of the symmetry reduction

of the disordered and ordered cubic structure, respectively, for the most observed crystal symmetries. When the symmetry reduction happens into a primitive space group (*e.g.* $P2_1/n$), new peaks are observed in the diffraction patterns related to primitive cell. This type reflection (*hkl*) condition are $h + k + l = 2n + 1$ [13].

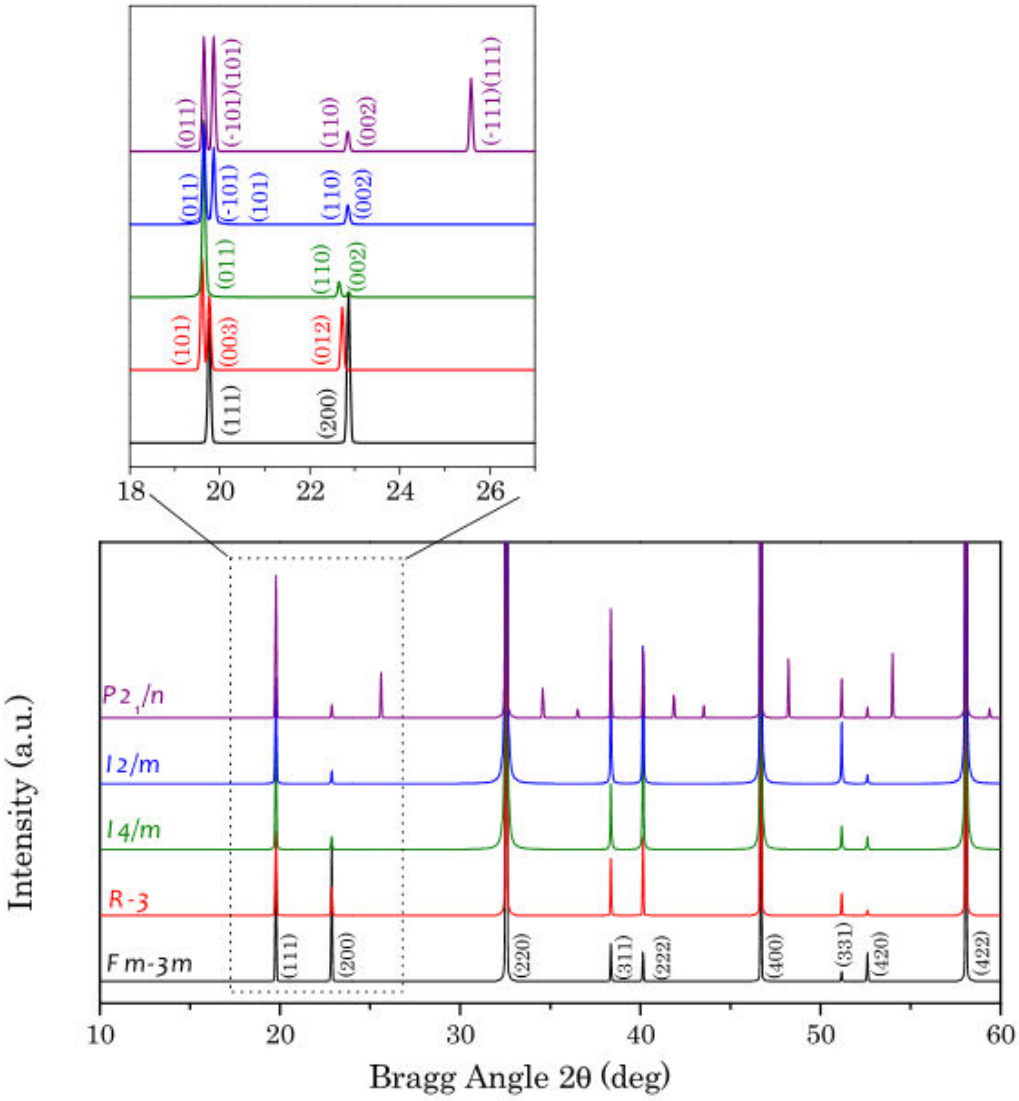

Figure 4.1.5 Simulated X-Ray diffraction patterns for the ordered $A_2B'B''O_6$ cubic structure (black) and the most common distorted symmetries: $R\bar{3}$ (red), *I*4/*m* (green), *I*2/*m* (blue) and *P*21 /*n* (purple). In the inset is shown the splitting of the peaks [13]

Recently several groups of scientists [46-49] examined the structures of A_2LnTaO_6 and A_2LnNbO_6 and determined space-group assignments, cation ordering and unit-cell dimensions of ordered perovskites from the analysis of synchrotron and monochromatic laboratory X-Ray data. These studies taken together with previous works reveal a strong correlation between the tolerance factor and the space-group symmetry. It was found that the structures of the double perovskites

Ba_2LnNbO_6 (Ln = La, Pr, Nd, Sm, Eu, Gd, Tb, Dy, Ho, and Y) can all be derived from the primitive cubic aristotype by ordering the LnO_6 and NbO_6 octahedra, and by tilting the octahedra around one of the principal axis of the cubic cell. In Ba_2LnNbO_6 with Ln = La, Pr, Nd, and Sm, the octahedra are tilted around the two-fold $[110]_p$-axis, resulting in the monoclinic symmetry with the space group *I*2/*m*. The tilting of the octahedra reduces the *c*-axis with the reduced cell axes ratio, defined as $a_p(b_p) = a(b)/\sqrt{2}$ and $c_p = c/2$, being $c_p/a_p(b_p) < 1$. For compounds with Ln = Eu, Gd, Tb, and Dy, the LnO_6/NbO_6 octahedra are tilted around the four-fold $[001]_p$-axis, corresponding to the tetragonal symmetry of the space group *I*4/*m*. The rotation of octahedra causes the decrease of the *a*-axis leading to $c_p/a_p > 1$. As the size of *Ln* further decreases, e.g. Ln = Ho and Y, no octahedral tilting exists any more, and the structure is a cubic with space group $Fm\bar{3}m$ [46]. Thereby phase sequence clearly shows the dependence of the crystal structure on the ionic radii, *i.e.* the tolerance factor. Table 4.5 shows the lattice parameters of a few representative Ba_2LnNbO_6 and Table 4.6 lists some selected interatomic distances.

The mentioned work [46] also confirms the existence of the monoclinic symmetry in Ba_2LnNbO_6, but the space group is found to be *I*2/*m* instead of $P2_1/n$ as was previously suggested by Hemni *et al.* [43]. Since no diffraction lines that associate with the in-phase tilting are present, it does not seem logical to adopt the space group $P2_1/n$ for Ba_2LnNbO_6.

Table 4.5 Refined lattice parameters of some selected Ba_2LnNbO_6 in the space groups *I*2/*m*, *I*4/*m*, and $Fm\bar{3}m$, respectively [46]

I*2/*m				***I*4/*m***				***Fm*$\bar{3}$*m***	
Ba_2LaNbO_6		Ba_2NdNbO_6		Ba_2GdNbO_6		Ba_2TbNbO_6		Ba_2YNbO_6	
a	6.1444(8) (Å)	*a*	6.0791(8) (Å)	*a*	5.9985(6) (Å)	*a*	5.9842(8) (Å)	*a*	8.4316 (8) (Å)
b	6.0913(1) (Å)	*b*	6.0454(7) (Å)	*c*	8.5200(4) (Å)	*c*	8.4817(3) (Å)		
c	8.6040(1) (Å)	*c*	8.5390(9) (Å)						
β	90.348(1) (°)	*β*	90.134(1) (°)						

Table 4.6 Selected interatomic distances (Å) in Ba_2LnNbO_6 (Ln = La, Gd, and Y) [46]

	Ba_2LaNbO_6 (sp.gr. *I2/m*)		**Ba_2GdNbO_6 (sp.gr. *I4/m*)**		**Ba_2YNbO_6 (sp.gr. *Fm$\bar{3}$m*)**	
Ln–O(1)	2.461(13)	2×	2.294(15)	2×	2.247(6)	6×
Ln–O(2)	2.338(9)	4×	2.316(9)	2×		
Nb–O(1)	1.960(13)	2×	1.966(15)	2×	1.969(6)	6×
Nb–O(2)	2.015(9)	4×	1.955(10)	2×		
Ba–O(1)	2.614(13) 3.101(2) 3.556(14)	1× 2× 1×	3.0038(9)	2×	2.9842(3)	12×
Ba–O(2)	2.798(9) 3.041(13) 3.068(14) 3.327(9)	2× 2× 2× 2×	2.843(6) 3.189(7)	2×		

From the physical point of view there are three main differences between La^{3+} and Pr^{3+} and the heavier lanthanides. The first of these is that they have less *f*-electrons with La^{3+} and Pr^{3+} having f^0 and f^1 configurations, respectively. They are also less electronegative than the other lanthanides and have a larger ionic radii, 1.032 and 0.99 Å compared to 0.983–0.912 Å (according to Shannon radii). Studies of Ba_2YTaO_6 and Ba_2YNbO_6 now become interesting since Y^{3+} has a f^0 configuration, an electronegativity intermediate between La^{3+} and Pr^{3+} and a ionic radii of 0.900 Å. If the smaller number of *f*-electrons or electronegativities causes the La^{3+} and Pr^{3+} compounds to adopt a rhombohedral structure then Ba_2YMeO_6 (Me = Nb^{5+}, Ta^{5+}) would also be expected be rhombohedral. However, on practice Ba_2YMeO_6 (Me = Nb^{5+}, Ta^{5+}) was obtained in a cubic form at room temperature. Ba_2YTaO_6 has tetragonal symmetry while the La^{3+} and Pr^{3+} compounds adopt a rhombohedral structure suggests that the La^{3+} and Pr^{3+} compounds have rhombohedral symmetry as a consequence of their larger ionic radii suggesting that the difference in size of the two B-type ionic radii is an important contributing factor.

Another controversial issue is the determination of the degree of cation ordering in Ba_2YNbO_6 compound, because Y^{3+} and Nb^{5+} are formally isoelectronic. This can easily lead to the incorrect assumption that Y^{3+} and Nb^{5+} cations are completely disordered. Yet, yttrium(III) and niobium(V) have an oxidation state difference of two and more importantly a large difference in ionic radii (0.260 Å). This combination should stabilize a highly ordered arrangement of yttrium (III) and niobium (V) [31]. Close examination of the XRPD data shows evidence of a small peak at *ca* 18.2° in 2θ, corresponding to the (111) reflection. This reflection is also seen in the NPD data, as shown in the inset of **Figure 4.1.6** [47].

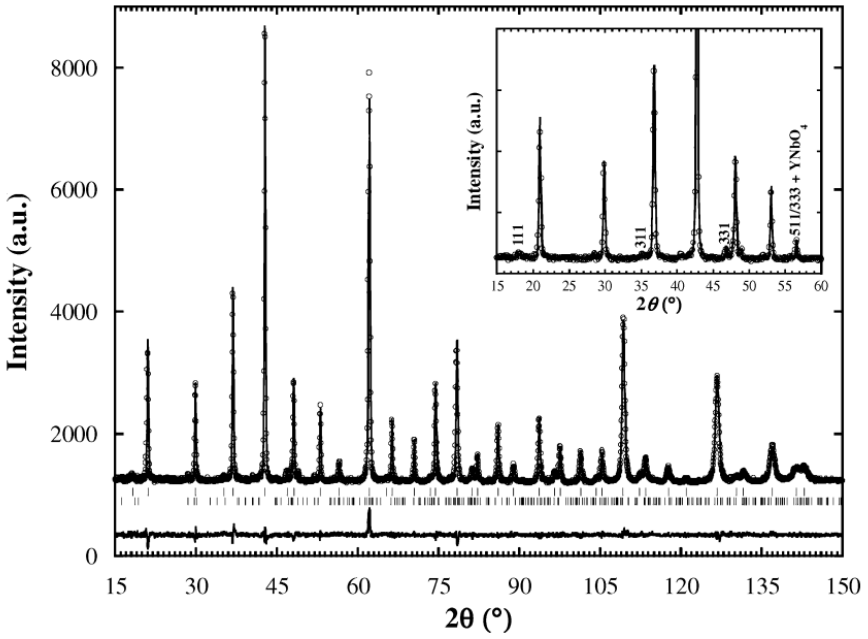

Figure 4.1.6 Observed neutron diffraction pattern along with calculated and difference patterns from the Rietveld refinement of Ba_2YNbO_6. The upper set of vertical tick marks indicates the expected 2 position of the reflections. The lower set of reflection position markers corresponds to a trace of unreacted $YNbO_4$. The inset emphasizes key R-point reflections that reveal the cation ordering and the oxygen displacement toward niobium [47]

P. J. Saines *et al.* [48, 49] along with structural analysis of the A_2LnTaO_6 and A_2LnNbO_6 compounds, provides information about the phase transition depending of the temperature change. The X-Ray diffraction patterns revealed a phase transition from *I*2/*m* monoclinic (tilt system $a^-a^-c^0$) to $R\bar{3}$ rhombohedral ($a^-a^-a^-$) near room temperature. Further heating of the sample revealed another transition to $Fm\bar{3}m$ cubic symmetry ($a^0a^0a^0$), see **Figure 4.1.7 (a).** The phase transition between the monoclinic and rhombohedral phases is discontinuous as indicated by the large two-phase region which starts at 140 K and ends in the range 300–398 K. It should also be noted that there was a significant increase between the lattice parameter, *a*, measured at 300 and 400 K. The transition between the rhombohedral and cubic phases was continuous and, from the loss of resolved splitting in the diffraction patterns, was estimated to occur between 798 and 823 K, see **Figure 4.1.8 (a)** [49]. As it was mentioned above Ba_2YTaO_6 has a cubic structure at room temperature. Because of that its structure was examined at low temperature to establish the structure of the distorted variant. At the temperature range of 234 K was indicated a phase transition between tetragonal *I*4/*m* and cubic $Fm\bar{3}m$ symmetry (see **Figure 4.1.7 (b)** and **Figure 4.1.8 (b)**) which in an agreement with previous results [50]. The **Table 4.7** below shows several examples of the phase transition temperatures for the A_2LnTaO_6 and A_2LnNbO_6 series of compounds.

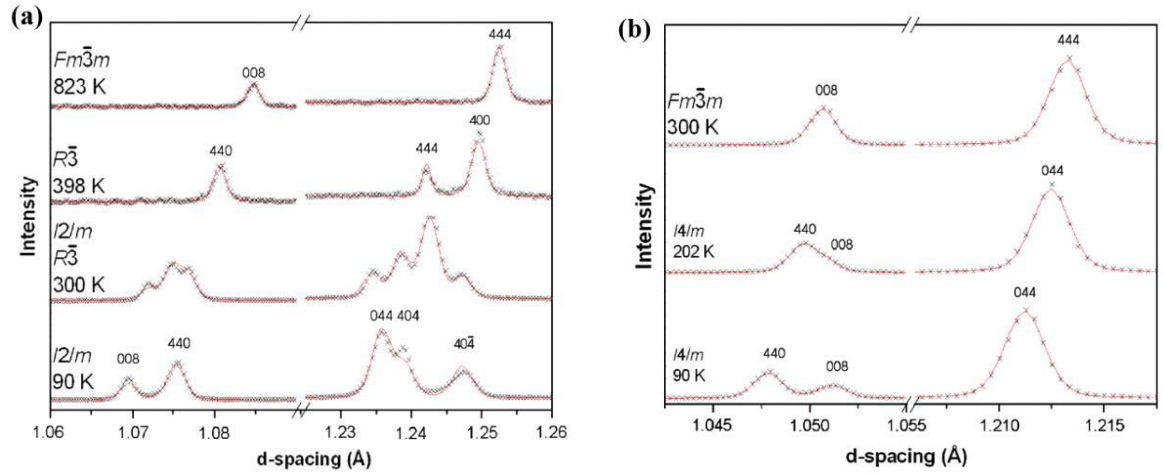

Figure 4.1.7 Selected sections of diffraction patterns of Ba_2LaTaO_6 (a) and Ba_2YTaO_6 (b) with changing temperature indicating the symmetry of the various structures found to be adopted [49]

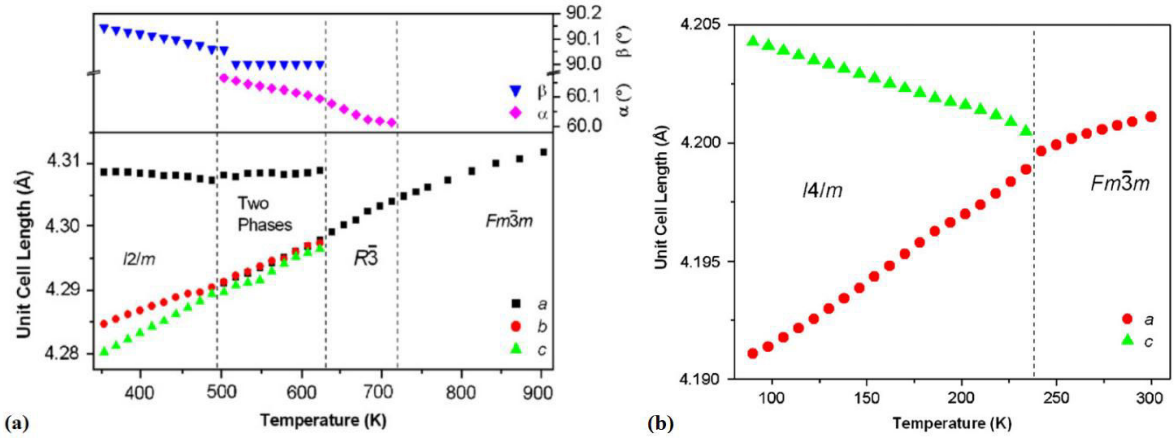

Figure 4.1.8 Lattice parameters versus temperature for Ba_2LaTaO_6 (a) and Ba_2YTaO_6 (b) indicating the sequence of phase transitions adopted with increasing temperature. The unit cell lengths have been reduced to the same size as a primitive cubic perovskite unit cell [49]

Table 4.7 Transition temperatures for the niobate and tantalate double perovskites, where a two-phase region of co-existence is noted by and the data collected do not fully cover the range of phase co-existence

Compound	**Temperature range of two-phase coexistance of monoclinic and intermediate phases (K)**	**Transition temperature to cubic**	
		From splitting (K)	**From strain (K)**
Ba_2LaNbO_6	~ 398-523	823-848	862(6)
Ba_2LaTaO_6	~ 140-298	798-823	838(4)
Ba_2PrNbO_6	503-623	713-728	-
Ba_2PrTaO_6	453-528	663-678	656(3)
Ba_2NdNbO_6	508-628	688-698	695(2)

Ba_2NdTaO_6	523-598	698-723	-
Ba_2SmNbO_6	~ 298	573-598	582(1)

4.1.4 Electrical properties of $A_2LnB'X_6$ (A= Ba^{2+}, Sr^{2+}, Ca^{2+}, *Ln*=lanthanide, In and Y, B'= Nb^{5+} and Ta^{5+})

There is a lack of knowledge concerning the electrical properties of $A_2LnB'X_6$ double perovskite niobate / tantalate compounds, although some related works are found in the literature [51-61]. In the work [57] were first studied the electrical properties of the phases Ba_2InMO_6 (M = Nb, Ta) and a composite systems (1-*x*) $Ba_2In_2O_5$ · *x*Ba_2InMO_6. Over the whole temperature range Ba_2InMO_6 electrical conductivity is low and does not exceed the conductivity $Ba_2In_2O_5$ (**Figure 4.1.9**). It has been observed a slight increase of Ba_2InMO_6 conductivity in a humid atmosphere at temperatures below 700 °C. The total conductivity Ba_2InMO_6 is mixed ionic-electronic in nature (**Figure 4.1.10**). In the dry air atmosphere predominates p-type conductivity. In a humid atmosphere below 500 °C contribution of the ionic component increases to ~ 60 % due to the appearance of proton contribution.

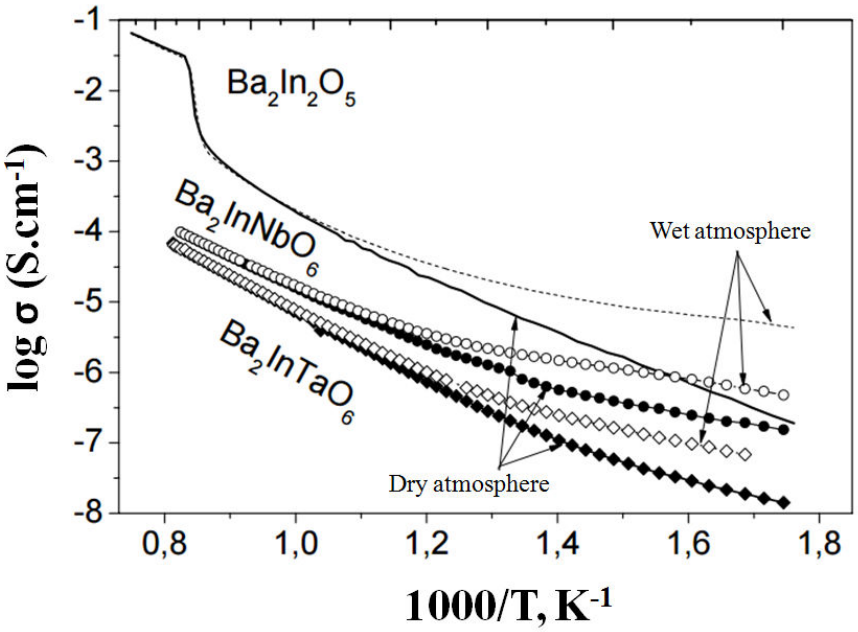

Figure 4.1.9 Temperature dependence of total electrical conductivity of the Ba_2InMO_6 compared with $Ba_2In_2O_5$ in the atmospheres of different humidity [57]

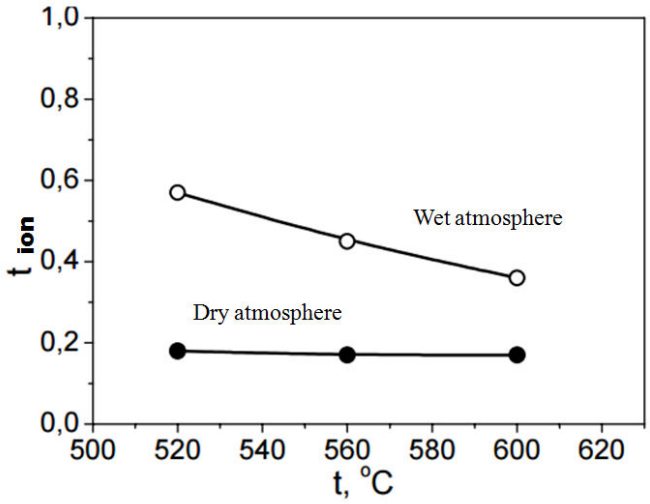

Figure 4.1.10 The temperature dependence of ion transport numbers for Ba_2InTaO_6 [57]

The concentration dependence of conductivity for the systems (1-*x*) $Ba_2In_2O_5 \cdot xBa_2InMO_6$ in dry and wet atmospheres is non monotonic. For small values of *x*, the electrical conductivity increases significantly by 1-2 orders of magnitude compared to the values obtained for the phases $Ba_2In_2O_5$ and Ba_2InMO_6 (**Figure 4.1.11**). The total conductivity of heterophasic systems is not the sum of the conductivities of the constituent phases, due to the presence of a potential (1-*x*) $Ba_2In_2O_5 \cdot xBa_2InMO_6$ composite effect. The composites obtained at 1300 °C, i.e. below eutectic temperature, had conductivity 0.5 order of magnitude lower. This confirms the role of dispersion in the formation of high ionic conductivity. Studies of conductivity depending on the partial oxygen pressure showed that samples have a 2 phases with mixed ion electronic conductivity.

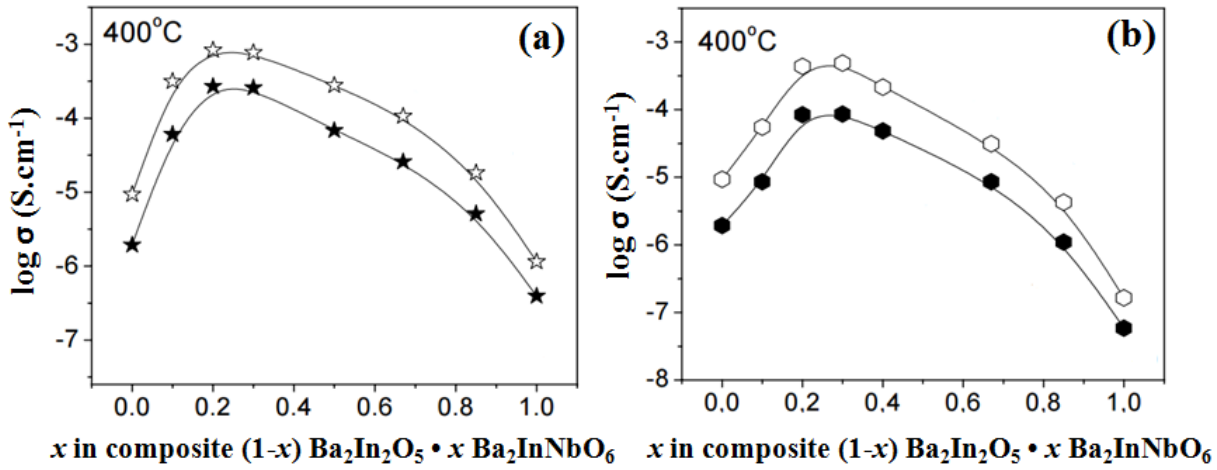

Figure 4.1.11 The concentration dependence of the total electrical conductivity of the (1-x) $Ba_2In_2O_5 \cdot xBa_2InMO_6$: (a) M = Nb; (b) M = Ta; in the atmospheres of different humidity [57]

T.P. Sinha *et al.* [51-54, 58] studied the dielectric properties and relaxation behavior of the several series of compounds as A_2HoTaO_6 and A_2CeNbO_6 (A = Ba^{2+}, Sr^{2+} and Ca^{2+}). A relaxation is observed in the entire temperature range. Complex impedance plane plots of A_2CeNbO_6 show only one semicircular arc, indicating only the grain contribution of dielectric relaxation as it shown on the **Figure 4.1.12** (a)**.** The scaling behavior of imaginary part of electric modulus (M") and imaginary part of electrical impedance (Z") suggests that the relaxation describes the same mechanism at various temperatures. The values of electrical conductivities varies from $2.79*10^{-7}$ to $3.5*10^{-5}$ Sm^{-1} with the increase in temperature from 100 to 450 °C. The activation energies (0.37 eV) extracted from M"(ω) and Z"(ω) peaks are found to follow the Arrhenius law [52]. A similar behavior of Z" has been observed for perovskite oxides strontium magnesium niobate, $SrMg_{1/3}Nb_{2/3}O_3$ [58].

Relaxation processes involve with their own discrete relaxation times depending on the temperature. It is to be mentioned that the samples has been synthesized at high temperature ≥ 1300 °C, a slight amount of oxygen loss can occur and may be expressed as per the Kroger-Vink notation:

$$O_o^x = V_o^{\cdot\cdot} + \frac{1}{2} O_2(\text{gas}) + 2e' \qquad (4.3)$$

where O_o^x is the loss of lattice oxygen, $V_o^{\cdot\cdot}$ is the presence of oxygen ion vacancy and e' is the electron released or captured. Oxygen vacancies facilitate the appearance of dipoles formed with an adjacent host ion and enlarge the rattling space available for dipole vibration, which as a consequence leads to the short-range hopping of the ions and gives rise to relaxation [51].

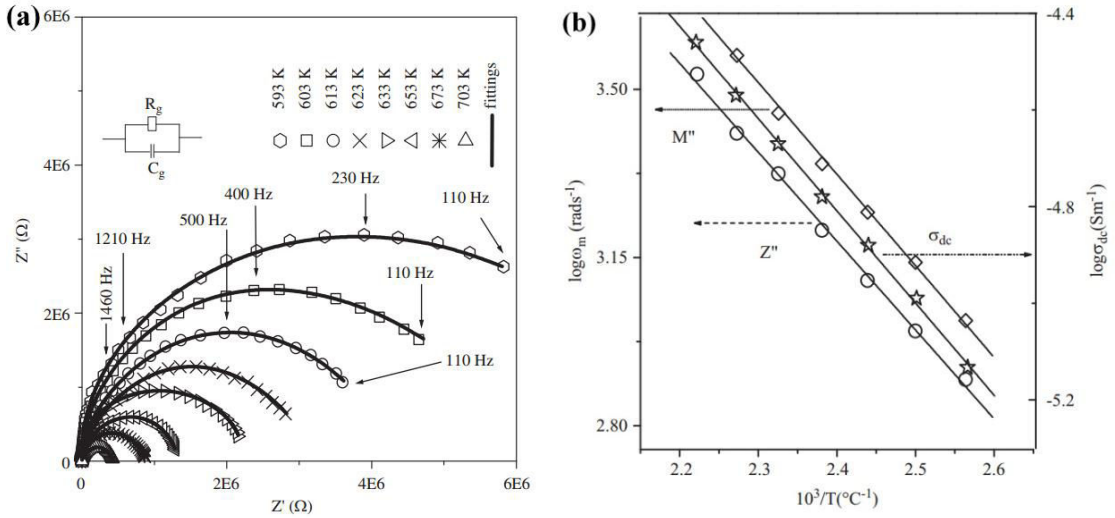

Figure 4.1.12 (a) Complex plane impedance plots of Sr_2CeNbO_6 at various temperatures where open symbols are experimental data points and solid line is the fitting of equivalent RC circuit. Inset shows the equivalent RC circuit [51]; (b) Arrhenius plots of Ba_2CeNbO_6 of ω_m for M"(ω), Z"(ω) and σ_{dc}. The symbols are experimental data points and the solid lines are the least squares straight-line fit [52]

As it was noticed in [54], in double perovskites, the structural distortion from the cubic structure is observed as the ionic radius of the A-site cation decreases. The distortion is caused by concerted rotation of the BO_6 octahedra and displacement of the A and B cations within the cage. These distortions give rise to a change in dielectric properties. As pointed out by Woodward [36], if the electronegativity of A-cation increases, *i.e.,* from Ba to Sr or from Sr to Ca, the covalent A–O bonding interaction plays a prominent role in double perovskites. **Figure 4.1.13** shows the Arrhenius plots of *dc* conductivity of Ba_2HoTaO_6, Sr_2HoTaO_6 and Ca_2HoTaO_6. The activation energies (E_σ) as obtained from the linear fit of the experimental data of the samples are found to be 0.93, 0.94, and 0.87 eV for Ba_2HoTaO_6, Sr_2HoTaO_6 and Ca_2HoTaO_6 respectively. The values of the activation energy suggest that the conduction mechanism may be due to the movement of oxygen-ion vacancies inside the grains in these materials. The oxygen ion jumps, between the vacancies, are considered to be responsible for the transition from short-range to long-range hopping and may explain the marked conductivity.

It is therefore evident that the information about the structural and electrical properties of $A_2LnB'X_6$ is still not complete and consistent. Therefore, to have knowledge about the performance of $A_2LnB'X_6$, it becomes important to know the carrier transport mechanism and hence the system deserved further investigation.

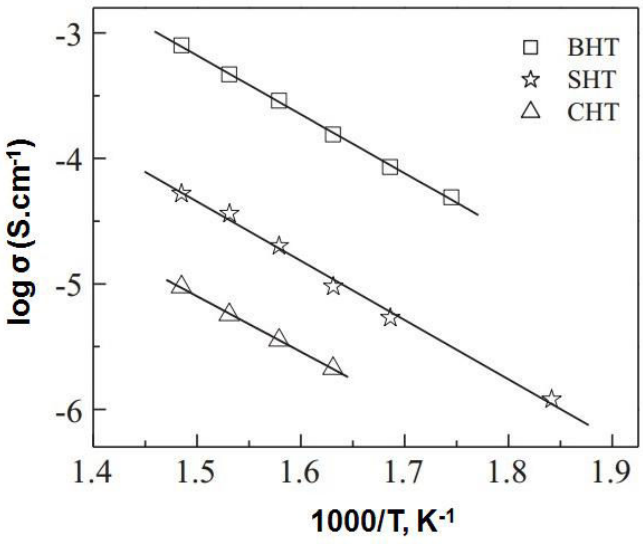

Figure 4.1.13 Arrhenius plots of the dc conductivity (σ_{dc}) for Ba_2HoTaO_6, Sr_2HoTaO_6 and Ca_2HoTaO_6 [54]

In another case, when B' and B" ions are 2+ and 5+, respectively, forming $A_3(B'B"_2)O_9$ triple perovskite. Among the complex perovskites, $Ba_3Ca_{1.18}Nb_{1.82}O_{9-\delta}$ (BCN18) has drawn attention due to its high proton conductivity and excellent chemical stability in CO_2 and H_2O [63-71]. Ca^{2+} and Nb^{5+} ions in this compound are taken off stoichiometry by 18 % (in opposite directions) to create negatively charged defects with which oxygen vacancies and/or protons can compensate, has been demonstrated almost pure proton conduction in reducing atmospheres. As it is known that the choice

of 1.18 for Ca sites is based on the ordering structure of B-sites ions. When the ratio of Ca^{2+} reaches 1.18, the B-sites ions are more randomly distributed, which is more favored on conductivity compared with pure $Ba_3CaNb_2O_9$ [65, 66].

BCN18 has been reported in literature as a good proton conductor, with conductivity values of $1*10^{-4}$ S.cm^{-1} at 200 °C [65]. Bohn H.G. and Schober T. [65] found that BCN18 has good proton conductivity in the interior of the grains, whereas the grain boundaries serve as obstacles to proton conduction. The authors have suggested that once the oxygen ion vacancies are filled in the structure, the concentration of electron hole may be frozen and resulting in a high conductivity during the cooling cycle with activation energy of 0.82 eV, see **Figure 4.1.14.** At high temperature (above 700 °C) the proton concentration in BCN18 is reduced to values below 1%. At high pO_2 values, the DC conductivity is dominated by electronic conduction which leads to small proton transport numbers. Annealing of BCN18 in hydrogen atmospheres was found to lead to a degradation of mechanical strength.

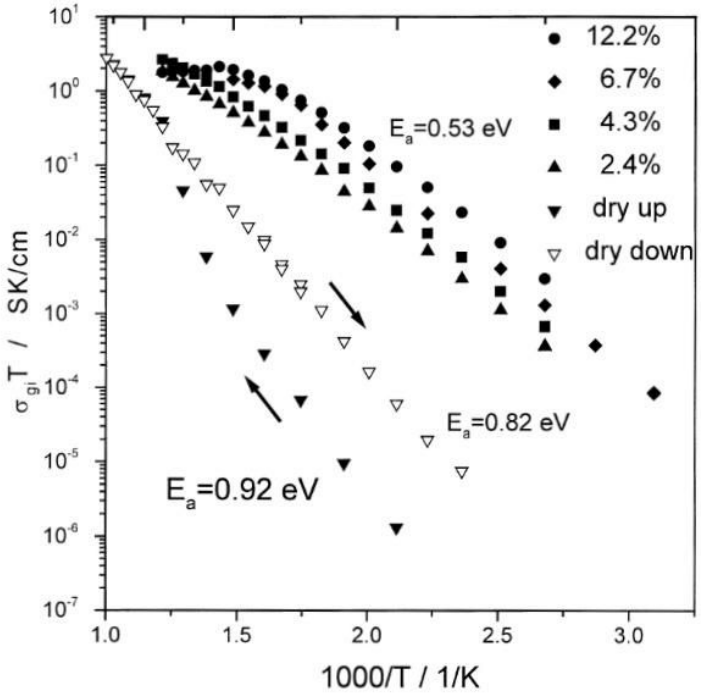

Figure 4.1.14 Temperature dependence of the grain interior conductivity of BCN18. All indicated concentrations are total proton concentrations obtained from the weight increase of the sample [65]

S. Wang et al. [72] investigated the effects of Ce doping on the Ca and Nb ions in complex perovskite BCN18 proton conductor. The conductivity measurements for the samples are conducted in wet air and wet H_2. In both air and H_2 atmospheres, substitution of Nb^{5+} with Ce ions leads to a decrease in activation energy as well as an increase in bulk conductivity. The activation energy for grain boundary conduction remains almost the same with different substitution of Ce ions. **Figure 4.1.15 (a)** is clearly showing the effect of Ce doping on the crystal structure and consequently

influence on the electrical conductivity. A larger decrease in activation energy is observed with Nb sites doped samples. This can be understood that more B-sites ions are "randomly" distributed rather than ordered because of the Ce ions doping, thus the charged ions can move more easily. As it can be seen at **Figure 4.1.15 (b)** for samples tested in wet H_2 atmosphere, a decrease in activation energy at high temperature range (higher than 550 °C) has been observed, indicative of change in conduction mechanism. When the testing temperature increases, a decrease in proton conductivity is anticipated as a result of the dehydration of the oxide lattice due to the exothermal nature of reaction (4.4). A gradual change from proton conduction into mixed oxygen ion and proton conduction is expected. Electronic conduction may also exist under high temperature regime.

$$H_2O + V_O^{\cdot\cdot} + O_O^{\times} \leftrightarrow 2OH_O^{\cdot} \qquad (4.4)$$

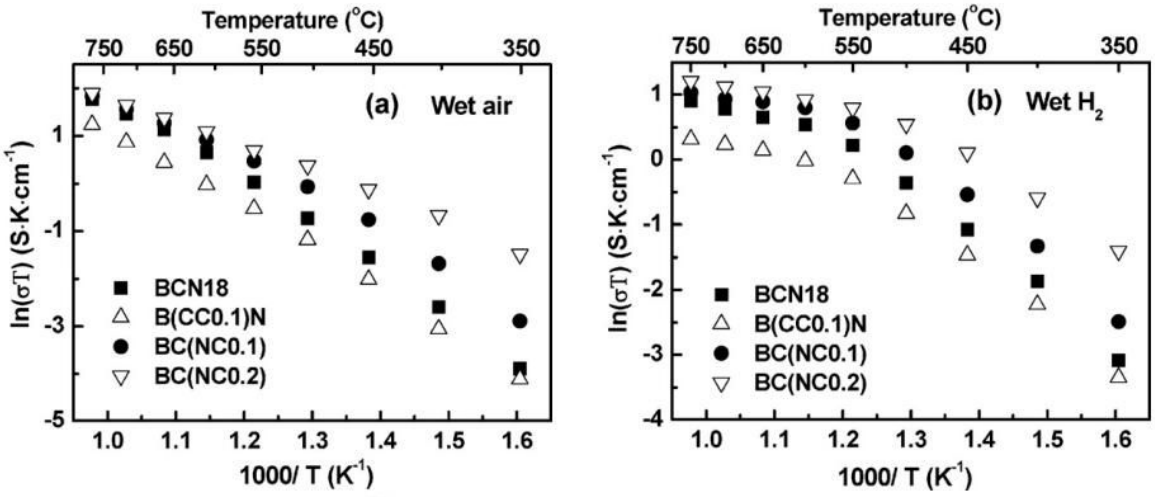

Figure 4.1.15 Arrhenius plots of total conductivity for samples (a) in wet air and (b) in wet H_2 [72]

As very few studies of the substitution on the B-sites in BCN18 have been reported before, it requires further studies, especially by exploring other potential B-site dopants of BCN18 in the pursuit of novel proton conducting materials.

4.2 Objectives of the study

In connection with the foregoing, the objectives of this chapter are:

- Synthesis of solid solutions $Ba_2Y_{1+x}Nb_{1-x}O_{6-\delta}$ with different content of Y^{3+} (x = 0, 0.05, …, 0.25) and study of their crystal structure;

- The study of the electrical conductivity in the temperature range 300 - 900 °C in different atmospheres with different oxygen partial pressures;

- Investigation of these phases on a possibly proton transfer;

- Examine its stability under operating conditions.

4.3 Structural properties of $Ba_2Y_{1+x}Nb_{1-x}O_{6-\delta}$ compounds (x = 0, 0.05, …, 0.25)

Nanopowders of the desired stoichiometry were prepared by the freeze-drying process as described in the **Chapter 2** and calcined at 900 °C for 30 min in ambient atmosphere. The X-Ray diffraction patterns of powders are presented in **Figure 4.3.1**. Excepted the presence of residual $BaCO_3$ impurity, there are no other impurities observed. It was found that the samples $Ba_2Y_{1+x}Nb_{1-x}O_{6-\delta}$ are single-phase in the range $0 \leq x \leq 0.2$ and the diffraction pattern could be indexed in a cubic structure of double perovskite (space group $Fm\bar{3}m$). The degree of order generally increases with increasing synthesis temperature. The amount of cation ordering is, therefore, primarily controlled by kinetic processes and not by thermodynamic equilibrium considerations. So, it means that consistent with a low temperature synthesis route, $Ba_2Y_{1+x}Nb_{1-x}O_{6-\delta}$ compounds could also indexed in disordered perovskite system.

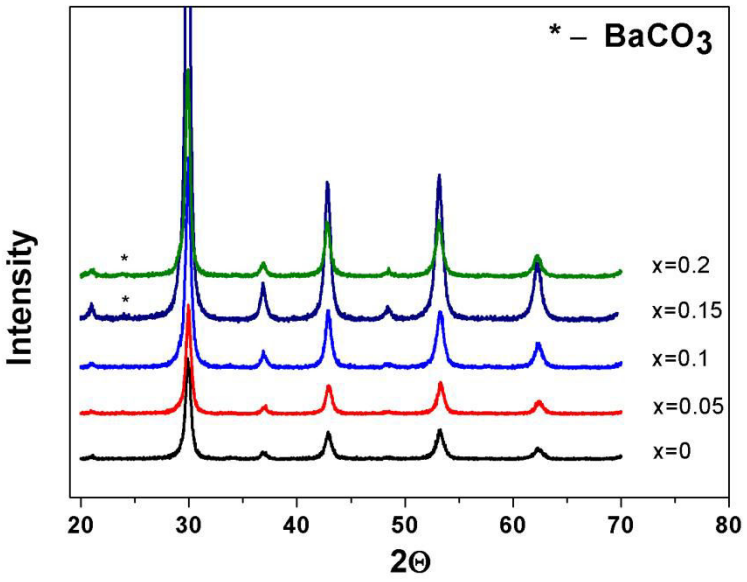

Figure 4.3.1 X-Ray diffraction of powders $Ba_2Y_{1+x}Nb_{1-x}O_{6-\delta}$ calcinated at 900 °C for 30 min

4.3.1 Structural characterization of sintered pellets

Powders were pressed into pellets under pressure 750 MPa, and sintered at 1450 °C for 24 h to obtain the dense materials. **Figure 4.3.2** presents a color change of the samples $Ba_2Y_{1+x}Nb_{1-x}O_{6-\delta}$ from yellow to white with increasing of Y^{3+} dopant content. In connection with this, it could be seen a decrease of density of the sintered samples. The XRD patterns of the sintered $Ba_2Y_{1+x}Nb_{1-x}O_{6-\delta}$ are shown in **Figure 4.3.3**. Data were collected over the angular range from 10° to 90° with step of 0.02°.

To simplify notation hereinafter, the names of compounds are written in a form (BYNO_percent of dopant content), for example $Ba_2Y_{1.25}Nb_{0.75}O_{6-\delta}$ = BYNO_25. The results of the X-Ray difraction measurements show that all the samples except for BYNO_25 present in a single phase, the peak corresponding to the phase of Y_2O_3 impurity being not detected. Solid solutions are formed till 20 % of yttrium doping. The XRD data were indexed with a cubic unit cell with a space group $Fm\bar{3}m$. The diffraction profiles of all the compounds showed the existence of the super lattice reflection at $2\theta \approx 18°$ (see **Figure 4.3.4).** It is concluded that these compounds are ordered perovskites and their lattice parameters are double those of the single perovskite. The degree of ordering is nevertheless difficult to evaluate at this stage. The cell parameters, volume and relative densities of sintered compounds are summarized in **Table 4.8**. It can be noticed that density of sintered samples is decreasing with the increase of Y^{3+} content.

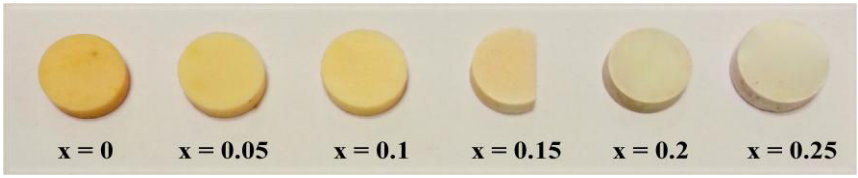

Figure 4.3.2 The color change of the $Ba_2Y_{1+x}Nb_{1-x}O_{6-\delta}$ samples depends on the dopant concentration

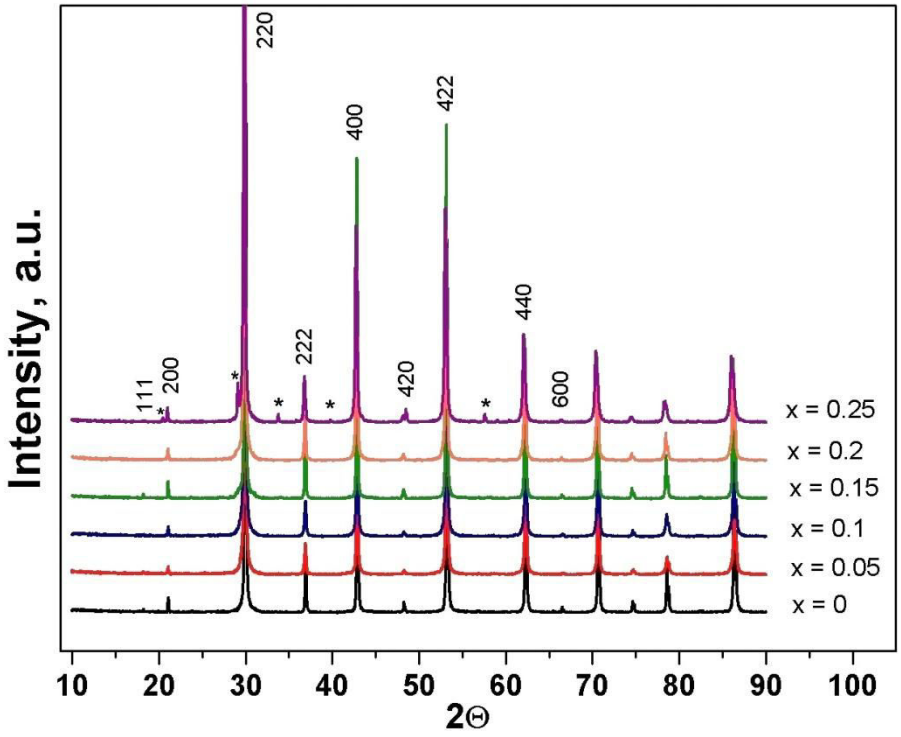

Figure 4.3.3 X-Ray diffraction of pellets $Ba_2Y_{1+x}Nb_{1-x}O_{6-\delta}$ sintered at 1450 °C for 24 h.
(*) indicates a presence of impurities of Y_2O_3

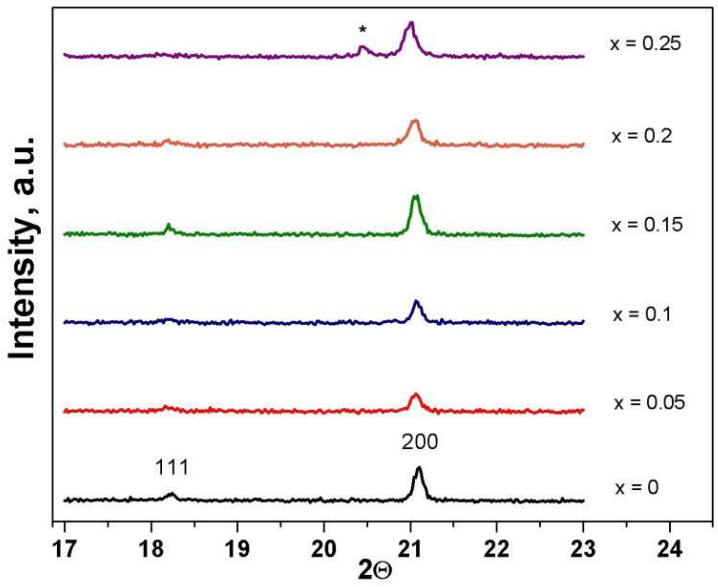

Figure 4.3.4 Enlarged section in a range of diffraction angles 2θ = 17-23° showing the basic (111) and (200) reflections of $Ba_2Y_{1+x}Nb_{1-x}O_{6-\delta}$ at room temperature. (*) indicates a presence of Y_2O_3 impurity

Table 4.8 Cell parameters, volume and relative densities of compounds $Ba_2Y_{1+x}Nb_{1-x}O_{6-\delta}$ sintered at 1450 °C for 24 h

x (Y), %	**a, Å**	**Unit cell volume, Å^3**	**Space group**	**Relative density, %**
0	8.4128(2)	595.437	$Fm\bar{3}m$	96
5	8.4054(1)	593.864	$Fm\bar{3}m$	95
10	8.4093(3)	594.681	$Fm\bar{3}m$	96
15	8.4202(5)	597.008	$Fm\bar{3}m$	94
20	8.4252(3)	598.060	$Fm\bar{3}m$	91
25	8.4318(1)	599.475	$Fm\bar{3}m$	80

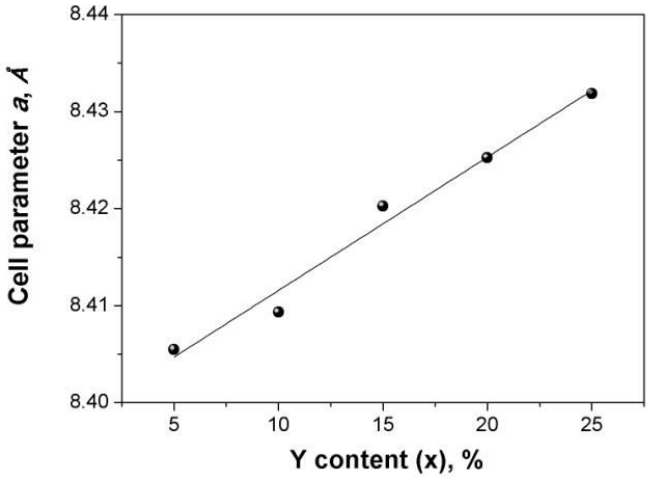

Figure 4.3.5 Evolution of cell parameters as a function of Y^{3+} content of $Ba_2Y_{1+x}Nb_{1-x}O_{6-\delta}$ compounds

The original structural information given by Woodward *et al.* [47] was used as a model for the refinement of the structure of $Ba_2Y_{1+x}Nb_{1-x}O_{6-\delta}$. **Figure 4.3.6** shows a crystal structure of Ba_2YNbO_6. It consists of rock salt ordering of Y^{3+} and Nb^{5+} cations, the oxygen atoms are slightly shifted away from Nb along the pseudo-cubic $[100]_p$-axis, resulting in two distinct YO_6 and NbO_6 octahedra. It is generally accepted that the extent of ordering in double perovskites is influenced by the differences in the charge and size of the octahedral-site cations [31], as well as bonding characteristics of the octahedral-site cations. Furthermore, the degree of long-range order is often kinetically limited and thus synthetic conditions can also play an important role [34, 47]. In a case of Ba_2YNbO_6 it is difficult to determine the degree of cation ordering from the XRD data because Y^{3+} and Nb^{5+} are formally isoelectronic. In spite of their difference in ionic radius, this can easily lead to the incorrect assumption that Y^{3+} and Nb^{5+} cations are completely disordered. Yet, yttrium(III) and niobium(V) have an oxidation state difference of two and more importantly a large difference in ionic radii (0.260 Å). This combination should stabilize a highly ordered arrangement of yttrium(III) and niobium(V) [31].

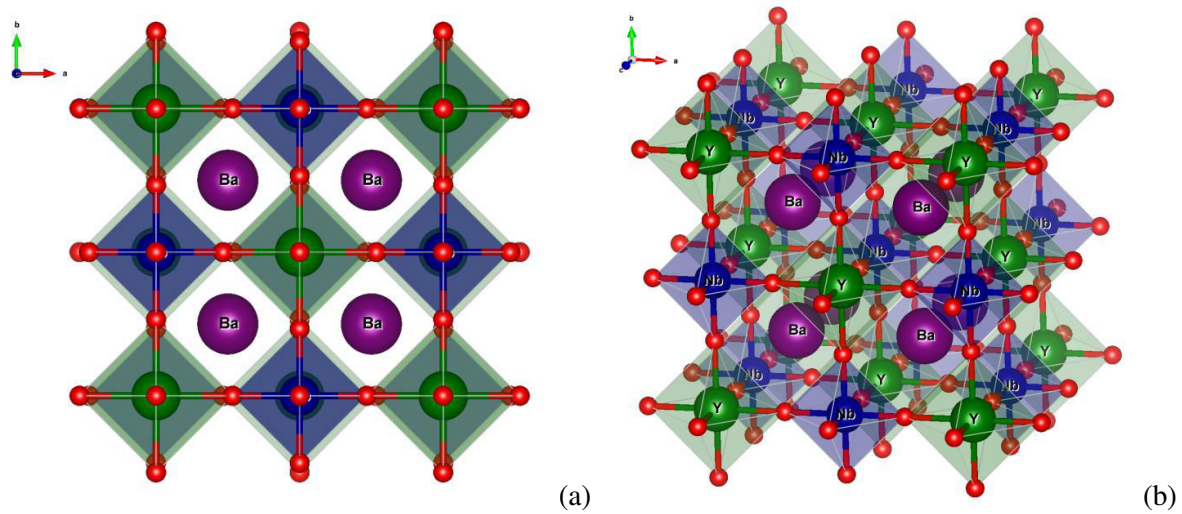

Figure 4.3.6 View of the double cubic perovskite structure Ba_2YNbO_6 in the direction [001] (a) and showing NbO_6/YO_6 octahedra (b), Ba and O atoms (small red circles)

Rietveld refinements in the space group *Fm*$\bar{3}$*m* yielded satisfactory results. **Figure 4.3.7** depicts the observed, calculated and difference XRD profiles for Ba_2YNbO_6 and (b) BYNO_15 after final cycle of refinement. It can be seen that the profiles for observed and calculated one are in a good agreement, that can be confirmed with R-factors (see Table 4.9). The refined cell parameters at room temperature for Ba_2YNbO_6 and BYNO_15 are a = 8.4128(2) Å and a = 8.4202(5) Å respectively. The lattice information as obtained for Ba_2YNbO_6 is in good agreement with the literature report [47]. Detailed information of structure of BYNO_ 15 including atomic positions and Wyckoff coefficients are listed in Table 4.9.

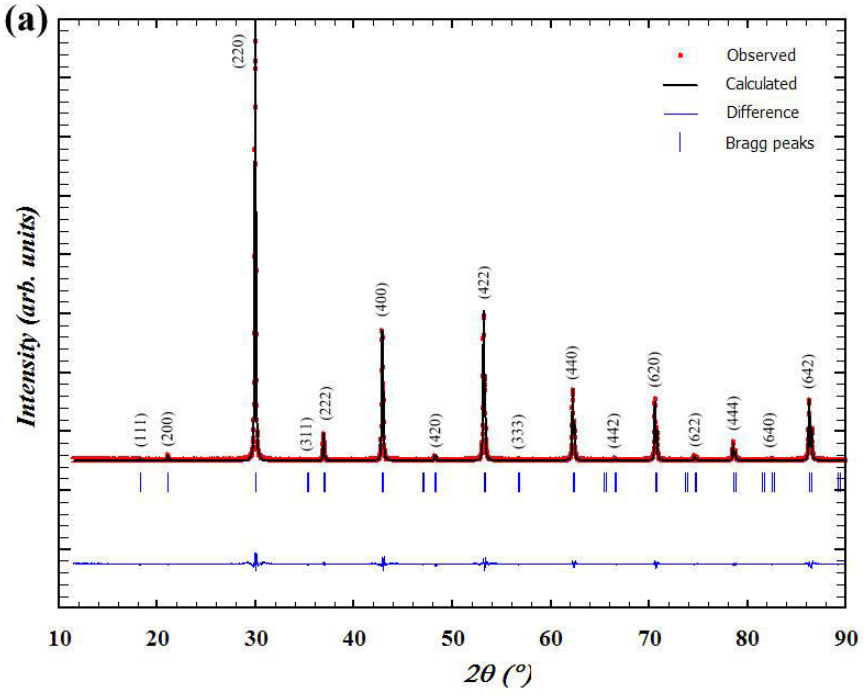

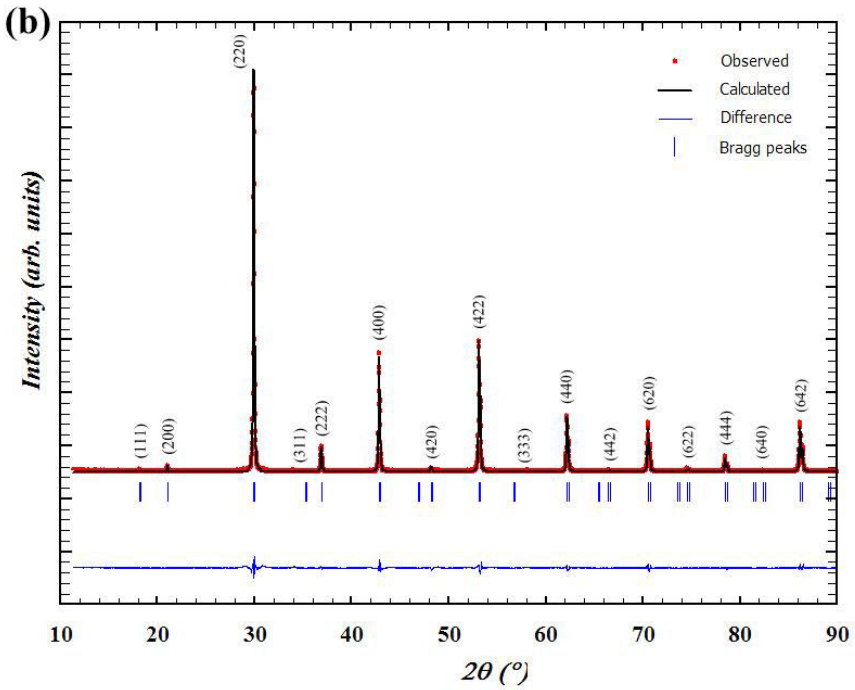

Figure 4.3.7 Diagram of XRD powder diffraction data for (a) Ba_2YNbO_6 and (b) BYNO_15 refined by Rietveld method

Table 4.9 Structural parameters and reliability factors for the Rielveld refinement of BYNO_15

x = 0.15	**$Ba_2Y_{1.15}Nb_{0.85}O_{6-\delta}$**	
Cell parameters **Space group**	a = 8.4202(5) Å $Fm\bar{3}m$	
Atom	**Wyckoff**	**x, y ,z positions**
Ba	*8c*	x = 0.25000, y = 0.25000, z = 0.25000
Y	*4a*	x = 0, y = 0, z = 0
Nb	*4b*	x = 0.50000, y = 0.50000, z = 0.50000
O	*24c*	x = 0.22758, y = 0, z = 0
R_{Bragg}, R_f	R_{Bragg} = 10.4, R_f = 11.2	

Table 4.10 represents bond lengths for the BYNO_15 at room temperature. The Y–O bond length is 2.2911 Å, which are very close to the values of the sum of Shannon's ionic radii of the corresponding ions (2.3 Å). On another hand, Nb–O bond length is 1.9204 Å and this value is shorter than the Nb–O bond length calculated from Shannon's ionic radii, 2.04 Å. This result indicates the existence of the covalency in the Nb–O bond in this compound. The Ba–O bond distance, 2.9837 Å, is also in agreement with the sum of the ionic radii (3.01 Å).

Table 4.10 Interatomic distances (Å) in BYNO_15

Bond Me – O	**Interatomic distance, Å**	**Number of bonds**
Y–O(1)	2.2911	6×
Nb–O(1)	1.9204	6×
Ba–O(1)	2.9837	12×

In order to measure thermal expansion coefficient of this group of materials, high-temperature X-Ray diffraction experiments were performed. A study of the cell parameters as a function of temperature has been carried out under air on powder samples, and the resulting expansion coefficients between 295 K and 995 K are summarized in Table 4.11. Profile matching of the XRD pattern was performed using FullProf suite program using a LeBail fitting. Atomic parameters were not refined. All unit cell parameters increase with temperature and as expected no temperature induced phase transition was observed. 15% Y-doped Ba_2YNbO_6 (BYNO_15) as an example is presented in **Figure 4.3.8**. The indexation of the peaks is done considering a cubic perovskite structure in a space group $Fm\bar{3}m$. The evolution of the lattice parameter with temperature is shown in **Figure 4.3.9.** Values of TEC are in the usual range for fuel cell applications [30], and there is a small increase of the expansion coefficients α_L going from small concentrations of yttrium (III) to greater ones.

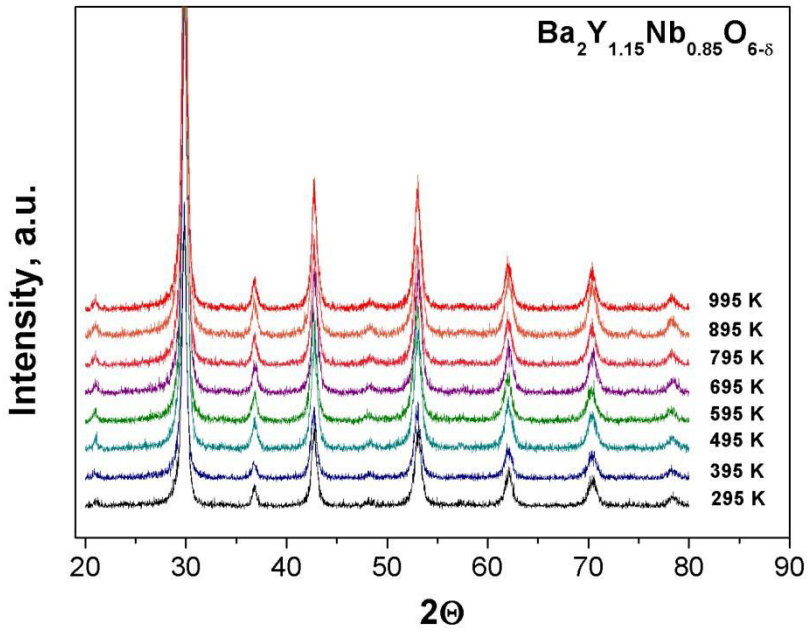

Figure 4.3.8 High-temperature X-Ray diffraction of BYNO_15 powder at different temperatures with cubic phase

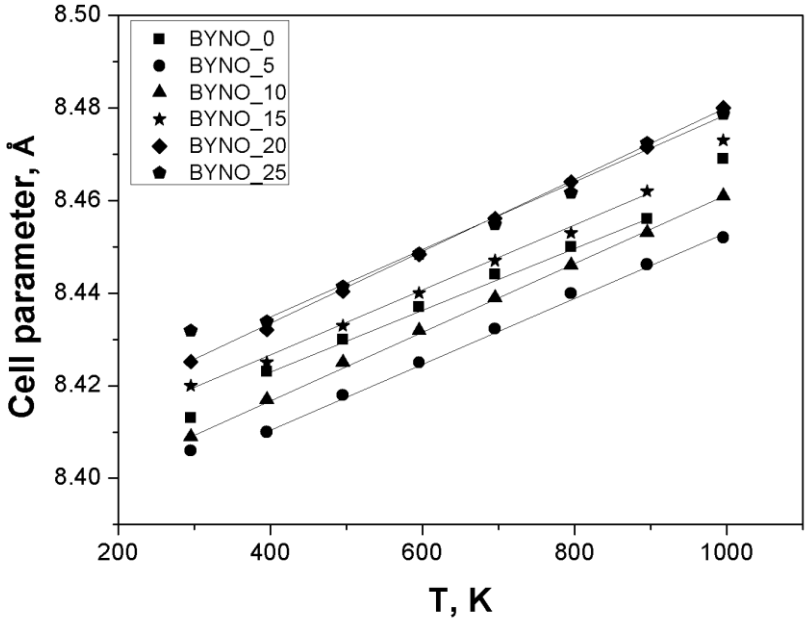

Figure 4.3.9 Cell parameter of $Ba_2Y_{1+x}Nb_{1-x}O_{6-\delta}$ at different temperatures

Table 4.11 Thermal expansion coefficient of $Ba_2Y_{1+x}Nb_{1-x}O_{6-\delta}$ sintered at 1450 °C for 24 h

Dopant content, %	TEC, K^{-1}	Temperature range, K
0	$8.36*10^{-6}$ (±0.01)	400-1000
5	$8.39*10^{-6}$ (±0.01)	300-1000
10	$8.69*10^{-6}$ (±0.01)	400-900
15	$8.81*10^{-6}$ (±0.01)	300-900
20	$8.87*10^{-6}$ (±0.01)	300-1000
25	$9.31*10^{-6}$ (±0.01)	400-1000

4.3.2 Microstructural characterization of sintered pellets

The polished pellets were thermally etched ($T_{etching} = T_{sintering} - 100$ °C), and the microstructures were observed by using SEM. **Figure 4.3.10** shows the SEM images of samples sintered at 1450 °C for 24 h. All specimens for *x* values equal or below 0.15 were quite dense, with relative densities of approximately 94–96 %. Extremely sparse, small pores were present in the grain boundaries or trapped inside the grains. The micrograph exhibits the polycrystalline texture of the material. As can be seen the samples consist of large grains with clean grain area. The average grain size also increased significantly with increasing amount of Y, *e.g.,* from 1 to 5 μm.

Figure 4.3.11 and **Figure 4.3.12** depict the EDX pattern and maps for the constituent ions of BYNO_15. All the peaks in the EDX pattern have been assigned to the elements present in BYNO_15. No further semi-quantitative analysis was performed. The EDX mapping clearly indicates the chemical homogeneity of the sample. **Figure 4.3.12** shows the distribution of Ba, Y, Nb and O (K, L-lines) in the grain volume. The color scale corresponds to the element content at a given point in the surface at. %. It can be seen uniform distribution of all components in the polycrystalline volume, even if a slight contrast is observed for yttrium.

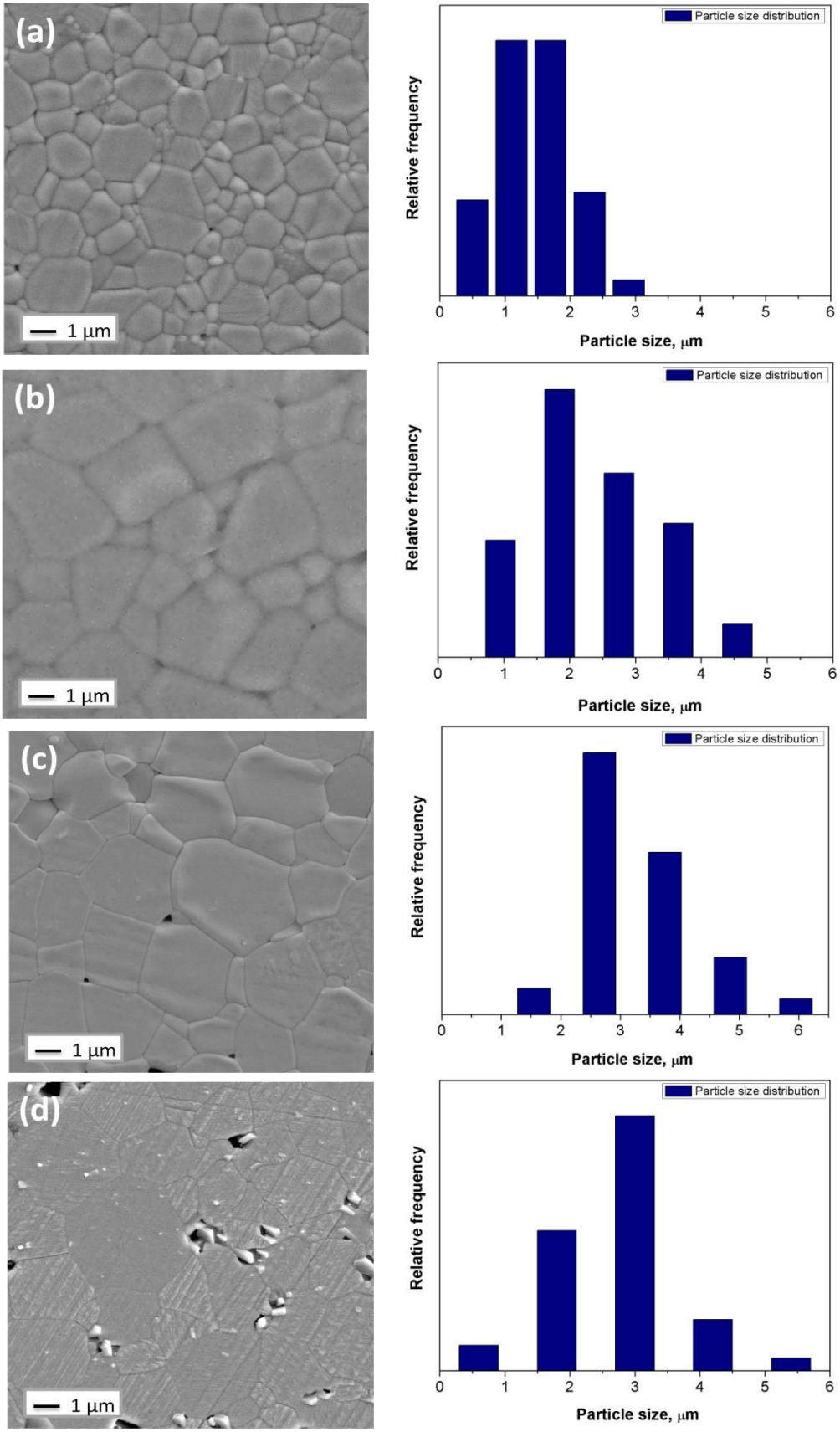

Figure 4.3.10 SEM pictures of pellet surface of $Ba_2Y_{1+x}Nb_{1-x}O_{6-\delta}$ (x=0, 0.05, 0.1, 0.15) sintered at 1450 °C for 24 h

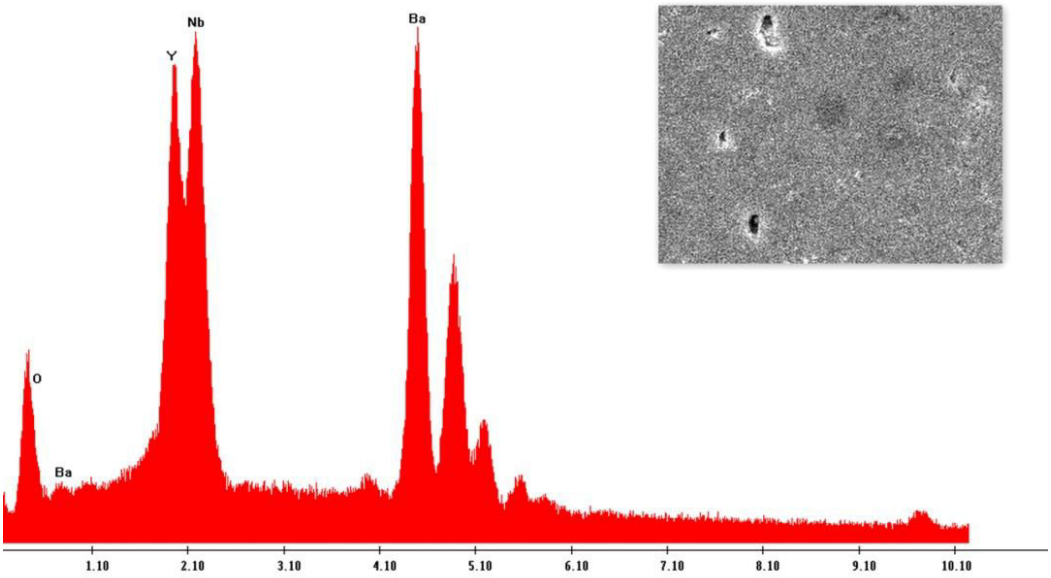

Figure 4.3.11 Energy-dispersive analysis of pellet surface of BYNO_15 and characteristic shape of the spectrum

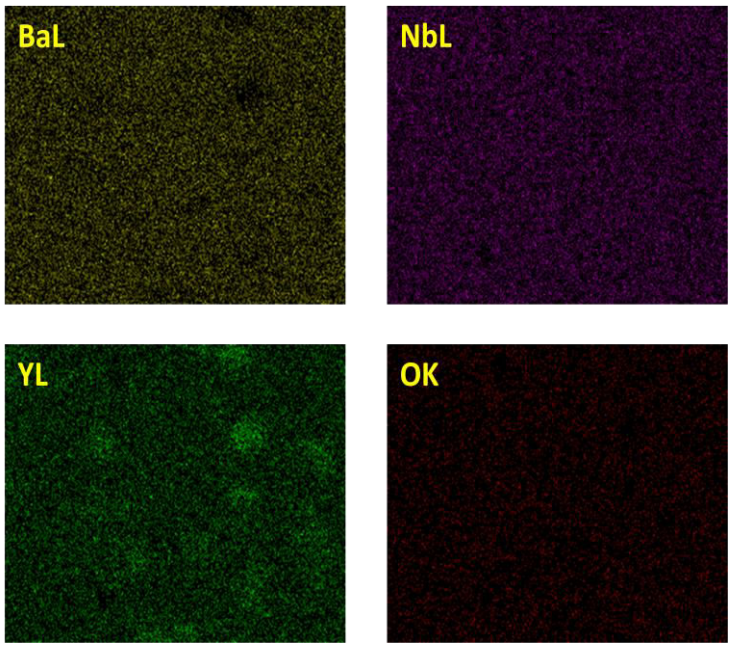

Figure 4.3.12 Distribution of Ba, Nb, Y and O (K, L-lines) in the grain volume for BYNO_15

4.3.3 Chemical stability

In order to study the yttrium content dependence of chemical stability in different conditions, we studied the stability of samples under different atmospheres, including wet Ar, 5%H_2/Ar and CO_2, and also in boiling water. All powders from the $Ba_2Y_{1+x}Nb_{1-x}O_{6-\delta}$ series were investigated in boiling water. **Figure 4.3.13** shows that after 10 h of boiling water treatment, the main phase is not changed

but could be noticed a small presence of $BaCO_3$ phase from X-ray diffraction pattern.

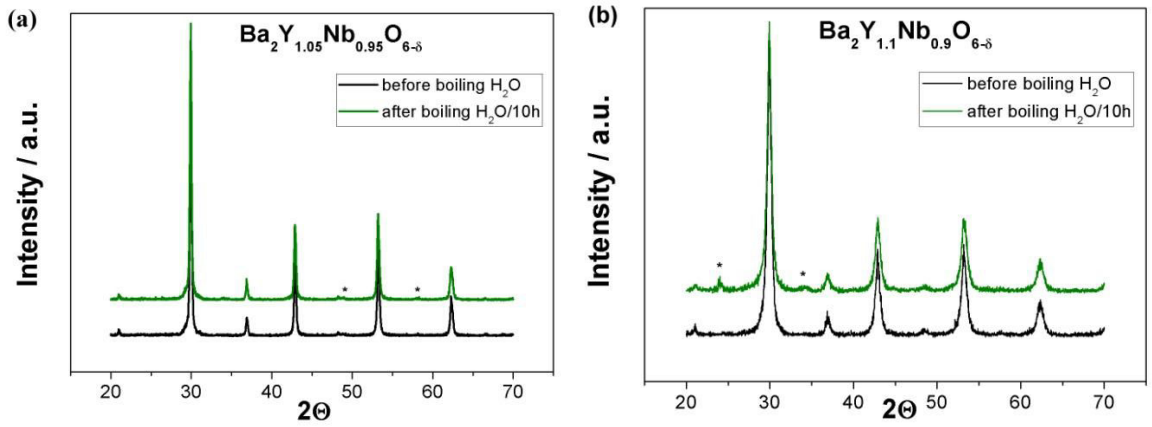

Figure 4.3.13 XRD patterns of powders of (a) BYNO_5 and (b) BYNO_10 in boiling water for 10 h; * - $BaCO_3$

Pellets of all compositions $Ba_2Y_{1+x}Nb_{1-x}O_{6-\delta}$ were treated thermally at 600 °C for 50 h under wet CO_2 and 600 °C for 50 h under wet 5% H_2/Ar. The X-ray diffraction patterns are shown in **Figure 4.3.14** and **Figure 4.3.15**, respectively. No extra-phases or phase changes were observed on these diffractograms. **Figure 4.3.16** under wet 5% H_2/Ar it could be seen a slight color change of the pellet surface, because of a potential reduction of Nb^{5+}**.**

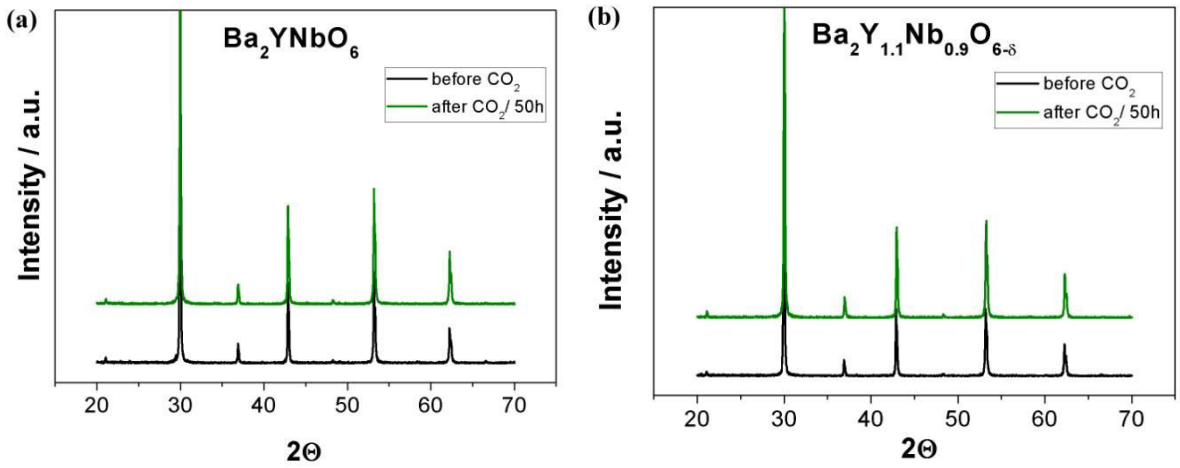

Figure 4.3.14 XRD patterns of pellet surface of (a) Ba_2YNbO_6 and (b) BYNO_10 in wet CO_2 at 600 °C for 50 h

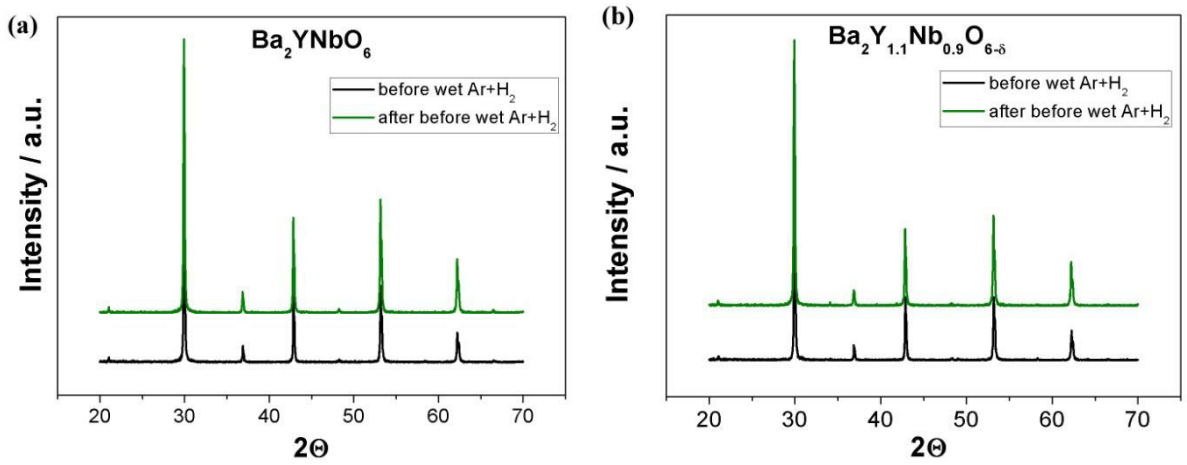

Figure 4.3.15 XRD patterns of pellet surface of (a) Ba_2YNbO_6 and (b) BYNO_10 in wet $Ar+H_2$ at 600 °C for 50 h

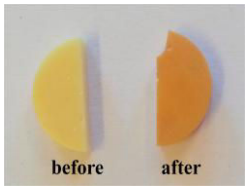

Figure 4.3.16 The pellet surface of $Ba_2Y_{1+x}Nb_{1-x}O_{6-\delta}$ in wet $Ar+H_2$ at 600 °C for 50 h

4.4 Transport properties

There is no reported study of single phase $Ba_2Y_{1+x}Nb_{1-x}O_{6-\delta}$ to the best of our knowledge using impedance spectroscopy (IS). This section presents the results of a study of the electrical properties of the $Ba_2Y_{1+x}Nb_{1-x}O_{6-\delta}$ phases by varying environmental parameters (T, pO_2).

4.4.1 Transport properties as a function of T. Analysis of impedance spectra

Impedance spectroscopy (IS) was performed on dense pellets with both sides coated with golden paint as electrodes, using a Solartron 1260 Frequency Response Analyser in the 1 MHz – 0.1 Hz frequency range under mixture of wet and dry $Ar+H_2$ in the temperature range 300 – 900 °C. Conductivity measurements were also performed under dry and wet argon, but because of low conducting properties of ceramics it was not possible to extract data from the impedance spectra below 700 °C because of the limit of impedancemeter, see **Figure 4.4.1.**

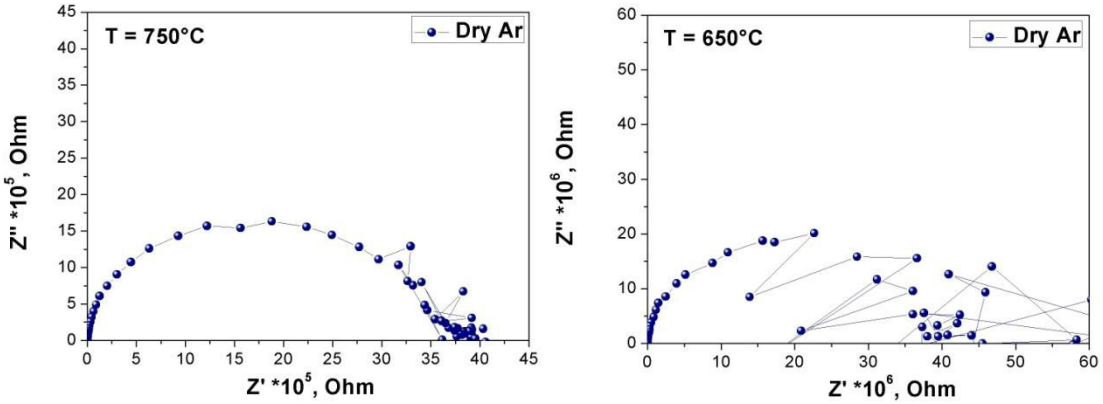

Figure 4.4.1 Degradation of impedance spectra with temperature under dry Ar for $Ba_2Y_{1+x}Nb_{1-x}O_{6-\delta}$

The modeling of the impedance spectra was done by using ZView software. It gives access to the values of the conductivity for the different contributions. The calculations used the resistance value of the sample obtained by extrapolation of the first semi-circle on the x-axis. Typical Nyquist plots are presented on the **Figure 4.4.2**. These graphs are representative of the general aspect of impedance spectra observed in the whole series of samples. It can be seen that the spectrum consists of one semicircle which lies in the range of high frequencies. As shown in this figure it was not possible to separated bulk and grain boundaries contributions at all range of temperatures. Under wet atmosphere, the impedance of sample diminishes strongly as compared to dry atmosphere. This sensitivity of the electric conductivity to the presence of water vapor in the gas phase indicates the appearance of proton conduction contribution.

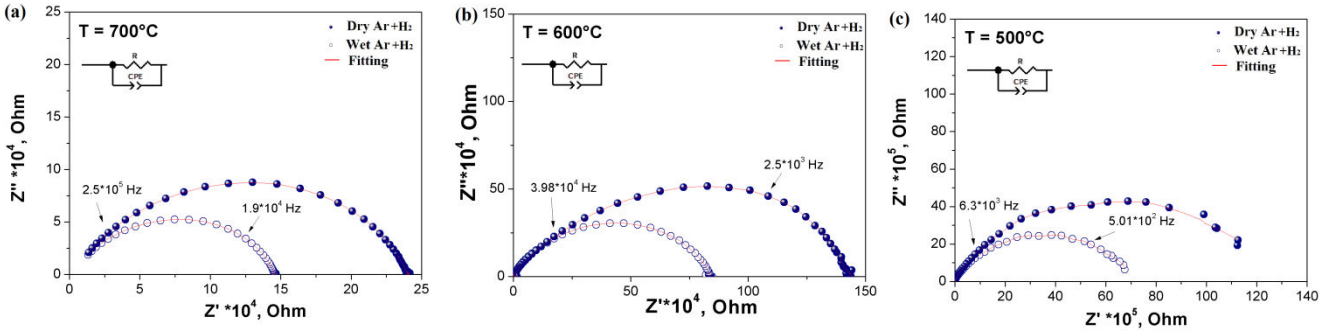

Figure 4.4.2 The Nyquist plots of $Ba_2Y_{1+x}Nb_{1-x}O_{6-\delta}$ in dry and humidified $Ar+H_2$ at different temperatures: 700 °C (a), 600 °C (b) and 500 °C (c)

Figure 4.4.3 shows the Arrhenius plots of the total conductivity determined by IS for $0 \leq x(Y) \leq 20$ %. All samples exhibit similar Arrhenius type of behavior. The partial replacement of 20 % of niobium by yttrium noticeably improves the conductivity. For example, it increases from 1.2×10^{-5} to 2.5×10^{-4} S*cm^{-1} at 800 °C. This difference is even more pronounced at lower temperatures. Besides, the activation energy decreases from 1.21 to 0.78 eV, still in the range of typically ion conducting crystals. However, the decrease of activation energy upon substitution seems to point to a change in

the nature of carriers, likely dominated by intrinsic defects in the parent material and by extrinsic defects in the Y-substituted ones.

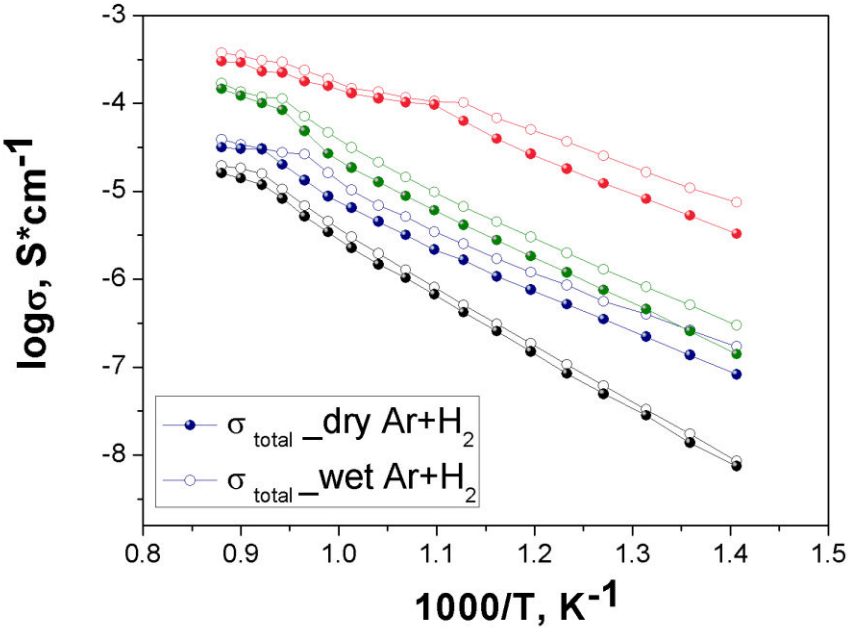

Figure 4.4.3 Arrhenius plots of total conductivities of $Ba_2Y_{1+x}Nb_{1-x}O_{6-\delta}$ in dry and wet $Ar+H_2$. BYNO_0 (●- dry atm, ○- wet atm), BYNO_10 (●- dry atm, ○- wet atm), BYNO_15 (●- dry atm, ○- wet atm), BYNO_20 (●- dry atm, ○- wet atm)

Conductivity values of undoped Ba_2YNbO_6 are quite low at all temperatures. With increasing humidity values of the total conductivity Ba_2YNbO_6 vary little, the sample is hardly affected by water vapor. For the other samples $Ba_2Y_{1+x}Nb_{1-x}O_{6-\delta}$ conductivity curves can be approximated by straight lines with different activation energies in a high temperature (HT, above 750 °C) and low temperature (LT, below 750 °C) range, see Table 4.4.1. At HT range it could be seen a change of activation energies because of change of charge carrier: from oxygen-ion to electron one. That was proved by conductivity measurements versus pO_2, which will be shown below. In a humid atmosphere we observed an increasing of conductivity at temperatures below 800 °C. The difference in the values of the conductivity reaches 0.5 orders of magnitude. This is probably due to the presence of proton conductivity contribution.

Table 4.4.1 Activation energy for conduction properties of $Ba_2Y_{1+x}Nb_{1-x}O_{6-\delta}$ compounds under $Ar+H_2$ atmosphere

Composition	HT range, eV		LT range, eV	
	Dry $Ar+H_2$	Wet $Ar+H_2$	Dry $Ar+H_2$	Wet $Ar+H_2$
Ba_2YNbO_6	0.64	0.64	1.21	1.21
$Ba_2Y_{1.1}Nb_{0.9}O_{6-\delta}$	0.50	0.49	0.89	0.89
$Ba_2Y_{1.15}Nb_{0.85}O_{6-\delta}$	0.70	0.70	0.85	0.85
$Ba_2Y_{1.2}Nb_{0.8}O_{6-\delta}$	0.55	0.55	0.78	0.78

Figure 4.4.4 shows the concentration dependence of the total conductivity of solid solutions $Ba_2Y_{1+x}Nb_{1-x}O_{6-\delta}$. The formation of oxygen vacancies by doping in the Ba_2YNbO_6 structure induces a significant increase of the ionic conductivity. The maximum difference between dry and wet atm observed for the $Ba_2Y_{1.2}Nb_{0.8}O_{6-\delta}$.

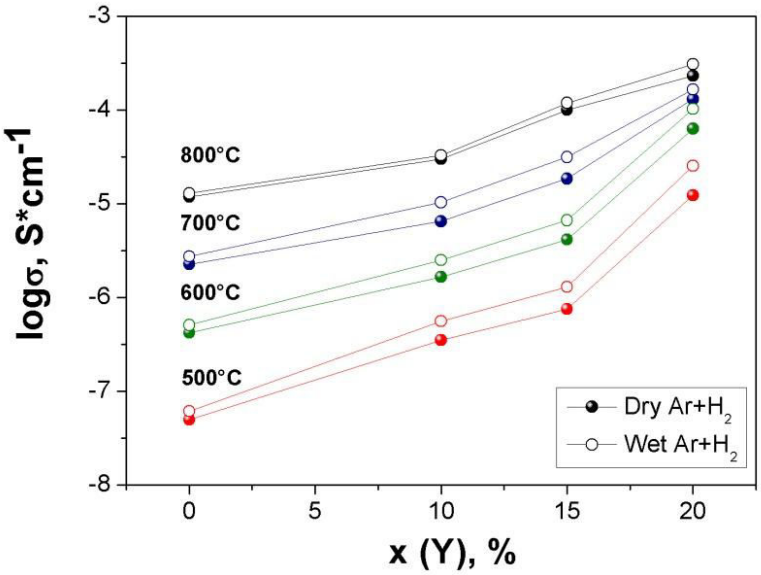

Figure 4.4.4 Evolution of total conductivity values of $Ba_2Y_{1+x}Nb_{1-x}O_{6-\delta}$ with temperature in wet $Ar+H_2$

4.4.2 Transport properties as a function of $p(O_2)$

Considering that aliovalent substitution induces oxygen vacancies, the enhancement of conductivity can be ascribed to improvement of the ionic conductivity associated with such a type of defect. Therefore, to further investigate this hypothesis and the possible participation of other defects, the dependence of conductivity on the oxygen partial pressure $p(O_2)$ has been studied. **Figure 4.4.5** illustrates the $p(O_2)$ dependence of total conductivity at different temperatures for $Ba_2Y_{1+x}Nb_{1-x}O_{6-\delta}$ ($0 \leq x \leq 0.2$).

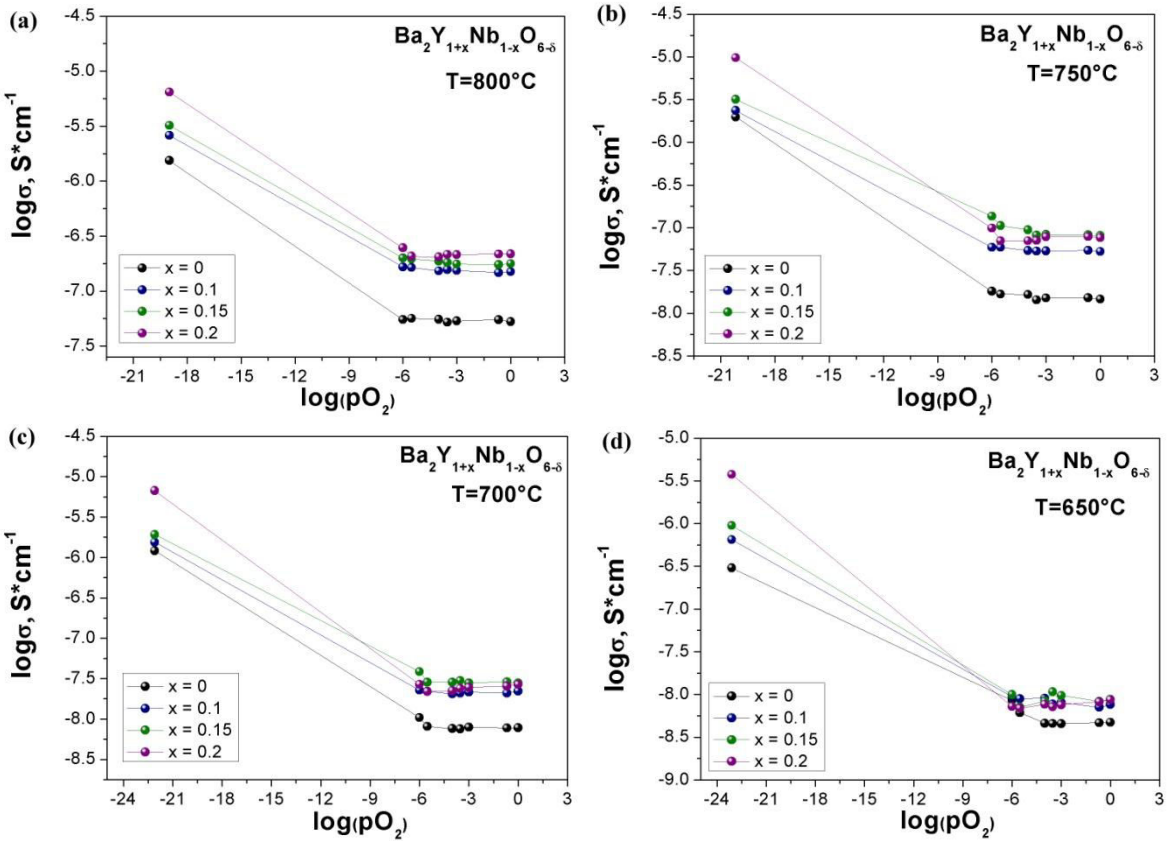

Figure 4.4.5 Log ($p(O_2)$) dependency at (a) 800 °C, (b) 750 °C, (c) 700 °C, (d) 650 °C for various compounds of $Ba_2Y_{1+x}Nb_{1-x}O_{6-\delta}$

For all samples we could observed two major regions:

- at high and intermediate $p(O_2) \geq 10^{-6}$, the conductivity is relatively stable. This is an indication of a pure ionic (mixed oxide/protonic) conduction;
- at low $p(O_2)$, we observe a complete change in conductivity. We assumed that in our case, the reducibility of Nb^{5+} plays a key role in this change in conductivity, enhancing the electron transport. Equation (4.4) represents oxygen vacancies and electron formation upon reduction:

$$O_o^x \leftrightarrow \frac{1}{2}O_2 + V_o^{\cdot\cdot} + 2e' \qquad (4.4)$$

In this case, we assume the high temperature behavior in wet H_2 atmosphere is essentially of electronic nature. While the low temperature behavior in wet H_2 also presents a proton transport contribution. This should be confirmed by further experiments with measurements under D_2O.

4.5 Molecular dynamics simulations

In order to understand better why the level of ion conduction is so low in $Ba_2Y_{1+x}Nb_{1-x}O_{6-x}$ in spite of high doping levels and adequate microstructure, we performed Molecular dynamics simulations. The idea behind these simulations is to be able to correlate the (bad) oxygen diffusion coefficient with some specific mechanism at the atomic scale.

4.5.1 Calculations details

MD simulations were done with the DLPOLY Classic code [73, 74] using a supercell of 8×8×8 cubic perovskite unit cells (containing for the undoped phase 512 Ba, 256 Y, 256 Nb, 1536 O atoms). Different compositions were tested corresponding to the formula $Ba_2Y_{1+x}Nb_{1-x}O_{6-x}$ with x = 0.00, 0.05 , 0.10, 0.15, 0.20. For the undoped compound, Y and Nb atoms were ordered according to the double perosvkite structure presented above. For the doped compounds, Nb atoms were substituted randomly by Y atoms. For doped compounds, oxygen vacancies induced by yttrium doping were also distributed randomly. During these simulations, the system was first equilibrated at temperatures between 1500 and 1900 K and at zero pressure for 20,000 time steps with a time step of 1 fs in the isothermal-isobaric (NPT[1]) ensemble with the Nosé-Hoover thermostat. Afterwards, the equilibrium lattice parameters were calculated with 100,000 time steps more. Then, simulations were performed in the NVT[2] mode during 100,000 time steps, after a 10,000 equilibration steps. Finally, NVE[3] simulations were realized corresponding to 1,000,000 to 2,000,000 time steps. Trajectories were analyzed from these latter simulations.

For such simulations, interactions between ions were described by a long-range Coulombic term calculated by Ewald summation and a short-range Buckingham pair potential. For Coulombic interactions, the formal charges +2, +3, +5 and −2 were used respectively for Ba, Y, Nb and O ions. The use of formal ionic charge was shown to describe correctly the dynamical features of atoms in most oxide compounds.

The Buckingham potential is described by:

$$\varphi_{ij}(r) = A_{ij} \exp\left(-\frac{r}{\rho_{ij}}\right) - \frac{C_{ij}}{r^6} \qquad (4.5)$$

[1] NPT : Constant number N of particles, constant pressure P, constant temperature T
[2] NVT : Constant number N of particles, constant volume V, constant temperature T
[3] NVE : Constant number N of particles, constant volume V, constant energy E

where r is the distance between the atoms i and j, and A_{ij}, ρ_{ij} and C_{ij} are potential parameters specific to each ion pair whose values are given in Table 4.5.1. The set of potentials was taken from previous studies, which were shown to reproduce correctly oxide materials properties.

Table 4.5.1 Inter-atomic Buckingham potentials used for energy minimisation and molecular dynamics calculations. M-O interactions are taken from: Ba-O [75], Y-O [75], Nb-O [76], O-O [75]

Interaction	**A (eV)**	**ρ (Å)**	**C (eV.Å^6)**
Ba^{2+} - O^{2-}	931.7	0.3949	0.0
Y^{3+} - O^{2-}	1345.10	0.3491	0.0
Nb^{5+} - O^{2-}	1333.44	0.36404	0.0
O^{2-} - O^{2-}	22764.3	0.149	27.89

4.5.2 Results

4.5.2.1 Room temperature simulations

Using the presented potential, we simulated the undoped ordered phase Ba_2YNbO_6 at room temperature. The results of such simulation give precious information on structural aspects and are compared to the experimental values.

Table 4.5.2 Structural data at room temperature for Ba_2YNbO_6 as obtained from diffraction experiment [46] and from MD simulations

	Experimental value	**Calculated value**	**Error**
Cell parameter, *a*	8.431589 Å	8.52056 Å	+ 1.05 %
x, oxygen atomic position (x, 0, 0)	0.2665	0.2722	+ 2.0 %
Ba-O distance	2.984 Å	3.018 Å	+ 1.1 %
Y-O distance	2.247 Å	2.319 Å	+ 3.2 %
Nb-O distance	1.969 Å	1.941 Å	- 1.4 %

This table indicates a rather good agreement between observed and calculated structural properties, in particular for the cell parameter of the undoped phase whose error remains close to 1%. Nevertheless, the error on interatomic distance reaches several percents, which clearly indicates the limits of such simple potentials. We actually tried other potentials found in literature but the results

were worse than the ones presented here. These results validate the use of such potentials to describe atomic scale diffusion mechanisms, even if some error might be expected due to the very simple nature of the potential considered. From our experience, the calculations presented here would qualitatively reproduced the real mechanisms but might fail to evaluate precisely the activation energy of diffusion coefficient.

4.5.2.2 High temperature simulations

From high temperature, we can extract information concerning the dynamics and displacement of ions, in particular oxygen anions. On the following graph, we plot the mean square displacement of all atoms constituting the BYNO_20 compound. In **Figure 4.5.1**, we separated the Yttrium atoms on Y-site from the Yttrium atoms on Nb-site.

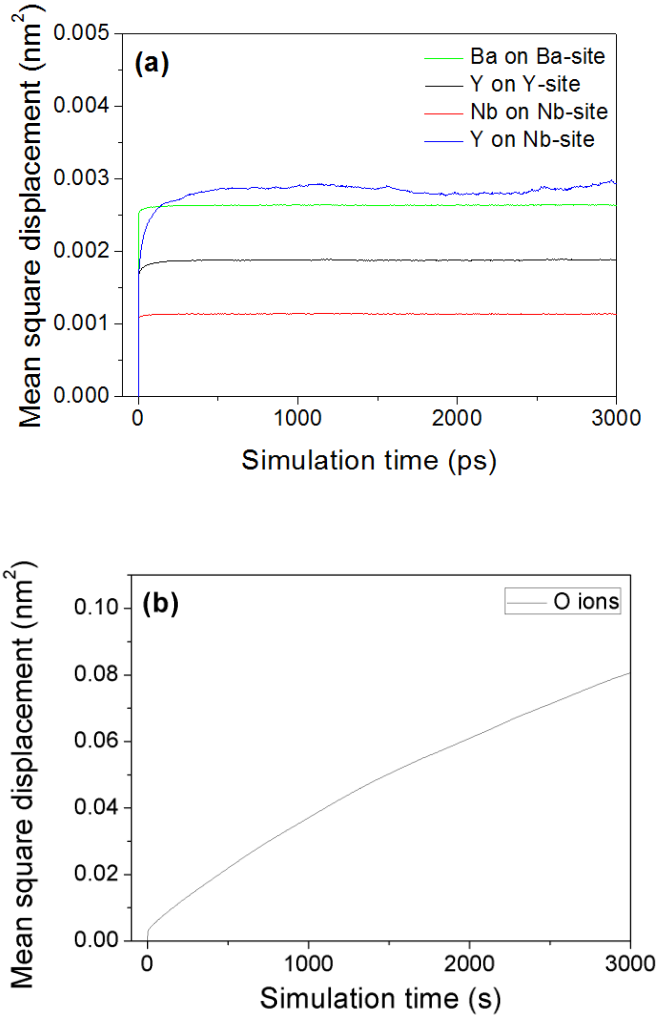

Figure 4.5.1 Mean square displacement for ions for the BYNO_20 sample at 2000 K (a) Ba, Y and Nb ions (b) O ions

This figure evidences first that cations remain on their site, their displacement corresponding to a simple vibration. The highest vibration is nevertheless observed for the yttrium on Nb site (dopant atom) despite being a big atom on a small site. For oxygen ions, we observe that the mean square displacement becomes asymptotic with a straight line with non-zero slope, indicating that oxygen ions have a long range diffusion. The fitting of this curve with a straight line allows obtaining diffusion coefficient as deduced from the Einstein'law :

$$MSD(t) = 8Dt \tag{4.6}$$

Where *MSD* is the Mean Square Displacement, *D* is the diffusion coefficient and *t* is the time. This formula supposes 8 possible jumps for each oxygen ion, which corresponds to the number of first nearest neighbors in the perovskite structure.

The results of extracted diffusion coefficients are plotted in **Figure 4.5.2**. We must precise here that in some cases (low doping level; low temperature), the diffusion coefficient was extracted from very small values of Mean Square Displacements (MSD < 0.01 nm^2) which correspond to less than 1 Å displacement. This would mean that low diffusion coefficients should be considered with caution, even if the qualitative behavior remains valid. The diffusion coefficients for the best BYNO doped compound are roughly 2 orders of magnitude smaller than the one calculated for Yttrium-doped zirconia (8YSZ) with the same approach, in spite of presenting a similar amount of oxygen vacancies (3.3% of oxygen vacancies on oxygen sites for BYNO_20 against 3.75% for the 8YSZ case). These simulations thus confirm that a low diffusion coefficient and thus a low oxygen ion conduction should be expected in such compounds.

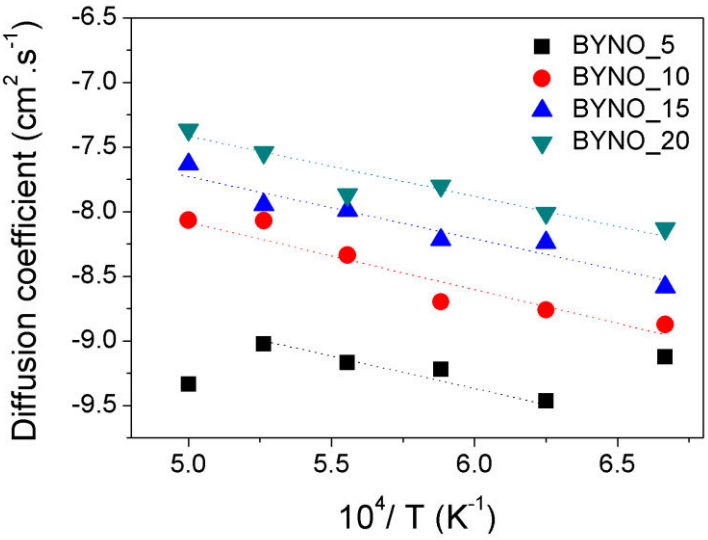

Figure 4.5.2 Diffusion coefficients as extracted from MD simulations for compositions $Ba_2Y_{1+x}Nb_{1-x}O_{6-x}$ with x = 0.05, 0.10, 0.15, 0.20

In order to understand better the origin of these bad diffusion coefficients, we used the same Molecular dynamics simulations to give insight on the atomic scale mechanisms. On the following graph (**Figure 4.5.3**), we present the environment of Yttrium, Niobium and Yttrium dopant atoms for the highest doped compound (BYNO_20) at a temperature of 1500 K.

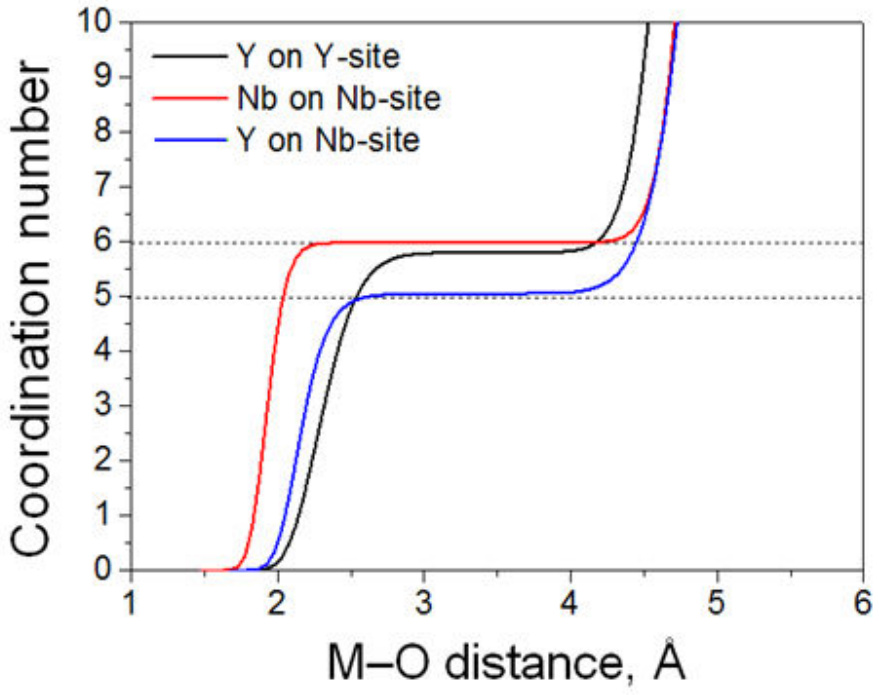

Figure 4.5.3 Coordination number of Y atoms on Y-site, of Nb atoms on Nb-site and of Y atoms on Nb-site for the BYNO_20 compound at 1500 K

This previous graph clearly shows that the environment of the different cations on B site differ strongly depending on cation/site nature. Niobium atoms show a 6-fold environment, Yttrium atoms on Y-site show a coordination number slightly below 6 in agreement with the total oxygen content (5.8 oxygen atoms per formula in BYNO_20 instead of 6 in the undoped compound), while yttrium atoms on Nb-site have a 5-fold environment. This later result is particularly interesting. It indicates that the oxygen vacancies created by Yttrium doping almost always locate on a site close to this dopant (6 sites possible). While the doping level is low, a long range diffusion would suppose that oxygen vacancies also locate close to Niobium atoms which does not seem to be possible in this material. Thus, the only way for oxygen vacancies to participate to long range ion diffusion is to percolate from a site close to a Y dopant to another site close to a Y dopant. This of course implies that the doping level is not low.

The main result from our simulation was thus to confirm that oxygen diffusion is low in Y-doped Ba_2YNbO_6 compounds, this being due to the fact that Yttrium dopant located on Nb-sites act as strong trap for oxygen vacancies. This strong trapping effect can be related to the great difference of

size between Niobium atoms (r_{Nb5+} = 0.64 Å) and Yttrium dopants atoms (r_{Y3+} = 0.90 Å). The location of an oxygen vacancy close to the Yttrium dopant atom allows relaxing slightly the induced stress. This simulation also suggests that a significant improvement would be to dope niobium sites with trivalent atoms with radius close to the one of Niobium. Gallium (r_{Ga3+}= 0.62 Å) might be a good candidate.

4.6 Transmission Electron Microscopy (TEM)

4.6.1 Objective

Basing on the previous results of molecular dynamics, it was particularly interesting to try to explore the local chemistry of doped BYNO compounds with Transmission Electron Microscopy (TEM). The main purpose of this study was to confirm the scenario proposed in paragraph 4.5: Yttrium dopants go on Nb site and the induced oxygen vacancies tend to locate around these dopant atoms *i.e.* are not free to move at long range in the material (only at short range around Y dopant atoms).

To achieve this, the first idea was to be able to observe the ordered structure in both undoped and doped compounds, taking benefit from the possible high resolution EDX-based element mapping from the available microscope (see below). Second, once this ordered structure could be observed in undoped and doped compounds, we wanted to have precise information of the environment of yttrium atoms located on Nb-sites (observable in Nb columns in ordered compounds). This information could be obtained by High resolution EELS where the environment of a Yttrium in 5-fold or 6-fold environment could be distinguished.

4.6.2 Description of the experiment

4.6.2.1 Principle of the Focus Ion Beam

The focused ion beam (Focused Ion Beam, FIB) is a thinning technique used primarily for creating cuts (cross-sections) of a sample for submission to a method of imaging by electron microscopy (SEM or TEM). This technique uses an ion beam with an energy of about 30 keV, focused on the sample surface. The interaction of these ions with the material causes the movement of atoms (or ions). The successive collisions between the atoms of the material eventually expel a portion of the surface of it, it is called sputtering. To prepare the FIB cuts, the ion gun is coupled with a conventional electron gun (type SEM). In addition, a micromanipulator and a micro-injector used to weld and transport the sample very precisely and for example installing it on a microscope in transmission grid. The energy of the incident ions is a particularly important parameter since if the energy is too low, no material spray (or at least the yield will be poor); but conversely if energy is too large, the ion only foothold in the material.

4.6.2.2 FIB preparation for TEM

Several steps are needed to obtain a thin section from a solid sample for TEM observation (**Figure 4.6.1**). First of all, platinum is deposited on the sample surface (**Figure 4.6.1, a**). This sacrificial plate serves to protect the sample during cutting, since the implanting gallium ions focused on the first few nanometers in depth. Thus, only the platinum layer will be polluted by gallium. Then the material is sprayed from both sides to release a thin lamella (**Figure 4.6.1, b**). This strip is then welded to the micro-manipulator (**Figure 4.6.1, c**) and then installed on the transmission grid (**Figure 4.6.1, d**) where the final thinning takes place until the sample becomes transparent to electrons. FIB lamella is represented on the **Figure 4.6.2.**

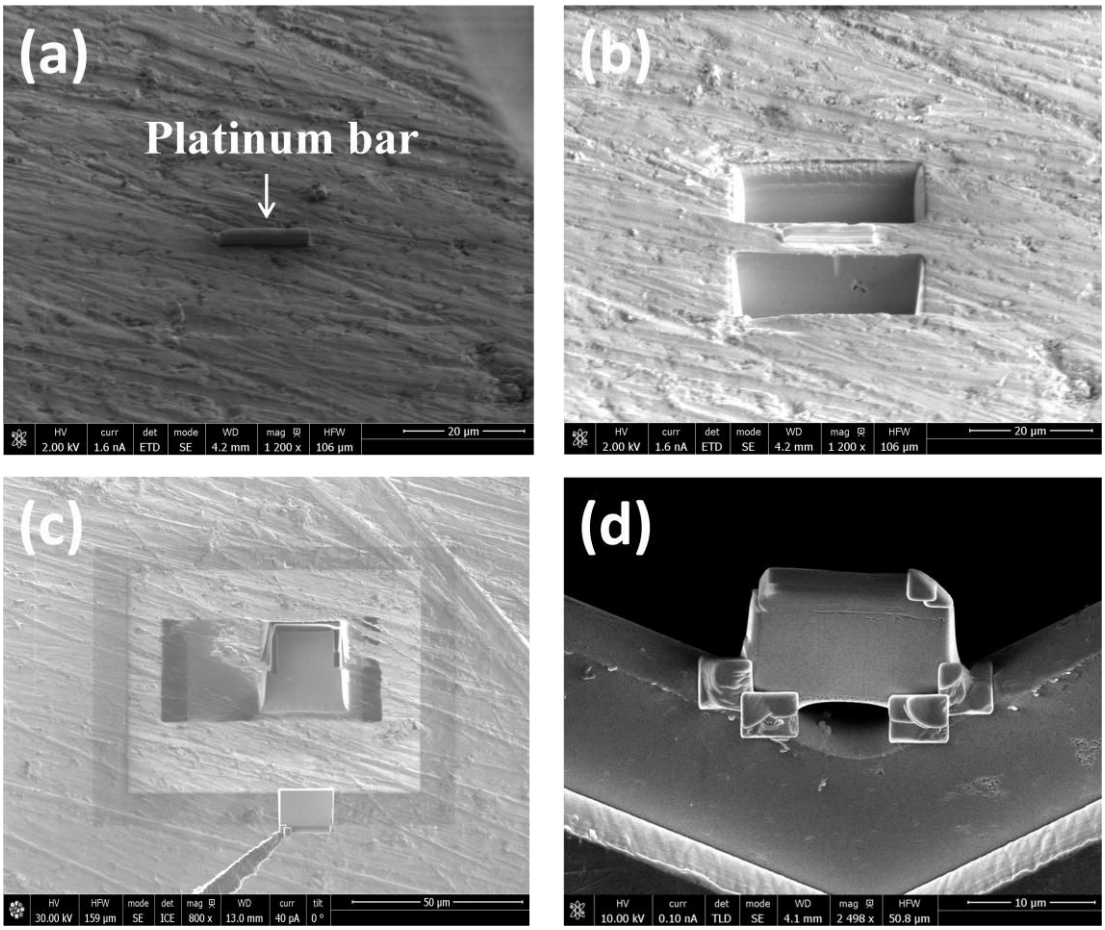

Figure 4.6.1 Different stages of a FIB cutting

4.6.3 Results

Analyzes were performed with an electron microscope equipped with a spherical aberration corrector Cs to achieve atomic resolution STEM method (~ 0.5 Å) and an HAADF detector (High Angle Annular Dark Field) giving a chemical contrast proportional to the atomic number Z (~ of $Z^{1.5}$ to $Z^{1.8}$) [77, 78]. The advantage of this technique is a possibility to make an image with the certainty arrangement of heavy atoms. Thus, the elements Ba, Nb and Y are brighter than oxygen (which is not

heavy enough to produce a contrast, so it is not clearly visible). Therefore, the local chemical and structural information given by this technique will help us better understand the cationic order in the layers of material. STEM analyzes were performed on a cutting lamella which was obtained from the pellet of $Ba_2Y_{1.1}Nb_{0.9}O_{6-\delta}$ material. This lamella has a uniform thickness of about 80 nm (see **Figure 4.6.2**).

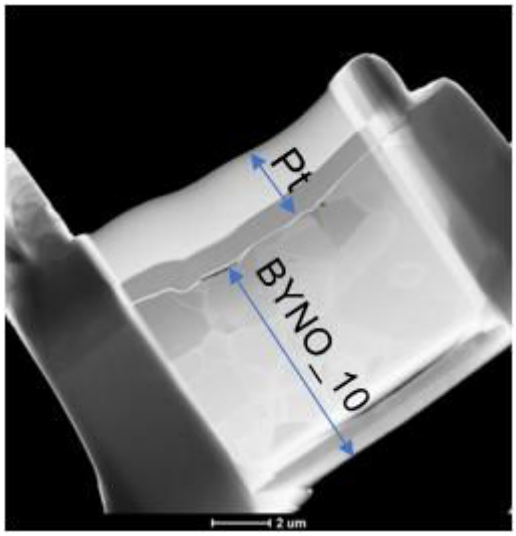

Figure 4.6.2 STEM image of FIB lamella of BYNO_10 material

Images HRSTEM-HAADF of $Ba_2Y_{1.1}Nb_{0.9}O_{6-\delta}$ compound, following the directions [111], [001] and [110], and also the Fast Fourier Transform (FFT) are shown in **Figure 4.6.3**. The arrangement of the atomic planes of BYNO_10 material shown next to each image to properly visualized following cation order for each crystallographic orientation (**Figure 4.6.3** c, f, i.) [46]. Following the zone axis [111], it was not possible to identify the cationic order of elements because the Y is superimposed by Ba and Nb. On the STEM image, there is a homogeneity of the spots intensities of atomic columns (**Figure 4.6.3** , a). Similarly, for the zone axis [001], the Y is superimposed with Nb. Only Ba columns can be identified because they are more intense (Ba is heavier than the Y and Nb). Ba columns are also easily observed along the zone axis [110] because they are more intense compare to the columns of Y and Nb. The representative scheme of the unit cell shows the presence of a periodicity between the Y and Nb in this direction. This periodicity manifests as superstructure reflections which are clearly seen on the FFT [110] (reflections of low intensities indicated by the yellow arrows, **Figure 4.6.3** h). The presence of superstructure reflections also shows that BYNO material structure is described in a right space group $Fm\bar{3}m$ [40]. On the HRSTEM images, the intensities of the columns of Y and Nb are very similar that's why it is difficult to distinguish them. To check the cationic order, we have performed a chemical analysis at the atomic scale. Unfortunately, the quality of chemical mapping obtained by the spectrometer EDS-super X was bad. Indeed, inadequate thickness of the FIB lamella induced a high background on the chemical analyzes.

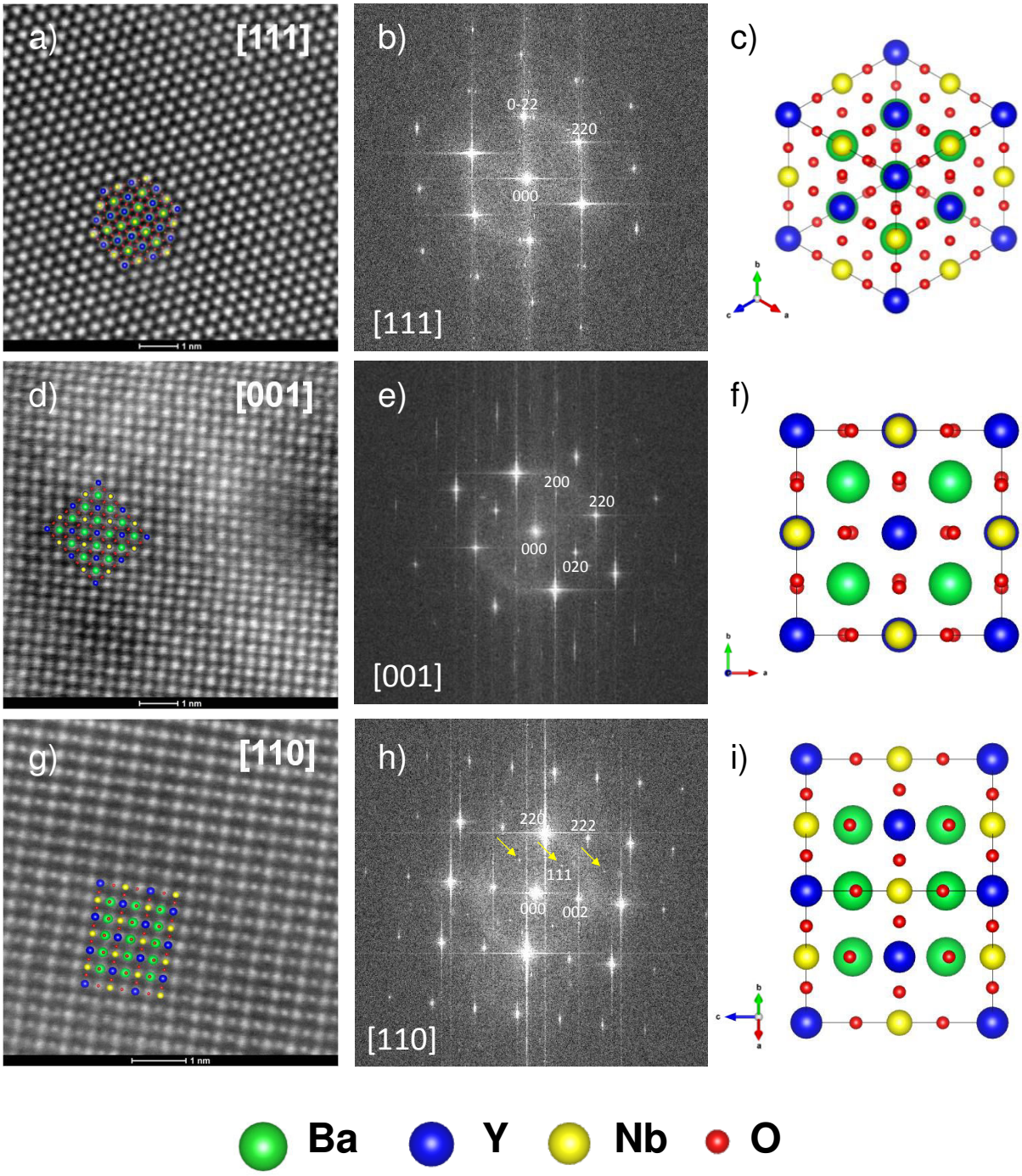

Figure 4.6.3 HRSTEM-HAADF images of BYNO_10 compound at different zone axis:
(a) [111], (d) [001] and (g) [110].
(b), (e) and h) Fast Fourier Transform of HRSTEM pictures of (a), (d) and (g) respectively.
(c), (f) and(i): schematic representations of the unit cell along the zone axis BYNO_10: [111], [001] and [110] respectively. The colors green, blue, yellow and red correspond to atoms of Ba, Y, Nb and O, respectively

Some simulations were also carried out. The results show a slight difference between the intensities of Nb and Y columns, confirming the possibility to reveal the existence of a cationic order within BYN material (**Figure 4.6.4**). This study will be followed by high resolution EELS analyzes to verify the results of the numerical simulation. In this case, the sample will be prepared by FIB so as to obtain a maximum thickness of 20-30 nm.

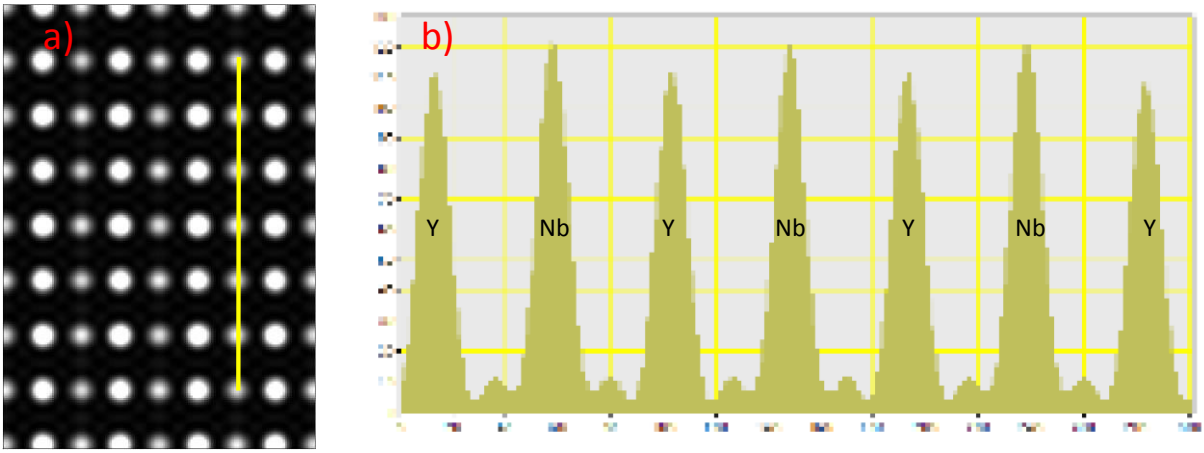

Figure 4.6.4 (a) simulating the HRSTEM picture following the zone axis [110], (b) intensities of Y and Nb according to the profile line drawn in (a)

4.7 Conclusion

We have successfully synthesized $Ba_2Y_{1+x}Nb_{1-x}O_{6-\delta}$ series dense compounds by freeze-drying method. All materials present a cubic perovskite structure with cell parameters following the evolution of mean radius on B-site. Electron diffraction patterns obtained from TEM confirm as well a cubic structure of double perovskite (space group $Fm\bar{3}m$). Atomic columns of Ba and (Y, Nb) are easily distinguished following the zone axis [110] but the degree of ordering is nevertheless difficult to evaluate because of the thickness of lamella made by FIB is too high. There is thus further need for structural and chemical analysis at the atomic scale using EDS and EELS techniques. All doped compounds are oxygen ion conducting at high temperature and present an electronic-like type of behavior under hydrogen. The best conduction properties are observed for higher yttrium contents and it reach 2.5×10^{-4} $S.cm^{-1}$ at 800 °C. **Figure 4.4.5** presents a comparison of conductivity values of different materials with double perovskite structure as reported in the literature. It could be noticed that BYNO_20 has quite similar conductivity as Sr_2LuNbO_6 [62].

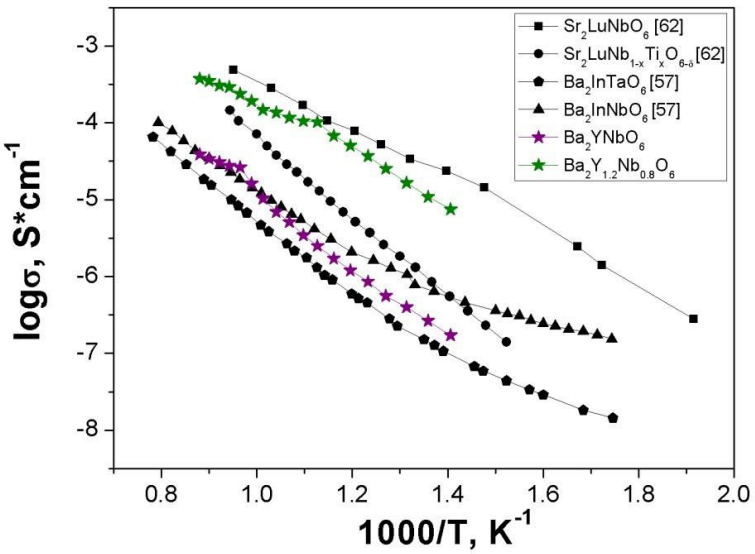

Figure 4.4.5 Total conductivities for different double perovskites in dry Ar+H_2 (Sr_2LuNbO_6, $Sr_2LuNb_{1-x}Ti_xO_{6-\delta}$, Ba_2YNbO_6, $Ba_2Y_{1.2}Nb_{0.8}O_{6-\delta}$) and in dry air ($Ba_2InNbO_6$, Ba_2InTaO_6)

To conclude this study, we can say that the proton conduction properties were slightly improved with the partial substitution of niobium by yttrium. The stability of $Ba_2Y_{1+x}Nb_{1-x}O_{6-\delta}$ compounds was investigated under different atmospheres and conditions. Under CO_2 and Ar+H_2 mixture the Y-doped compounds get partially reduced. After treatment in boiling water for after 10 h, could be noticed the main phase contains a small amount of $BaCO_3$.

The main result from MD simulations was thus to confirm that oxygen diffusion is low in Y-doped Ba_2YNbO_6 compounds, this being due to the fact that Yttrium dopant located on Nb-sites act as strong trap for oxygen vacancies. This strong trapping effect can be related to the great difference of size between Niobium atoms (r_{Nb5+} = 0.64 Å) and Yttrium dopants atoms (r_{Y3+} = 0.90 Å).

References:

[1] A.S. Bhalla, R. Guo, R. Roy, *Mater. Res. Innov.*, **2000**, 4, 3.

[2] W.E. Pickett, D.J.Singh, *Phys. Rev.,* **1996**, 53, 1146.

[3] R.J. Cava, B. Batlogg, J.J. Krajewski, R. Farrow, L.W. Rupp, A.E. White, *Nature*, **1988**, 332, 814.

[4] J.B. Goodenough, J.M. Longo, *Berlin, Springer*, **1970**, 4, 126.

[5] S.-W. Cheong, M. Mostovoy, *Nat. Mater.,* **2007**, 6, 13.

[6] P.D. Battle, T.C. Gibb, C.W. Jones, F. Studer, *J. Solid State Chem.*, **1989**, 78, 281.

[7] C.R. Wiebe, J.E. Greedan, P.P. Kyriakou, G.M. Luke, J.S. Gardner, A. Fukaya, *Phys. Rev.*, **2003**, 68, 134-410.

[8] M. Li, M.J. Pietrowski, R.A. De Souza, H. Zhang, I.M. Reaney, S.N. Cook, Nat. Mater., **2014**, 13-31.

[9] H. Tanaka, M. Misono, *Solid State Mater.*, **2001**, 5, 381.

[10] Y.-H. Huang, R.I. Dass, Z.-L. Xing, J.B. Goodenough, *Science,* **2006**, 312, 254.

[11] M. A. Green, A. Ho-Baillie, H.J. Snaith., *Nat. Photonics*, **2014**, 8, 506.

[12] C. J. Howard, B. J. Kennedy, B. C. Chakoumakos*, J. Phys.-Cond. Matter*, **2000**, 12(4), 349– 365.

[13] E.I. Zabal, Crystal structure and phase transition studies in perovskite-type oxides using powder-diffraction techniques and symmetry-mode analysis, **2012**, Leioa.

[14] W. G. Ralph, Wyckoff. Crystal structures, volume 2, *John Wiley & Sons, 2nd edition*, **1964.**

[15] V.M. Goldschmidt, *Naturwissenschaften,* **1926**, 14, 477.

[16] I. H. Robert, PhD thesis, **1997**, Bristol.

[17] C.B. Jurca, Synthese et caracterisation de perovskites doubles magnetoresistives derivees de Sr_2FeMoO_6, **2004**, Paris.

[18] J. L. Garcia-Munoz, J. Rodriguezcarvajal, P. Lacorre, J. B. Torrance, *Phys. Rev. Cond. Matter*, **1992**, 46(8), 4414–4425.

[19] R. J. Roy, *J. Amer. Ceram. Soc*., **1954**, 37(12), 581-588.

[20] E. G. Steward, H. P. Rooksby, *Acta Crystallogr*., **1951**, 4, 503-507.

[21] F. Galasso, R. J. Ward, L. Katz, *J. Amer. Ceram. Soc*., **1959**, 81, 820-823.

[22] E. J. Fresia, R. J. Ward, L. Katz, *J. Amer. Ceram. Soc*., **1959**, 81, 4783-4785.

[23] T. Nakamura, J.-H. Choy, *J. Solid State Chem*., **1977**, 20, 233-244.

[24] G. J. Blasse, *J. Inorg. Nucl. Chem*., **1965**, 27, 993-1003.

[25] N. Ramadass, J. Gopalakrishnan, M. V. C. Sastri, *J. Inorg. Nucl. Chem*., **1978**, 40, 1453.

[26] V. S. Filip'ev, E. G. Fesenko, Soviet Physics-Crystallography, **1966**, 10(3), 243-247.

[27] C.P. Khattak, D.E.Cox, F.F.Y. Wang, *J. Solid State Chem.,* **1976**, 17, 323.

[28] P. J. Saines, B.J. Kennedy, *J. Solid State Chem.,* **2008**, 181, 298.

[29] Y. Yasukawa, J. Linden, T. S. Chan, R. S. Liu, H. Yamauchi, M. J. Karppinen, *J. Solid State Chem.,***2004***,* 177, 2655.

[30] R.B. Macquart, B.J. Kennedy, *Chem. Mater.,* **2005**, 17, 1905.

[31] M. T. Anderson, K. B. Greenwood, G. A. Taylor, K. R. Poeppelmeier, *Prog. Solis St. Chem.,* **1993**, 22, 197-233.

[32] E. J. Cussen, J. F. Vente, P. D. Battle, T. C. Gibb, *J. Mater. Chem,* **1997**, 7, 459-463.

[33] W. Barnes, M. W. Lufaso, P. Woodward, *Acta Cryst.,* **2006**, B 62, 384-396.

[34] P. M. Woodward, PhD thesis, **1996**, Oregon State University.

[35] A. M. Glazer, Acta Cryst., **1972**, 28, 3384-3392.

[36] P. M. Woodward, *Acta Cryst.,* **1997**, 53, 32-43.

[37] C. J. Howard, H. T. Stokes, *Acta Cryst.,* **1998**, 54, 782-789.

[38] H. Brixner, *J. Inorg. Nucl. Chem.*, **1960**, 15, 352.

[39] V.S. Filip'ev, E.G. Fesenko, *Kristallografiya*, **1967**, 6, 770.

[40] F. Galasso, W. Darb, *J. Phys.Chem.,* **1962,** 66, 131-132.

[41] U. von Wittmann, G. Rauser, S. Kemmler-Sack, Z. *Anorg. Allg. Chem.*, **1981**, 482, 143.

[42] A.A. Evdokimov, N.F. Men'shenina, *Russ. J. Inorg. Chem.*, **1982**, 27, 1208.

[43] K. Henmi, Y. Hinatsu, N.M. Masaki, *J. Solid State Chem.*, **1999**, 148, 353.

[44] V. Ting, Y. Liu, R.L. Withers, E. Krausz, *J. Solid State Chem.*, **2004**, 177, 979–986.

[45] V. Ting, Y. Liu, R.L. Withers, L. Nore´n, M. James, J.D. Fitz Gerald, *J. Solid State Chem.*, **2006**, 179, 551–562.

[46] W.T. Fu, D.J.W. IJdo, *J. Solid State Chem.*, **2006**, 179, 1022–1028.

[47] P. W. Barnes, M. W. Lufaso, P. M. Woodward, *Acta Cryst.*, **2006,** B62, 384–396.

[48] P. J. Saines, J. R. Spencer, B. J. Kennedy, M. Avdeev, *J. Solid State Chem.*, **2007**, 180, 2991–3000.

[49] P. J. Saines, J. R. Spencer, B. J. Kennedy, M. Avdeev, *J. Solid State Chem.*, **2007**, 180, 3001–3007.

[50] R. Zurmuhlen, E. Colla, D.C. Dube, J. Petzelt, I. Reaney, A. Bell, N. Setter, *J. Appl. Phys.,* **1994**, 76, 5864–5873.

[51] C. Bharti, T.P. Sinha , *Physica B*, **2011**, 406, 624–627.

[52] C. Bharti, T.P. Sinha , *Physica B*, **2011**, 406, 1827–1832.

[53] C. Bharti, T.P. Sinha , *Solid State Science*, **2010**, 12, 498–502.

[54] A. Dutta, T.P. Sinha, D. Das, *J. Magnetism and Magnetic Mater.*, **2014**, 360, 211–216.

[55] K. Zheng, K. Swierczek, W. Zajac, A. Klimkowicz, *Solid State Ionics*, **2014**, 257, 9-16.

[56] K. Prasad, Priyanka, K. P. Chandra, A.R. Kulkarni, *J. Non-crystal. Sol.*, **2011**, 1209–1217.

[57] I.V. Aliabysheva, PhD thesis, Transport and thermal properties of mono- and hetero-based composition $Ba_2In_2O_5$, **2013**, UrFU, Russia.

[58] A. Dutta, C. Bharti, T.P. Sinha, *Physica B*, **2008**, 403, 3389–3393.

[59] A. Dutta , T.P. Sinha, *Physica*, **2010**, B 405, 1475–1479.

[60] M. M. Hoque, A. Dutta, S. Kumar, T.P. Sinha, *Physica,* **2012**, B 407, 3740–3748.

[61] K. Prasad, S. Bhagat , Priyanka, K. AmarNath, K.P. Chandra, A.R. Kulkarni, *Physica B*, **2010**, 405, 3564–3571.

[62] Z. Maupoey, M. T. Azcondo, J. C. Pérez-Flores, C. Ritter, K. Boulahya, U. Amadora, F. García-Alvarado, *Dalton Trans.,* **2014**, 43, 14099–14108.

[63] D. Hassan, S. Janes, R. Clasen, *J. Eur. Ceram. Soc*., **2003**, 23, 221.

[64] S.S. Bhella, V. Thangadurai, *J. Power Sources,* **2009**, 186, 311.

[65] H.G. Bohn, T. Schober, T. Mono, W. Schilling, *Solid State Ionics*, **1999**, 117, 219-228.

[66] D.J.D. Corcoran, J.T.S. Irvine, *Solid State Ionics*, **2001,** 145, 307.

[67] H.D.A.L. Viana, J.T.S. Irvine, *Solid State Ionics*, **2007,** 178, 717.

[68] K. Oikawa, T. Kamiyama, S. Ikeda, T. Shishido, S. Yamaguchi, *Solid State Ionics*, **2002,** 154–155, 641.

[69] A.S. Nowick, Y. Du, *Solid State Ionics*, **1995,** 77, 137.

[70] S. Valkenberg, H.G. Bohn, W. Schilling, *Solid State Ionics*, **1997,** 97, 511.

[71] H.d.A.L. Viana, J.T.S. Irvine, *J. Mater. Chem.***, 2010,** 20, 8506.

[72] S. Wang, F. Zhao, L. Zhang, K. Brinkman, F. Chen, *J. Pow. Sour.,* **2011**, 196, 7917–7923.

[73] http://www.ccp5.ac.uk/DL_POLY_CLASSIC/.

[74] W. Smith, T. R. Forester, I. T. Todorov, The DL_POLY Classic User Manual, Daresbury Laboratory, United Kingdom, **2011**.

[75] G.V. Lewis, C.R.A. Catlow, *J. Phys. C: Solid St. Phys.,* **1985**, 18, 1149.

[76] H. Donnerberg, M. Exner, *Phys. Review B*, **1994,** 49, 3746–3754.

[77] S. J. Pennycook, *Ultramicroscopy,* **1989**, 30, 58-69.

[78] E. M. James, N. D. Browning, *Ultramicroscopy,* **1999**, 78, 125-139.

Chapter 5 Synthesis, structure and electrical properties of BZY15

5.1 Introduction

5.1.1 Structure of Barium Zirconate

Barium zirconate, $BaZrO_3$, is one of the most studied compounds with the perovskite-related structure. Because of its very high melting point (2920 °C) and low chemical reactivity with corrosive compounds, $BaZrO_3$ is an interesting material for the refractory industry and a good candidate for manufacturing high temperature superconductors [1-3]. In addition, $BaZrO_3$ has excellent thermal stability and resistance due to a low coefficient of thermal expansion (0.87×10^{-5} / °C between 25 and 1080 °C) [4, 5]. These physical properties make $BaZrO_3$ an ideal candidate for applications as crucibles when conducting reactions in presence of corrosive oxide melts, substrates for thin films deposition, and for thermal barrier coatings in aerospace industries. In addition, barium zirconate is a potential material as humidity sensor [5]. When doped, it has attracted many researchers as an electrolyte of intermediate temperature operating Solid Oxide Fuel Cells (IT-SOFC), because it shows the highest proton conductivity among the perovskite type proton conductors which have high chemical stability in CO_2 containing atmospheres [6, 7].

Yttrium is regarded as the most suitable dopant for $BaZrO_3$ to obtain the highest proton conductivity (with yttrium doping content between 5 % and 20 % of the B-site), presumably as a result of its good ionic radius match to Zr. Much research effort has been devoted to achieving BZY with high stability, conductivity, and sinterability, by choosing different chemical and physical preparation methods, while the fundamental structure-property relationships have been rather overlooked in the last years [8-15]. Unfortunately, these compounds require very high sintering temperature to achieve densities of over 90%: for example, Duval *et al.* [15] obtained 91 % dense BZY10 after 24 h at 1720 °C, Iguchi *et al.* [17] reported a densification between 96 and 98 % while sintering BZY5 at 1700 to 1800 °C and Katahira *et al.* [6] obtained BZY10 with density exceeding 95 % after 5 h at 1800 °C. One should also be aware that barium evaporation can occur during sintering at high temperature, with a detrimental effect on the conductivity [18]. Yttrium doped barium zirconate, $BaZr_{1-x}Y_xO_{3-\delta}$, is commonly accepted as a single-phase, cubic perovskite (with space group $Pm\bar{3}m$), similar to the undoped composition, see **Figure 5.1**. However, Kreuer has reported that at the intermediate Y content and 1700 °C sintering temperature, barium zirconate adopts a tetragonal structure, reverting to a cubic phase at higher Y doping (25 mol %) [12].

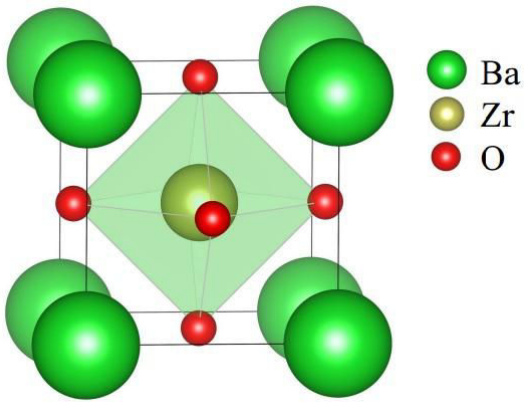

Figure 5.1 A unit cell of the ideal $BaZrO_3$ perovskite crystal structure [16]

In an acceptor-doped barium zirconate, one possibility is the replacement of Zr^{4+} with Y^{3+} ions. Acceptor doping with trivalent cations onto the Zr^{4+} site generates oxygen vacancies as charge compensating defects. With a significant dopant concentration, extrinsic oxygen vacancy defects are the dominant species. Proton conduction then can occur via the incorporation of protonic defects as the result of the B-site acceptor doping. In Kröger-Vink notation, this can be written as:

$$Zr_{Zr}^{x} + O_O^x + Y_2O_3 \rightarrow 2Y_{Zr}^{'} + V_O^{\cdot\cdot} + 2ZrO_2 \qquad (5.1)$$

The incorporation of water into the perovskite structure is achieved by treatment in water vapour, in which the oxygen vacancies are replaced by protonic defects (in the form of hydroxyl ions) as shown by the following equation [11]:

$$H_2O_{(g)} + V_O^{\cdot\cdot} + O_O^x = 2(OH_O^{\cdot}) \qquad (5.2)$$

Protons are not part of the nominal structure, but are present as defects in equilibrium with ambient hydrogen or water vapor. Due to the negative enthalpy and entropy of hydration [12], higher temperatures result in a reversible loss of protons.

5.1.1 Chemical Stability

Stability problems in atmospheres containing water (H_2O) and carbon dioxide (CO_2) generally arise due to the typical thermodynamic instability of Ba containing oxides towards these gases. **Figure 5.2** shows the calculation results using a thermodynamic database [19] for the possible reaction:

$$BaZrO_3 + H_2O = Ba(OH)_2 + ZrO_2 \qquad (5.3)$$

It can be observed that the Gibbs free energy (ΔG) for the reaction is above zero for the whole temperature range from room temperature to 1000 °C, suggesting that $BaZrO_3$ is thermodynamically stable towards H_2O. It should be emphasized that good stability over the whole temperature range (not only at the cell working temperatures) is important for practical applications since H_2O may attack the

electrolyte at low temperatures during cell thermal cycles of the cooling and heating operations [20]. As it was shown by E. Traversa *et al.* [20] the BZY electrolyte film has a single phase both before and after the treatments in boiling water or steam at 600 °C, suggesting that the as-prepared BZY electrolyte shows a good chemical stability against H_2O. The surface morphologies shown in **Figure 5.3** further confirm the excellent chemical stability of BZY as no damage can be observed on the BZY electrolyte surfaces after these treatments.

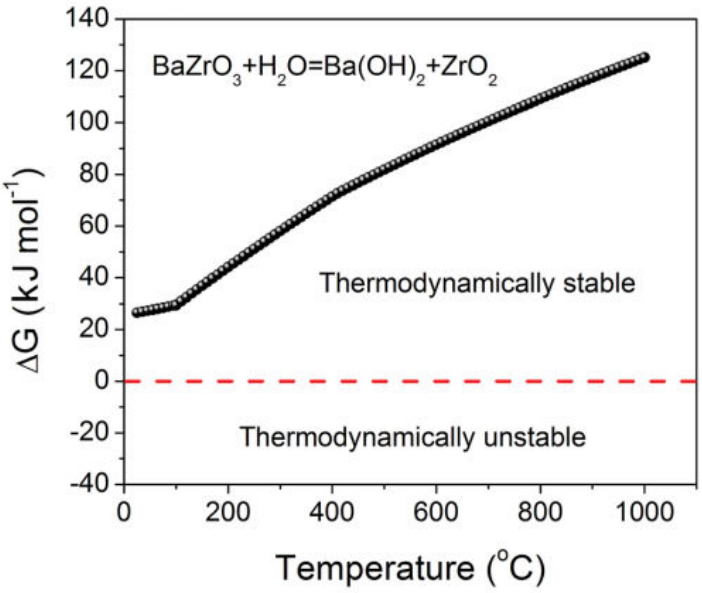

Figure 5.2 Calculated Gibbs free energy (ΔG) for the possible reaction between $BaZrO_3$ and H_2O as a function of temperature. H_2O is considered as being in the liquid phase below 100 °C and gaseous phase above 100 °C [20]

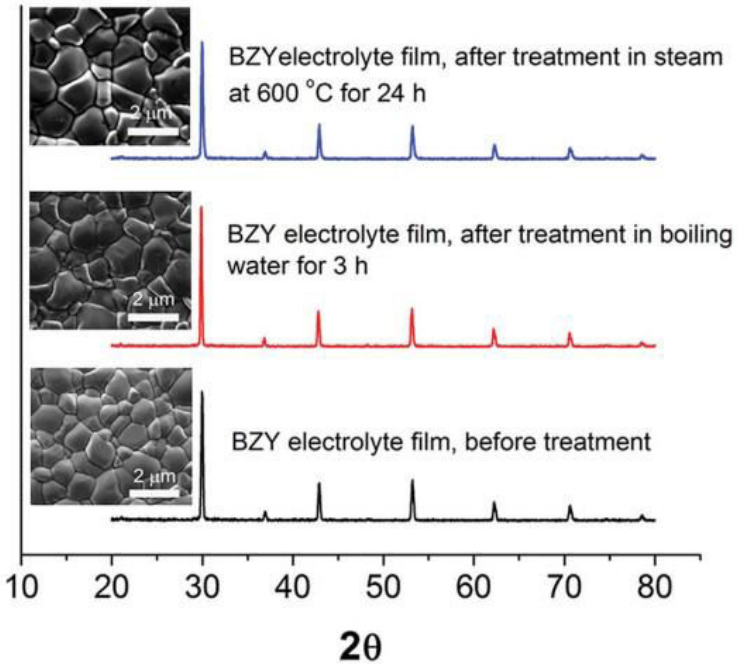

Figure 5.3 XRD patterns and SEM micrographs of the BZY electrolyte surfaces before and after the treatments in boiling water for 3 h and in steam at 600 °C for 24 h [20]

5.1.2 Conductivity properties of Doped Barium Zirconate

The literature data about the conductivity of Y-substituted barium zirconate vary by more than 1 order of magnitude [9, 21-23]. This can be explained by differences in the synthesis and sintering processes (shape, size of the grains and grain boundaries), the evaporation of barium during sintering (leading to secondary phases or distortions of the cell) and/or the electrodes used for conductivity measurements: at high temperature, Pt electrodes exhibit electrode resistance effects which can be mistakenly ascribed to the electrolyte. According to Equations 5.1 and 5.2, it is clear that the concentration of protons depends on the yttrium content. Discrepancies in the conductivity of barium zirconate are present in literature and have been carefully summarized by Babilo *et al*. [24], see Table 5.1.

The early misinterpretation of the behavior of doped barium zirconate originates from the high refractory nature of this material, which results in samples with small grain sizes and high total grain boundary area. As a consequence, the resistive grain boundaries produce a material with an overall low conductivity, and, in the absence of low temperature *ac* impedance measurements (< 200 °C), the individual bulk and grain boundary contributions to conductivity were not resolved in the early literature. Barium zirconates exhibit lower conductivity than cerates do, although the bulk conductivity of barium zirconate is higher than the one of cerate [24-28]. It follows

that the difference is due to the grain boundary conductivity which is much lower for zirconate than for cerate. Many explanations have been proposed for this effect:

-inevitable lattice distortion at intergranular boundaries which affects the mobility of protonic defects as well as structures arising at the boundaries with small point contact between grains [27],

-evaporation of barium [24],

-incorporation of yttrium in the A-site of the perovskite [24],

-nonstoichiometry [24],

-second phases [28].

Table 5.1 Conductivity of doped $BaZrO_3$ as reported in the literature [24]

Composition	**Sintering conditions**	**Conductivity at 600°C (bulk or total), S/cm**	**Conductivity measurement conditions**	**Ref.**
$BaZr_{0.95}Y_{0.05}O_{3-x}$	1800 °C/ 20 h	1×10^{-2}	Wet Ar + O_2 (pH_2O = 0.023 atm)	17
$BaZr_{0.9}Y_{0.1}O_{3-x}$	1800 °C/ 5 h	1.1×10^{-3} (total)	Wet H_2 (pH_2O = 0.017 atm)	6
$BaZr_{0.9}Y_{0.1}O_{3-x}$	1715 °C/ 30 h	3×10^{-3} (bulk)	Wet air	23
$BaZr_{0.93}Y_{0.07}O_{3-x}$	1700 °C/ 1 h	5×10^{-4} (total)	Wet air (room temperature water)	14
$BaCe_{0.9}Y_{0.1}O_{3-x}$	1700 °C/ 10 h	1.1×10^{-2} (total)	Wet H_2 (pH_2O = 0.017 atm)	6
$BaZr_{0.85}Y_{0.15}O_{3-x}$	1700 °C/ 20 h	1.6×10^{-3} (total)	Wet N_2 (pH_2O = 0.023 atm)	7
$BaZr_{0.93}Y_{0.07}O_{3-x}$	1650 °C/ 10 h	3.8×10^{-3} (total) 4.2×10^{-3} (total)	Wet N_2 (pH_2O = 0.023 atm) Wet air (pH_2O = 0.025 atm)	39
$BaZr_{0.9}Y_{0.1}O_{3-x}$	1400 °C/ 10 h	1.3×10^{-6} (bulk)	Wet N_2 (room temperature water)	9
$BaZr_{0.9}Y_{0.1}O_{3-x}$	1400 °C	2.8×10^{-4} (bulk)	Wet Ar - 5%H_2 (pH_2O = 0.03 atm)	40
$BaZr_{0.95}Y_{0.05}O_{3-x}$	1350-1400 °C/ 20-40 h	1.8×10^{-6} (bulk)	Wet N_2 (pH_2O = 0.031 atm)	38

In the $BaZrO_3$ system, many researchers have mentioned the origins of low $\sigma_{sp.g.b.}$ in the literature. Kreuer insisted that symmetry reduction in grain boundaries led to a decrease of proton mobility and concentration [7]. Many researchers discussed the decrease of effective dopant concentration caused by Ba evaporation and yttrium incorporation. As other origins, low grain boundary conductivity caused by impurity phases of SiO_2 at grain boundaries were frequency reported

in oxygen ionic conductors [29-32]. Although those origins seemed to affect grain boundary conductivity more or less, contributions of those origins have been not clear yet in the $BaZrO_3$ system.

5.2 Objectives of the study

The main purpose of our synthesis of BZY15 was to obtain dense materials for atomic scale characterizations of proton conductors:

- Ion exchange depth Profile: the oblation of dense samples could allow using this material as a standard for calibration proton exchange measurements.

- Atomic Probe Tomography: this method allows obtaining an atomic scale distribution of the elements. In our case, it could be applied on nanostructured ceramics to locate potential Y/Zr segregation or Ba depletion at grain boundary, this to explain the specificity of BZY15 conductivity.

Unfortunately, for now, none of the two techniques has given the expected results, so we will not present them here. Due to the failure of these two advance characterizations, we decided to present here:

- An extended characterization of 15% Y-substituted barium zirconate synthesised by the modified citrate-EDTA complexing method;

- The study of the electrical conductivity in the temperature range 300 - 900 °C in different atmospheres;

- Explore alternative densification procedures with the use of sintering aids. Characterize the effects of the sintering aid on sintering, microstructure and electrical properties.

5.3 Structural and microstructural properties of BZY15

$BaZr_{0.85}Y_{0.15}O_{3-\delta}$ (BZY15) has been synthesized by a modified citrate-EDTA complexing method (described in the Chapter 2). The samples were calcinated in ambient atmosphere at 1000 °C for 5 h to yield well-crystallized BZY15 powders. Synthesized barium zirconate fine powders were milled using an agate mortar. The powders were axially pressed (2 MPa) into a pellet. The pre-formed pellets were then isostatically pressed (750 MPa). The pellets were surrounded with a powder mixture of already sintered Y-substituted barium zirconate powder mixed with 10 % of $BaCO_3$, as it was suggested by Babilo *et al.* [24] (**Figure 5.2.1**) and then sintered at 1600 °C for 24 hours.

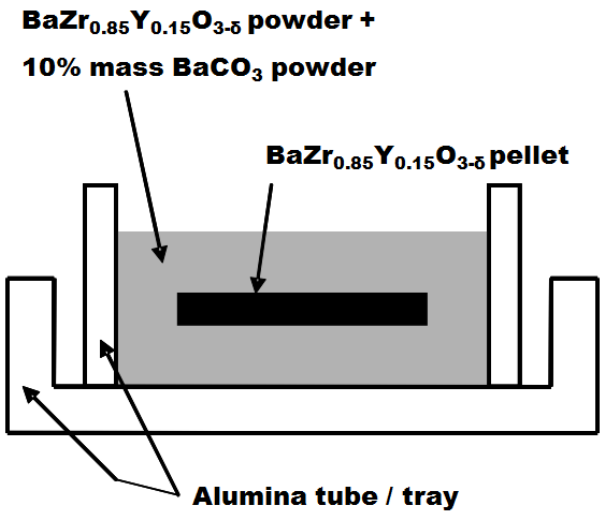

Figure 5.2.1 Schematic diagram of the sintering configuration: BYZ15 green pellet covered with a powder mixture of BYZ15 and $BaCO_3$ (about 10 mass %) [24]

As seen in **Figure 5.2.2**, all the peaks in the XRD could be indexed for BZO and there is no extra XRD peak is found. **Figure 5.2.2** shows that the XRD pattern of BZY15 consists of strong peaks which are characteristics of a cubic perovskite ABO_3, where A=Ba is the large ion (1.49 Å) suitable to the 12-coordinated cube-octahedral sites and B=Zr is the smaller ion (0.86 Å) suitable to the 6-coordinated octahedral site. No evidence for a distortion from the cubic symmetry is observed in the XRD pattern. F. Iguchi *et al.* [32] and Duval *et al.* [33] found a cubic lattice parameter, which is comparable (or slightly lower for [33] and slightly higher for [32]) than the results from this work, for substituted barium zirconate with an 15 % Y content. Above 10 mol. % of Y, Kreuer *et al.* [12] found an increasing tetragonal distortion, whereas, in the present work the structure remains cubic. Collected data were refined by the Rietveld method using Fullprof suite program. Detailed information, extracted from the Rietveld refinement, of BZY15 structure is listed in Table 5.2, based on which the refinement are carried out. The Rietveld parameters were $\chi^2 =$ 1,497 and $R_F = 5$ %, which are between the considered acceptable values $\chi^2 < 2$ and $R_F < 10$ %.

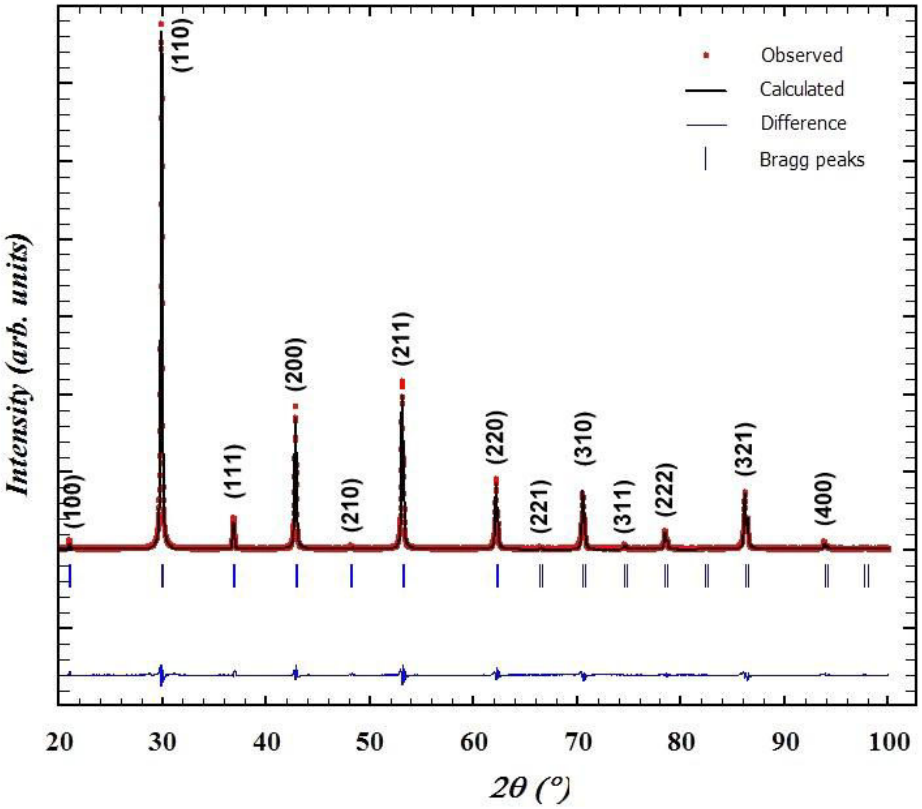

Figure 5.2.2 Diagram of XRD powder diffraction data for $BaZr_{0.85}Y_{0.15}O_{3-\delta}$ refined by Rietveld method

Table 5.2 Structural parameters and reliability factors for the Rielveld refinement of $BaZr_{0.85}Y_{0.15}O_{3-\delta}$

x = 0.15	$BaZr_{0.85}Y_{0.15}O_{3-\delta}$	
Cell parameters **Space group**	a = 4.2179(2) Å $Pm\bar{3}m$	
Atom	**Wyckoff**	**x, y ,z positions**
Ba	*2a*	x = 0.5000, y = 0.5000, z = 0.5000
Zr	*2a*	x = 0, y = 0, z = 0
Y	*2a*	x = 0, y = 0, z = 0
O	*6b*	x = 0.5000, y = 0, z = 0
R_{Bragg}, R_f		R_{Bragg} = 3.54, R_f = 5, R_{wp} = 10.2

The surface morphology of sintered BZY15 pellet was investigated by scanning electron microscopy (SEM). The result for the BZY15 is shown in the micrograph of **Figure 5.2.3**. This indicates that the surface of the samples presents a crystalline character; the relative density of the samples reaches 95 %. The average grain size is approximately 0.5 µm, with a wide distribution of grain sizes (0.2–1 µm). The small grain size is consistent with the observation that BZY is highly refractory with low rates of grain growth under typical sintering conditions. The step of covering the samples had little effect on density, but tended to yield materials with slightly larger grain sizes.

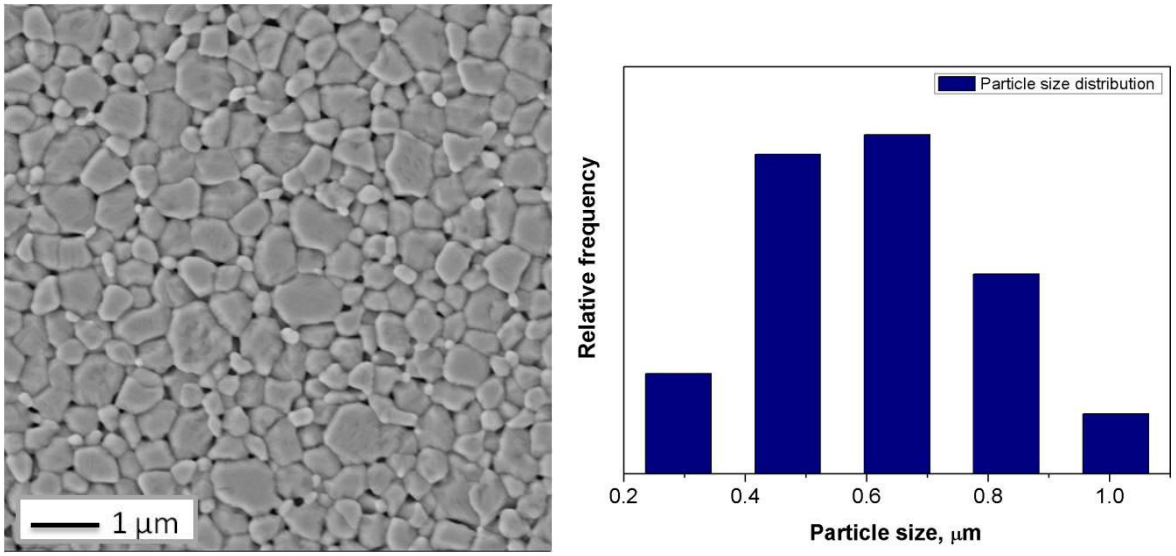

Figure 5.2.3 SEM picture of pellet surface of $BaZr_{0.85}Y_{0.15}O_{3-\delta}$ sintered at 1600 °C for 24 h

5.3.1 Enhanced Sintering of Yttrium doped Barium Zirconate by addition of ZnO and NiO

Given the difficulties in sintering $BaZrO_3$-based materials, the use of sintering aids was an obvious choice to improve the $BaZrO_3$ sinterability. Babilo and Haile [26] screened a number of transition metal oxides as sintering aids for BZY powders prepared by a combustion method, such as NiO, CuO and ZnO which could be the most effective additives for enhancing barium zirconate densification. Recently, both Haile's and Irvine's groups have reported that ZnO as an additive or a second dopant can favour a high densification at low sintering temperature (1300 – 1350 °C), and can strengthen the chemical stability, even if this slightly decreases the total conductivity [26, 34-37]. The results reported are nevertheless contradictory concerning zinc position in the materials. Babilo *et al.* [26] reported that ZnO accumulates in the intergranular regions as observed by SEM and energy dispersive X-Ray spectroscopy (EDS). This could also be expected to increase the vacancy concentrations on both the Ba and oxygen sites:

$$ZnO \rightarrow Zn''_{Zr} + O^{\times}_{O} + 2V^{\cdot\cdot}_{O} + V''_{Ba} \qquad (5.4)$$

where Zn''_{Zr} and $O^{\times}_{O}$ represent Zn ion occupying Zr lattice site and O ion at normal lattice site, respectively, V''_{Ba} is vacancy of Ba. On the other hand, Tao *et al.* [34] reported that zinc enters the lattice structure because of the ionic size of Zr^{4+} and Zn^{2+} ions are 0.72 and 0.74 Å, respectively, which are fairly close. From this point of view, Zn^{2+} ions are easier to enter the $BaZrO_3$ lattice than other transition ions and this could be the reason why zinc is a more effective additive than other transition metal oxides. ZnO reacts with barium oxides to form intermediate barium zinc oxides with relative lower melting point decreasing the sintering temperature. Another possibility is that zinc enters the perovskite lattice and the Zn-containing perovskite exhibits a lower melting point, which further leads to denser samples. Herein we describe use of ZnO and NiO sintering aids to achieve higher densification of BZY15 at lower sintering temperatures.

The calcined powders of BZY15 were mixed with given quantities of ZnO and NiO and then milled in a planetary mill (300 rpm) for 24 hours. A ZrO_2 container and ZrO_2 balls of 5 mm diameter were used. The powders were axially pressed pressed into 10 mm pellets by uniaxial pre-pressing in a steel die under 2 t pressure for 1 min, and then isostatically pressed at 750 MPa during 10 min (green densities ~ 60-70 %). The pellets were surrounded with a powder mixture of already sintered Y-substituted barium zirconate powder mixed with 10% of $BaCO_3$, as it was suggested by Babilo *et al.*[26] (**Figure 5.2.1**) and then sintered at 1300 °C for 24 hours. The relative densities of sintered pellets were determined by measuring the dimensions and weight of each sample, as described in Chapter 2 and presented in Table 5.4. NiO sintering aid can increase significantly the density of samples at 1300 °C, but still the density is lower than for pure BZY15 at higher temperature. In case of ZnO additive, we could observe a maximum in density 97 % for 1 % of ZnO, and then slight decrease of density for higher doping levels. X-Ray diffraction patterns of sintered pellets of BZY15 with ZnO and NiO sintering aids are presented in **Figure 5.2.4.** As we could notice, there is no new phase formed. In all cases, a single phase with a cubic structure is observed (space group $Pm\bar{3}m$). The lattice parameters were refined using FullProf program, see in Table 5.4. Dense single phases of BZY15 compound are obtained at 1300 °C, which is about 300 °C lower than for BZY15 without ZnO and NiO. A similar behavior was shown in the compound BZY20, for which the dense single phase preparation temperature with ZnO is roughly 350 °C lower than that required for pure BZY20 [34].

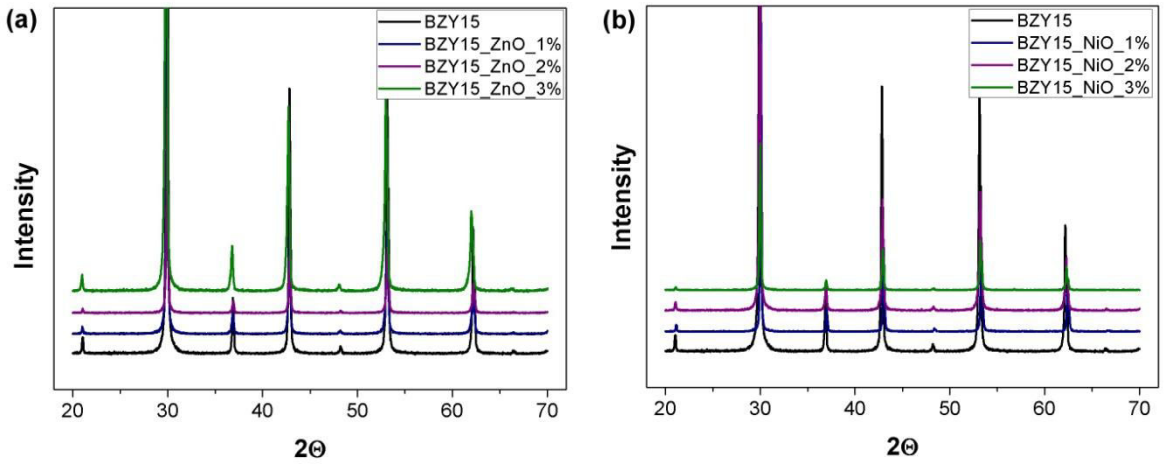

Figure 5.2.4 XRD patterns of sintered pellets of BZY15 with ZnO (a) and NiO (b) additives after sintering at 1300 °C

Table 5.4 The lattice parameters and relative densities of BZY15 compounds after sintering at 1300 °C

Sample	Cell parameter a, Å	Cell volume, Å^3	Relative density, %
BZY15 + ZnO 1%	4.2201(2)	75.159	97
BZY15 + ZnO 2%	4.2219(4)	75.258	92
BZY15 + ZnO 3%	4.2285(2)	75.611	90
BZY15 + NiO 1%	4.2065(1)	74.437	84
BZY15 + NiO 2%	4.2118(1)	74.719	90
BZY15 + NiO 3%	4.2131(2)	74.784	94

The microstructure of sintered pellets is shown in **Figure 5.2.5** and **5.2.6.** The SEM pictures of BZY15+ZnO are presented in **Figure 5.2.5.** The grain size grows obviously with increasing the percent of ZnO: from 0.7 - 1 µm for 1 % of ZnO to 1.5 - 2.5 µm for 3 % of ZnO. **Figure 5.2.6** illustrates the microstructure of samples with NiO as a sintering aid sintered at 1300 °C. We can see the similar behavior as for the ZnO samples: an increase of grain size from 0.5 - 1 µm for 1 % of NiO to 1.5 - 2.5 µm for 3 % of NiO. It confirms the same results which were reported in [26] that the grain size of Y-doped $BaZrO_3$ with 4 mol % ZnO is higher than that of simple Y-doped $BaZrO_3$ for samples sintered at 1300 °C. Hence, considering the great difference of temperature between the two treatments, we can consider that NiO and ZnO favours grain growth.

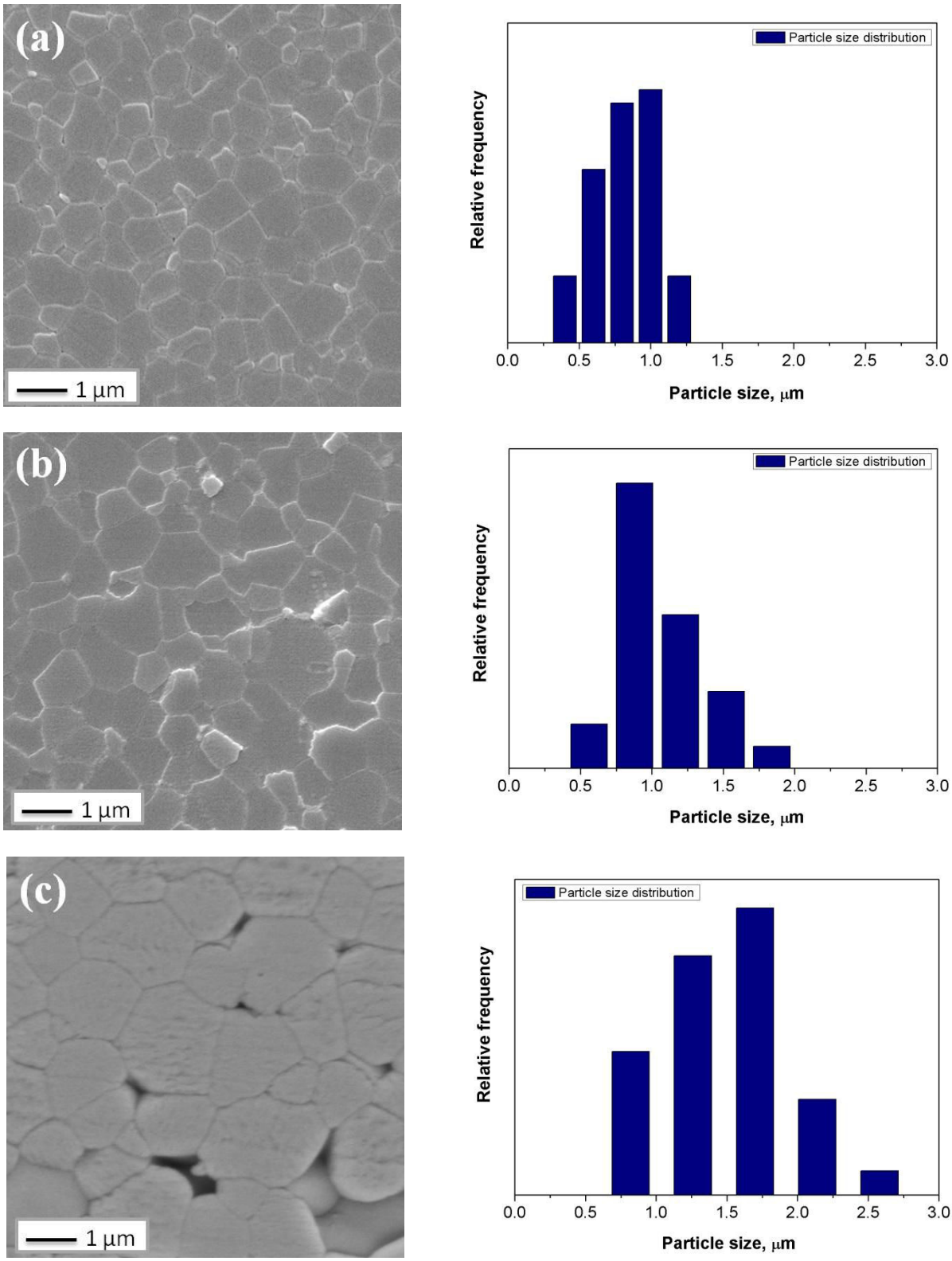

Figure 5.2.5 SEM pictures of pellet surface of BZY15+ ZnO (1, 2, 3% respectively) sintered at 1300 °C for 24 h

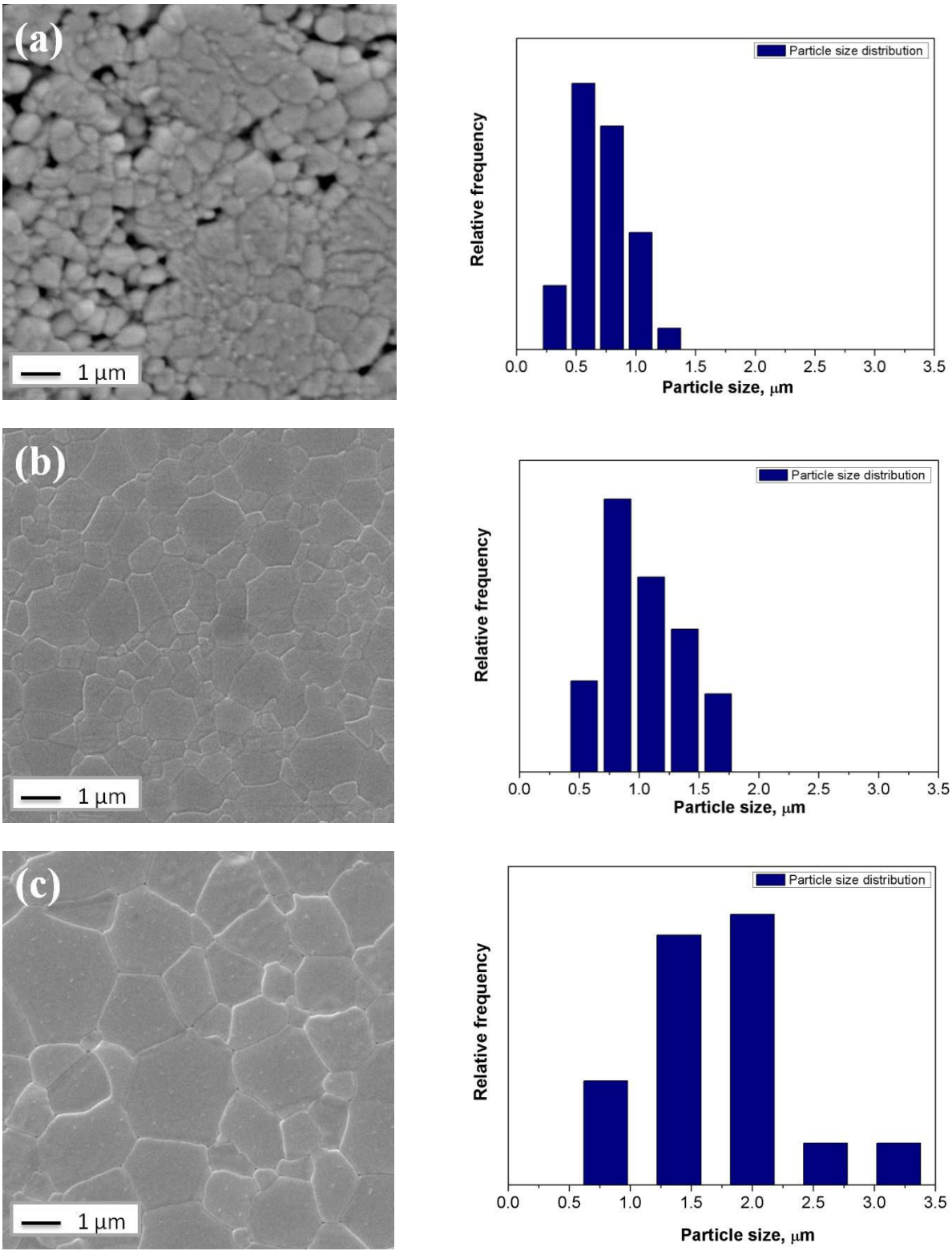

Figure 5.2.6 SEM pictures of pellet surface of BZY15+ NiO (1, 2, 3% respectively) sintered at 1300 °C for 24 h

5.4 Transport properties

Impedance spectroscopy (IS) was performed on dense pellets with both sides coated with platinum paste as electrodes, using a Solartron 1260 Frequency Response Analyser in the 1 MHz – 0.1 Hz frequency range under dry and wet Ar in the temperature range 300 – 900 °C. The modelling of the impedance spectra gives access to the values of the conductivity for the different contributions. The Nyquist representation (Z" versus Z' as parametric functions of the frequency) for BZY15 sample monitored at different temperatures under dry and wet conditions is shown in **Figure 5.3.1.** The fitting of the data is illustrated by the red line. The modeling of the impedance spectra was done by using ZView software.

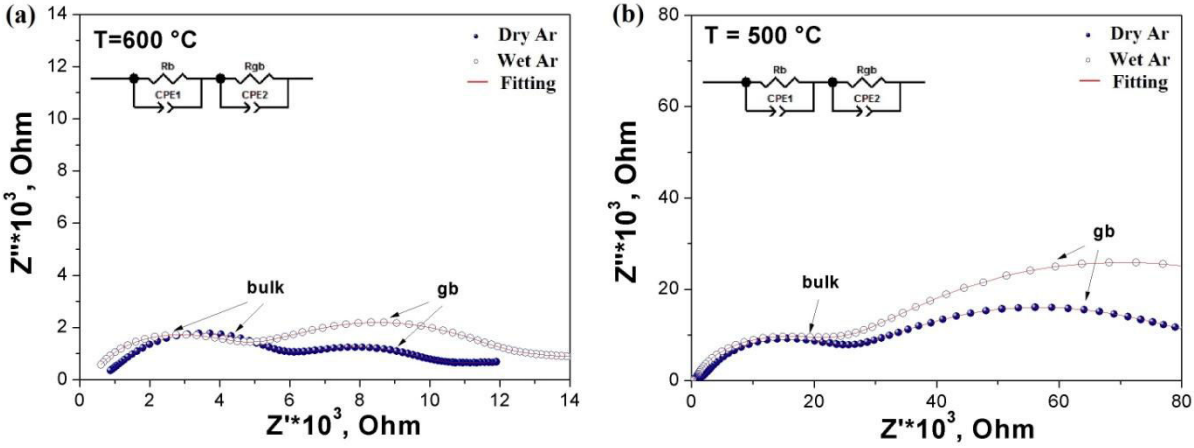

Figure 5.3.1 The Nyquist plots of BZY15 in dry and humidified Ar at different temperatures: 600 °C (a) and 500 °C (b)

A general trend can be observed for all samples: at high temperatures, conductivities are the same under wet and dry conditions but at low temperatures, conductivities in wet argon become higher than those in dry argon. This indicates that proton conductivity is certainly dominant at low temperature. **Figure 5.3.2** shows dependences of electrical conductivity for BZY15 sample. The conductivity of BZY15 measured under dry conditions is of about 0.5 order of magnitude lower for the bulk and about 0.3 order of magnitude lower for the grain boundary than under wet conditions. The bulk conductivity is 3×10^{-4} S.cm^{-1} at 600 °C what is 1 order of magnitude lower than reported by Schober *et al.* [10] and Snijkers *et al.* [31]. Activation energies for BZY15 are listed in the Table 5.5. According to literature, the activation energy for yttrium-substituted $BaZrO_3$ was about 0.42 eV - 0.31 eV in the 5 mol % to 15 mol% of Y^{3+} on Zr site [32]. Kreuer reported that the activation energy was about 0.44 eV in the Y^{3+} concentration range of 2 mol % to 10 mol % and 0.48 eV for BZY20 [12]. These last results for zirconates compounds suggest that the proton transport activation energy is constant at low substituant concentration, and might increase for higher Y^{3+} concentration.

Our results for pure BZY15 indicate activation energy of 0.54 eV which is significantly higher to that observed by the previously mentioned authors. A possible explanation is that our sample was not at thermodynamical equilibrium in spite of low cooling ramp (12 °C/ h).

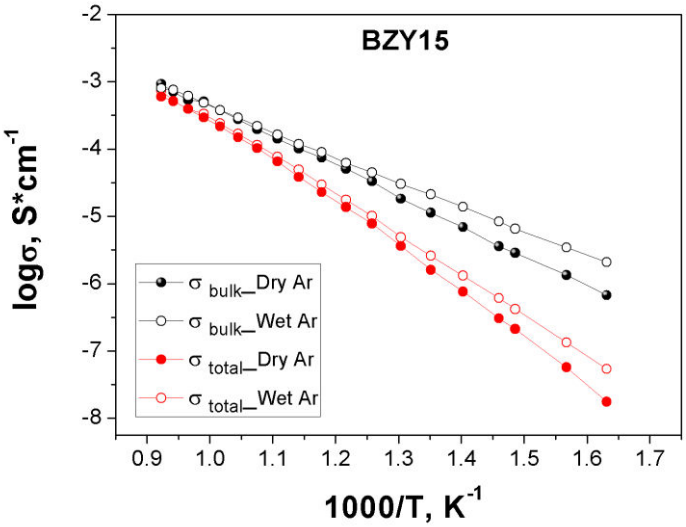

Figure 5.3.2 Bulk and total conductivities of BZY15 under dry and wet Ar

Figures 5.3.3 and **5.3.4** show that the conductivities are affected by the ZnO and NiO as a sintering aid. The results for all compositions show that the conductivity is dominated by grain boundary conductivity and that the effect is more evident under wet atmosphere since grain boundary conductivity evolves only slightly with humidity. A similar behavior exists in most of proton conductors, in particular barium zirconate compounds [12, 17, 32, 33]. For ZnO as a sintering aid, Babilo *et al*. [24] reported that the bulk conductivity of 4 mol % ZnO modified $BaZr_{0.85}Y_{0.15}O_{3-\delta}$ is lower than that of unmodified. However, in this study, we observed that 1 mol % ZnO as a sintering aid increase the bulk conductivity. Further increase of ZnO quantity leads to a decrease of bulk and total conductivity, which possibly reflects of the lower sample's density. The linear behavior of the logarithm of conductivity versus 1/T is observed at all temperatures in the dry Ar, from which the activation energy of the total, bulk and grain boundary conductivity can be extracted. In Table 5.5 are gathered the activation energy in the dry and wet Ar as obtained from the measurements between 300 °C and 900 °C. The activation energy of the bulk conductivity for ZnO modified BZY15 samples increases from 0.52-0.56 eV under wet conditions to ~0.70 eV under dry conditions, whereas the activation energy of the grain boundary conductivity is similar for both atmospheres with a value of ~ 1.1 eV.

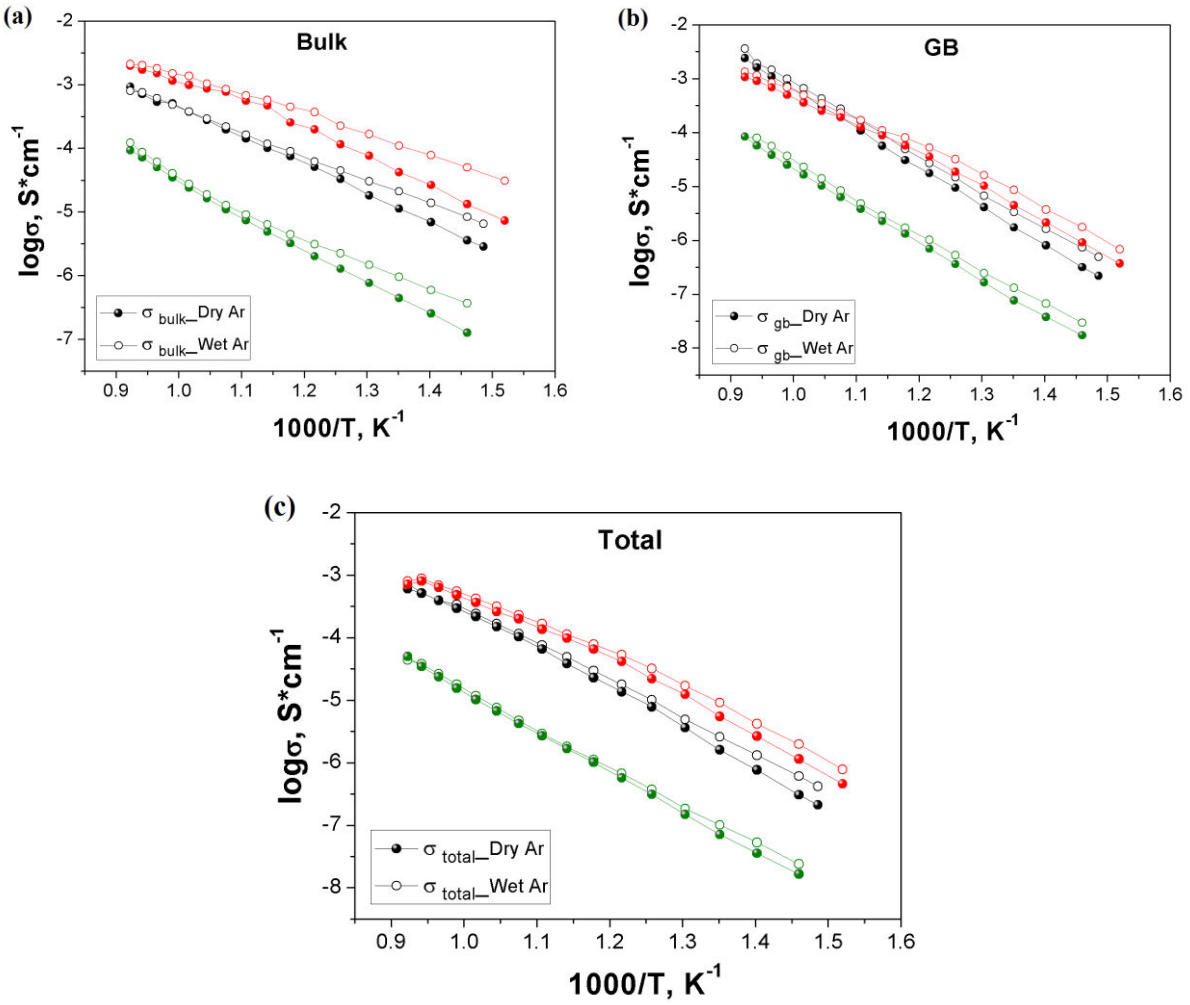

Figure 5.3.3 The conductivity of samples measured in dry and wet Ar: BZY15 (●- dry Ar, ○- wet Ar), BZY15+ZnO 1% (●- dry Ar, ○- wet Ar), BZY15+ZnO 2% (●- dry Ar, ○- wet Ar)

Table 5.5 Activation energy of bulk, grain boundary and total conductivities of BZY15 compounds under Ar atmosphere

Composition	Total Dry (eV)	Bulk Dry (eV)	GB Dry (eV)	Total Wet (eV)	Bulk Wet (eV)	GB Wet (eV)
BZY15	1.17	0.70	1.11	1.10	0.54	1.04
BZY15 + ZnO 1%	1.08	0.72	1.14	1.01	0.52	1.08
BZY15 + ZnO 2%	1.18	0.71	1.09	1.13	0.56	1.02
BZY15 + NiO 1%	1.15	0.70	1.10	1.08	0.55	1.04
BZY15 + NiO 2%	1.01	0.69	0.99	1.01	0.48	1.00

In the case with NiO modified BZY15 samples we observed another behavior: due to the low density of 1 mol % NiO sample, conductivity is significantly lower (1.5 order of magnitude) than pure BZY15. With increasing density and grain size for 2 mol % NiO we could noticed a slight increase of total conductivity comparing to the 1 mol % NiO sample, what is still lower than total conductivity of unmodified BZY15. In a low temperature range difference in conductivity values in dry and wet atmosphere reaches 1 order of magnitude for 2 mol % NiO sample. Activation energy for all conductivities is presented in Table 5.5. The activation energies of bulk conductivities were between 0.48 eV and 0.55 eV, which is typical for proton conductors (0.4 - 0.5 eV) [19, 20].

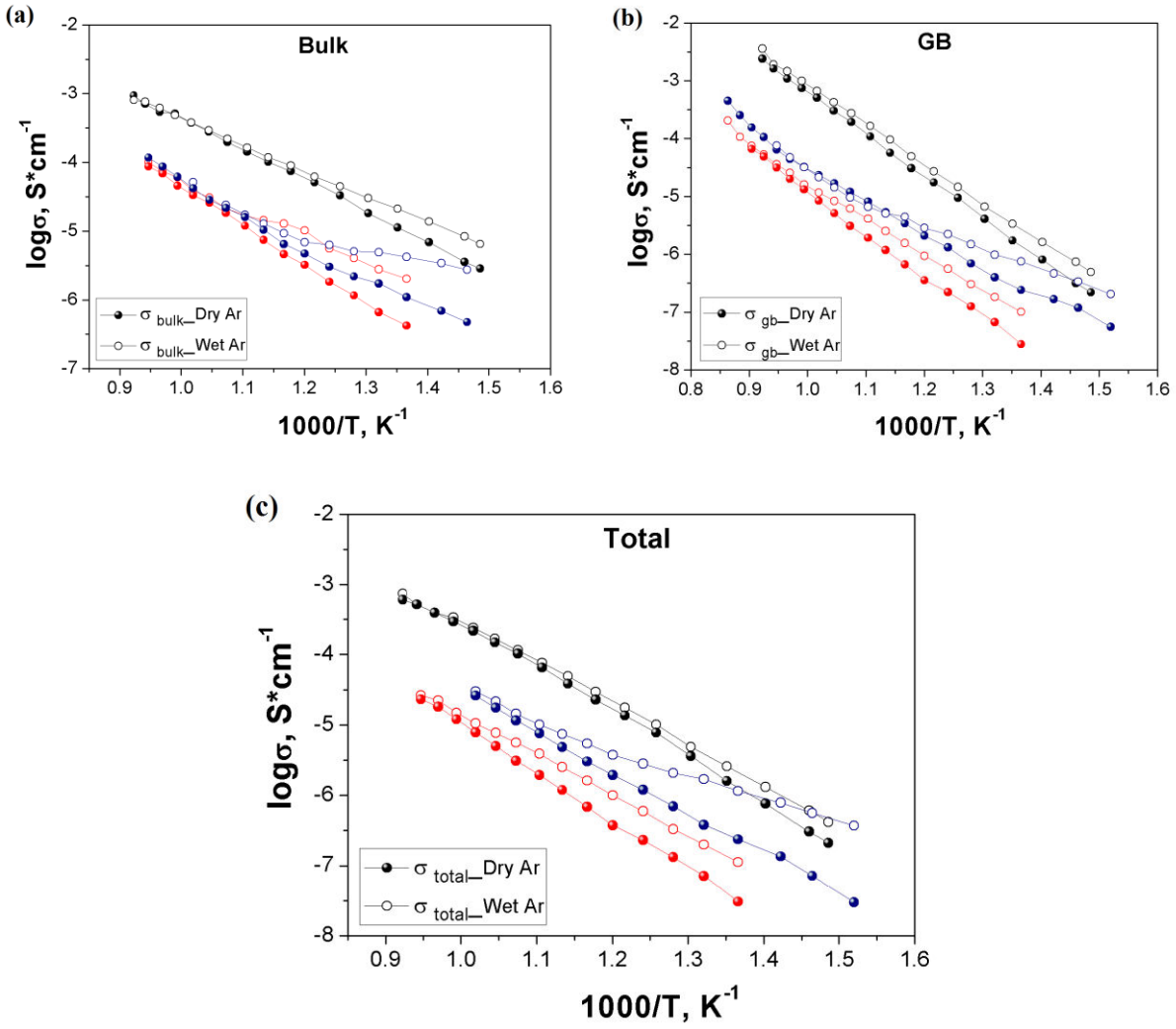

Figure 5.3.4 The conductivity of samples measured in dry and wet Ar: BZY15 (●- dry Ar, ○- wet Ar), BZY15+NiO 1% (●- dry Ar, ○- wet Ar), BZY15+NiO 2% (●- dry Ar, ○- wet Ar)

5. 5 Conclusion

Crystalline fine powders of BZY15 have been prepared by a modified citrate-EDTA complexing method. Dense BZY15 (95% of the theoretical density) is prepared by compaction of the green body at 750 MPa and sintering at 1600 °C. Homogeneous grains with a mean grain size of ~ 0.5 µm are obtained. Single-phase and dense BZY15 compounds have been successfully prepared at 1300 °C by adding 1-3 mol % ZnO and NiO as a sintering aid using a planetary ball mill. This temperature is significantly lower than the one to obtain dense ceramics (1600 °C) without sintering aid. Structural characterization reveals that all compounds present a cubic perovskite structure with a space group $Pm\bar{3}m$. Maximum density is obtained for 1 mol % ZnO modified BZY15 (97% of the theoretical density). SEM observations confirmed that grain size grows with an increase of mol % of sintering aid.

Measurements by impedance spectroscopy were performed under dry and wet argon. The bulk and the grain boundary contributions were separated. The bulk conductivity is dominated by proton transport. At low temperature, proton conduction is observed in humid atmosphere for all compounds. Indeed, the bulk conduction increases greater in humid atmosphere while it increases only slightly for GBs. Bulk conductivity of 1 mol % zinc oxide modified BZY15 is higher than that of unmodified BZY15. It reaches 9×10^{-3} S.cm^{-1} at 600 °C that still lower than reported by Schober *et al.* [10] and Haile *et al.* [26]. The grain boundaries are the limiting contribution to the total conductivity. Although the conductivity of NiO modified BZY15 is somewhat lower than the unmodified counterpart, the dramatic reduction in sintering temperature (from ~1600 –1700 °C), which will enable the exploration of a wider variety of potential electrode materials, renders the modified composition an attractive alternative to simple BZY15. Therefore, optimization of transport properties relies heavily on the ability to grow grains to moderate sizes so as to reduce total grain boundary area. Modification of BZY15 with sintering aids enhances grain growth and addresses precisely this challenge, although further optimization will be necessary in order to obtain total grain boundary conductivity that is greater than that of unmodified BZY15.

References:

[1] S. Parida, S.K. Rout, L.S. Cavalcante, E. Sinha, M.S. Li, V. Subramanian, *Ceram. Int.,* **2012**, 38, 2129–2138.

[2] A.M. Azad, S. Subramaniam, T.W. Dung, *J. Alloy. Compd.,* **2002**, 334, 118–130.

[3] Z. Sherafat, I. Antunes, C. Almeida, J.R. Frade, M.H. Payder, G.C. Mather, D.P. Fagg, *Dalton Trans*., **2014**, 43, 9324–9333.

[4] P.G. Sundell, M.E. Bjorketun, G.Wahnstrom, *Phys. Rev.,* **2006**, B 73, 104-112.

[5] A. Erb, E. Walker, R. Flukiger, *Physica*, **1995,** C 245, 245.

[6] K. Katahira, Y. Kohchi, T. Shimura, H. Iwahara, *Solid State Ionics*, **2000**, 138, 91.

[7] K.D. Kreuer, *Annual Review of Material Research*, **2003**, 33, 333.

[8] K.H. Ryu, S.M. Haile, *Solid State Ionics*, **1999,** 125, 355.

[9] R. C. T. Slade, S. D. Flint, N. Singh., *Solid State Ionics,* **1995,** 82, 135.

[10] T. Schober, H.G. Bohn, *Solid State Ionics*, **2000,** 127, 351.

[11] Stephen J. Stokes , M. Saiful Islam, *J. Mater. Chem.,* **2010**, 20, 6258–6264.

[12] K.D. Kreuer, St. Adams, W. Münch, A. Fuchs, U. Klock, J. Maier, *Solid State Ionics*, **2001,** 145, 295.

[13] Y. Yamazaki, P. Babilo, S.M. Haile, *Chemistry of Materials*, **2008,** 20, 6352.

[14] V.P. Gorelov, V.B. Balakireva, *Rus. J. Electrochem*., **2009,** 4 (45), 476.

[15] S.B.C. Duval, P. Holtappels, U.F. Vogt, E. Pomjakushina, K. Conder, U. Stimming, T. Graule, *Solid State Ionics*, **2007,** 178, 1437.

[16] Erik Jedvik, *Master Thesis*, Goteborg, Sweden, **2014**.

[17] F. Iguchi, T. Yamada, N. Sata, T. Tsurui, H. Yugami, *Solid State Ionics*, **2006,** 177, 2381.

[18] D. Shima, S.M. Haile, *Solid State Ionics*, **1997,** 97, 443.

[19] Thermodynamic database MALT group, Thermodynamic database MALT for Windows, Kagaku Gijutsu-Sha, **2005**.

[20] L. Bi, S. P. Shafi, E. Traversa, *J. Mater. Chem*., **2015**, 3, 5815–5819.

[21] H. Iwahara, T. Yajima, T. Hibino, K. Ozaki, H. Suzuki, *Solid State Ionics*, **1993,** 61, 65-69.

[22] F. M. M. Snijkers, A. Buekenhoudt, J. Cooymans, J. J. Luyten, *Scripta Mater*., **2004,** 50, 5, 655-659.

[23] H. G. Bohn, T. Schober, *J. Am. Ceram. Soc*., **2000,** 83, 4, 768-772.

[24] P. Babilo, T. Uda, S.M. Haile, *J.Mat. Res.,* **2007,** 22, 1322.

[25] S. Ricote, N. Bonanos, H.J. Wang, B.A. Boukamp, *Solid State Ionics*, **2012,** 213, 36–41.

[26] P. Babilo, S.M. Haile, *J. Am. Ceram. Soc*., **2005,** 88 (9), 2362.

[27] X. Guo, R. Waser, Progr.Mat. Scien., **2006**, 5 (2), 151.

[28] S. Imashuku, T. Uda, Y. Nose, K. Kishida, S. Harada, H. Inui, Y. Awakura, *J. Electrochem. Soc*., **2008,** 155, B581.

[29] Y.-S. Jung, J.-H. Lee, J.-H. Lee, D.-Y. Kim, *J. Electrochem. Soc.*, **2003,** 150, J49.

[30] X. Guo, *J. Am. Ceram. Soc*., **2003,** 86, 1867.

[31] M.C. Martin, M.L. Mecartney, *Solid State Ionics*, **2003,** 161, 67.

[32] F. Iguchi, N. Sata, T. Tsurui, H. Yugami, *Solid State Ionics,* **2007,** 178, 691–695.

[33] S. Duval, *PhD thesis*, Munich, **2008**.

[34] S. Tao, J. T. S. Irvine, *J. Solid St. Chem.,* **2007**, 180, 3493.

[35] C. Savaniu, J. T. S. Irvine, *Solid State Ionics,* **2003**, 162-163, 105.

[36] T. S. I. S. W. Tao, *Advanced Materials,* **2006**, 18, 1581.

[37] A. K. Azad, J. T. S. Irvine, *Solid State Ionics,* **2008**, 179, 678.

[38] M. Laidoudi, I. Abu Talib, R. Omar., *J. Phys. D: Appl. Phys.,* **2002**, 35, 397.

[39] W. S. Wang, A. V. Virkar., *J. Power Sources,* **2005**, 142, 1.

[40] C. D. Savaniu , J. Canales-Vazquez, J. T. S. Irvine, *J. Mater. Chem.* **2005,** 15, 598.

Chapter 6 General conclusions and perspectives

6.1 Summary

This work mainly concerned three families of compounds $Gd_{3-x}Me_xGaO_{6-\delta}$ (Me = Ca^{2+}, Sr^{2+}), $Ba_2Y_{1+x}Nb_{1-x}O_{6-\delta}$ and $BaZr_{0.85}Y_{0.15}O_{3-\delta}$ (BZY15) which have been systematically investigated as potential electrolyte materials for solid oxide cells.

In the first part of this thesis, we showed that $Gd_{3-x}Me_xGaO_{6-\delta}$ (Me = Ca^{2+}, Sr^{2+}) materials have been successfully synthesized by microwave-assisted citric acid combustion method. Low levels of oxygen vacancies were created in the Gd_3GaO_6 structure by doing cationic substitutions (Ca^{2+}, Sr^{2+}) on Gd-sites. Pure and homogeneous powders were obtained after calcinations at 900 °C for 5 h. According to SEM observations the average particle size is around 100 nm. The sinterability of nanopowders is dependent on the dopant nature but, in all cases, rather high if compared to the pristine composition Gd_3GaO_6. The highest density of samples, after sintering at 1450 °C for 10 h, was found for 10 % doping level and it reaches 94 % for $Gd_{2.9}Ca_{0.1}GaO_{6-\delta}$ and 96 % for $Gd_{2.9}Sr_{0.1}GaO_{6-\delta.}$ Detailed crystal structural information was obtained from Rietveld refinement of X-Ray diffraction data. Solid solutions are formed till 10 % of doping content and all the compositions in this range have a single phase and are isostructural with pure Gd_3GaO_6 (non-centrosymmetric orthorhombic structure, space group $Cmc2_1$). Cell parameters increase slightly with increasing dopant concentration. The conductivity of the well-sintered Ca/Sr-doped samples of Gd_3GaO_6 was measured in dry and wet argon. When dealing now with the behavior of such compounds as proton conductors, we observed that all compounds present at intermediate temperature dominating proton conduction in wet atmosphere. The best conduction properties are observed for higher Ca^{2+} and Sr^{2+} contents, 7.1×10^{-5} $S.cm^{-1}$ and 7.5×10^{-4} $S.cm^{-1}$ at 600 °C in wet argon respectively. Our compounds have the same level of conductivity comparing with materials whose structure contains tetrahedral units, such as $La_{0.99}Ca_{0.01}NbO_4$. The stabilities of $Gd_{3-x}Me_xGaO_{6-\delta}$ (Me = Ca^{2+}, Sr^{2+}) were investigated under different atmospheres and conditions. In H_2O, CO_2 and H_2-containing atmospheres, all materials show an excellent stability, as confirmed by XRD.

The second part was an exploration of $Ba_2Y_{1+x}Nb_{1-x}O_{6-\delta}$ group of oxides. Nanopowders of the desired stoichiometry were prepared by the freeze-drying process and then calcinated at 900 °C for 30 min in ambient atmosphere. Solid solutions are formed till 20% of yttrium doping. It was found that the samples $Ba_2Y_{1+x}Nb_{1-x}O_{6-\delta}$ are single-phase in the range $0\leq x \leq 0.2$ and the diffraction pattern could be indexed in a cubic structure of double perovskite (space group $Fm\bar{3}m$). The microstructures of sintered samples were observed by using SEM and it shows that the average grain size increased

significantly with increasing amount of Y, *e.g.*, from 1 to 5 µm. First TEM observations confirm the cubic structure, but the degree of ordering is nevertheless difficult to evaluate because of the too high thickness of lamella made by FIB.

The conductivity measurements were performed under mixture of $Ar+H_2$ in different humidity of atmosphere. As a general rule, the highest conduction properties are obtained for the highest doping levels, which indicate that for the range of composition studied the conductivity is driven by the number of charge carriers. For instance, the partial replacement of 20 % of niobium by yttrium noticeably improves the conductivity till 2.5×10^{-4} S.cm^{-1} at 800 °C. Nevertheless, in the conditions of measurements (Ar/H_2), the charge carriers are certainly of mixed nature (electron/oxygen-proton), since measurements in air lead to a too insulating compound. We assume thus that there is a partial reduction of niobium under hydrogen for this series of compounds. In order to understand better why the level of ion conduction is so low in $Ba_2Y_{1+x}Nb_{1-x}O_{6-x}$ in spite of high doping levels and adequate microstructure, we performed Molecular dynamics (MD) simulations. MD confirms the fact that local environment is different for Nb^{5+} and Y^{3+} ions with a tendency of yttrium dopant ion to trap oxygen vacancies. This strong trapping effect can be related to the great difference of size between Niobium atoms (r_{Nb5+} = 0.64 Å) and Yttrium dopants atoms (r_{Y3+} = 0.90 Å). Stability under wet atmospheres and against CO_2 were also explored and all compounds get partially reduced.

The third part was presented a study of the sintering of BZY15 compound, without and with ZnO and NiO additives. BZY15 powders were prepared by a modified citrate-EDTA complexing method. This nanopowder fabrication process provides good phase purity at a low synthesis temperature. XRD patterns indicated that powders have characteristic diffraction peaks of a crystalline structure of $BaZrO_3$. We showed that the use of ZnO and NiO as sintering aids for the BZY15 compound allows obtaining a relative density till 97 % for 1 % ZnO after a sintering at 1300 °C. This temperature is significantly lower than the required sintering temperature 1600 °C without additive. In all cases, a single phase with a cubic structure is observed (space group $Pm\bar{3}m$). The grain size grows obviously with increasing the percent of sintering aid from 0.5 µm for BZY15 to 2.5 µm for 3 % of additive what confirmed by SEM observations. Measurements by impedance spectroscopy were performed under dry and wet argon. Our results for pure BZY15 indicate activation energy of 0.54 eV which is significantly higher to that observed in literature. A possible explanation is that our sample was not at thermodynamical equilibrium in spite of low cooling ramp (12 °C/ h) due to low diffusion rate in high density nanocrystalline samples. At low temperature, the proton conduction is limited by the grain boundary rather than the bulk. However, we could notice that 1 % of Zinc oxide as a sintering aid slightly increases bulk and total conductivity comparing with pure BZY15. The best conductivity for these series of samples has 1 % of ZnO and reaches 9×10^{-3} S.cm^{-1} above 600 °C.

6.2 Perspectives

Further work is suggested on the following topics:

1. $Gd_{3-x}Me_xGaO_{6-\delta}$ (Me = Ca^{2+}, Sr^{2+}):

- MD simulations would concern the modeling of protons inside the doped Gd_3GaO_6 materials. This would give some indications on the localization of protons, migration energies and mechanism of migration. More interesting would be to determine the possible dopant–proton interaction energies that would help determining the best dopant elements. Such simulations could also concern the behavior of oxygen vacancies.

- Transport numbers measurements by EMF method.

- Due to their stability, the gallates could be used in high temperature devices expecting that the amount of filled vacancies could increase under several atmospheres of water vapour.

- The performances of the doped Gd_3GaO_6 materials operating in fuel cells have never been tested so far. It would be of main interest. Therefore, adequate electrodes have to be developed.

2. $Ba_2Y_{1+x}Nb_{1-x}O_{6-\delta}$:

- Further exploration of local structure by TEM technique. In particular, the study of the environment of yttrium dopant atoms will give a definite confirmation of the proposed mechanism of oxygen vacancy trapping.

- Transport numbers measurements by EMF method.

- Since Yttrium dopant is thought to ask as a trap for oxygen vacancies. Further dopants might explored. MD simulations might play a significant role to anticipate which dopant would give the best oxygen diffusion coefficient. We anticipate that dopant with a size closer to that of Nb^{+5} would be more adequate. Experiments are currently performed with Sc^{+3} and Ga^{+3} dopants.

3. BZY15:

- Densification and microstructure of BZY15 at low temperature should be improved.

- Perform a conductivity measurement with different cooling rate to reach a thermodynamical equilibrium with the objective to obtain a bulk conductivity closer to that of previous works.

- Ion exchange depth Profile: the oblation of dense samples could allow using this material as a standard for calibration proton exchange measurements.

- Atomic Probe Tomography: this method allows obtaining an atomic scale distribution of the elements. In our case, it could be applied on nanostructured ceramics to locate potential Y/Zr segregation or Ba depletion at grain boundary, this to explain the specificity of BZY15 conductivity. The very first experiments did not give the expected results.